Title

Biomineralized matrix and small molecule for bone tissue engineering

Author

Kang, Heemin

Publication Date

2016

UNIVERSITY OF CALIFORNIA, SAN DIEGO

Biomineralized matrix and small molecule for bone tissue engineering

A dissertation submitted in partial satisfaction of the
requirements for the degree Doctor of Philosophy

in

Materials Science and Engineering

by

Heemin Kang

Committee in Charge:

Professor Shyni Varghese, Chair
Professor Prabhakar Rao Bandaru
Professor Ratneshwar Lal
Professor Yu-Hwa Lo
Professor Vlado Lubarda

2016

The dissertation of Heemin Kang is approved, and it is acceptable in quality and form for publication on microfilm and electronically:

Chair

University of California, San Diego

2016

Epigraph

“In their hearts humans plan their course, but the LORD establishes their steps.”

Proverbs 16:9

Table of Contents

Chapter 4: Biomineralized matrices dominate soluble cues to direct osteogenic differentiation of human mesenchymal stem cells through adenosine signaling 95

List of Figures

List of Tables

Acknowledgements

There is a great deal of people that I would like acknowledge for helping me succeed in the PhD study. I would like to first and foremost thank my advisor, Prof. Shyni Varghese. Her persistent guidance and criticism have given me an opportunity to grow as a scientist and team player. I largely attribute my success in PhD study to her professional and personal advice. She allowed me to realize many attributes required for one to succeed in the academic field and offered me many opportunities to make significant improvements. In short, she has made me stand where I am now. I hope that I continue to have opportunities to repay her in any forms after my graduation.

I would like to extend my thankfulness to the present and past members of the Varghese research group. In particular, I would like to thank Dr. Yu-Ru Vernon Shih, Dr. Ameya Phadke, and Prof. Yongsung Hwang for their mentorship, collaborations, and friendship. I was fortunate to learn from these people, especially during my early days in the Varghese laboratory. Dr. Shih has inspired me with scientific criticism as well as his in-depth and broad knowledge of cell biology. I wish all the best in his academic career and hope to continue on our fruitful works and discussions. My dissertation was an extension of Dr. Phadke's works on biomineralized matrices for bone tissue engineering and I thank him for transferring knowledge and skills to me. I truly believe he will be an excellent industrial leader. I also thank Prof. Hwang for teaching me many hands-on experimental skills and personally advising me. I wish the best success in his faculty career.

There are still numerous Varghese group members to whom I would like acknowledge my indebtedness. They have been great collaborators and friends all throughout my PhD study. In the musculoskeletal co-works, I first thank Vikram Rao for spending lots of time together on the experiments, discussion, and personal matters. I also thank other past members, Dr. Cai Wen, Samuel Suk, Young Nam Seo, Andrew Richards, Harsha Kabra, Gus Patton, Dr. Manando Nakasaki, and Dr. Mrityunjoy Kar for interacting with me on the experiments and discussions for a long time and staying as friends after leaving the lab. I would to acknowledge new and current members, including Eva Gonzalez, Jasper Zeng, Mengqian Liu, Sara Hariri, and Priya Nayak, for working closely on the projects to continue on our intriguing works as well as having an overall fun time together. I extend my gratitude to current and past senior members, including Aereas Aung, Han Liang Lim, Shruti Davey, Gaurav Agrawal, and Susan Lin, for their help, comradeship, and long-term interpersonal interactions. I express my gratitude to professors, including Prof. Sungwook Seo, Prof. Seong Keun Kwon, Prof. Jae-Min Oh, Prof. Jaekwang Kim, Prof. Dongan Wang, and Prof. Gaurav Arya, for their professional discussions and personal interactions.

I also thank all my current committee members, Prof. Prabhakar Bandaru, Professor Ratneshwar Lal, Prof. Yu-Hwa Lo, and Prof. Vlado Lubarda as well as previous committee member, Prof. Sungho Jin, for helpful guidance and suggestions on my PhD works.

I appreciate editors in Acta Biomaterialia journal, including Prof. William R. Wagner, Prof. Subhash Mahajan, Prof. Marc Bohner, and Prof. William L. Murphy, for selecting me as a recipient of the Acta Student Award. I also thank the Jacobs School of

Engineering communications team for publishing a story detailing my receiving this award. It is important to acknowledge Prof. Varghese for nominating me for this award in the first place as well as Prof. Sungho Jin and Prof. Sungwook Seo for their support.

I would like to acknowledge my friends and family. I thank Hanbit Church friends for their support and prayer. I appreciate many friends in Materials Science and Engineering program and Bioengineering department. My wife, Hyojung Kim, and daughter, Grace Haeun Kang, have been my love and support in all circumstances. I thank my parents, Ansam Kang and Kyungok Han, parents-in-law, Moonsae Kim and Eunmi Kim, and brothers, Hyomin Kang and Hyunmin Kang, for their love and encouragement. Finally, I thank God for being my Lord to lead all my life.

Chapter 1, in full, has been submitted for publication of the material as it may appear in Handbook of Intelligent Scaffolds for Tissue Engineering and Regenerative Medicine, 2nd Edition. “Biomineralized matrices as intelligent scaffolds for bone tissue regeneration”. Kang, Heemin; Shih, Yu-Ru V.; Rao, Vikram; Varghese, Shyni. Pan Stanford Publishing Pte. Ltd. The dissertation author was the primary investigator and author of this paper.

Chapter 2, in full, is a reprint of the material as it appears in Journal of Materials Chemistry B, vol. 2, 2014. “Biomineralized matrix-assisted osteogenic differentiation of human embryonic stem cells”. Kang, Heemin; Wen, Cai; Hwang, Yongsung; Shih, Yu-Ru V.; Kar, Mrityunjoy, Seo, Sung Wook; Varghese, Shyni.. The dissertation author was the primary investigator and author of this paper.

Chapter 3, in full, is a reprint of the material as it appears in Acta Biomaterialia, vol. 10, 2014. “Mineralized gelatin methacrylate-based matrices induce osteogenic differentiation of human induced pluripotent stem cells". Kang, Heemin; Shih, Yu-Ru V.; Hwang, Yongsung; Wen, Cai; Rao, Vikram; Seo, Timothy; Varghese, Shyni. The dissertation author was the primary investigator and author of this paper.

Chapter 4, in full, is a reprint of the material as it appears in Biomacromolecules, vol. 16, 2015. "Biomineralized matrices dominate soluble cues to direct osteogenic differentiation of human mesenchymal stem cells through adenosine signaling". Kang, Heemin; Shih, Yu-Ru V.; Varghese, Shyni. The dissertation author was the primary investigator and author of this paper.

Chapter 5, in full is currently being prepared for submission for publication of the material. "Small molecule-driven direct conversion of human pluripotent stem cells into functional osteoblasts". Kang, Heemin; Shih, Yu-Ru V.; Nakasaki, Manando; Kabra, Harsha; Gonzalez-Diaz, Eva; Varghese, Shyni. The dissertation author was the primary investigator and author of this material.

Chapter 6, in full is currently being prepared for submission for publication of the material. "In vivo engineering of stratified, integrated osteochondral tissue by trilayered scaffold with varying pore microstructure and osteoinductivity". Kang, Heemin; Shih, Yu-Ru V.; Kar, Mrityunjoy; Hwang, Yongsung; Zeng, Yuze; Varghese, Shyni. The dissertation author was the primary investigator and author of this material.

Vita

2005	Bachelor of Engineering in Materials Science and Engineering, Korea University, Seoul, South Korea
2008	Master of Science in Materials Science and Engineering, Stanford University, Stanford
2016	Doctor of Philosophy in Materials Science and Engineering, University of California, San Diego

Publications

Kang H, Shih YRV, Hwang Y, Vecchio KS, Varghese S. The effect of calcium phosphate extent and serum proteins in biomineralized matrices on stem cell growth and osteogenic commitment. (Manuscript in preparation).

Kang H, Shih YRV, Kar M, Hwang Y, Zeng Y, Varghese S. In vivo engineering of stratified, integrated osteochondral tissue by trilayered scaffold with varying pore microstructure and osteoinductivity. (Manuscript in preparation).

Kang H, Shih YRV, Nakasaki M, Kabra H, Gonzalez-Diaz E, Varghese S. Small molecule-driven direct conversion of human pluripotent stem cells into functional osteoblasts. (Manuscript in preparation).

Shih YRV, **Kang H**, Rao V, Chiu RYJ, Lo YH, Varghese S. In vivo engineering of bone organoids with hematopoietic functions. (Under revision).

Mo AH, Landon PB, Gomez KS, **Kang H**, Zhang C, Janetanakit W, Akkiraju S, Dossou S, Colburn DA, Varghese S, Glinskii G, Lal R. Magnetically responsive silica-gold nanobowls for targeted delivery and SERS-based sensing. (Under revision).

Kang H, Shih YRV, Rao V., Varghese S. Biomineralized matrices as intelligent scaffolds for bone tissue regeneration. Handbook of Intelligent Scaffolds for Tissue Engineering and Regenerative Medicine, 2nd Edition, Pan Stanford Publishing Pte. Ltd. (In press).

Rao V, Shih YRV, **Kang H**, Kabra H, Varghese S. Adenosine signaling mediates osteogenic differentiation of human embryonic stem cells on mineralized matrices. Frontiers in Bioengineering and Biotechnology, 2015;3:1-10.

Wen C, **Kang H**, Shih YRV, Hwang Y, Varghese S. In vivo comparison of biomineralized scaffold-directed osteogenic differentiation of human embryonic and mesenchymal stem cells. Drug Delivery and Translational Research, 2015;1-11.

Kang H, Kim H, Kim TH, Choy JH, Oh JM. Intracrystalline structure and release pattern of ferulic acid intercalated into layered double hydroxide through various synthesis methods. Applied Clay Science, 2015;112:32-9.

Shih YRV, Tomonori Y, Phadke A, **Kang H**, Masuda K, Varghese S. Synthetic bone mimetic matrix-mediated in situ bone tissue formation through host cell recruitment. Acta Biomaterialia, 2015;19:1-9.

Kang H, Shih YRV, Varghese S. Biomineralized matrices dominate soluble cues to direct osteogenic differentiation of human mesenchymal stem cells through adenosine signaling. Biomacromolecules, 2015;16:1050-61.

Kang H, Shih YRV, Hwang Y, Wen C, Rao V, Seo T, Varghese S. Mineralized gelatin methacrylate-based matrices induce osteogenic differentiation of human induced pluripotent stem cells. Acta Biomaterialia, 2014;10:4961-70.

Kang H, Wen C, Hwang Y, Shih YRV, Kar M, Seo SW, Varghese S. Biomineralized matrix-assisted osteogenic differentiation of human embryonic stem cells. Journal of Materials Chemistry B, 2014;2:5676-88.

Shih, YRV, Hwang YS, Phadke A, **Kang H**, Hwang N, Caro E, Nguyen, S, Siu M, Theodorakis EA, Gianneschi NC, Vecchio KS, Chien S, Lee OK, Varghese S. Calcium phosphate-bearing matrices induce osteogenic differentiation of stem cells through adenosine signaling. Proceedings of the National Academy of Sciences U.S.A., 2014;111:990-5.

Kim DH, Lee, BL, Moon H, **Kang H**, Jeong EJ, Park JI, Han KM, Lee S, Yoo BW, Koo BW, Kim JY, Lee, WH, Cho K, Becerril HA, Bao Z. Liquid-crystalline semiconducting copolymers with intramolecular donor-acceptor building blocks for high-stability polymer transistors. Journal of the American Chemical Society, 2009;131:6124-32.

Abstract of the Dissertation

Biomineralized matrix and small molecule for bone tissue engineering

by

Heemin Kang

Doctor of Philosophy in Materials Science and Engineering

University of California, San Diego, 2016

Professor Shyni Varghese, Chair

2.2 million surgical procedures for bone grafting are performed annually worldwide. While natural bones, such as autografts and allografts, and growth factors are commonly utilized in the procedures, they suffer from various shortcomings, such as high cost, donor site morbidity, and potential side effects. Alternatively, inspired by mineralized, dynamic environment of native bone, we developed biomineralized matrix recapitulating calcium phosphate (CaP)-rich mineral microenvironment that undergoes

dynamic dissolution and reprecipitation. In this dissertation, we focus on the application of biomineralized matrix to induce osteogenesis of human pluripotent stem cells (hPSCs) for bone formation.

Chapter 1 describes the progress in the development of CaP-based biomaterials and their applications in directing stem cell differentiation and supporting bone tissue formation. It includes our prior findings of biomineralized matrix-mediated osteogenesis of human mesenchymal stem cells (hMSCs) and bone formation *in vivo*. Chapter 2 demonstrates that biomineralized matrix can direct osteogenic differentiation of human embryonic stem cells (hESCs) by matrix-based cues alone, both *in vitro* and *in vivo*. Chapter 3 shows that the biomineralized matrix can solely induce osteogenic commitment of human induced pluripotent stem cells (hiPSCs) that can offer clinical benefits of autologous therapy. In chapter 4, we employ biomineralized matrix to study the effect of mineralized microenvironment on fate decision of hMSCs in presence of adipogenic-inducing medium. We show that biomineralized matrix dominates adipogenic soluble cues to direct osteogenic differentiation of hMSCs through adenosine A2b receptor (A2bR) signaling. Chapter 5 demonstrates utilization of adenosine, naturally small molecule to induce direct conversion of both hESCs and hiPSCs into osteoblasts. The osteoblasts derived from hiPSCs through adenosine treatment were found to contribute to the healing of critical-sized bone defects. Chapter 6 shows the application of biomineralized trilayered scaffold to induce subchondral bone formation for osteochondral tissue engineering *in vivo*. Chapter 7 concludes the dissertation and presents future directions, including functional bone tissue engineering and mechanistic studies of biomineralized matrix- and small molecule-driven osteogenic differentiation of hPSCs.

Chapter 1: Biomineralized matrices as intelligent scaffolds for bone tissue regeneration

1.1. Introduction

Bone is an example of a biomineralized functional living tissue. The mineralized components of bone tissue endow them with unique mechanical and chemical functions. Specifically, bone tissue is composed of inorganic calcium phosphate (CaP)-rich mineralized phases built upon the organic substrate (osteoid) whose major components are type I collagen and non-collagenous proteins, such as osteocalcin (OCN) and bone sialoprotein (BSP) [1, 2]. One of the key functions of these organic proteins is to mediate mineralization of bone tissue. Native bone contains a mixture of various minerals, such as non-stoichiometric crystalline hydroxyapatite (HA) and amorphous calcium phosphate (ACP) [3]. Bone minerals also contain other mineral components including carbonate, sodium, and magnesium. Native bone exhibits excellent regenerative capacity; however, critical-sized bone defects often require exogenous interventions, such as bone grafts to assist tissue regeneration or implants to fix nonunion defects. While native bone tissue and its derivatives are still the best solutions to treat critical-sized bone defects, emerging studies implicate that CaP-based synthetic biomaterials, which emulate a bone-specific mineral environment, could be used as an alternative to treat such bone defects. Over the past decade, a number of CaP mineral-based matrices have been examined to promote bone tissue regeneration, which include CaP-based ceramics and polymer composites containing CaP minerals. In this chapter, we describe the development of CaP-based biomaterials and their applications in bone tissue regeneration ranging from directing stem cell differentiation to supporting bone tissue formation *in vitro* and *in vivo*. We also discuss the molecular mechanism through which CaP-based biomaterials promote bone tissue regeneration and the importance of CaP mineral phase in mediating the tissue repair. We finally conclude the chapter with future perspectives towards the translational applications of synthetic CaP-bearing materials for bone tissue regeneration.

1.1.1. Bone tissue: A mineralized hierarchical living structure

Bone is known for its hierarchical structure, which ranges from nanoscopic to macroscopic scale (Figure 1.1) [4-6]. Bone extracellular matrix (ECM) consists of organic and inorganic components where inorganic CaP minerals are arranged along the collagenous network. The basic building blocks are small plate-shaped crystals of carbonate apatite, tens of nm in length and width and 2-3 nm in thickness, which nucleate and grow on collagen [1] as well as non-collagenous proteins (NCPs), such as OCN, BSP, osteopontin (OPN), and osteonectin (ON) [2]. At the next hierarchical level, these mineralized collagen fibrils, 300 nm in length and 1.5 nm in thickness, are ordered into arrays in a 3-dimensional structure that builds up a single layer or lamella of bone. This lamella, which spans a few μm in thickness, further assembles to make up the macroscopic structure of bone.

Bone is a highly dynamic tissue undergoing continuous remodeling. The function and homeostasis of bone tissue are maintained by highly coordinated activities of bone cells, which include osteoblasts, osteocytes, and osteoclasts. Osteoblasts are derived from mesenchymal progenitor cells and synthesize the organic constituent of osteoid which mineralizes as bone tissue matures [7, 8]. The process of depositing minerals into the organic matrix is commonly referred to as biomineralization. Once new bone is created, osteoblasts become trapped within the new bone and transform into osteocytes. On the other hand, osteoclasts, the multinucleated cells formed by the fusion of mononuclear progenitors of the macrophage family, degrade the bone matrix by creating an acidic microenvironment which liberates Ca^{2+} and PO_4^{3-} ions during bone remodeling [9].

1.1.2. Mineralized biomaterials for bone tissue repair

As stated earlier, despite the regenerative ability of bone, critical-sized bone defects, arising from trauma, congenital defects, and tumor excision, often require exogenous interventions and one of them being bone grafts [10]. For optimal tissue regeneration, bone grafts are desirable to be osteoinductive and osteoconductive [11]. Osteoinduction refers to the recruitment of progenitor and stem cells from the host tissue and their subsequent differentiation for bone tissue formation. Osteoconduction is the stimulation of natural bone ingrowth by osteoblasts. Native bone tissues (allogenic or autogenic) and their derivatives have been so far the best solution for treating bone defects due to their potential to provide many cues relevant for bone healing and tissue regeneration. The advantage of such native bone derivatives has led to the development of a number of commercially available products, such as ALLOPURE® [12], CANCELLO-PURE™ Wedges [13], NuOss™ [14], and Bio-Oss® [15]. Although native bone and its derivatives are ideal candidates to augment bone healing and tissue repair, they suffer from various shortcomings, such as donor site morbidity, limited availability, and potential for disease transmission [11]. To this end, both naturally and synthetically derived biomaterials with the ability to support bone tissue regeneration have been explored as an alternative solution. Of these, materials containing some form of CaP minerals have been extensively studied. In fact, coating of implants with CaP minerals has been widely employed to improve the integration of the implants with the host tissue through bone ingrowth [16-19].

1.2. CaP-biomaterials

CaP-biomaterials such as CaP ceramics have been extensively utilized for bone and dental restorations [20]. In addition to serving as a structural substitute, CaP-materials could contribute to bone regeneration. The CaP-biomaterials are known to be osteoconductive and/or osteoinductive [11, 20]. The physicochemical properties of the CaP minerals, such as their crystalline nature, play an important role in determining their osteoinductive and osteoconductive properties. The crystalline properties of CaP minerals can be controlled through precursors, pH, and temperature used during synthesis [20]. The experimental conditions used could also have a significant impact on other physical properties of CaP minerals, such as particle sizes, morphology, macroporosity, and microporosity [20]. The single crystalline phases of CaP minerals exist in various chemical compositions and mineral phases, which include hydroxyapatite (HA) (Figure 1.2a), β-tricalcium phosphate (TCP) (Figure 1.2a), octacalcium phosphate (OCP), and dicalcium phosphate dihydrate (DCPD). Synthetic HA, ($Ca_{10}(PO_4)_6(OH)_2$) with a Ca/P molar ratio of 1.67, exhibits highly pure and crystalline characteristics and has been employed as a reference material to represent a major constituent of bone mineral [21].

Studies have also reported synthesis of TCP ($(Ca)_3(PO_4)_2$) with a Ca/P ratio of 1.5 [22], OCP ($Ca_8H_2(PO_4)_6{\cdot}5H_2O$) with a Ca/P ratio of 1.33 [23], and DCPD ($CaHPO_4{\cdot}2H_2O$) with a Ca/P ratio of 1.00 [24]. Synthesis of biphasic calcium phosphate (BCP) generally uses calcium-deficient apatite as a precursor, which results in a mixture of HA and TCP [25]. ACP exhibits a Ca/P ratio of approximately 1.5, resembling that of TCP [26]. Although CaP ceramics mimic the mineral environment of bone tissue, the brittle nature of these materials limits their widespread applications [27]. To this end, composite materials with organic components have been developed by physical dispersion of CaP particles [28-34] or through biomineralization [35, 36]. While the former does not necessitate any interaction between the organic matrices and the inorganic minerals, the latter requires functional groups of the organic matrices to nucleate CaP minerals for their growth. Hence, biomaterials developed through biomineralization exhibit a strong interface between the organic matrix and inorganic minerals. Biomineralized matrices with CaP minerals, exhibiting either crystalline [37] or apatite-like semicrystalline phases [38-40], can be synthesized. Biomineralization is a naturally occurring process that assists mineralization of living systems.

Biomineralization has often been conducted in a physiologically similar aqueous environment such as simulated body fluid (SBF) [35]. Common approaches [35, 36] include the incubation of organic substrates that bear charged functional groups [38, 41-44] in a medium containing inorganic Ca^{2+} and PO_4^{3-} ions [37, 38, 45-47]. Some studies have also utilized mineralization solutions containing inorganic Ca^{2+} and PO_4^{3-} ions within liposomes [48] or organic phosphate with an enzyme such as alkaline phosphatase [49, 50] to achieve mineralization. Physicochemical characteristics of resultant CaP minerals in biomineralized matrices, which play a key role in their osteogenic function, can differ considerably depending on the organic matrices used and the mineralization process [37, 38, 40, 47, 51-53]. Choi *et al*. have showed that biomineralized poly(lactide-*co*-glycolide) (PLG) surfaces with different morphology of CaP minerals can be created by varying concentrations of Ca^{2+} and PO_4^{3-} ions in the mineralizing medium [51]. Suarez-Gonzalez and colleagues acquired biomineralized polycaprolactone (PCL) surfaces with disparate morphology and dissolution kinetics of minerals by modulating the concentration of HCO_3^- in the mineralizing medium [47]. Biomineralized matrices (Figure 1.3a) containing CaP minerals with varying morphology can be developed through manipulation of functional groups [52, 53] or hydrophobicity [38] of organic templates.

1.3. CaP-based biomaterial-assisted osteogenic differentiation of stem cells

CaP-biomaterials have been extensively utilized to direct osteogenic commitment of progenitor cells and stem cells. Stem cells, that are available in large numbers and can be easily expanded *ex vivo*, offer a cell population to assist bone tissue regeneration. However, controlled lineage commitment of stem cells towards osteoblasts is a vital requirement for their use in bone tissue repair and regeneration. One type of widely used stem cells for bone tissue regeneration is mesenchymal stem cells (MSCs), owing to their inherent ability to differentiate into osteoblasts [54]. CaP-based matrices have been shown to promote osteogenic differentiation of MSCs, but mostly in conjunction with osteogenic soluble factors [55-57]. We and others have shown that biomaterials containing CaP moieties can direct osteogenic commitment of MSCs even in the absence of any osteogenic-inducing small molecules, such as dexamethasone, β-glycerophosphate, and growth factors (Fig. 3b) [58-60]. The stem cell-laden matrices can be implanted with or without pre-differentiation of cells into osteoblasts. Pre-differentiation of stem cells prior to their implantation was often employed to promote the *in vivo* survival and function of transplanted cells [28, 55, 61].

Due to the limited self-renewal property of MSCs, especially when isolated from aged donors, pluripotent stem cells (PSCs), which include both embryonic stem cells (ESCs) and induced pluripotent stem cells (iPSCs), have recently gained tremendous attention as attractive cell sources for bone tissue regeneration [62]. In particular, patient-specific iPSCs circumvent concerns regarding immune responses and ethical issues related to ESCs [62-64]. However, controlling osteogenic lineage specificity of PSCs poses a significant challenge owing to their pluripotency and the possibility to form tumors *in vivo* if undifferentiated PSCs are present within transplanted cells. Therefore, PSC-derived mesodermal or mesenchymal progenitor cells as cell sources along with CaP-biomaterials have been used to derive osteoblasts from PSCs [29, 65-69]. Interestingly, recent studies have shown that material-based cues from CaP-biomaterials could solely direct osteogenic differentiation of ESCs, both *in vitro* and *in vivo* (Figures 1.3c-d) [70], as well as iPSCs [71].

1.4. CaP-matrices for bone tissue engineering and repair

The ability of CaP-matrices to promote osteogenic commitment of stem cells and progenitor cells makes them an ideal scaffold for bone tissue regeneration. Cell-laden

CaP-matrices have been extensively investigated to treat critical-sized bone defects. CaP-biomaterials coupled with MSCs have shown some success in inducing bone formation in segmental bone defects [72-74]. Marcacci *et al*. have demonstrated a complete fusion between hMSC-laden HA implants and host bone in the segmental bone defects of patients [75]. Furthermore, Levi and colleagues have shown bone formation in calvarial bone defects by HA-incorporated matrices with an addition of hPSCs and BMP-2 [65].

While the above-described studies demonstrate how delivery of stem cells/osteoprogenitor cells through CaP-based materials could be a powerful therapeutic strategy to treat critical-sized bone defects, biomaterials that could recruit endogenous cells to regenerate bone tissues are clinically beneficial. To this end, a number of studies have investigated the application of CaP-biomaterials, which are osteoinductive and osteoconductive, to promote bone tissue regeneration *in vivo*. Such an approach that relies on the regenerative potential of endogenous cells for tissue repair will circumvent limitations associated with conventional tissue engineering approaches that are laborious, such as *ex vivo* cell processing, thereby accelerating the translational aspects of regenerative medicine [76].

A number of studies have demonstrated that CaP-based biomaterials can promote bone regeneration upon their implantation in the absence of exogenous cells or growth factors [55, 77, 78]. We present the summary of recent literature that demonstrated bone formation by implanting CaP-bearing materials alone into various animal models in Table 1.1. Yuan and colleagues have examined how various CaP ceramics differ in their potential to contribute to bone tissue regeneration *in vivo*. Specifically, they have investigated the effect of changes in chemical composition of CaP ceramics (HA, TCP, and BCP) on their ability to contribute to bone tissue regeneration [55]. Among the CaP ceramics tested, TCP was found to contribute to excellent bone formation, both in the spinal fusion (Figure 1.2b) and critical-sized defect models (Figures 1.2c-d), even outperforming autografts. Although the TCP matrices promoted bone tissue repair in critical-sized bone defects, they failed to induce bone formation when implanted subcutaneously. These findings suggest that the TCP materials used in this study were mostly osteoconductive in nature as compared to being osteoinductive. Similarly, a study by Hong *et al*. showed no ectopic bone formation by BCP particles when subcutaneously implanted [79]. Bone regeneration in the ectopic site is an indication for osteoinductivity of biomaterials. Incorporating osteoinductive growth factors, such as BMP-2, has been shown to enhance the poor bone-forming ability of CaP-matrices in the ectopic sites [80]. Recently, we have shown that biomineralized matrices containing CaP minerals can contribute to ectopic bone formation in the absence of exogenous cells and osteoinductive growth factors (Figure 1.3d) [77]. Such discrepant results could probably be due to differences in the crystalline nature of the CaP minerals.

1.5. CaP mineral-based matrices as a delivery vehicle for growth factors and genes

In addition to being a bone substitute, CaP-based biomaterials have been employed as a delivery vehicle for various growth factors that promote bone tissue formation, adding a new dimension to their application [81]. Among relevant growth factors, BMP-2 and BMP-7 are clinically approved and have been harnessed extensively with CaP-biomaterials to stimulate bone tissue regeneration [80, 82]. It has been shown that BMPs have high affinity to CaP minerals, such as HA [83], suggesting the potential application of CaP-biomaterials as a delivery vehicle for growth factors.

Various CaP ceramics, such as TCP, BCP, and HA, demonstrated excellent adsorption capacities for recombinant human BMP-2 when incubated in a solution containing such biomolecules [80, 84]. Such BMP-bound CaP-matrices have been successfully employed as bone-inducing scaffolds [28, 65, 85-87]. Besides physisorption, studies have also used other approaches to incorporate growth factors within the mineralized layer. For instance, Kong et al. have incorporated BMP-2-loaded polymer nanospheres into the mineralized layer [88]. Yu and colleagues have included BMP-2 between two mineralized layers of microparticles [89].

CaP ceramics (TCP and HA) and TCP-incorporated matrices containing BMP-2 or BMP-7 have been shown to promote the healing of critical-sized bone defects [28, 90-92]. In a long-term study with high clinical relevance, Reichert et al. implanted biodegradable TCP-incorporated composites with BMP-7 for 12 months and showed the healing of segmental bone defects with physiologically remodeled bone exhibiting higher bone density and superior biomechanical strength compared to autografts [28].

CaP mineral-based matrices have not only been used to deliver BMP proteins, but also plasmid-DNA (pDNA) encoding BMP-2 gene [93, 94]. In particular, HA nanoparticles-pDNA complex was shown to induce bone formation by MSCs [93]. Furthermore, subcutaneous injection of CaP nanoparticles-pDNA hybrid with osteoprogenitor cells yielded bone formation [94].

1.6. CaP-assisted stem cell osteogenesis and bone tissue regeneration: Mechanisms

Both physical and chemical properties of the CaP minerals play a key role in determining their osteoinductive and osteoconductive properties. Particle size, morphology, macroporosity, microporosity, and specific surface area have been reported to influence the osteogenic capacity of CaP minerals [20]. Of those, the effect of porosity and pore size of CaP mineral-based matrices on bone regeneration has been extensively documented [95]. In particular, recent studies showed that high porosity in either BCP or TCP ceramics enhanced bone formation compared to their counterparts with low porosity [55, 96]. In other studies, various morphology of CaP minerals was shown to result in different degrees for osteogenic commitment of MSCs [97, 98]. Sphere-like HA microparticles promoted osteogenic differentiation of MSCs compared to rod-like controls [97]. Plate-like or net-like CaP mineral coatings exhibited higher osteostimulatory effects on MSCs as compared to granule-like counterparts [98].

In addition to topographical cues arising from morphological and physical properties of CaP minerals, their dissolution-precipitation plays an equally important role in their ability to support bone tissue regeneration. The crystalline nature of the CaP minerals determines the kinetics of the mineral dissolutions. Dissolution of CaP minerals in a medium lacking Ca^{2+} and PO_4^{3-} [20, 55, 58, 99] or a physiological environment [100] has been previously demonstrated. The release of Ca^{2+} and PO_4^{3-} ions often results in their supersaturation, leading to subsequent precipitation of Ca^{2+} and PO_4^{3-} ions onto CaP minerals [20, 100]. Such processes, termed as dynamic dissolution-precipitation, govern the local levels of extracellular Ca^{2+} and PO_4^{3-} ions and thus regulate osteogenic commitment of stem cells (Figures 1.4a-b) [39, 101]. The dissolution of CaP minerals is heavily determined by their crystalline nature and studies have demonstrated higher dissolution rates of CaP minerals to Ca^{2+} and PO_4^{3-} for TCP compared to HA [55, 99], which correlates with their ability to promote osteogenic differentiation of MSCs [102] and bone tissue regeneration [55]. However, excessive dissolution of CaP moieties from ACP surfaces led to negative effect on the osteogenic differentiation of MSCs compared to crystalline CaP surfaces [57, 103]. This is consistent with a recent study by Liu *et al.*, who reported the stimulatory effect of exogenous Ca^{2+} and PO_4^{3-} supplements on the osteogenic commitment of MSCs only within certain concentrations [104]. Extracellular Ca^{2+} and PO_4^{3-} ions contribute to bone tissue regeneration through various signaling pathways [39, 102, 105, 106]. In particular, Ca^{2+} ions have been demonstrated to promote osteogenic differentiation of MSCs through L-type voltage-gated calcium channels (L-VGCC) [105, 106]. Furthermore, PO_4^{3-} ions liberated from biomineralized matrices were shown to induce osteogenic differentiation of MSCs via phosphate metabolism and adenosine signaling (Figure 1.4a) [39].

In addition to regulating the local levels of extracellular Ca^{2+} and PO_4^{3-} ions, dissolution-precipitation of CaP minerals could also modulate the adsorption of growth factors and their subsequent release. Prior works by Liu *et al.* provided evidence for co-precipitation of CaP moieties and BMP-2 [84]. In addition to contributing to the adsorption of BMPs through co-precipitation, the dissolution kinetics of CaP minerals could contribute to the release profile of adsorbed BMPs [47, 107], thus regulating signaling pathways relevant to bone formation and homeostasis.

1.7. Conclusion and future perspectives

This chapter discussed the development of synthetic CaP-biomaterials and their applications towards bone tissue regeneration with or without stem cells and/or osteoinductive growth factors. We also examined the underlying molecular mechanisms for CaP mineral-driven osteogenic differentiation of stem cells and bone formation.

Various kinds of CaP mineral-based matrices have been developed and utilized to treat critical-sized bone defects. Their use alone without exogenous stem cells or growth factors offers simple and cost-effective solution in a clinical setting. Of these, TCP ceramics alone were recently shown to promote healing of critical-sized bone defects, presenting bright prospects for replacing the current use of native bone and its derivatives for treating such defects [55]. Semicrystalline biomineralized matrices [38-40] are also promising CaP mineral-based matrices for bone tissue regeneration owing to their inherent osteoinductivity and osteoconductivity [58, 70, 71, 77]; however, their *in vivo* function in treating critical-sized bone defects needs to be further evaluated. To keep pace with tremendous advancements of CaP-biomaterials towards clinical applications, the molecular mechanisms for CaP mineral-mediated bone tissue regeneration through Ca^{2+} and PO_4^{3-} regulatory pathways necessitate further elucidation.

In order to regenerate load-bearing bone tissues, it is important for the grafts to have structural and mechanical properties amenable to promote bone tissue formation without detrimental effect to the surrounding native bone tissue. To this end, polymer composites containing CaP minerals in hierarchical structure have been developed [108-111], including some materials exhibiting similar biomechanical properties of bone [111]. Furthermore, 3-D printed CaP-based matrices offer great translational potential for personalized medicine and enhanced functional outcome through fabrication of custom-designed bone architecture [112-115]. The presence of physiologically remodeled neo-bone, with vasculature and marrow cavities containing hematopoietic stem cells, further ensures the functionality of regenerated bone as an integral part of host tissue [116]. Taken together, substantial advancements in the development of CaP-biomaterials as intelligent scaffolds and understanding in their osteogenic function would benefit clinical practices for bone tissue regeneration.

1.8. Acknowledgements

Authors gratefully acknowledge the financial support from National Institutes of Health (NIH, Grant 1 R01 AR063184-01A1) and California Institute of Regenerative Medicine (CIRM, RN2-00945 and RT2-01889).

Chapter 1, in full, has been submitted for publication of the material as it may appear in Handbook of Intelligent Scaffolds for Tissue Engineering and Regenerative Medicine, 2nd Edition. “Biomineralized matrices as intelligent scaffolds for bone tissue regeneration”. Kang, Heemin; Shih, Yu-Ru V.; Rao, Vikram; Varghese, Shyni. Pan Stanford Publishing Pte. Ltd. The dissertation author was the primary investigator and author of this paper.

1.9. Figures

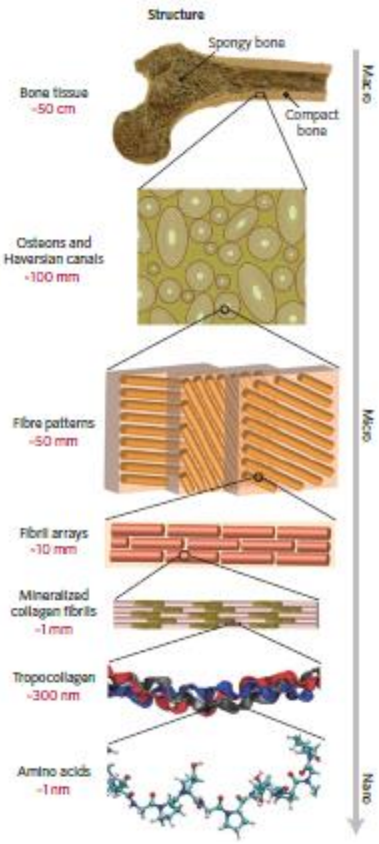

Figure 1.1. Hierarchical structure of bone.

Macroscopic structure of bone consists of CaP minerals built upon assemblies of tropocollagen in nanometer scale that make up fibril arrays in micrometer scale. (Reproduced from [6] with permission from Nature Publishing Group, 2011.)

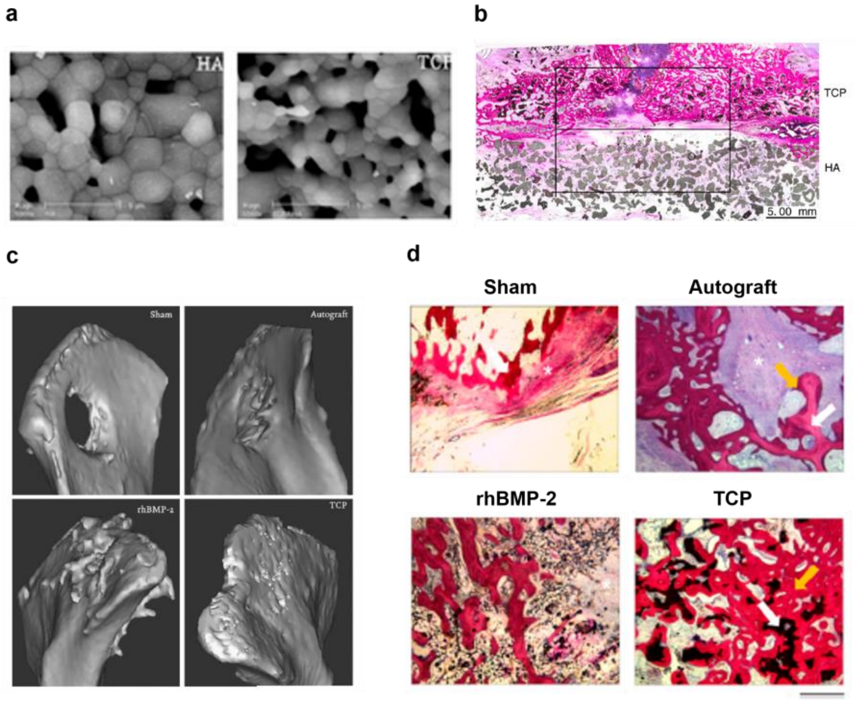

Figure 1.2. CaP ceramic-assisted skeletal bone regeneration.

(a) SEM images for two representative CaP ceramics: hydroxyapatite (HA) and tricalcium phosphate (TCP). Scale bars indicate 1 µm. (b) Basic Fuchsin and Methylene blue staining of HA and TCP implants for posterolateral spinal fusion. Scale bars represent 5 mm. (c) 3-D µCT models and (d) Basic Fuchsin and Methylene blue staining of ilium critical-sized defect following implantation of autograft, collagen sponges with rhBMP-2, and TCP ceramics with a sham control. Orange arrows indicate newly formed bone while white arrows indicate autograft or TCP implants. Scale bars indicate 200 µm. (Adapted from [55] with permission from National Academy of Sciences, 2010.)

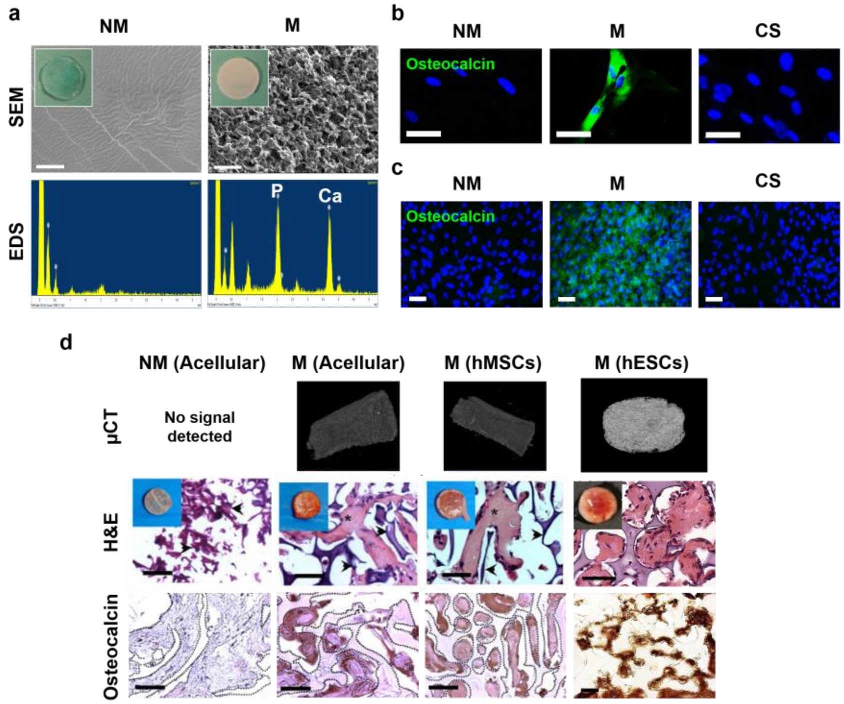

Figure 1.3. Biomineralized matrix-directed stem cell differentiation into osteoblasts and ectopic bone formation.

(a) SEM photographs and corresponding EDS of non-mineralized (NM) and mineralized (M) poly(ethylene glycol)-diacrylate-*co*-acryloyl 6-aminocaprioic acid (PEGDA-*co*-A6ACA) matrices. Scale bars represent 2 µm. Inset shows gross images. Immunofluorescent staining for osteocalcin (green) and nucleus (Hoechst; blue) of (b) human mesenchymal stem cells (hMSCs) and (c) human embryonic stem cells (hESCs) on non-mineralized and mineralized matrices and coverslips (CS) after *in vitro* culture. (d) 3-D µCT images, H&E staining, and immunohistochemical staining of osteocalcin for acellular, hMSC-laden, and hESC-laden mineralized matrices with acellular non-mineralized control, following *in vivo* subcutaneous implantation. Inset shows gross images. (b-d) Scale bars indicate 50 µm. (a,c,d: adapted from [70] with permission from the Royal Society of Chemistry, 2014; b: adapted from [58] with permission from John Wiley & Sons, Inc., 2012; d: adapted from [77] with permission from eCM journal.)

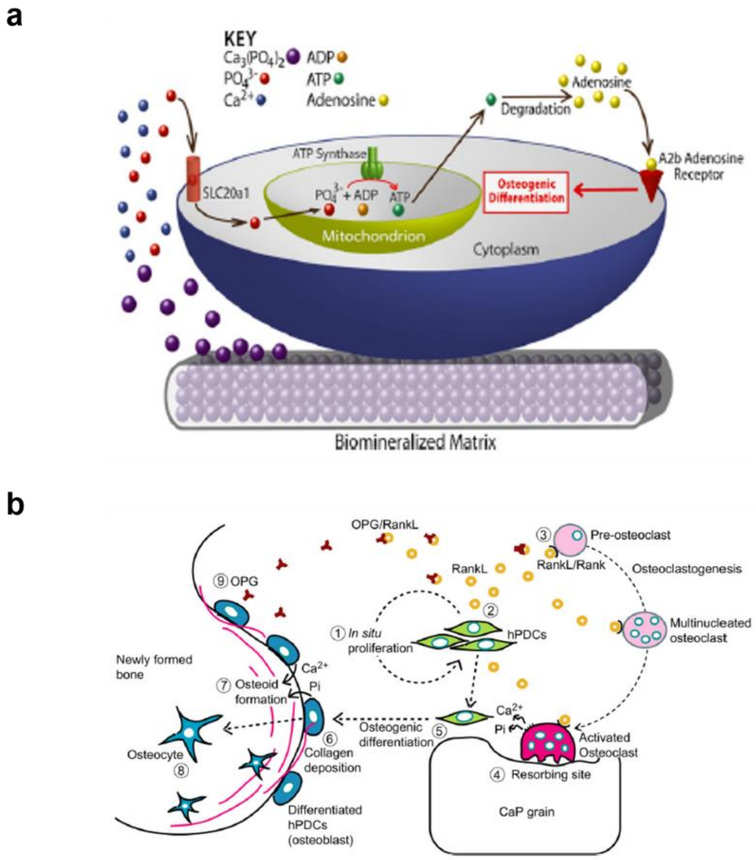

Figure 1.4. Schematic models of CaP mineral-bearing matrices driving osteogenic differentiation of human mesenchymal stem cells (hMSCs) and bone formation.

(a) The proposed model for CaP-rich biomineralized matrix-assisted osteogenic commitment of hMSCs. (Reproduced from [39] with permission from National Academy of Sciences, 2014.) (b) The proposed model for *in vivo* bone formation mediated by the interaction between hMSCs and CaP minerals. (Reproduced from [101] with permission from Elsevier B.V., 2012.)

1.10. Tables

Table 1.1. Summary of recent literature reporting various CaP-based material-mediated bone formation.

Implantation sites of CaP-materials in animal models include subcutaneous pocket (SP), paraspine muscle (PM), ilium defect (ID), skull defect (SD), and segmental tibia defect (STD). The degree of bone formation was summarized as described in each study (-: no; +: low; ++: high).

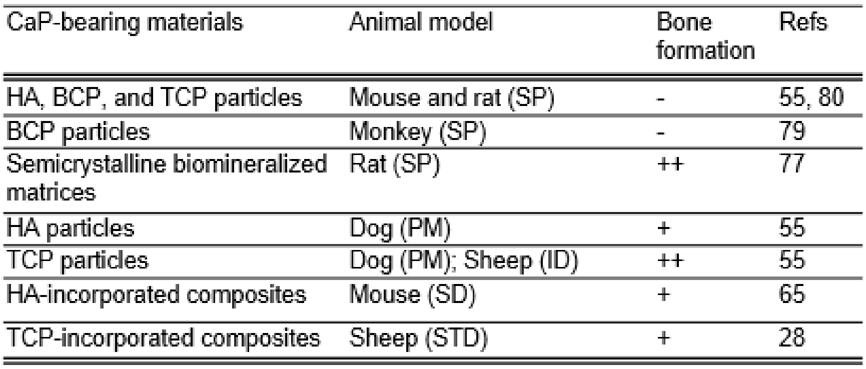

CaP-bearing materials	Animal model	Bone formation	Refs
HA, BCP, and TCP particles	Mouse and rat (SP)	-	55, 80
BCP particles	Monkey (SP)	-	79
Semicrystalline biomineralized matrices	Rat (SP)	++	77
HA particles	Dog (PM)	+	55
TCP particles	Dog (PM); Sheep (ID)	++	55
HA-incorporated composites	Mouse (SD)	+	65
TCP-incorporated composites	Sheep (STD)	+	28

Chapter 2: Biomineralized matrix-assisted osteogenic differentiation of human embryonic stem cells

2.1. Abstract

Physical and chemical properties of the matrix play an important role in determining various cellular behaviors including lineage specificity. We demonstrate that the differentiation commitment of human embryonic stem cells (hESCs), both *in vitro* and *in vivo*, can be achieved solely through synthetic biomaterials. hESCs cultured using mineralized synthetic matrices mimicking calcium phosphate (CaP)-rich bone environment differentiated into osteoblasts in the absence of any osteogenic inducing supplements. When implanted *in vivo*, these hESC-laden mineralized matrices contributed to ectopic bone tissue formation. In contrast, cells within the corresponding non-mineralized matrices underwent either osteogenic or adipogenic fate depending upon the local cues present in the microenvironment. To our knowledge, this is the first demonstration where synthetic matrices are shown to induce terminal cell fate specification of hESCs exclusively by biomaterial-based cues both *in vitro* and *in vivo*. Technologies that utilize tissue specific cell-matrix interactions to control stem cell fate could be a powerful tool in regenerative medicine. Such approaches can be used as a tool to advance our basic understandings and translational potential of stem cells.

2.2. Introduction

Human embryonic stem cells (hESCs), with unlimited self-renewal potential and ability to differentiate into all cell types in the human body, hold great promise to treat various diseases and tissue loss.[117] In addition to regenerative therapy, hESC-based tissue models could also be used as a tool to study developmental processes and disease progression, and as drug-screening platforms.[118, 119] Despite the progress made over recent years, widespread application of hESCs has been impeded by several challenges, of which the main concern is lack of approaches to direct their differentiation into targeted cells. Advancements over the years have developed a number of strategies ranging from small molecules to mRNAs to genetic manipulations to direct differentiation of hESCs into various phenotypes.[120-122] While the importance of soluble factors has been extensively documented, emerging studies show that physical and chemical cues of the matrix could play an equally important role in directing stem cell differentiation and function.[123-128]

Matrix-assisted differentiation and transplantation of stem cells to treat compromised tissues and organs has enormous potential in wound and fracture healing, tissue regeneration, and restoration of organ functionality.[129-131] A number of physical and chemical properties of the matrix such as functional groups, hydrophobicity, topography, and rigidity have been identified to influence stem cell differentiation.[124-128] Most of these studies; however, utilize matrix cues in conjunction with medium containing inductive factors to direct differentiation, thus making it difficult to delineate the contributions of individual components.[124] Furthermore, the extent to which the matrix-based cues can direct differentiation of more naïve stem cells like embryonic stem cells to terminally differentiated cells remains unclear.

In this study, we employ a synthetic matrix recapitulating the calcium phosphate (CaP)-rich bone microenvironment to determine if the synthetic matrix–based cues alone are sufficient to direct osteogenic differentiation of hESCs. Previously, we and others have shown that biomaterials containing CaP moieties can promote osteogenic differentiation of osteoprogenitor cells and adult stem cells like mesenchymal stem cells (MSCs).[55, 59, 60, 98, 132-137] However, the role of CaP minerals on directing osteogenic commitment of hESCs is not clear. Efficient osteogenic differentiation of hESCs is often achieved through derivation of mesenchymal progenitor cells and/or culturing them in medium containing osteogenic inducing components such as β-glycerophosphate, ascorbic acid 2-phosphate, dexamethasone, and/or bone morphogenetic proteins (BMPs).[29, 65, 67, 68, 138-140] Studies have also utilized incorporation of bone specific matrix components, such as hydroxyapatite and decellularized bone matrices, in concert with osteogenic inducing soluble factors to promote osteogenic differentiation of hESCs and hESC-derived progenitor cells.[29, 67, 68]

We demonstrate that synthetic matrices containing CaP minerals induce osteogenic differentiation of hESCs in both two-dimensional (2-D) and three-dimensional (3-D) culture conditions in basal growth medium lacking any osteogenic inducing components. When implanted subcutaneously *in vivo*, the hESC-laden mineralized matrices contributed to ectopic bone formation without teratoma. On the contrary, cells in non-mineralized matrices underwent either osteogenic or adipogenic fate in response to the local biomaterial-based cues.

2.3. Materials and Methods

2.3.1. Materials

Poly(ethylene glycol)-diacrylate (PEGDA) and acryloyl 6-aminocaproic acid (A6ACA) were prepared as previously described.[125, 141] Briefly, 5.29 mmol of poly(ethylene glycol) (32 g for M_n = 6 kDa or 18 g for M_n = 3.4 kDa; Sigma Aldrich, catalog numbers: 81260 and 202444, respectively) was dissolved in 300 ml of toluene at 125 °C, followed by refluxing for 4 hours with vigorous stirring. Azeotropic distillation was used to remove the traces of water in the reaction mixture. On cooling this solution to room temperature (~25 °C), 180 ml of anhydrous dichloromethane followed by 1.623 ml (11.64 mmol, 2.2. equivalents) of triethylamine was added with vigorous stirring. The reaction mixture was then transferred to an ice bath to attain 4 °C. To this reaction mixture, 0.942 ml (11.64 mmol, 2.2 equivalents) of acryloyl chloride in 15 ml of anhydrous dichloromethane was added in drop-wise manner for 30 minutes. Following an additional 30 minutes at 4 °C, the reaction mixture was raised to 45 °C and kept overnight. The reaction mixture was filtered at 25 °C through diatomaceous earth to remove quaternary ammonium salt. The filtrate was concentrated using a rotary evaporator and precipitated in excess diethyl ether. Precipitated product was re-dissolved in dichloromethane and re-precipitated in diethyl ether. The resultant PEGDA was filtered and dried under vacuum at 25 °C for 24 hours. The dried PEGDA was further purified using a Sephadex fine G-25 column (GE Healthcare Life Sciences, catalog number: 17-0032-01) and lyophilized. The PEGDA product was characterized by using NMR. ^{1}H NMR (300 MHz, $CDCl_3$): 6.39-6.36 ppm (d, 2H), 6.17-6.11 ppm (dd, 2H), 5.93-5.91 ppm (d, 2H), 4.28-4.26 (t, 4H), 3.75-3.74 ppm (m, 8H), 3.62 ppm (broad), 3.48-3.47 ppm (t, 4H)

N-acryloyl 6-aminocaproic acid (A6ACA) was prepared as described by Ayala *et al*.[125] Briefly, 13.11 g (100 mmol) of 6-aminocaproic acid (Sigma Aldrich, catalog number: A2504) and 4.4 g (110 mmol, 1.1 equivalents) of NaOH were dissolved in 80 ml of deionized (DI) water at 4 °C under vigorous stirring. To this, 8.937 ml (110 mmol, 1.1 equivalents) of acryloyl chloride in 15 ml of anhydrous tetrahydrofuran was added dropwise for 30 minutes. The pH of the reaction mixture was maintained between 7.5 and 7.8 until the reaction was complete. The pH of the reaction mixture was then moved to pH 3 by using 6 N HCl at 0 °C and extracted using ethyl acetate. The organic layers were collected, combined, and dried over sodium sulfate. The solution was then filtered, concentrated, and precipitated in petroleum ether. The resultant A6ACA was further purified by silica gel (100-200 mesh) column chromatography using 1% methanol in ethyl acetate as eluent mixture. The purified product was collected and dried overnight prior to use and characterized using NMR. ^{1}H NMR (300 MHz, CDCl3): 6.17-6.12 ppm (dd, 1H), 6.07-6.03 ppm (d, 1H), 5.64-5.62 ppm (d, 1H), 3.17-3.14 ppm (t, 2H), 2.08-2.05 ppm (t, 2H), 1.49-1.42 ppm (dd, 4H), 1.25-1.19 ppm (t, 4H)

2.3.2. Synthesis of PEGDA-co-A6ACA hydrogels

Poly(ethylene glycol) diacrylate-co-acryloyl 6-aminocaproic acid (PEGDA-co-A6ACA) hydrogels were synthesized by reacting 1 M A6ACA and 4% PEGDA (M_n = 6 kDa) with 0.5% ammonium persulfate (APS) and 0.15% N, N, N'-N'-tetramethylethylenediamine (TEMED) in a glass mold with 1 mm spacer for 15 minutes at 25 °C.[132] The resulted hydrogels were incubated in phosphate buffered saline (PBS) overnight with two changes of PBS. The equilibrium-swollen hydrogels were then cut into discs of 1 cm^2. To create bulk rigidity matched biomineralized matrices, the above procedure was repeated, except using 2% PEGDA in the precursor solution.[132] The hydrogel discs were biomineralized as described elsewhere.[132] Briefly, hydrogel discs were incubated in DI water for 6 hours and then in modified simulated body fluid (m-SBF) for 6 hours. The hydrogel discs were then rinsed with DI water and incubated in 40 mM Ca^{2+} and 24 mM HPO_4^{3-} solution (pH = 5.2) at 25 °C for 45 minutes on a rotating shaker (VWR Mini-shaker) at 200 rpm. The discs were rinsed with DI water, incubated in m-SBF at 37 °C for 48 hours with the daily exchange of m-SBF followed by incubating them in PBS for 6 hours. Both non-mineralized and mineralized hydrogels were sterilized through immersion in 70% ethanol (EtOH) for 6 hours, followed by washing in PBS for 4 days with three times of daily exchange prior to cell culture.

2.3.3. Synthesis of PEGDA-co-A6ACA macroporous hydrogels

We used PEGDA-co-A6ACA macroporous hydrogels synthesized by PMMA microsphere templating[142] for 3-D cell culture. The PMMA templates were fabricated using a cylindrical polypropylene mold measuring 8 mm in diameter filled with 60 mg of

PMMA microspheres (Mean diameter = 165 µm, Bangs Laboratories, Catalog number: BB05N). The PMMA bead column was vigorously tapped for 1 minute to facilitate their packing. 60 µL of a mixture consisting of 20% acetone and 80% EtOH was gently added into the mold. The mold was incubated at 25 °C for 1 minute to soften the PMMA microspheres allowing them to fuse together, then at 80 °C for 1 hour to evaporate the solvent. A precursor solution of 0.5 M A6ACA and 20% PEGDA (M_n = 3.4 kDa) with 0.3% Irgacure was poured and allowed to infiltrate into the PMMA-packed mold under vacuum for 5 minutes. The mixture was polymerized using UV light at a wavelength of 365 nm (intensity of 42 W/cm^2) for 10 minutes. PMMA template was dissolved in acetone for 3 days with three times of daily exchange. Upon leaching PMMA templates, the macroporous hydrogels were gradually hydrated using acetone-water mixtures with decreasing concentrations of acetone (100 to 0%) for one day. The macroporous hydrogels were washed in PBS for 6 hours and punched into cylindrical constructs measuring 5 mm in diameter and 2 mm in height for 3-D *in vitro* culture and 7 mm in diameter and 2 mm in height for subcutaneous implantation. Mineralization of macroporous hydrogels was conducted as described earlier.[133] Macroporous hydrogels were incubated in m-SBF for 6 hours, then in 40 mM Ca^{2+} and 24 mM HPO_4^{3-} solution (pH = 5.2) under vacuum for 5 minutes to facilitate the infiltration of solution, followed by moving to a rotating shaker at 25 °C for 30 minutes at a speed of 200 rpm. These treated macroporous hydrogels were rinsed with DI water, incubated in m-SBF at 37 °C for 48 hours with daily change of m-SBF, and immersed in PBS for 6 hours. The non-mineralized and mineralized macroporous hydrogels were sterilized using 70% EtOH for 6 hours and washed with PBS for 4 days prior to cell culture.

2.3.4. Scanning electron microscopy (SEM) & energy dispersive spectra (EDS)

To examine the morphology and composition of mineralized matrices, they were rinsed in DI water for 5 minutes, sliced into flat pieces, flash-frozen in liquid nitrogen, and lyophilized overnight. Prior to SEM imaging, the samples were subjected to Ir coating for 7 seconds using Emitech sputter coater (Emitech, K575X). The SEM images were acquired using Philips XL30 ESEM. The Ca/P atomic ratio was obtained from elemental analysis using Oxford Energy Dispersive Spectra (EDS) with INCA software. The pore diameter of macroporous hydrogels in their dried state was measured from three different SEM images using ImageJ. The pore diameters of non-mineralized and mineralized macroporous hydrogels in the swollen state were measured from three different bright-field images using ImageJ. Roughly 10-15 pores within each image were analyzed to determine the pore diameter. The data are presented as mean ± standard errors.

2.3.5. Cell culture

Human embryonic stem cells (hESCs; HUES9 and H9) were cultured on mitotically inactivated mouse embryonic fibroblasts (MEFs) using Knockout DMEM (Life Technologies, catalog number: 10829-018) supplemented with 10% Knockout Serum Replacement (KSR; Life Technologies, catalog number: 10828028), 10% human plasmonate (Talecris Biotherapeutics), 1% non-essential amino acids, 1% penicillin/streptomycin, 1% Gluta-MAX, and 55 μM 2-mercaptoethanol as previously described.[143] Cells were passaged using Accutase (Millipore) at approximately 80%

confluency and supplemented with fresh media containing 30 ng/ml of bFGF (Life Technologies) daily.

Prior to seeding hESCs, the sterilized hydrogel discs, macroporous hydrogels, and cell culture grade coverslips (CS; diameter = 15 mm, Fisherbrand, catalog number: 1254582) were coated with matrigel (BD Biosciences, catalog number: 354277) following manufacturer's protocol to promote cell adhesion. Briefly, matrigel solution was thawed overnight at 4 °C and diluted with chilled DMEM solution at 1:86 ratio. All matrices (mineralized and non-mineralized hydrogels and coverslips) were then coated with matrigel solution at 4 °C for overnight followed by incubating at 37 °C for 1 hour. For 2-D cultures, cells were seeded onto the matrices at an initial cell density of 1×10^4 cells/cm^2 and cultured in growth medium consisting of high glucose DMEM, 5% fetal bovine serum (FBS; hyclone), 4 mM L-glutamine, and 50 U/ml penicillin/streptomycin at 37 °C and 5% CO_2 with media change every two days. For 3-D cell culture involving macroporous hydrogels, the hydrogels were partially dried for 1 hour to reach approximately a weight loss of 40 % prior to plating hESCs; the weight loss is attributed to evaporation of water from the macroporous hydrogels. 10 µl of cell suspension containing 3×10^5 cells (HUES9 or H9) was seeded into the macroporous hydrogels, incubated at 37°C and 5% CO_2 for 2 hours to allow their infiltration, followed by adding 1.5 ml of growth medium.

2.3.6. Calcium and phosphate assays

To determine Ca^{2+} and PO_4^{3-} contents of the mineralized matrices, samples were rinsed with DI water for 5 minutes to remove non-bound CaP moieties followed by their lyophilization for 24 hours. The lyophilized samples were homogenized in 0.5 M HCl under vortexing at 25 °C for 3 days. To probe dissolution of CaP moieties from the mineralized matrices, matrigel-coated and non-coated mineralized matrices were incubated in 1.5 ml of 50 mM Tris-HCl buffer (pH = 7.4) at 37 °C for 7 days; 300 µl of incubation media was collected and replaced with fresh solution on a daily basis. The measurements of Ca^{2+} and PO_4^{3-} were conducted for matrix homogenates and collected media. For calcium assay, 20 µl of sample solution was mixed with 1 ml of assay solution (Pointe Scientific, catalog number: C7503) and its absorbance was measured at 570 nm using a UV/Vis spectrophotometer (Beckman Coulter, DU 730). Phosphate assay was conducted by following a method described elsewhere.[144] Briefly, 125 µl of sample solution was mixed with 1 ml of assay solution consisting of 1 part 10 mM ammonium molybdate, 2 parts acetone, and 1 part H_2SO_4 followed by 100 µl of 1 M citric acid. Absorbance of the solution was measured at 380 nm using a UV/Vis spectrophotometer.

2.3.7. Immunofluorescent staining

To evaluate the pluripotency of hESCs prior to culture, the cells were stained for NANOG and OCT4. Osteogenic differentiation of hESCs was examined by staining for osteocalcin (OCN). For immunofluorescent staining, the cells were fixed with 4% paraformaldehyde at 25 °C for 10 minutes and blocked for 30 minutes in a buffer solution containing 3% bovine serum albumin (BSA) and 0.1% Triton^{TM} X-100 at 25 °C. The fixed cells were incubated with primary antibodies against NANOG (1:200; rabbit polyclonal, Santa Cruz Biotechnology, catalog number: sc-33759), OCT4 (1:200; rabbit polyclonal, Santa Cruz Biotechnology, catalog number: sc-9081) or OCN (1:100; mouse monoclonal, Abcam, catalog number: ab13420) in a blocking solution at 4 °C for 16 hours. After washing in PBS, the cells were incubated with secondary antibodies (1:250; goat anti-rabbit Alexa Flour 647, Life Technologies or goat anti-mouse Alexa Flour 568, Life Technologies) for 60 minutes and rinsed with PBS. The nuclei were stained with Hoechst 33342 (2 µg/ml; Life Technologies, catalog number: H1399) at 25 °C for 5 minutes, mounted onto glass slides with Vectashield, and imaged using a fluorescence microscope (Axio Observer.A1, Carl Zeiss). Images were taken in the linear mode for the same exposure time and the background was uniformly subtracted from all images using ImageJ. For F-actin staining, the fixed cells were incubated with phalloidin (1:250; Alexa Flour 288, Life Technologies) in a blocking buffer solution at 25°C for 60 minutes. F-actin staining images at 3 days of culture were used to quantify the circularity of the cells using the equation below.[132] Approximately 30 cells from three different images were used for the calculation.

$$\text{Circularity} = \frac{4\pi A}{p^2} \qquad (1)$$

where A and p represent the cellular area and perimeter, respectively.

2.3.8. Quantitative Polymerase chain reaction (q-PCR)

Following RNA extraction of homogenized samples in TRIzol, 1 µg of RNA was reverse-transcribed to cDNA using iScript cDNA synthesis kit (Bio-Rad). Human Osteogenesis PCR array (RT^2 Profiler^{TM} PCR Array Human Osteogenesis, SA

Biosciences, catalog number: PAHS-026) was used to determine the changes in transcription profile of the hESCs cultured on various matrices. The heat map was generated to compare relative expressions for each gene with the colors red (high), green (low), and black (medium). The differentiated hESCs were also characterized for a number of target genes such as RUNX2, OCN, SPP1, and NANOG as a function of culture time via qPCR. Quantitative real-time PCR (qPCR) reactions were performed using SYBR select master mix (Life technologies, catalog number: 4472908) and the ABI Prism 7700 Sequence Detection System (Applied Biosystems). Expression at each time point was normalized to the corresponding housekeeping gene (GAPDH) and to the undifferentiated hESCs, and expressed as fold change thereof. The primers used in qRT-PCR are listed in the Supplementary Table 2.S1.

2.3.9. Live-dead assay

Live-dead assay for 3-D cultures was performed 3 days post cell seeding to examine cell viability (LIVE/DEAD Viability/Cytotoxicity kit, Life technologies, catalog number: L-3224). Cell-laden macroporous hydrogels were cut into thin slices and incubated in the assay solution containing 0.05 v/v% of calcein-AM and 0.2 v/v% of ethidium homodimer-1 in DMEM at 37 °C for 30 minutes. Matrix slices were then rinsed with PBS and imaged using a fluorescence microscope. The percentage of viable cells was determined by counting the live cells, which were stained with green dye, relative to the total number of cells. Images from 3-4 different sections were used to determine the viability. All 3-D matrices supported similar cell viability, approximately 90%.

2.3.10. DNA assay

DNA assay was performed at 7 and 28 days of culture for HUES9 and H9-laden macroporous hydrogels to determine the cell numbers. Collected samples were frozen, lyophilized, and digested in 1 ml of papain solution consisting of 125 μg/ml of papain in 10 mM L-cysteine, 100 mM phosphate, and 10 mM EDTA at pH = 6.3 for 16 hours at 60 °C. DNA contents were measured by using Quant-iT PicoGreen dsDNA kit (Life technologies, catalog number: P11496) according to manufacturer's protocol. Briefly, digested samples and PicoGreen reagent were diluted with TE butter at 1:50 and 1:200 dilutions, respectively. One part each of sample solution and PicoGreen reagent were mixed and their fluorescence was measured at 535 nm using a multimode detector (Beckman Coulter, DTX 880). The DNA contents were normalized to the dry weight of the cell-laden matrix.

2.3.11. Subcutaneous implantation

Animal experiments were performed according to the protocols approved by Institutional Animal Care and Use Committee (IACUC) of University of California, San Diego and National Institute of Health (NIH). Macroporous hydrogels (7-mm diameter and 2-mm in height) were seeded with 1 million hESCs (HUES9 and H9) and incubated in growth media for 6 days *in vitro*. For subcutaneous transplantation of the cell-laden matrices, 3-month-old immunodeficient NOD.CB17-Prkdc^{scid}/J mice were administered with ketamine (100 mg/kg) and xylazine (10 mg/kg) and 1 cm-long incision was made in the back of the mice and four subcutaneous pouches (cranial-left and -right and caudal-left and -right) were constructed by blunt dissection using a 1 cm-wide spatula. Four of either hESCs-laden non-mineralized or mineralized matrices were subcutaneously transplanted into the end of each pouch (n=8 per group; left and right sides of cranial and caudal back of mice) and the skin was carefully sutured. After the surgery, all mice were housed in separated cages.

2.3.12. Micro-computed tomography (μCT) of implanted matrices

For μCT analysis, excised implants were fixed in 4% paraformaldehyde at 4 °C for 4 days and dehydrated in ethanol-water mixture with gradual increase in ethanol until equilibrated in pure ethanol. The fixed implants were then dried and subsequently placed in 15 ml centrifuge tubes along with phantom calibration rods prior to measurements. Time-dependent hard tissue formation was evaluated at 4 and 8 weeks of post-implantation. Mineralized matrices prior to implantation were imaged using μCT to account for the effect of mineralization. Matrices were scanned at 9 μm/pixel resolution using SkyScan 1076 μCT scanner (Bruker). Scans were reconstructed via NRecon software (SkyScan) and built into 3-dimensional models using CTAn software (SkyScan) after applying the same threshold values of 90-190 for all groups to selectively account for the minerals, while eliminating the background. Quantification of mineral density was performed as percentage of mineral volume per total volume of the matrix (BV/TV) with CTAn software. Cross-sectional images in coronal, transverse, and sagittal planes at the center of implants were analyzed with DataViewer and CTAn softwares.

2.3.13. Histology for 3-D in vitro cultured matrices and implanted matrices

For histological analysis, cell-laden matrices were fixed with 4% paraformaldehyde at 4 °C for 1 day for *in vitro* cultures and 4 days for excised implants. The constructs were processed as reported elsewhere.[145] Briefly, the fixed samples were decalcified in 10% ethylenediaminetetraacetic acid (EDTA, Fluka, catalog number: 03677, pH = 7.3) at 4 °C for 3 hours for *in vitro* cultures and 2 days under gentle rotation for excised implants. The decalcified samples were washed gently with PBS.

For paraffin-embedded sections, demineralized samples were gradually dehydrated in ethanol-water mixture with increasing ethanol concentrations until reaching pure ethanol. Following incubation of samples in CitriSolv (Fisher scientific, catalog number: 22-143975) for 1 hour with two changes, samples were transferred into a mixture of paraffin (Richard-Allan Scientific, catalog number: 8337) containing 5% poly(ethylene-*co*-vinyl acetate) (PEVA; vinyl acetate, 25 wt%; melt index: 19 g/10 minutes; Sigma Aldrich, catalog number: 437220) and incubated at 70 °C under vacuum for one day with three vent/vacuum cycles. Following embedding in paraffin-PEVA mixture, sample blocks were sliced into 8 µm-sized sections using a rotary microtome (Leica, RM2255). The sections were briefly hydrated in DI water at 40 °C for 5 minutes, and dried overnight at 37°C. Prior to histological staining, sections were deparaffinized in CitriSolv at 60°C for 15 minutes with two changes and hydrated in ethanol-water mixture with decreasing ethanol concentrations. For H&E staining, rehydrated paraffin-embedded sections were incubated in hematoxylin solution (Ricca Chemical Company, Gill 2, catalog number: 3536-16) for 5 minutes and thoroughly rinsed with DI water. Sections were then stained with Eosin-Y (Richard-Allan Scientific, catalog number: 7111) for 30 seconds, followed by three washes in DI water. The stained sections were visualized using a microscope under bright-field mode.

For immunohistochemical (IHC) staining of osteocalcin (OCN) and human-specific lamin B, rehydrated paraffin-embedded sections were subjected to antigen retrieval by incubating in 10 mM citric acid buffer (EMD Millipore, catalog number: CX 1725, pH = 6.0) at 85°C for 20 minutes, followed by cooling at 25°C for 20 minutes. Sections were washed in PBS, treated with a blocking buffer solution containing 3% BSA and 0.1% Triton^{TM} X-100 at 25°C for 60 minutes, and incubated overnight with primary antibodies against OCN (1:100; mouse monoclonal, Abcam, catalog number: ab13420) or lamin B (1:100; rabbit polyclonal, Thermo Scientific, catalog number: RB-10569-P0) in a blocking buffer at 4°C. Following thorough washes in a mixture of PBS with 0.05 v/v% Tween 20 (PBS-Tween 20), sections were immersed in 3% hydrogen peroxide (Acros Organics, catalog number: 41188) for 7 minutes, followed by washing in PBS-Tween 20. Sections were exposed to horseradish peroxidase (HRP)-conjugated secondary antibodies (1:100; goat anti-mouse, Santa Cruz Biotechnology, catalog number: sc-2005 or donkey anti-rabbit, Jackson ImmunoResearch, catalog number: 711-035-152) in a blocking buffer at 25°C for 60 minutes. After several washes in PBS-Tween 20, sections were developed in 3-3’ diaminobenzidine (DAB) peroxidase substrate (Vector Laboratories, catalog number: SK-4100) for 10 minutes to produce the brown reaction product. Following three times of washing in PBS-Tween 20, sections were imaged using a microscope in color mode under H-filter. For lamin B staining, mouse skin tissue was used as a negative control.

For frozen sections, demineralized samples were incubated in 20% sucrose solution and gradually embedded in OCT at 4°C for 1 day. OCT-embedded samples were transferred into isopentane, frozen in liquid nitrogen, and sectioned into 12 µm-thick slices using cryostat (Leika CM3050). For Oil Red O staining, OCT-embedded frozen sections were dried in air for 30 minutes, incubated in DI water at 4°C for 20 minutes to dissolve OCT, and air-dried for 10 minutes. Samples were immersed in propylene glycol (Sigma-Aldrich, catalog number: W294004) at 25°C for 10 minutes to completely remove residual water. Sections were stained with 0.5% Oil Red O (Sigma-Aldrich, catalog number: O-0625) solution in propylene glycol at 60°C for 10 minutes. Afterwards, stained sections were thoroughly washed in 85% propylene glycol, briefly rinsed in DI water, and subsequently imaged using a microscope in color mode under H-filter.

2.3.14. Statistical analysis

Statistical analyses were carried out using Graphpad Prism 5. Two-tailed Student's t-test was used to compare two groups. One-way analysis of variance (ANOVA) with Tukey-Kramer post-hoc test was used to compare multiple groups in the same time point and two-way ANOVA with Bonferroni post-hoc test was used to compare multiple groups across different time points and p-values were obtained from each test.

2.4. Results and discussion

2.4.1. Development and characterization of mineralized matrices.

Synthetic matrices containing CaP minerals (termed as mineralized matrices) were developed by mineralizing poly(ethylene glycol)-diacrylate hydrogels containing acryloyl-6-aminocaproic acid (A6ACA) moieties (PEGDA-co-A6ACA) as described elsewhere.[146] We used mineralized hydrogels for 2-D culture and mineralized macroporous hydrogels for 3-D culture. Macroporous hydrogels with interconnected pores were fabricated by poly(methyl methacrylate) templating.[142] The matrices were characterized for the presence of mineral content, morphology, calcium (Ca^{2+}) and phosphate (PO_4^{3-}) contents, and dissolution of CaP minerals into Ca^{2+} and PO_4^{3-} (Figures 2.1, 2.S1a-b, and 2.S2a-c).

As evident from the scanning electron microscopy (SEM) images, the matrix-bound CaP minerals showed a plate-like morphology (Figures 2.1a,d). The presence of CaP minerals was further confirmed by elemental analysis (Figures 2.1a,d) as well as the measurement of Ca^{2+} and PO_4^{3-} contents on mineralized matrices (Figures 2.1b-c,e-f). Elemental analysis revealed a Ca/P ratio of 1.40 and 1.57 for mineralized hydrogels and mineralized macroporous hydrogels, respectively. Similar to prior studies, CaP components of the mineralized matrices dissociate into Ca^{2+} and PO_4^{3-} when incubated in medium lacking these ions (Figures 2.S1a-b, 2.S2b-c).[58] Since the matrices were coated with matrigel to enhance the adhesion of hESCs, we compared the dissolution profiles between matrigel-coated and non-coated mineralized hydrogels and observed a similar dissolution profile (Figures 2.S1a-b). This suggests that the matrigel coating did not have any effect on CaP dissolution, which is in good agreement with a previous work.[147] The dissociation kinetics of the CaP minerals in conjunction with our previous report including XRD analyses of these biomineralized matrices suggest that the CaP minerals exhibit a semicrystalline structure.[38, 39] The pore size of the macroporous hydrogels was determined from the SEM and bright field images (Figures 2.1d, 2.S2a). The macroporous hydrogels exhibited a pore diameter of 77.7 ± 6.7 µm in their dried state as determined from the SEM images. This corresponded to a pore diameter of 123.6 ± 4.9 µm and 118.2 ± 3.6 µm (estimated from the bright field images) for the non-mineralized and mineralized macroporous hydrogels, respectively, in their swollen state. This is in agreement with our previous report, which shows no significant reduction in pore size due to mineralization.[133]

2.4.2. Mineralized matrices induce osteogenesis of hESCs in 2-D culture.

The effect of mineralized matrices on hESCs (HUES9) was examined and compared against that of corresponding non-mineralized matrices and cell culture grade coverslips. All the cultures were carried out in basal growth medium in the absence of any osteogenic inducing soluble factors. Pluripotent state of the hESCs prior to their culture on various matrices was characterized by their colony formation and staining for NANOG and OCT4 (Figure 2.S3). The hESCs adhered onto non-mineralized (NM) and mineralized (M) hydrogels and coverslips (CS) and were grown to confluence within 7 days of culture (Figure 2.S4a). As evident from F-actin staining at 3 days of post-plating, the cells adhered onto all surfaces with similar circularity (Figure 2.S4b). Analysis of gene expression profile of HUES9 cells demonstrated considerably higher osteogenic gene expression on mineralized matrices compared to non-mineralized matrices and coverslips after 28 days of culture (Figure 2.2a). The gene expression profile was further confirmed by quantitative PCR (qPCR) analyses, for markers that are characteristic of cells undergoing osteogenesis, as a function of culture time. The qPCR analyses showed that HUES9 cells cultured on mineralized matrices consistently exhibited an upregulation of osteogenic markers such as RUNX2, OCN, and SPP1 (Figure 2.2b). The mineralized matrix-assisted osteogenic differentiation was also evident in protein level. Cells cultured on mineralized matrices stained positive for OCN, an osteoblast specific marker, where the intensity of OCN staining increased with culture time (Figures 2.2c, 2.S5). No such OCN presence was observed on other substrates, suggesting that the mineral environment provided by the biomineralized matrix is sufficient to direct osteogenic differentiation of hESCs. Figure 2.S6 shows the F-actin staining of the cells on all substrates as a function of culture time. Concomitant with differentiation, the hESCs showed downregulation of pluripotent marker (NANOG) (Figure 2.S1c). Downregulation of NANOG was observed on all substrates, indicating that none of the culture conditions under study are conducive for supporting pluripotency of HUES9 cells. This is in agreement with previous studies, which showed that self-renewal of hESCs requires a combination of matrix-based cues and soluble factors such as basic fibroblast growth factor (bFGF).[143] While hESCs cultured on all substrates (non-mineralized and mineralized matrices and coverslips) showed downregulation of NANOG, only the cells cultured on mineralized matrices were found to undergo efficient osteogenic differentiation. This finding implies that although the hESCs cultured *in vitro* were poised to differentiate through a loss of pluripotent phenotype, their efficient differentiation into osteoblasts required a bone-specific mineral environment.

2.4.3. Mineralized matrices promote osteogenesis of hESCs in 3-D culture.

Having established the potential of mineralized matrices to induce osteogenic differentiation of HUES9 cells in 2-D culture, we subsequently evaluated the ability of mineralized matrices to direct osteogenic differentiation of hESCs in a 3-D environment. Mineralized macroporous hydrogel-assisted osteogenic differentiation was compared against that of non-mineralized macroporous hydrogels cultured under identical conditions. We have used two different cell lines, HUES9 and H9. Following 3 days after cell seeding, most of the cells were found to be viable in all matrices (Figure 2.S2d). DNA quantification as a function of post cell seeding suggested no significant change in cell number between the mineralized and non-mineralized matrices (Figures 2.S2e-f). Similar to 2-D culture, the hESCs on mineralized matrices showed distinct upregulation of osteogenic markers (RUNX2, OCN, and SPP1) (Figures 2.3a-b). Immunohistochemical staining for OCN corroborated the findings from the gene expression (Figures 2.3c-d). The cells cultured on all the matrices showed downregulation of pluripotent gene (NANOG) akin to 2-D culture systems (Figures 2.3e-f). Despite the geometrical differences between the 2-D hydrogel assisted culture and 3-D macroporous hydrogel assisted culture, the hESCs exposed to the mineralized matrices underwent osteogenic differentiation, thus underscoring the instructive cues that the mineralized environment provides to direct osteogenic commitment of hESCs.

In addition to the physical cues such as topographical cues, the mineralized matrices containing CaP minerals could contribute to osteogenesis of stem cells through biochemical signaling triggered by the local Ca^{2+} and PO_4^{3-} ions.[102, 148, 149]. As evident from the dissolution studies, the CaP minerals readily dissociate into Ca^{2+} and

PO_4^{3-} resulting in an increase in their local concentration. The dissociation and precipitation of the CaP moieties responding to their local concentration play not only a key role in the binding and release of various osteoinductive growth factors like BMPs,[47, 150, 151] but will also regulate various signaling cascades involving Ca^{2+} and PO_4^{3-} ions. Studies have shown that influx of Ca^{2+} ions through L-type calcium channels promote osteogenic differentiation of MSCs.[152] Recently, we have shown the role of PO_4^{3-}-ATP-Adenosine signaling cascade in CaP-bearing matrix-mediated osteogenic differentiation of hMSCs.[39]

2.4.4. Biomineralized matrices support osteogenesis of hESCs *in vivo*.

To determine the potential of mineralized matrices to support osteogenic differentiation of hESCs *in vivo*, hESC-laden matrices (hESC-laden mineralized and non-mineralized macroporous hydrogels) were subcutaneously implanted into 3-month-old NOD/SCID mice. Subcutaneous implantation is often used to assess the potential contribution of stem cells and scaffolds to *in vivo* bone tissue formation and to determine the pluripotency of hESCs.[29, 67] The implants were retrieved after 4 and 8 weeks and analyzed for bone tissue formation. Gross images of the excised implants indicated hard tissue formation in all implants with significant differences (Figures 2.4a-b). 3-D micro-computed tomography (μCT) image analyses concurred with the above observations wherein cell-laden mineralized matrices exhibited homogeneous and dense calcification at 4 and 8 weeks post-implantation (Figures 2.4c-d). Unlike cell-laden mineralized matrices, their non-mineralized counterparts showed non-uniform calcification concentrated along the periphery of the implants. The μCT analyses of mineralized matrices prior to implantation indicated that the implants themselves were not radio-opaque and thus, were not detectable in µCT (Figure 2.S7). 3-D µCT models with 360° views and 2-D cross-sectional images confirmed uniform mineral formation throughout the porous network by hESCs coupled with mineralized matrices and non-uniform mineralization for their non-mineralized counterparts (Figures 2.S8a-b). Furthermore, the hESC-laden mineralized matrices were found to have higher mineral densities (BV/TV) compared to their non-mineralized counterparts (Figures 2.4c-d, bar graphs).

To verify whether the hard tissue formation observed by 3-D µCT analyses is indeed due to bone tissue formation, histological examinations were conducted. H&E staining of the cell-laden mineralized matrices demonstrated progressive accumulation of dense extracellular matrix (ECM) that resembles bone tissue at 4 and 8 weeks post-implantation (Figures 2.5a-b, right panels). High magnification images demonstrated that a majority of cells were populated along the periphery of newly assembled ECM for cell-laden mineralized matrices at 8 weeks post-implantation. The bone tissue formation was further confirmed by OCN staining, where the hard tissue layer within the cell-laden mineralized matrices was stained positive for OCN at 4 and 8 weeks post-implantation revealing *in vivo* bone tissue formation (Figures 2.5c-d, right panels). In stark contrast, hESCs-laden non-mineralized counterparts displayed mainly a mixture of fibrous and fat tissue with a thin layer of bone tissue in the mineralized peripheral region of the implant (Figures 2.5a-b, left panels, Figure 2.S9a). Intense Oil Red O staining for lipid molecules further confirmed the presence of fat cells in non-mineralized matrices (Figures 2.5e-f, left panels). Amongst the two cell lines, HUES9-laden non-mineralized matrices were found to have higher Oil Red O staining compared to H9-laden matrices. This difference in adipogenic differentiation could be attributed to innate variations in different hESC lines with HUES9 cells retaining a higher adipogenic potential. This is consistent with previous studies that demonstrated cell line-dependent differentiation of pluripotent stem cells.[153] The human origin of the cells within the cell-laden implants after 8 weeks of transplantation was confirmed by human-specific lamin B staining, which reveals survival and contribution of transplanted hESCs towards tissue formation *in vivo* in all matrices (Figure 2.S9b); however, the involvement of infiltrated host cells could not be ruled out. Previously, we have shown the infiltration of host cells into mineralized macroporous hydrogels and their contribution to ectopic bone tissue in rats, but no such infiltration into the non-mineralized counterparts.[133] Although a long-term investigation is warranted, the *in vivo* findings demonstrate survival and continuous differentiation of transplanted cells responding to the local cues without teratoma formation. Previous studies involving hESCs have shown that they form teratoma by 7 weeks when subcutaneously implanted with biomaterials.[67] Lack of teratoma formation after 8 weeks of implantation in this study suggests that cells lost their pluripotency within the synthetic matrices.

A study by Both *et al*. has reported a lack of *in vivo* bone formation from hESCs transplanted using porous biphasic calcium phosphate ceramics even with preconditioning of cells in osteogenic-inducing medium for one week prior to their implantation.[154] The observed differences could be attributed to the cell lines and/or the matrix used. The dissolution kinetics of CaP minerals have been thought to play a key role in the ability of CaP-based matrices to direct osteogenic commitment of stem and progenitor cells and assist in bone tissue formation.[20, 45]. A recent study by Yuan *et al*.

has shown that subtle differences in the crystalline phase of CaP ceramics could endow them with different levels of osteoinductive function *in vivo*.[155]

2.5. Conclusion

In summary, results described in this article demonstrate that synthetic matrices, recapitulating a bone-like mineral rich environment, can direct osteogenic commitment of pluripotent hESCs both *in vitro* and *in vivo*. Together, our results show for the first time that differentiation of human embryonic stem cells into terminal phenotypes can be induced solely by synthetic matrices both *in vitro* and *in vivo*. Such synthetic matrix-mediated stem cell commitment will not only accelerate the translational potential of hESCs, but also provide a platform to elucidate the underlying molecular mechanism that regulate pluripotent stem cell commitment and the role of extracellular matrix in this process.

2.6. Acknowledgements

Authors gratefully acknowledge the financial support from National Institutes of Health and California Institute of Regenerative Medicine (NIH, Grant 1 R01 AR063184-01A1; CIRM, RN2-00945 and RT2-01889). We also thank Dr. Ameya Phadke and Dr. Manando Nakasaki for valuable discussions.

Chapter 2, in full, is a reprint of the material as it appears in Journal of Materials Chemistry B, vol. 2, 2014. “Biomineralized matrix-assisted osteogenic differentiation of human embryonic stem cells”. Kang, Heemin; Wen, Cai; Hwang, Yongsung; Shih, Yu-

Ru V.; Kar, Mrityunjoy, Seo, Sung Wook; Varghese, Shyni. The dissertation author was the primary investigator and author of this paper.

2.7. Figures

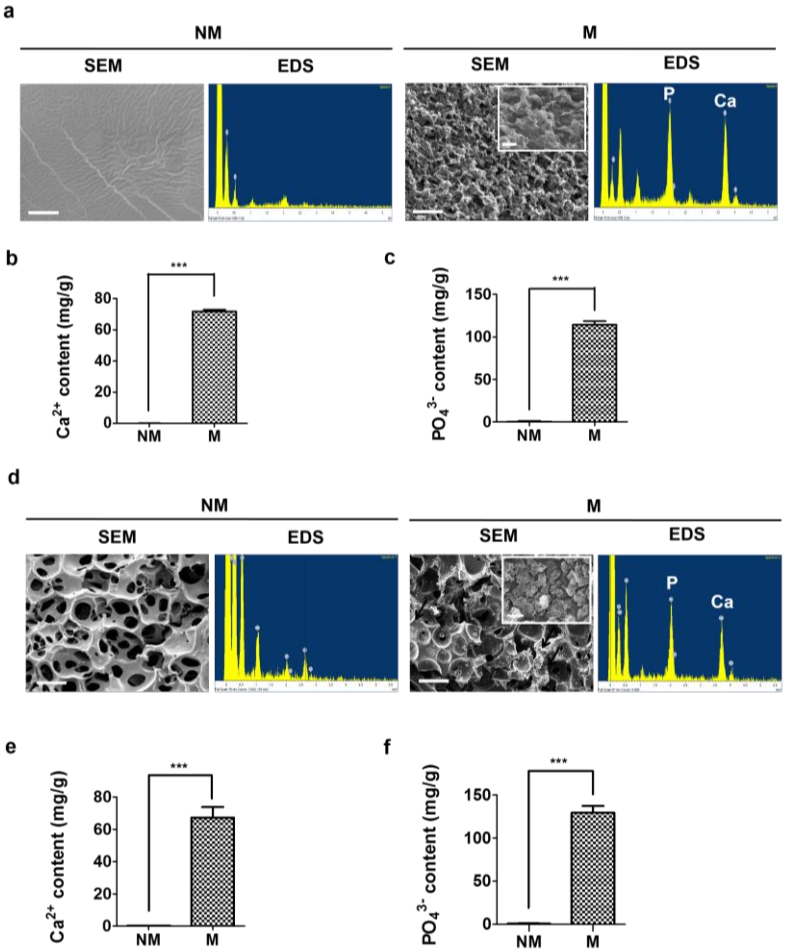

Figure 2.1. Characterization of mineralized matrices.

(a) SEM images and corresponding EDS of non-mineralized (NM) and mineralized (M) hydrogels. Scale bars represent 2 μm. Inset shows high magnification image. Scale bar represents 500 nm. (b) Ca^{2+} and (c) PO_4^{3-} amounts of NM and M hydrogels. (d) SEM images and corresponding EDS of NM and M macroporous hydrogels. Scale bars represent 100 μm. Inset shows high magnification image. Scale bar indicates 1 μm. (e) Ca^{2+} and (f) PO_4^{3-} contents of NM and M macroporous hydrogels. Data are presented as mean ± standard errors (n=3). Two-tailed Student's t-test was used to compare two groups. Asterisks indicate statistical significances according to p-values (***: $p < 0.001$).

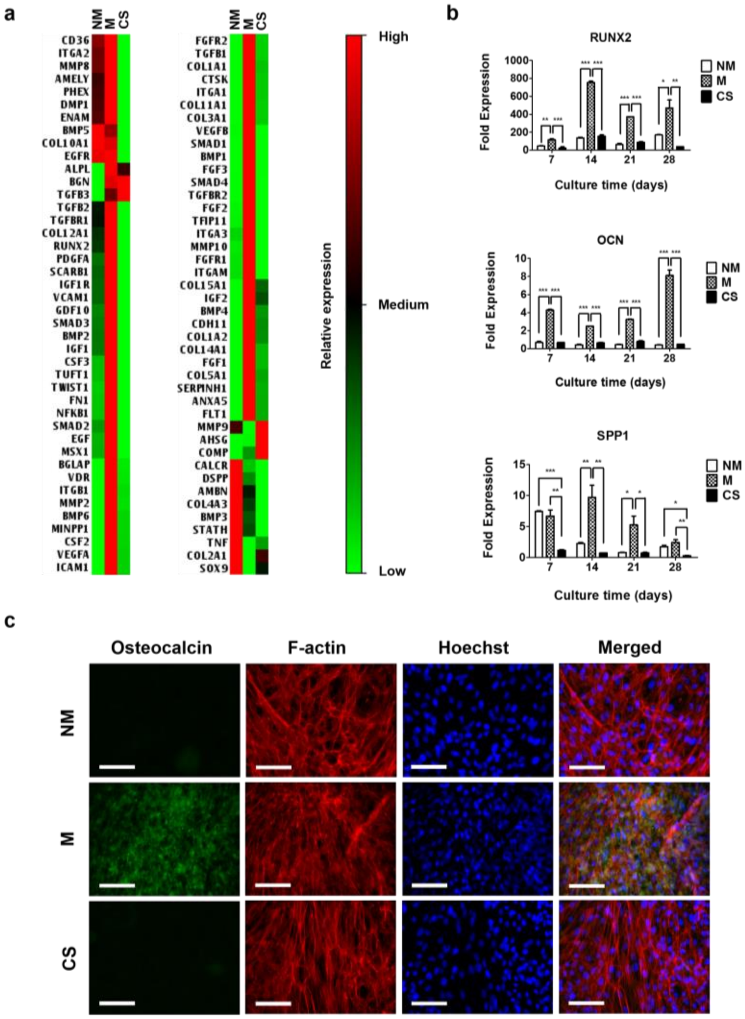

Figure 2.2. Mineralized matrix-assisted osteogenic differentiation of HUES9 cells in 2-D culture.

(a) Transcription profile of HUES9 cells cultured for 28 days in growth medium on non-mineralized matrices (NM), mineralized matrices (M), and coverslips (CS). Relative expressions: red (high), black (medium), green (low). (b) RUNX2, OCN, and SPP1 gene expressions as a function of culture time for HUES9 cells on NM and M matrices and CS in growth medium. (c) Immunofluorescent staining for OCN (green), F-actin (red), and nucleus (Hoechst; blue) of HUES9 after 28 days of culture on NM and M matrices and CS. Scale bars represent 100 µm. Data are presented as mean ± standard errors (n=3). Multiple groups in the same time point were compared by one-way ANOVA with Tukey-Kramer post-hoc test. Asterisks indicate statistical significances according to p-values (*: $p < 0.05$; **: $p < 0.01$; ***: $p < 0.001$).

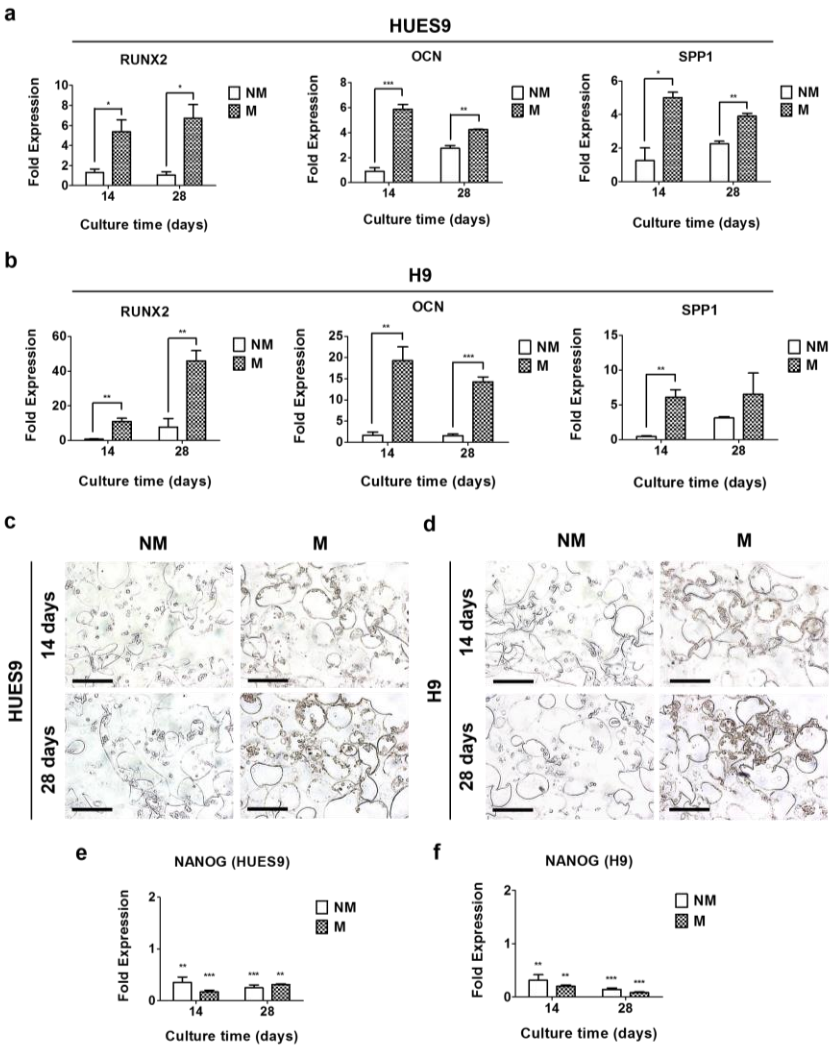

Figure 2.3. Mineralized matrix-assisted osteogenic differentiation of hESCs in 3-D culture.

RUNX2, OCN, and SPP1 gene expressions for (a) HUES9 and (b) H9 after 14 and 28 days of culture in growth medium on non-mineralized (NM) and mineralized (M) matrices. Immunohistochemical staining of OCN for (c) HUES9 and (d) H9 after 14 and 28 days of culture on NM and M matrices. Scale bars represent 100 μm. NANOG gene expression for (e) HUES9 and (f) H9 after 14 and 28 days of culture on NM and M matrices. Data are shown as mean ± standard errors (n=3). Two-tailed Student's t-test was used to compare two groups in the same time point. Two-way ANOVA with Bonferroni post-hoc test was used to compare multiple groups in different time points. Asterisks represent statistical significances with each p-value (*: $p < 0.05$; **: $p < 0.01$; ***: $p < 0.001$).

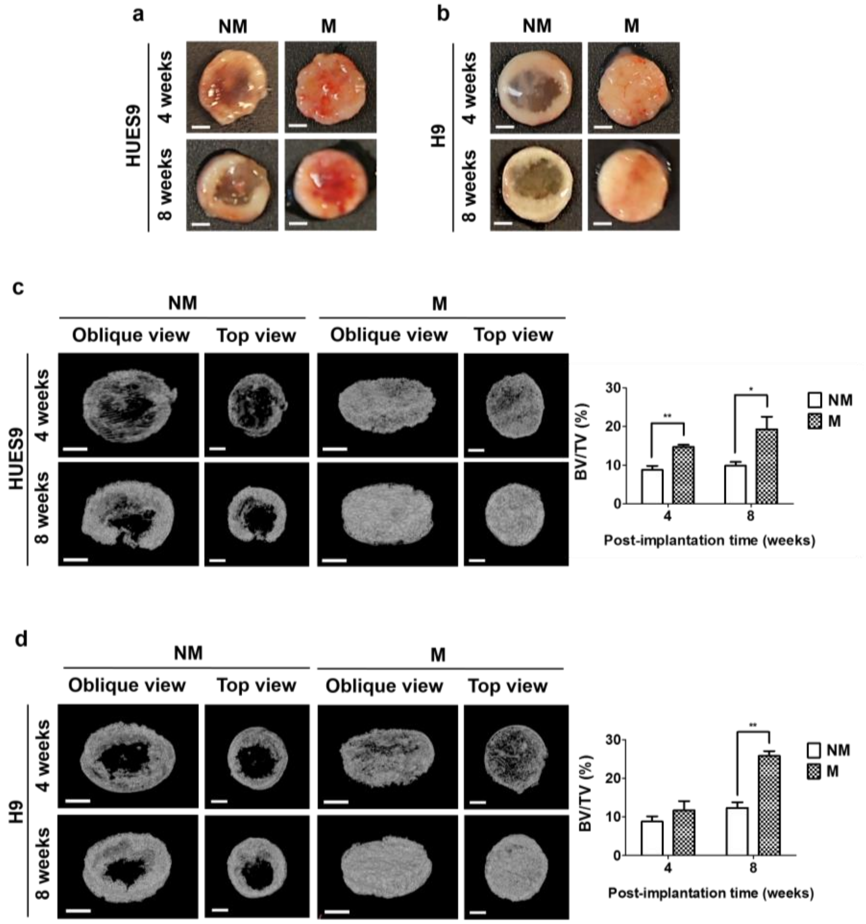

Figure 2.4. *In vivo* function of hESC-laden mineralized and non-mineralized matrices.

Gross images of (a) HUES9-laden and (b) H9-laden non-mineralized (NM) and mineralized (M) matrices after 4 and 8 weeks of implantation. 3-D µCT images of (c) HUES9-laden and (d) H9-laden NM and M matrices at 4 and 8 weeks post-implantation and corresponding bone mineral densities (BV/TV) as a function of post-implantation time. Scale bars indicate 2 mm. Data are displayed as mean ± standard errors (n=3). Comparisons of two groups in the same time point were made by two-tailed Student's t-test. Asterisks indicate statistical significances according to p-values (*: $p < 0.05$; **: $p < 0.01$).

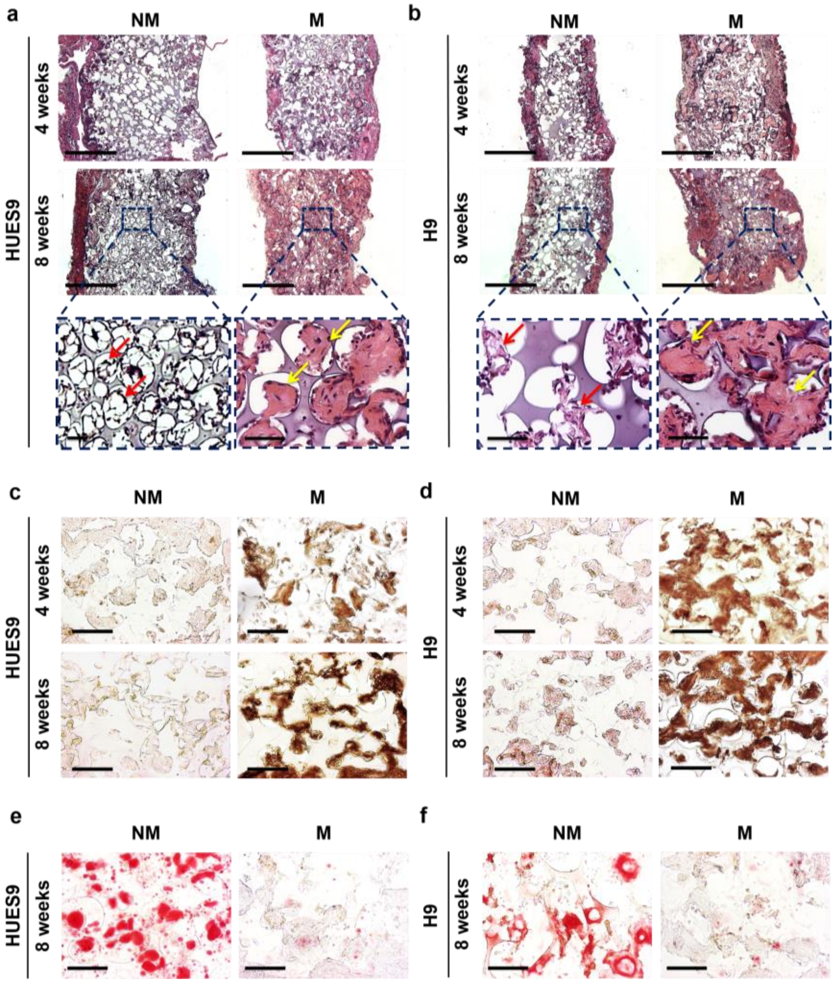

Figure 2.5. Biomaterial-dependent *in vivo* tissue formation of transplanted hESC-laden matrices.

H&E staining of (a) HUES9-laden and (b) H9-laden non-mineralized (NM) and mineralized (M) matrices after 4 and 8 weeks of implantation. Scale bars represent 500 µm. High magnification images from the center of NM and M matrices with HUES9 and H9 cells at 8 weeks post-implantation are also provided. Yellow arrows: Bone-like matrix formation. Red arrows: Fat and fibrous tissues. Scale bars indicate 50 µm. Immunohistochemical staining of OCN at the center of NM and M matrices containing (c) HUES9 and (d) H9 cells following 4 and 8 weeks of transplantation. Scale bars indicate 100 µm. Oil Red O staining of NM and M matrices containing (e) HUES9 and (f) H9 cells at 8 weeks post-implantation. Scale bars represent 100 µm.

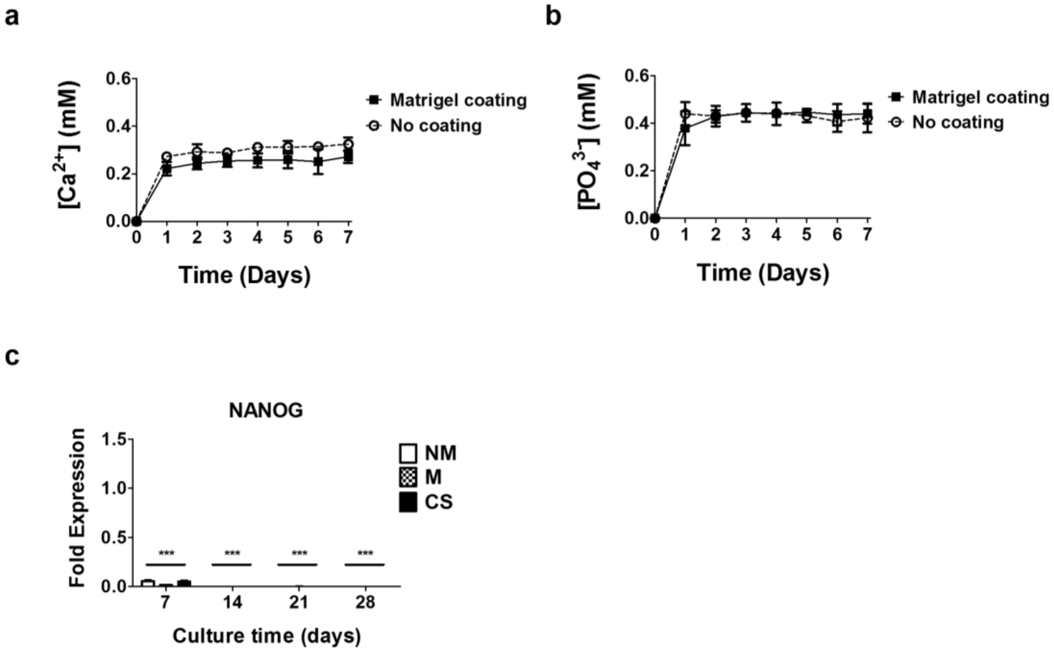

Figure 2.S1. Characterization of mineralized hydrogels and the effect of different substrates on the pluripotency of hESCs.

Release of (a) Ca^{2+} and (b) PO_4^{3-} from matrigel-coated or non-coated mineralized hydrogels incubated at 37 °C in Ca^{2+} and PO_4^{3-}-free Tris-HCl buffer as a function of time. Data are presented as mean ± standard deviations (n=3). (c) NANOG gene expression of HUES9 cells cultured in growth medium on non-mineralized (NM) and mineralized (M) hydrogels and coverslips (CS) as a function of culture time. Data are presented as mean ± standard errors (n=3). Two-way ANOVA with Bonferroni post-hoc test was used to compare multiple groups in different time points. Asterisks indicate statistical significances according to p-values (***: $p < 0.001$).

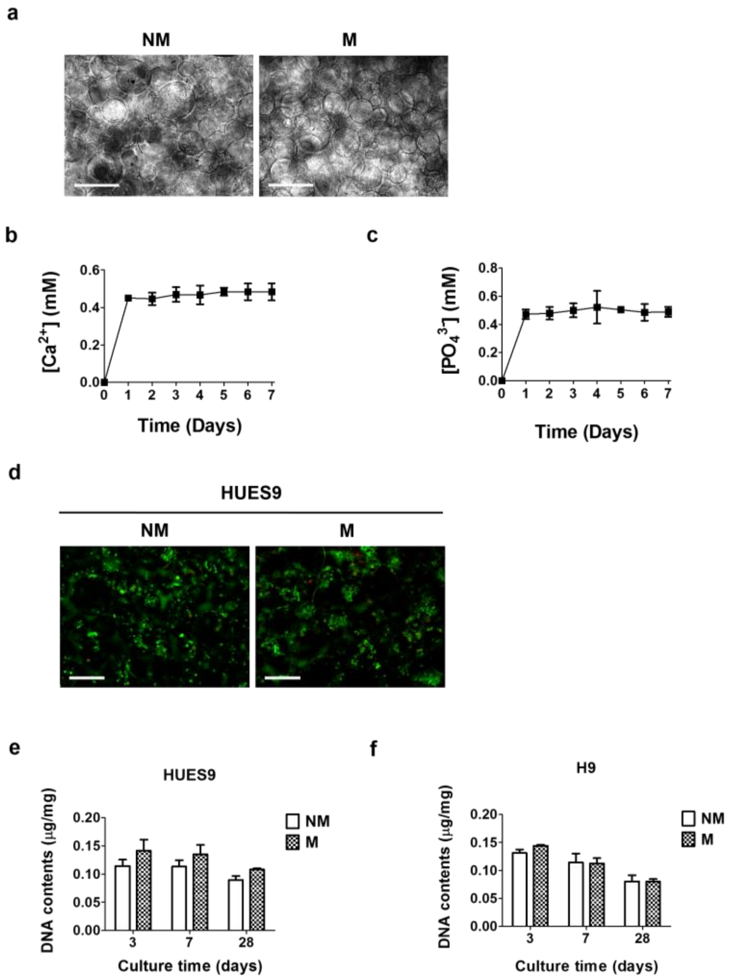

Figure 2.S2. Characterization of mineralized macroporous hydrogels and their effect on hESCs.

(a) Bright field images of non-mineralized (NM) and mineralized (M) macroporous hydrogels in their swollen state. Scale bars represent 200 µm. (b) Ca^{2+} and (c) PO_4^{3-} release from M macroporous hydrogels in Tris-HCl buffer at 37 °C for 7 days. Data are presented as mean ± standard deviations (n=3). (d) Representative live-dead image of hESC-laden matrix (HUES9-laden macroporous hydrogels) after 3 days of culture. Scale bars indicate 200 µm. DNA contents of (e) HUES9-laden and (f) H9-laden macroporous hydrogels as a function of culture time. Data are presented as mean ± standard errors (n=3).

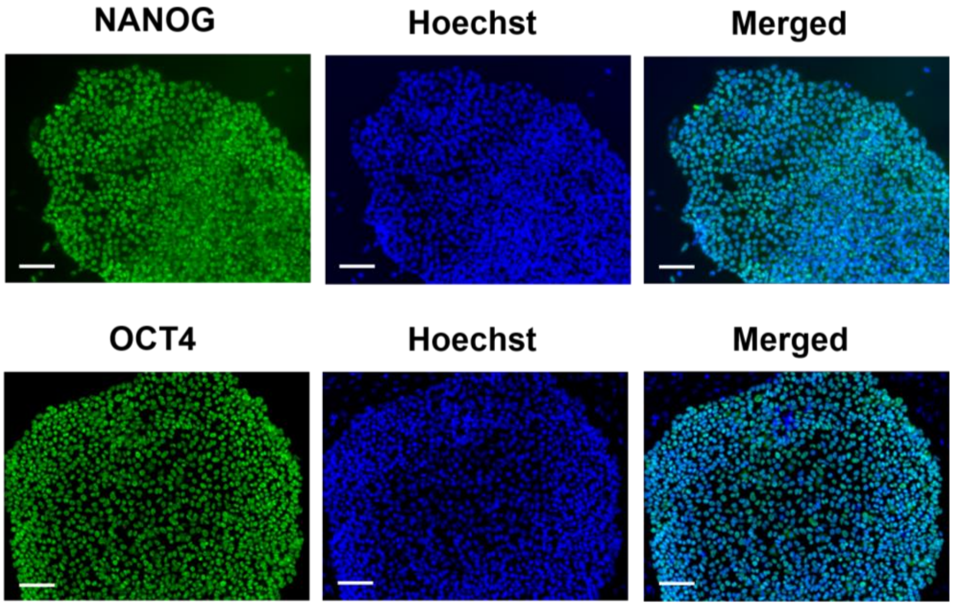

Figure 2.S3. Pluripotency of hESCs prior to their culture on various substrates.

Representative immunofluorescent staining image of hESCs (HUES9 cells) for NANOG (green) and OCT4 (green) with corresponding nucleus (Hoechst; blue) confirming their pluripotency. Scale bars represent 200 µm.

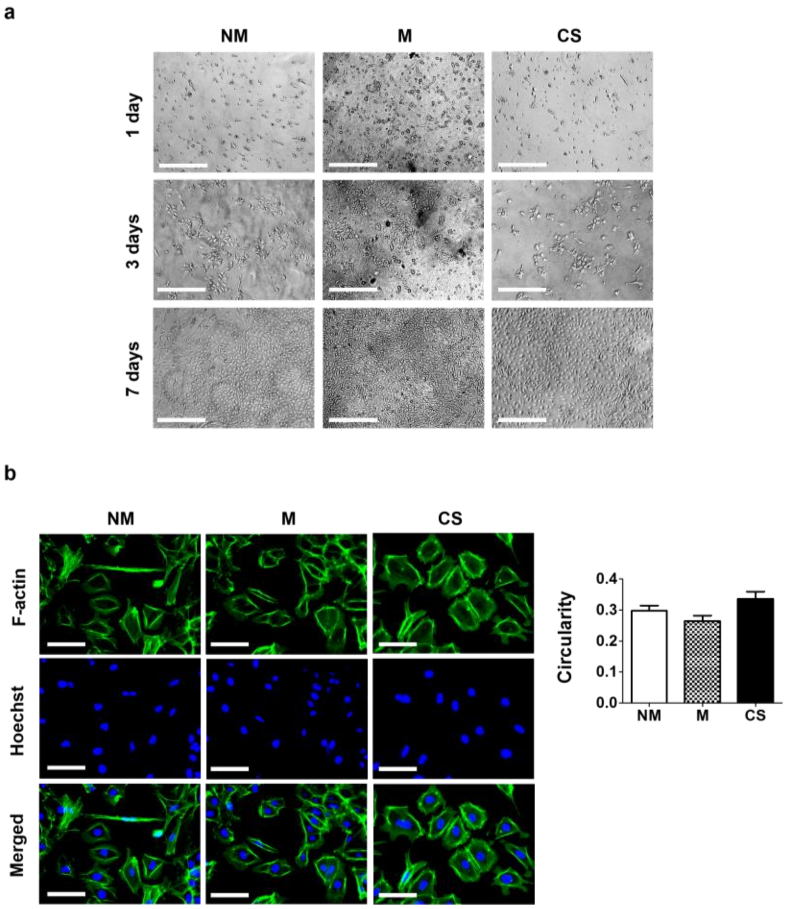

Figure 2.S4. Adhesion and proliferation of hESCs on the matrices in 2-D culture.

(a) Bright-field images of HUES9 after 1, 3, and 7 days of culture on non-mineralized (NM) and mineralized (M) matrices and coverslips (CS). Scale bars represent 500 µm. (b) Fluorescent staining for F-actin (green) and nucleus (Hoechst; blue) of HUES9 cells after 3 days of culture on NM and M hydrogels and CS. Scale bars indicate 100 µm. Circularity index of the cells (bar graph) on various matrices was determined from F-actin images. Data are presented as mean ± standard errors (n=30 cells).

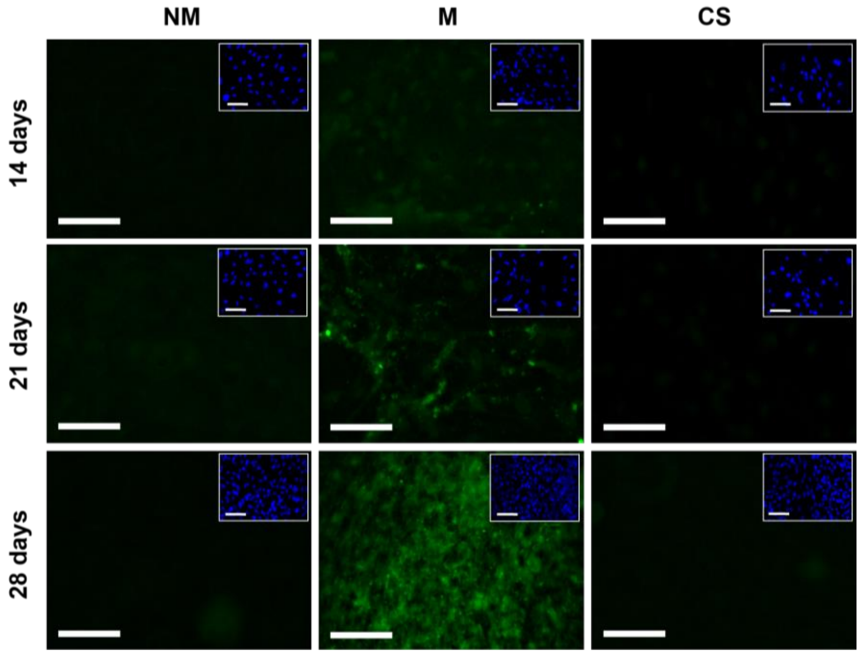

Figure 2.S5. Fluorescent staining for osteocalcin (green) and nucleus (Hoechst; blue; inset) after 2-D culture.

HUES9 cells were cultured for 14, 21, and 28 days on non-mineralized (NM) and mineralized (M) hydrogels and coverslips (CS). Scale bars represent 100 µm.

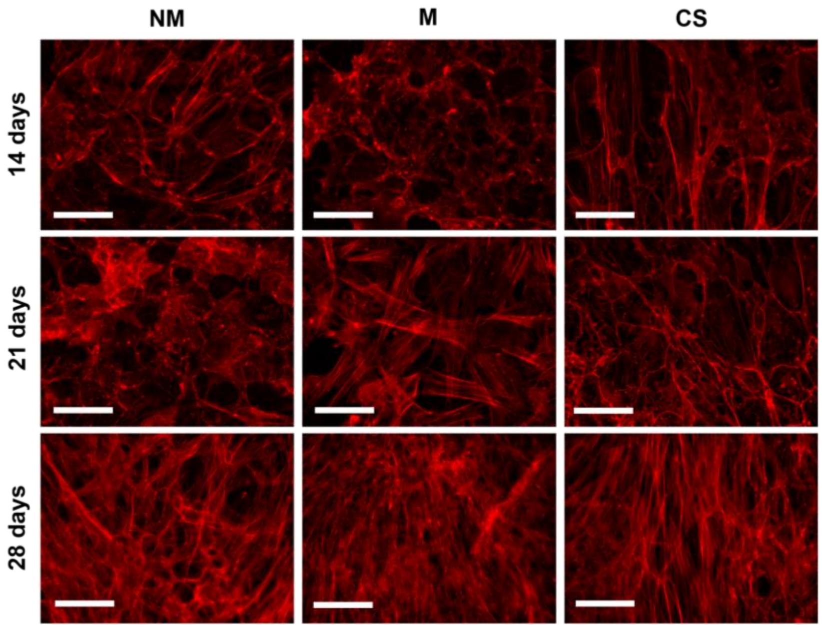

Figure 2.S6. Fluorescent staining for F-actin (red) after 2-D culture.

HUES9 cells were cultured for 14, 21, and 28 days on non-mineralized (NM) and mineralized (M) matrices and coverslips (CS). Scale bars represent 100 μm.

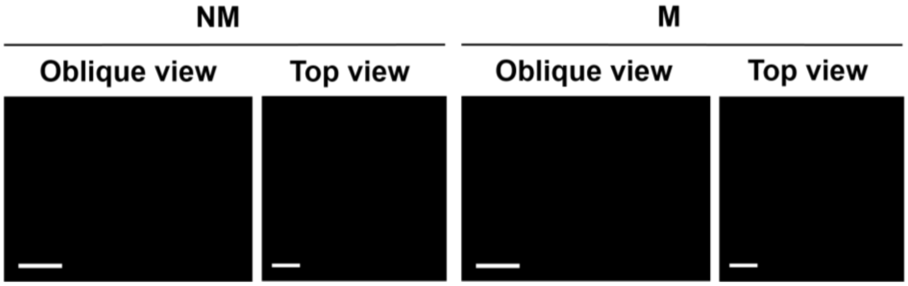

Figure 2.S7. µCT analyses prior to *in vivo* implantation.

µCT pre-implantation images of non-mineralized (NM) and mineralized (M) matrices confirm that the matrices themselves are not radio-opaque.

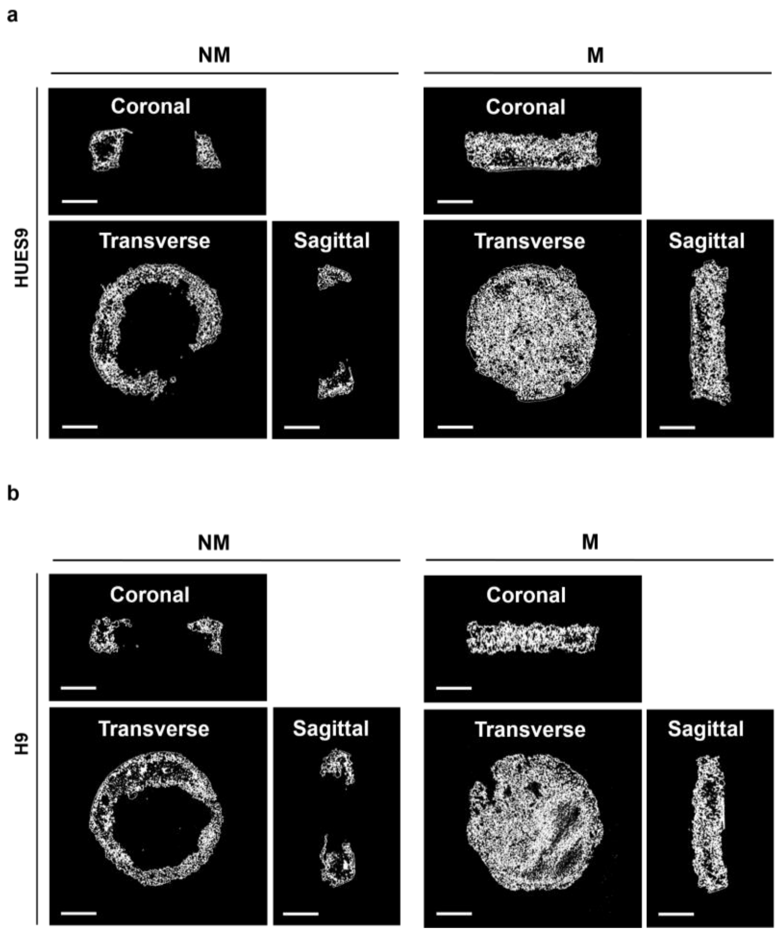

Figure 2.S8. μCT analyses of cell-laden matrices after *in vivo* implantation.

2-D cross-sectional μCT images in coronal, transverse, and sagittal planes of (a) HUES9 or (b) H9-laden non-mineralized (NM) and mineralized (M) matrices at 8 weeks post-implantation. Scale bars represent 2 mm.

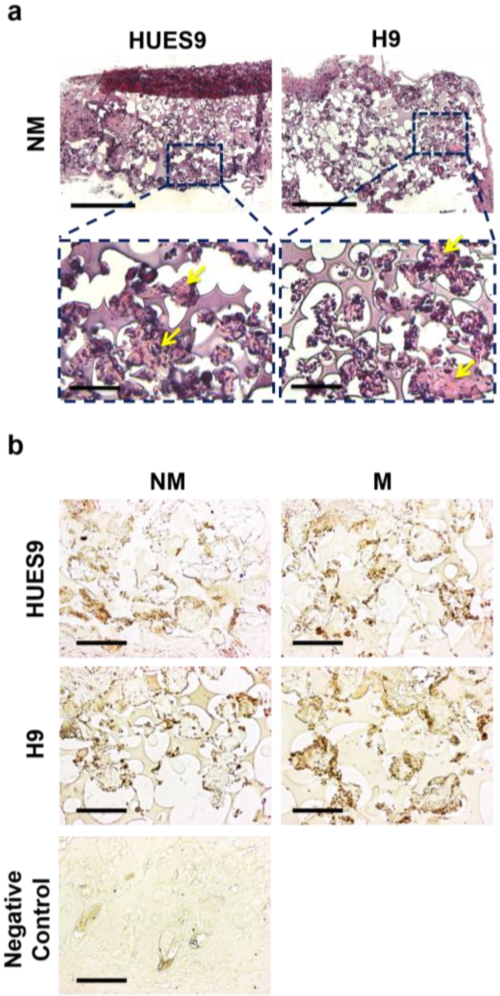

Figure 2.S9. Histochemical analyses of cell-laden matrices post *in vivo* implantation.

(a) H&E staining of HUES9-laden and H9-laden non-mineralized (NM) macroporous hydrogels after 8 weeks of implantation. Scale bars indicate 500 µm. High magnification images of the peripheral mineralized region in the cell-laden matrices are also shown. Yellow arrows indicate bone-like matrix formation. Scale bars represent 100 µm. (b) Immunohistochemical staining of HUES9 and H9-laden NM and mineralized (M) macroporous hydrogels for lamin B following 8 weeks of implantation. Mouse skin tissue was used as a negative control. Scale bars indicate 100 µm.

2.8. Tables

Table 2.S1. List of primers used in qRT-PCR experiments.

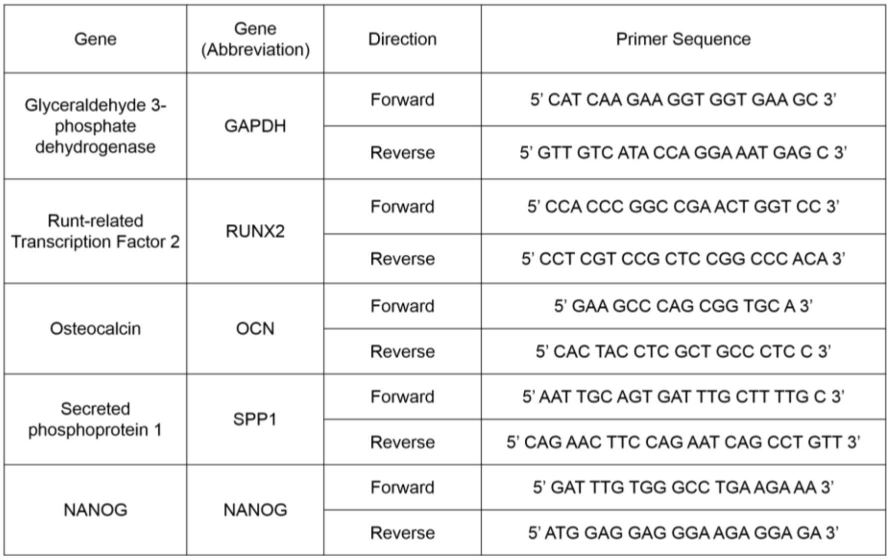

Gene	Gene (Abbreviation)	Direction	Primer Sequence
Glyceraldehyde 3-phosphate dehydrogenase	GAPDH	Forward	5’ CAT CAA GAA GGT GGT GAA GC 3’
		Reverse	5’ GTT GTC ATA CCA GGA AAT GAG C 3’
Runt-related Transcription Factor 2	RUNX2	Forward	5’ CCA CCC GGC CGA ACT GGT CC 3’
		Reverse	5’ CCT CGT CCG CTC CGG CCC ACA 3’
Osteocalcin	OCN	Forward	5’ GAA GCC CAG CGG TGC A 3’
		Reverse	5’ CAC TAC CTC GCT GCC CTC C 3’
Secreted phosphoprotein 1	SPP1	Forward	5’ AAT TGC AGT GAT TTG CTT TTG C 3’
		Reverse	5’ CAG AAC TTC CAG AAT CAG CCT GTT 3’
NANOG	NANOG	Forward	5’ GAT TTG TGG GCC TGA AGA AA 3’
		Reverse	5’ ATG GAG GAG GGA AGA GGA GA 3’

Chapter 3: Mineralized gelatin methacrylate-based matrices induce osteogenic differentiation of human induced pluripotent stem cells

3.1. Abstract

Human induced pluripotent stem cells (hiPSCs) are a promising cell source with pluripotency and self-renewal properties. Design of simple and robust biomaterials with an innate ability to induce lineage-specificity of hiPSCs is desirable to realize their applications in regenerative medicine. In this study, we investigated the potential of biomaterials containing calcium phosphate minerals to induce osteogenic differentiation of hiPSCs. hiPSCs cultured using mineralized gelatin methacrylate-based matrices underwent osteogenic differentiation *ex vivo*, both in two- dimensional (2-D) and three-dimensional (3-D) cultures, in growth medium devoid of any osteogenic-inducing chemical components or growth factors. Our findings that osteogenic differentiation of hiPSCs can be achieved through biomaterial-based cues alone present new avenues for personalized regenerative medicine. Such biomaterials that could not only act as structural scaffolds, but could also provide tissue-specific functions such as directing stem cell differentiation commitment, have great potential in bone tissue engineering.

3.2. Introduction

Human pluripotent stem cells (hPSCs), which include both embryonic stem cells and induced pluripotent stem cells, play an important role in regenerative medicine, developmental biology and pathology, and drug screening owing to their ability to give rise to any cells in the human body and indefinitely self-renew [64, 156]. hiPSCs developed from human autologous somatic cells could circumvent concerns regarding immune properties and ethical issues, making them an ideal cell source for regenerative medicine [157]. Despite the benefits that hiPSCs offer, controlling their differentiation into targeted cell type(s) remains a challenge. Studies over the years have shown that stem cells respond to their microenvironment composed of soluble and matrix-based cues to regulate their fate and commitment [158-160]. Synthetic biomaterials have been extensively used to recapitulate tissue-specific physicochemical cues to direct self-renewal and differentiation of stem cells [161, 162].

Biomaterials containing calcium phosphate minerals have been shown to promote osteogenic differentiation of stem cells [20, 55, 58, 137, 163, 164]. These materials have also been shown to support *in vivo* bone tissue formation [55, 134, 137, 163, 164]. Previously, we have shown that hydrogels containing acryloyl-6-aminocaproic acid (A6ACA) moieties promote their mineralization when exposed to a medium containing Ca^{2+} and PO_4^{3-} [38]. The carboxyl groups of A6ACA moieties bind to Ca^{2+} ions and promote nucleation and growth of calcium phosphate (CaP) minerals. By employing biomineralized poly(ethylene glycol)-diacrylate-co-acryloyl-6-aminocaproic acid (PEGDA-co-A6ACA) matrices, we have shown that mineralized matrices can direct osteogenic differentiation of human bone marrow-derived mesenchymal stem cells (hMSCs) and human embryonic stem cells (hESCs) [58, 165]. However, it required the biomineralized PEGDA-co-A6ACA matrices to be coated with Matrigel to promote initial attachment of the hESCs to the matrix. In this study, we have developed mineralized matrices containing gelatin methacrylate (GelMA) and examined their potential to direct osteogenic differentiation of hiPSCs. Gelatin, derived from natural collagen, possesses cell adhesion motifs that could promote adhesion of hiPSCs to the underlying matrix [166, 167]. Moreover, gelatin-based matrices have been demonstrated to degrade [30, 167-171] and have been studied extensively as a scaffold for tissue engineering [168, 169, 171, 172].

Studies that have reported osteogenic differentiation of hiPSCs often utilized derivation of MSCs or mesoderm-like progenitor cells and their subsequent differentiation into osteoblasts using osteogenic-inducing soluble factors such as β-glycerophosphate, ascorbic acid 2-phosphate, dexamethasone, and/or growth factors like bone morphogenetic protein-2 (BMP-2) [65, 68, 69, 173-176]. A recent study by de Peppo et al. has employed decellularized bone matrix to create bone tissues from hiPSC-derived mesoderm progenitor cells [68]. However, to our knowledge, there are no reports showing osteogenic differentiation of hiPSCs solely through biomaterial-based cues. Here, we demonstrate that biomaterials containing CaP minerals induce osteogenic differentiation of hiPSCs in growth medium devoid of any osteogenic-inducing small molecules or growth factors.

3.3. Materials and Methods

3.3.1. Materials

Synthesis and modification of materials: Poly(ethylene glycol)-diacrylate (PEGDA; M_n = 3.4 kDa) and N-acryloyl 6-aminocaproic acid (A6ACA) were synthesized as previously described [125, 141, 165]. Gelatin-methacrylate (GelMA) was prepared through methacrylation of gelatin (Sigma-Aldrich, catalog number: G1890) [167]. Briefly, 10 g of gelatin along with 100 mL of phosphate buffered saline (PBS) was added into a round-bottom flask purged with argon gas and dissolved under stirring at 60 ^{o}C. Around 8 mL of methacrylic anhydride (Polysciences, catalog number: 01517) was added in drop-wise under stirred conditions for 2 hours. The reaction mixture was kept at 60 ^{o}C for another 1 hour. 100 mL of pre-warmed PBS at 60 ^{o}C was added to the mixture and maintained at 60 ^{o}C for 15 minutes. The resulted GelMA was placed in a dialysis tube (Spectrum Laboratories, catalog number: 132676) in deionized (DI) water at 40 ^{o}C for 7 days with two daily changes of DI water and filtered through 40 µm-sized pores, lyophilized, and stored at -20 ^{o}C prior to use.

3.3.2. Synthesis of GelMA-co-A6ACA hydrogels

Gelatin-methacrylate-co-acryloyl 6-aminocaproic acid (GelMA-co-A6ACA) hydrogels were synthesized as follows. 30 w/v% GelMA was dissolved in DI water at 45 ^{o}C. 1 M A6ACA was dissolved in 1 M NaOH to deprotonate the carboxyl groups. One part each of 30 w/v% GelMA and 1 M A6ACA were mixed to yield a solution containing 15 w/v% GelMA and 0.5 M (equivalent to 9 w/v%) A6ACA. Around 0.3 w/v% of photoinitiator, 1-[4-(2-Hydroxyethoxy)-phenyl]-2-hydroxy-2-methyl-1-propane-1 (Ciba Specialty Chemicals, Irgacure 2959) in 70% ethanol, was added into the above solution. The solution was then dispensed into a Bio-Rad glass plate separated by a 1-mm spacer and allowed to polymerize at 25 ^{o}C under 365 nm UV light for 10 minutes. The resultant hydrogels were incubated in PBS for 24 hours with two changes of PBS. Hydrogels discs of 1 cm^2 (area) x 1 mm (height) dimensions were used for the cell culture experiments.

3.3.3. Synthesis of GelMA-co-A6ACA-co-PEGDA macroporous hydrogels

Gelatin-methacrylate-co-acryloyl 6-aminocaproic acid-co-poly(ethylene glycol)-diacrylate (GelMA-co-A6ACA-co-PEGDA) macroporous hydrogels were synthesized by using polymethylmethacrylate (PMMA) leaching method [177]. First, 8-mm-diameter cylindrical molds packed with PMMA were made from PMMA microspheres having a diameter of 165 µm (Bangs Laboratories, catalog number: BB05N). Each PMMA column was exposed to 60 µl of 20% acetone/80% ethanol mixture for 1 minute to fuse the PMMA beads. The mold was dried at 80 ^{o}C for 1 hour and stored at room temperature. Next, 50 µl of a precursor solution containing 10 w/v% GelMA, 9 w/v% A6ACA (treated with NaOH), 10 w/v% PEGDA, and 0.3 w/v% Irgacure 2959 (in 70% ethanol) was dispensed into PMMA-filled molds and photopolymerized using UV light for 10 minutes. The PMMA beads embedded within the GelMA-co-A6ACA-co-PEGDA networks were subsequently dissolved in acetone for 3 days while replenishing fresh acetone three times each day, yielding the macroporous hydrogels. The resultant macroporous hydrogels were gradually hydrated from pure acetone to acetone/DI water mixture and to pure DI water for a day. The macroporous hydrogels were equilibrated in PBS for 6 hours and punched out to obtain constructs with diameter and height dimensions of 5 mm and 2 mm, respectively.

3.3.4. Mineralization and sterilization of GelMA-based hydrogels

GelMA-co-A6ACA hydrogels and GelMA-co-A6ACA-co-PEGDA macroporous hydrogels were subjected to mineralization process as described elsewhere [165]. Briefly, both matrices were soaked in DI water for 6 hours and immersed in modified simulated body fluid (m-SBF; pH=7.4) at 25 ^{o}C for 6 hours. The m-SBF solution is composed of 142.0 mM Na^{+}, 5.0 mM K^{+}, 1.5 mM Mg^{2+}, 2.5 mM Ca^{2+}, 103.0 mM Cl^{-}, 10.0 mM HCO_3^{-}, 1.0 mM HPO_4^{2-}, and 0.5 mM SO_4^{2-} as described elsewhere [178]. The matrices were briefly rinsed with DI water and soaked in 40 mM Ca^{2+} and 24 mM HPO_4^{2-} solution (pH=5.2) at 25 ^{o}C for 45 minutes using VWR Mini Shaker (Catalog number: 12620-938) at 200 rpm. The matrices were then briefly rinsed in DI water, incubated in m-SBF at 37 ^{o}C for 2 days with daily change of m-SBF, and equilibrated in PBS for 6 hours.

The mineralized and non-mineralized matrices were sterilized by immersing in 70% ethanol for 6 hours. The ethanol-treated matrices were then washed in sterile PBS by replenishing the PBS four times each day for 4 days to fully remove residual ethanol. Sterile non-mineralized and mineralized GelMA-co-A6ACA hydrogels were employed for 2-D culture. Sterile non-mineralized and mineralized GelMA-co-A6ACA-co-PEGDA macroporous hydrogels were utilized for 3-D culture.

3.3.5. Scanning electron microscopy (SEM) & energy dispersive spectra (EDS)

SEM imaging was carried out to investigate the morphology of the mineralized matrices. EDS analysis was performed to determine the composition of the minerals. Samples were briefly rinsed in DI water to remove non-bound ions for 5 minutes, cut into thin slices and subjected to flash-freezing and lyophilization. After Iridium coating for 7 seconds in the sputter (Emitech, K575X), samples were imaged by using SEM (Philips XL30 ESEM) and analyzed for elemental spectra with integrated EDS system. INCA software was used to quantify Ca/P atomic ratio from elemental spectra. The pore diameter of the macroporous matrices was calculated either from SEM or bright field images to estimate the pore structures in the dry and wet state, respectively. Roughly 10 pores were chosen from each of three SEM or bright field images (n=30) and their diameter was determined using ImageJ. The data are presented as mean ± standard errors.

3.3.6. Calcium and phosphate assays

Calcium and phosphate assays were conducted to determine the amounts of Ca^{2+} and PO_4^{3-} in the mineralized matrices and to determine the dissolution of the minerals from the mineralized matrices. The matrices were rinsed in DI water, homogenized and freeze-dried, and their dry weights were measured. To measure the Ca^{2+} and PO_4^{3-} contents of the mineralized matrices, the dried matrices were subjected to vigorous shaking in 0.5 M HCl at 25 ^{o}C for 3 days. To examine the dissolution of CaP minerals from the mineralized matrices into Ca^{2+} and PO_4^{3-} in an environment lacking these ions, equilibrium swollen matrices were incubated in 1.5 mL of 50 mM Tris buffer (pH = 7.4), at 37 ^{o}C for 7 days and 0.3 mL of incubation medium was collected and replenished with a fresh medium daily. The collected medium was used to measure the dissolution of CaP as a function of the incubation time.

Calcium assay was carried out according to manufacturer's protocol (Calcium reagent set, Pointe Scientific, catalog number: C7503). Briefly, 20 μl of the sample solution was mixed with 1 mL of assay solution containing o-cresolphthalein complexone

(CPC). The reaction of calcium with CPC gives rise to a purple color. The absorbance of the resultant product was measured at 570 nm by using a UV/Vis spectrophotometer (Beckman Coulter, DU 730). The absorbance values were compared with those of standard solution at 0, 5, 10, and 15 mg/dl of Ca^{2+} in order to determine Ca^{2+} content of the sample solution.

Phosphate assay was performed as reported elsewhere [144]. Briefly, the assay solution was prepared by mixing 1 part of 10 mM ammonium molybdate, 2 parts of acetone, and 1 part of 5 N H_2SO_4. 125 µl of the sample solution was mixed with 1 mL of assay solution. To this, 100 µl of 1 M citric acid was added. The absorbance of the resulting solution was measured at 380 nm by using a UV/Vis spectrophotometer. The PO_4^{3-} concentration in solution was determined using the standard curve for PO_4^{3-}, which was generated for a concentration range of 0-4 mM PO_4^{3-}.

3.3.7. Degradation

Non-mineralized and mineralized hydrogels (15% GelMA-co-9% A6ACA in dimensions of 8 mm diameter x 1 mm height) and macroporous hydrogels (10% GelMA-co-9% A6ACA-co-10% PEGDA in dimensions of 5 mm diameter x 2 mm height) were examined for their degradation potential prior to cell cultures. All matrices were dried at 37 ^{o}C for 24 hours and their dry weights (W_{d0}) were measured. The dried matrices were equilibrated in PBS and incubated in 1.5 mL of 0.02 w/v% collagenase type II (Worthington Biochemical, catalog number: LS004177) in PBS at 37 ^{o}C [170]. The matrices incubated in 1.5 mL of PBS under identical experimental conditions were used to examine hydrolytic degradation. The incubation solution was replenished with a fresh solution every other day. After 1, 3, 7, and 14 days of incubation, the matrices were collected and briefly rinsed with PBS for 5 minutes to remove any soluble components from degraded matrices. The matrices were dried at 37 °C for 24 hours and their weights (W_{dt}) were measured. Weight percentage of the remaining matrix was calculated using the following equation.

$$\text{Weight of remaining matrices (\%)} = \frac{W_{dt}}{W_{d0}} \times 100$$

where W_{d0} and W_{dt} represent the weight of the matrix before and after degradation, respectively.

3.3.8. Cell culture

The hiPSC line (IMR90p18-iPS) was procured from WiCell Research Institute, which was generated as described elsewhere [179]. The hiPSCs were maintained on feeder layers of mitotically inactivated mouse embryonic fibroblasts (MEFs) using a medium consisting of knockout DMEM (Life Technologies, catalog number: 10829-018), 10 v/v% knockout serum replacement (Life Technologies, catalog number: 10828028), 10 v/v% human plasmanate (Talecris Biotherapeutics), 1 v/v% non-essential amino acids, 1 v/v% penicillin/streptomycin, 1 v/v% Gluta-MAX, and 55 µM 2-mercaptoethanol as previously reported [143]. The medium was changed daily with 30 ng/mL of bFGF (Life Technologies) supplementation.

Cell culture grade glass coverslips (Fisherbrand, catalog number: 1254582) coated with gelatin (Sigma-Aldrich, catalog number: G9391) was used as a control to compare the cellular behaviors on gelatin-based matrices. The gelatin coating of glass coverslips was carried out by incubating the coverslips with 0.1 w/v% gelatin solution at 37 ^{o}C for 3 hours. Sterile GelMA-co-A6ACA hydrogels and GelMA-co-A6ACA-co-PEGDA macroporous hydrogels as well as gelatin-coated coverslips were incubated in growth medium composed of DMEM with 10 v/v% FBS (Premium Select; Atlanta Biologicals, catalog number: S11550) at 37 ^{o}C for 48 hours prior to cell culture.

For 2-D culture, hiPSCs were seeded onto non-mineralized and mineralized GelMA-co-A6ACA hydrogels and gelatin-coated coverslips at a seeding density of 10,000 cells/cm^2. Cells were cultured in 1.5 mL of growth medium (high glucose DMEM containing 5 v/v% FBS and 1 v/v% penicillin/streptomycin) at 37 °C and 5% CO_2. Medium was changed every other day.

For 3-D culture, non-mineralized and mineralized macroporous hydrogels were air-dried at 25 °C for 1 hour. 10 µl of cell suspension containing ~ 300,000 hiPSCs was dispensed into the macroporous hydrogels. The hiPSCs-seeded matrices were incubated at 37°C and 5% CO_2 for 2 hours for cell infiltration. The matrices infiltrated with the cells were cultured in 1.5 mL of growth medium with media change every other day.

3.3.9. Cell Tracker Staining

To visualize cell attachment in 2-D culture, cells were stained with CellTracker (Life Technologies, catalog number: C34552) at 3 days post-plating. Briefly, the cells attached to the matrix were incubated in 20 µM CellTracker reagent in DMEM at 37 °C for 30 minutes and then in growth medium at 37 °C for an additional 30 minutes. The stained cells were imaged using a fluorescence microscope (Carl Zeiss, Axio Observer.A1). The images were used to determine the circularity of the cells using the equation below [58]. 10 cells per image from three different images were used to calculate the area (A) and perimeter (p) of the cells to estimate the circularity (n=30).

$$\text{Circularity} = \frac{4\pi A}{p^2}$$

3.3.10. Reverse Transcription-Polymerase chain reaction (RT-PCR)

PCR analysis was conducted to evaluate time-dependent changes in gene expressions of hiPSCs in 2-D and 3-D cultures. Total RNA was extracted from samples (n= 3 per group per time point) using TRIzol according to manufacturer’s protocol. For each sample, 1 μg of RNA was used to synthesize cDNA using iScript cDNA synthesis kit (Bio-rad, catalog number: 170-8891) following manufacturer’s protocol. Quantitative RT-PCR measurements were performed using SYBR Select Master Mix (Life technologies, catalog number: 4472908). In addition to Osteogenic PCR array (SA Biosciences, catalog number: PAHS-026), gene expression profile for a number of osteogenic markers (RUNX2, OCN, and SPP1) and pluripotency marker (NANOG) as a function of culture time was carried out. The primer sequences are provided in supplementary Table 3.S1. For PCR array, 84 gene expressions relevant to osteogenic differentiation were profiled and presented as a heat map. The colors of the heat map were scaled according to the relative expression of hiPSCs grown on different matrices (mineralized GelMA-based matrices, non-mineralized GelMA-based matrices, and gelatin-coated coverslips). Red color was assigned to the group with the highest expression while green color was assigned to the group with the lowest expression. The color between red and green was assigned to the group with the intermediate expression level. For RUNX2, OCN, SPP1, and NANOG, the gene expression was normalized to GAPDH, a housekeeping gene. The expression level of each target gene was calculated as $2^{-\Delta\Delta Ct}$. The expression level of hiPSCs grown on various matrices in 2-D and 3-D cultures was normalized to that of undifferentiated, pluripotent hiPSCs and presented as fold expression.

3.3.11. Immunofluorescent staining

The cells cultured on various matrices were fixed with 4% formaldehyde at 25 °C for 7 minutes, washed in PBS, and blocked/permeabilized in a blocking solution of PBS containing 3% BSA and 0.1% Triton-X at 25 °C for 30 minutes. The cells were then incubated with a blocking solution containing primary antibodies against OCT4 (1:200; rabbit polyclonal, Santa Cruz Biotechnology, catalog number: sc-9081), NANOG (1:200; rabbit polyclonal, Santa Cruz Biotechnology, catalog number: sc-33759), or OCN (1:100; mouse monoclonal, Santa Cruz Biotechnology, catalog number: sc-74495) at 4 °C for 16 hours. The cells were washed in PBS and incubated in a blocking solution containing secondary antibody raised against rabbit (1:250; Life Technologies, Alexa Flour 647) or mouse (1:250; Life Technologies, Alexa Flour 568) and phalloidin (1:100; Life Technologies, Alexa Flour 488) at 25 °C for 60 minutes. To counterstain the nuclei, cells were incubated in the Hoechst 33342 solution (2 µg/ml; Life Technologies) at 25 °C for 7 minutes. The images were acquired in a linear mode using the same exposure time for all samples. Using ImageJ software, the background of images was identically subtracted from all images by applying a rolling ball algorithm with rolling ball radius of 750 pixels.

To examine autofluorescence of minerals, acellular mineralized matrices were stained at the same time and the images were exposed to the same processing as those with the cells. To evaluate the specificity of osteocalcin antibody, hiPSCs cultured on mineralized matrices for 28 days were stained with secondary antibody without the use of primary antibody and the background of images was subtracted by using the identical method.

3.3.12. Live-dead assay

Live-dead assay was carried out to evaluate the viability and distribution of cells within the macroporous hydrogels after 3 days of cell seeding using Live/Dead Viability/Cytotoxicity kit, (Life technologies, catalog number: L-3224). Briefly, hiPSCs-seeded matrices were washed in PBS and cut into thin slabs. These thin slices were stained using a solution composed of DMEM with 0.05 v/v% green-fluorescent calcein-AM and 0.2 v/v% red-fluorescent ethidium homodimer-1 at 37 °C for 30 minutes. The stained sections were washed with PBS and imaged.

3.3.13. DNA assay

The hiPSCs-seeded macroporous hydrogels were subjected to the DNA assay at 3, 7, and 28 days of culture. The cell-laden matrices were lyophilized and their dry weights were measured. Each lyophilized sample was homogenized in 1 mL of papain solution and incubated at 60 °C for 16 hours. The papain solution was prepared by dissolving 125 µg/mL of papain in a buffer containing 10 mM L-cysteine, 100 mM phosphate, and 10 mM EDTA at pH 6.3. To measure DNA contents of the digested sample, Quant-iT PicoGreen dsDNA assay kit (Life technologies, catalog number: P11496) was used. One part each of digested samples and PicoGreen dsDNA reagent were mixed. Fluorescence of the resulting solution was measured using a microplate reader (Beckman Coulter, DTX 880). Fluorescence values of the samples were compared with those of Lambda DNA standard to quantify the DNA contents of the experimental samples. DNA content of each sample was normalized to the corresponding dry weight.

3.3.14. Immunohistochemical staining

The hiPSCs-laden matrices were fixed with 4% paraformaldehyde at 4 °C for 1 day, demineralized in 10% ethylenediaminetetraacetic acid (EDTA; pH = 7.3) at 4 °C for 3 hours, and equilibrated in PBS for 6 hours. Gradual dehydration of the samples was achieved by immersing them in water/ethanol mixtures and then in pure ethanol for 6 hours. The dehydrated samples were soaked in Citrisolv solution for 1 hour, incubated in a mixture of 95 w/w% paraffin and 5 w/w% poly(ethylene-co-vinyl acetate) (PEVA; Sigma Aldrich, catalog number: 437220) liquid at 70 °C under vacuum for 1 day. The specimens were embedded with paraffin-PEVA mixture through solidification at 25 °C for 1 day. The samples were subsequently sectioned into 10 µm-sized slices using a microtome (Leica, RM2255). The sections were placed into DI water at 40 °C for 5 minutes, then onto charged glass slides, and allowed to dry at 37 °C for 16 hours. The sections on the glass slides were immersed in Citrisolv at 60 °C for 15 minutes with two changes of Citrisolv to remove paraffin-PEVA mixture. The Citrisolv solution was then replaced with pure ethanol. The samples were progressively hydrated by using ethanol/DI water mixtures and followed by DI water.

The sections were incubated in a blocking solution composed of PBS with 3 w/v% BSA and 0.1 v/v% Triton X-100 at 25 °C for 60 minutes and incubated with primary antibody (diluted in blocking solution) against OCN (1:100, mouse monoclonal, Abcam, catalog number: ab13420) at 4 °C for 16 hours. The sections were washed in PBS containing 0.05 v/v% Tween 20 (PBS-Tween 20) three times and treated with 3 v/v% hydrogen peroxide for 7 minutes to deactivate endogenous peroxidases. The sections were then incubated in a blocking buffer containing horseradish peroxidase (HRP)-conjugated secondary antibody against mouse (1:100, Santa Cruz Biotechnology, catalog number: sc-2005) at 25 °C for 60 minutes. The sections were washed in PBS-Tween20 three times and exposed to a developing solution containing 3-3' diaminobenzidine (DAB) substrate (Vector Laboratories, catalog number: SK-4100) for 7 minutes, washed in PBS-Tween 20 three times, and subsequently imaged using a microscope in color mode.

3.3.15. Statistical analysis

Statistical analyses were performed using GraphPad Prism (version 5.00) software. Statistical significances were assigned for p-values less than 0.05. The asterisks were assigned to further demonstrate different degrees of statistical significances. Three different statistical methods were used to compare groups in various combinations. Two-tailed Student's t-test was employed to compare two groups at the same time point. One-way analysis of variance (ANOVA) with Tukey-Kramer post-hoc test was used to compare multiple groups at the same time point. Two-way ANOVA with Bonferroni post-hoc test was utilized to compare multiple groups at various time points.

3.4. Results

3.4.1. Synthesis, characterization, and degradation of mineralized matrices.

Hydrogels and macroporous hydrogels were used for 2-D and 3-D cultures, respectively. The hydrogel and macroporous matrices were mineralized to incorporate calcium phosphate moieties. Both mineralized hydrogels and macroporous hydrogels were found to be opaque in contrast to the transparent non-mineralized counterparts (Figures 3.S1a, 3.S2a). Scanning electron microscopy (SEM) images of the mineralized hydrogels and macroporous hydrogels showed matrix-bound minerals having a plate-like morphology; no such features were present in the corresponding non-mineralized controls (Figures 3.1a,e). Elemental dispersive spectra (EDS) revealed the presence of calcium and phosphorus elements in mineralized matrices with a Ca/P ratio of 0.99 and 1.42 for the mineralized hydrogels and macroporous hydrogels, respectively. As expected, no calcium or phosphorous elements were detected in their non-mineralized counterparts. As evident from Ca^{2+} and PO_4^{3-} measurements, the mineralized hydrogels contained 32.2 ± 1.5 and 50.3 ± 4.8 mg of Ca^{2+} and PO_4^{3-} per gram of dry weight, respectively (Figures 3.S1b-c). Similarly, the mineralized macroporous hydrogels had 68.4 ± 4.2 and 112.3 ± 4.7 mg of Ca^{2+} and PO_4^{3-} per gram of dry weight, respectively (Figures 3.S2c-d). Concurrent with previous findings, the CaP moieties of the mineralized matrices (mineralized hydrogels and macroporous hydrogels) dissociated into Ca^{2+} and PO_4^{3-} ions in a medium lacking these components (Figures 3.1b-c,f-g) [165]. Both mineralized hydrogels and macroporous hydrogels exhibited a rapid release of Ca^{2+} and PO_4^{3-} ions within 1 day followed by a slow release of Ca^{2+} and no significant release of PO_4^{3-} for 7 days.

Both non-mineralized and mineralized macroporous hydrogels exhibited interconnected pores as evident from the SEM images (Figure 3.1e). Furthermore, the pore diameter of the macroporous hydrogels in their dried state, estimated from the SEM images, was 50.2 ± 3.0 µm. The pore diameter of the non-mineralized and mineralized macroporous hydrogels in their swollen state, estimated from the bright field images, was 117.7 ± 5.7 and 115.2 ± 6.4 µm, respectively (Figure 3.S2b).

The ability to degrade in presence of collagenase is a characteristic of gelatin-based scaffolds. To evaluate the effect of mineralization on degradation of GelMA-based matrices, the mineralized and non-mineralized hydrogels and macroporous hydrogels were incubated in PBS or PBS containing collagenase type II. Enzymatic degradation of non-mineralized and mineralized GelMA-based hydrogels with collagenase type II resulted in ~ 29% and 25% of mass loss by 14 days, respectively, while their incubation in PBS exhibited less than 10% of mass loss during the same time period (Figure 3.1d). A similar degradation pattern was observed for macroporous hydrogels (Figure 3.1h). Enzyme-mediated degradation of non-mineralized and mineralized GelMA-based macroporous hydrogels yielded ~ 30% and 25% of mass loss after 14 days of incubation in collagenase type II, respectively. The hydrolytic degradation of such macroporous matrices was found to be negligible during 14 days of incubation in PBS.

3.4.2. Osteogenesis of hiPSCs on mineralized matrices in 2-D culture.

The pluripotency of hiPSCs prior to their culture on various matrices was confirmed by immunofluorescent staining for OCT4 and NANOG, well-established pluripotent markers (Figure 3.S3) [143]. The pluripotent hiPSCs were seeded onto mineralized and non-mineralized GelMA-co-A6ACA hydrogel matrices as well as gelatin-coated coverslips. The adhesion and growth of hiPSCs on mineralized GelMA-co-A6ACA hydrogels were examined and compared against those on non-mineralized hydrogels and gelatin-coated coverslips as a function of culture time (Figures 3.2a-b). All matrices supported the attachment of hiPSCs within 3 days of culture with no significant differences in cell adhesion (Figure 3.2a). The cell shape measured in terms of circularity suggests that cells on all matrices spread and acquired similar shape within 3 days of plating (Figure 3.2b). By 10 days of culture, hiPSCs on all the matrices grew to reach confluence (Figure 3.2a). Having verified that all matrices under investigation support the attachment and proliferation of hiPSCs in similar extents, we next evaluated the osteogenic differentiation of hiPSCs on various matrices. After 28 days of culture, PCR array revealed that the cells on mineralized matrices exhibited an upregulation of various genes relevant to cells undergoing osteogenesis compared to those on non-mineralized matrices and gelatin-coated coverslips (Figure 3.3a). The gene profile was further verified through time course analyses of different osteogenic gene markers and it was found that the cells on mineralized matrices showed higher expression of RUNX2, OCN, and SPP1 compared to those on non-mineralized and coverslip groups throughout 28 days of culture (Figures 3.3b-d). Immunofluorescent staining for OCN in hiPSCs on mineralized hydrogels revealed positive staining after 28 days of culture, which was not detected on non-mineralized hydrogels or coverslips (Figures 3.3e, 3.S4). Moreover, OCN staining intensity was found to gradually increase for hiPSCs on mineralized hydrogels with culture time (Figure 3.S5a). The corresponding Hoechst and F-actin staining of the cells on various matrices as a function of culture time are also shown

(Figures 3.S5a-b). The hiPSCs cultured on all matrices exhibited the downregulation of NANOG expression compared to pluripotent hiPSCs prior to their culture on various matrices (Figure 3.S5c).

3.4.3. Osteogenesis of hiPSCs on mineralized matrices in 3-D culture.

We next determined the potential of 3-D mineralized matrices in directing osteogenic commitment of hiPSCs by using mineralized GelMA-co-A6ACA-co-PEGDA macroporous hydrogels. The PEGDA molecules were incorporated to optimize pore interconnectivity and robustness of the macroporous matrices. The mineralized matrix-induced osteogenic differentiation was compared against that of corresponding non-mineralized macroporous hydrogels. Live-dead staining of hiPSC-laden matrices after 3 days of cell seeding demonstrated homogeneous distribution for a majority of live cells within the non-mineralized and mineralized matrices (Figure 3.4a). While both matrices supported cell survival, there were distinct differences in cell shape and cell-matrix interactions. Most cells within the non-mineralized matrices were aggregated to form small clusters while those within the mineralized matrices were found to spread on the pore walls of the matrices. Despite the differences in cell shape and adhesion between two matrices, DNA assay showed similar DNA contents of hiPSCs cultured in both non-mineralized and mineralized matrices at all experimental time points, suggesting that similar cell numbers were maintained between the mineralized and non-mineralized matrices (Figure 3.4b). Time-resolved gene expression of osteogenic markers for RUNX2, OCN, and SPP1 revealed significant upregulation of these markers in cells on mineralized matrices compared to those on non-mineralized matrices, akin to 2-D culture

(Figures 3.4c-e). Immunohistochemical staining for OCN further corroborated the gene expression pattern as prevalent staining for OCN was observed in mineralized matrices, which remained absent in non-mineralized counterparts (Figure 3.4g). Furthermore, pervasiveness of OCN stains in mineralized matrices progressively increased with culture time. Although only the hiPSCs on mineralized macroporous matrices were found to differentiate into osteoblasts, cells cultured in all macroporous matrices showed a significant downregulation of NANOG expression, similar to 2-D culture (Figure 3.4f).

3.5. Discussion

The potential of biomaterials in directing stem cell differentiation continues to be revealed, leading to new possibilities in regenerative medicine. Human pluripotent stem cells, such as hiPSCs that offer a unique cell source, in conjunction with biomaterials, could be powerful in treating compromised tissues and organs. Studies over the years have designed biomaterials with defined physicochemical cues to direct differentiation of stem cells into targeted phenotypes. Previously, we have shown that biomaterials containing CaP moieties promote osteogenic commitment of stem cells both *in vitro* and *in vivo* [58, 163, 165]. Here, by employing a mineralized GelMA-based matrix, we ask whether matrix-based cues alone can direct differentiation of pluripotent hiPSCs into osteoblasts.

Human iPSCs grown on GelMA-based matrices in 2-D culture demonstrated similar levels of attachment, spreading, and proliferation in growth medium. Though all the matrices supported the adhesion and growth of hiPSCs to similar extents, only the cells on mineralized matrices were found to undergo osteogenic differentiation. hiPSCs on mineralized matrices after 28 days of culture in a 2-D setting demonstrated intense staining for OCN, an osteoblast marker, coincident with F-actin staining in a majority of the cells. This finding suggests efficient osteogenic differentiation of hiPSCs in a mineralized environment. Previous studies demonstrated that biomaterial-assisted osteogenic differentiation of stem cells in 2-D culture was accompanied by changes in cell shape [180]. However, our findings that cells only on the mineralized matrices underwent osteogenic differentiation despite cells on all matrices having similar shape suggest that the observed osteogenic differentiation of hiPSCs on mineralized matrices is not attributed to the cell shape. This finding further implies that the osteogenic differentiation of hiPSCs observed on mineralized matrices is mainly attributed to the mineral environment-mediated differentiation cues. Similar results were also observed with 3-D culture, albeit within disparate spatial geometry in the culture. The findings that hiPSCs undergo osteogenic differentiation on CaP-rich GelMA-based matrices in 2-D and 3-D culture conditions are consistent with our previous findings that CaP-rich PEGDA-based matrices promote osteogenic differentiation of hMSCs and hESCs [58, 163, 165]. Together, these studies suggest that mineralized matrices containing CaP moieties offer a robust environment to support osteogenic commitment of stem cells despite the differences in the organic moieties of the scaffold.

In contrast to 2-D culture, cells in 3-D macroporous hydrogels showed significant differences in their attachment; cells on mineralized matrices exhibited more spread morphology whereas those on non-mineralized matrices showed aggregation. These results suggest enhanced cell-matrix interactions on mineralized macroporous matrices compared to their non-mineralized counterparts. The reason behind the observed difference between 2-D and 3-D cultures is not apparent. The hiPSCs cultured in all matrices showed significant downregulation of NANOG expression, indicating that all the matrices and culture conditions used in this study are not conducive for the maintenance of pluripotency. This is in agreement with previous studies that showed the importance of a delicate balance in physicochemical cues of the matrix on the maintenance of pluripotency for hiPSCs [143].

Although a number of studies have shown that materials containing CaP moieties promote osteogenic differentiation of progenitor cells and contribute to *in vivo* bone tissue repair, recent studies suggest that the osteoinductive function of such matrices is dependent upon their ability to regulate extracellular Ca^{2+} and PO_4^{3-} [20, 55]. This could partially explain the different extents of osteogenic outcomes observed among CaP-based matrices with different levels of crystallinity and composition, owing to disparate dissociation kinetics of CaP minerals into Ca^{2+} and PO_4^{3-}. Osathanon et al. previously reported that CaP-rich biomineralized matrices exhibiting faster dissolution rates have higher osteostimulatory effect on osteoblast-like cells when compared with hydroxyapatite-incorporated matrices [45]. Results from our dissolution studies suggest that the CaP minerals of the mineralized matrices readily dissociate into Ca^{2+} and PO_4^{3-} ions in a permissive environment. The extracellular Ca^{2+} and PO_4^{3-} ions have been shown to promote osteogenic commitment of stem cells through various signaling pathways. Studies by Wen et al. have shown that extracellular Ca^{2+} promotes osteogenic differentiation of MSCs through L-type calcium channels [105]. Recently, we have shown that mineralized matrices containing CaP moieties could direct osteogenic differentiation of stem cells through adenosine signaling [39]. In addition, the dissolution and re-precipitation of CaP minerals can adsorb and release osteoinductive growth factors [47, 107, 150]. All of these factors could be contributing to the observed CaP-bearing matrices-induced osteogenic commitment of hiPSCs.

3.6. Conclusion

In summary, the results described in this study show that mineralized GelMA-based matrices containing CaP mineral direct osteogenic differentiation commitment of hiPSCs in growth medium lacking osteoinductive soluble factors. To our knowledge, this is the first demonstration of osteogenic differentiation of hiPSCs by inherent material-based cues. Future work includes the transplantation of hiPSCs with GelMA-based matrices *in vivo* to study the effect of minerals and degradation on the osteogenic differentiation of hiPSCs and bone tissue formation.

3.7. Acknowledgements

Authors gratefully acknowledge the financial support from National Institutes of Health and California Institute of Regenerative Medicine (NIH, Grant 1 R01 AR063184-01A1; CIRM, RN2-00945 and RT2-01889).

Chapter 3, in full, is a reprint of the material as it appears in Acta Biomaterialia, vol. 10, 2014. “Mineralized gelatin methacrylate-based matrices induce osteogenic differentiation of human induced pluripotent stem cells”. Kang, Heemin; Shih, Yu-Ru V.;

Hwang, Yongsung; Wen, Cai; Rao, Vikram; Seo, Timothy; Varghese, Shyni. The dissertation author was the primary investigator and author of this paper.

3.8. Figures

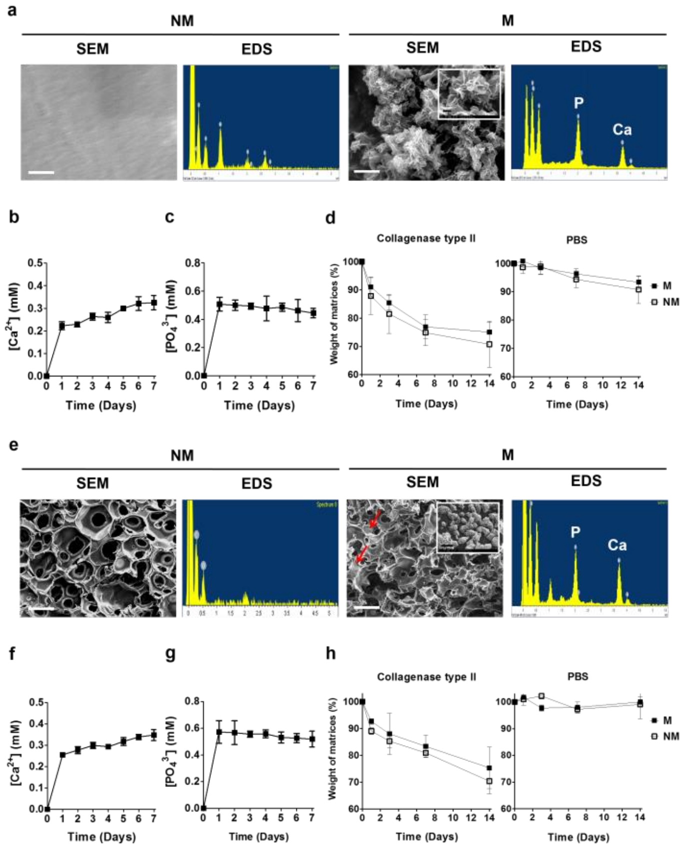

Figure 3.1. Development and characterization of GelMA-based matrices.

(a) SEM images and corresponding EDS for non-mineralized (NM) and mineralized (M) gelatin-methacrylate-co-acryloyl 6-aminocaprioic acid (GelMA-co-A6ACA) hydrogels. Scale bar: 1 µm. Inset shows high magnification image. Scale bar: 200 nm. Dissolution of (b) Ca^{2+} and (c) PO_4^{3-} from mineralized GelMA-co-A6ACA hydrogels incubated in Tris-HCl buffer at 37 °C as a function of time. (d) In vitro degradation of non-mineralized and mineralized GelMA-co-A6ACA hydrogels in 0.02 w/v% collagenase type II solution or PBS at 37 ^{o}C as a function of time. (e) SEM images and corresponding EDS for non-mineralized and mineralized gelatin-methacrylate-co-acryloyl 6-aminocaproic acid-co-poly(ethylene glycol)-diacrylate (GelMA-co-A6ACA-co-PEGDA) macroporous hydrogels. Red arrows indicate mineral structures. Scale bar: 100 µm. Inset shows high magnification image. Scale bar: 1 µm. Release of (f) Ca^{2+} and (g) PO_4^{3-} from mineralized GelMA-co-A6ACA-co-PEGDA macroporous hydrogels in Tris-HCl buffer at 37 °C as a function of time. (h) In vitro degradation of non-mineralized and mineralized GelMA-co-A6ACA-co-PEGDA macroporous hydrogels in 0.02 w/v% collagenase type II solution or PBS at 37 ^{o}C as a function of time. Data are presented as mean ± standard errors (n=3).

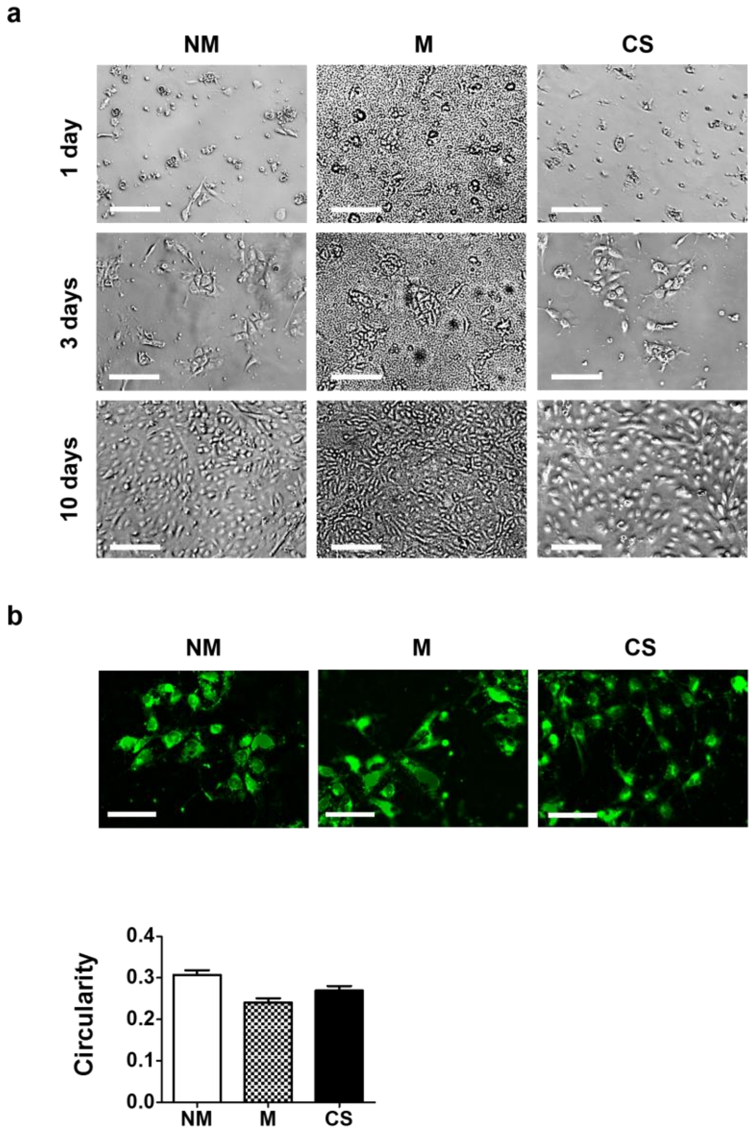

Figure 3.2. Attachment and proliferation of hiPSCs on different matrices.

(a) Bright field images for hiPSCs after 1, 3, and 10 days of culture on non-mineralized (NM) and mineralized (M) hydrogels and gelatin-coated coverslips (CS). Scale bar: 200 µm. (b) Images of hiPSCs labeled using CellTracker after 3 days of culture on non-mineralized and mineralized hydrogels and coverslips. Scale bar: 100 µm. The bar graph shows the quantitative representation of the circularity; the circularity indices were determined from the stained images. Data are shown as mean ± standard errors (n=30).

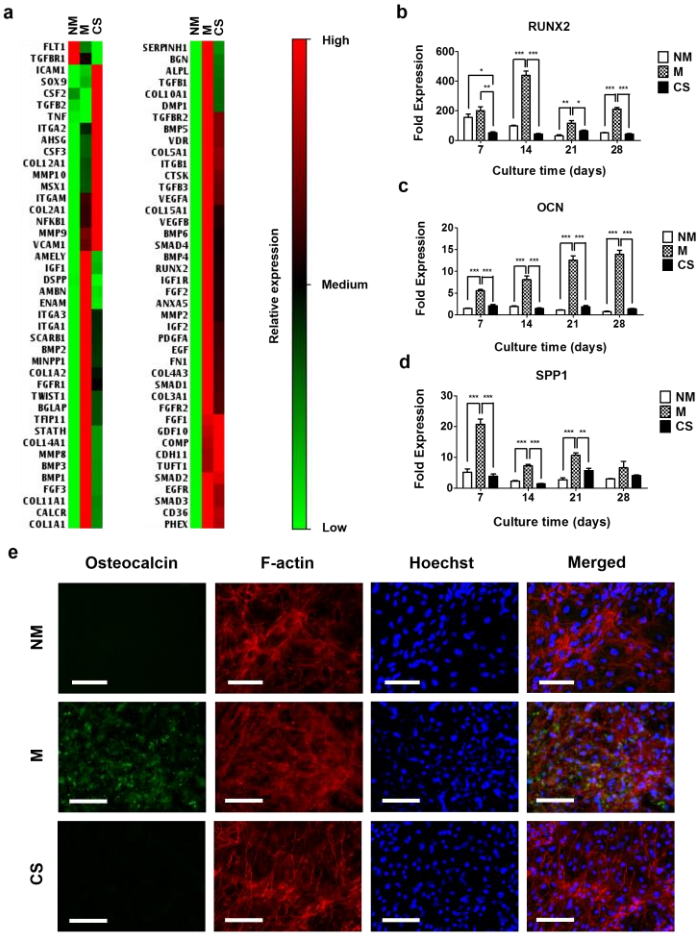

Figure 3.3. Osteogenic differentiation of hiPSCs on CaP-rich mineralized hydrogels in 2-D culture.

(a) Gene expression array analyses of hiPSCs cultured for 28 days on non-mineralized (NM) and mineralized (M) hydrogels and coverslips (CS). Relative expressions: red (high), black (medium), and green (low). Gene expressions of (b) RUNX2, (c) OCN, and (d) SPP1 for hiPSCs cultured on non-mineralized and mineralized hydrogels and coverslips as a function of culture time. Data are presented as fold expression of target genes after normalization to undifferentiated, pluripotent hiPSCs. (e) Immunofluorescent staining for OCN (green) and F-actin (red) of hiPSCs cultured on non-mineralized and mineralized hydrogels and coverslips for 28 days. Nuclei are stained blue with Hoechst. Scale bars represent 100 µm. Data are displayed as mean ± standard errors (n=3). (b-d) Comparison of multiple groups at the same time point was made by one-way ANOVA with Tukey-Kramer post-hoc test. Asterisks indicate statistical significances corresponding to p-values (*: $p < 0.05$; **: $p < 0.01$; ***: $p < 0.001$).

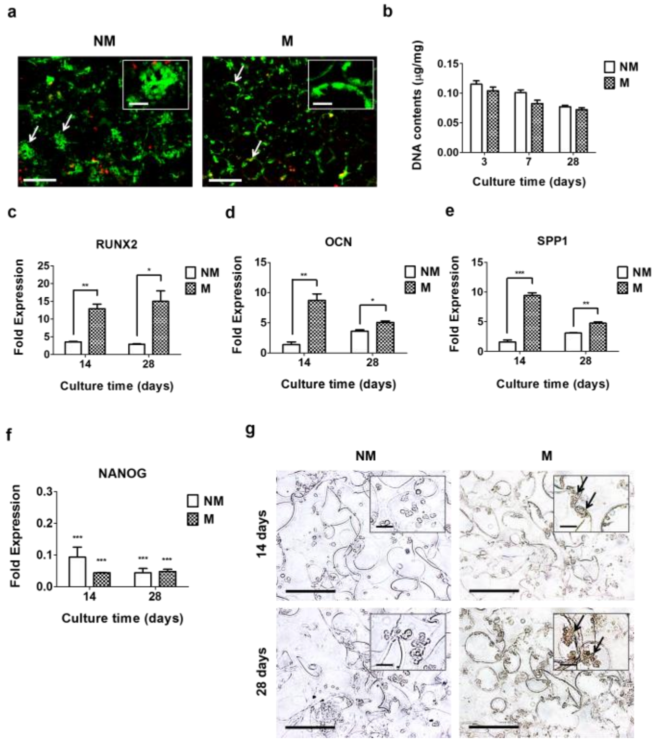

Figure 3.4. Osteogenic differentiation of hiPSCs on CaP-rich mineralized macroporous hydrogels in 3-D culture.

(a) Live-dead staining of hiPSC-laden non-mineralized (NM) and mineralized (M) macroporous hydrogels after 3 days of culture. Arrows and inset indicate aggregated and spread hiPSCs within the non-mineralized and mineralized matrices, respectively. Scale bars represent 200 µm and scale bars in the inset indicate 50 µm. (b) DNA contents of hiPSCs cultured using non-mineralized and mineralized matrices as a function of culture time. Data are presented as DNA contents after normalization to dry weight of matrices. Gene expression of (c) RUNX2, (d) OCN, (e) SPP1, and (f) NANOG of hiPSCs on non-mineralized and mineralized matrices as a function of culture time. Data are presented as fold expression of target genes after normalization to undifferentiated, pluripotent hiPSCs. (g) Immunohistochemical staining for OCN of hiPSCs on non-mineralized and mineralized matrices as a function of culture time. Scale bars represent 100 µm. Inset shows high magnification images. Arrows indicate positive stains. Scale bars in the inset represent 20 µm. Data are displayed as mean ± standard errors (n=3). (c-e) Two groups at the same time point were compared by two-tailed Student's t-test. (f) All the groups were compared to undifferentiated, pluripotent hiPSCs prior to their culture on all matrices by two-way ANOVA with Bonferroni post-hoc test. Asterisks represent statistical significances according to p-values. (*: $p < 0.05$; **: $p < 0.01$; ***: $p < 0.001$).

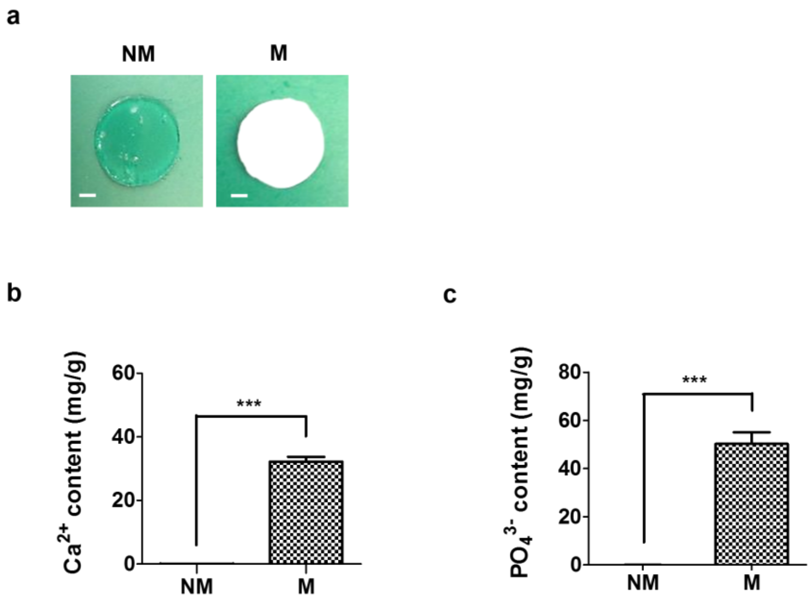

Figure 3.S1. Characterization of mineralized hydrogels.

(a) Gross images of non-mineralized (NM) and mineralized (M) gelatin-methacrylate-co-acryloyl 6-aminocaprioic acid (GelMA-co-A6ACA) hydrogels. Scale bars represent 2 mm. (b) Ca^{2+} and (c) PO_4^{3-} contents of non-mineralized and mineralized hydrogels. Data are presented as mean ± standard errors (n=3) of Ca^{2+} and (c) PO_4^{3-} contents after normalization to dry weight of matrices. (b-c) Two groups were compared by two-tailed Student’s t-test. Asterisks indicate statistical significances corresponding to p-values (***: $p < 0.001$).

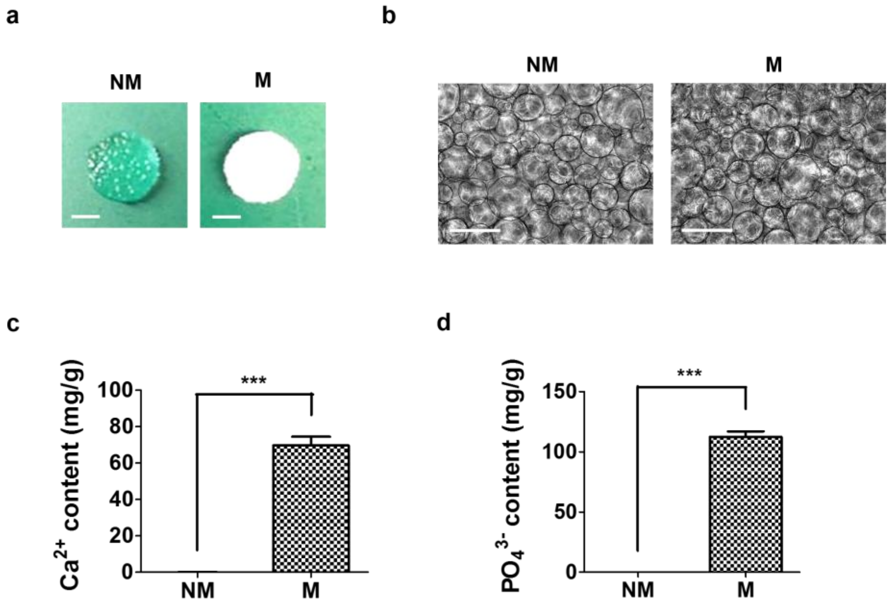

Figure 3.S2. Characterization of mineralized macroporous hydrogels.

(a) Gross images of non-mineralized (NM) and mineralized (M) gelatin-methacrylate-co-acryloyl 6-aminocaproic acid-co-poly(ethylene glycol)-diacrylate (GelMA-co-A6ACA-co-PEGDA) macroporous hydrogels. Scale bars indicate 2 mm. (b) Bright field images of non-mineralized and mineralized matrices in their swollen conditions. Scale bars represent 200 μm. (c) Ca^{2+} and (d) PO_4^{3-} amounts of non-mineralized and mineralized matrices. Data are presented as mean ± standard errors (n=3) of Ca^{2+} and (d) PO_4^{3-} amounts after normalization to dry weight of matrices. (c-d) Two-tailed Student's t-test was used to compare two groups. Asterisks represent statistical significances according to each p-value. (***: $p < 0.001$).

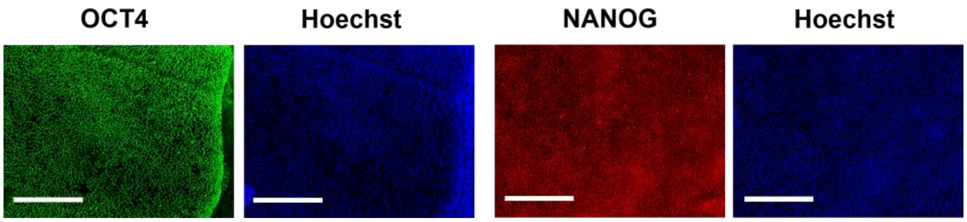

Figure 3.S3. Pluripotency of hiPSCs prior to their culture on various substrates.

Immunofluorescent staining for OCT4 (green) and NANOG (red) of hiPSCs with their corresponding nucleus (blue; Hoechst). Scale bars represent 500 µm.

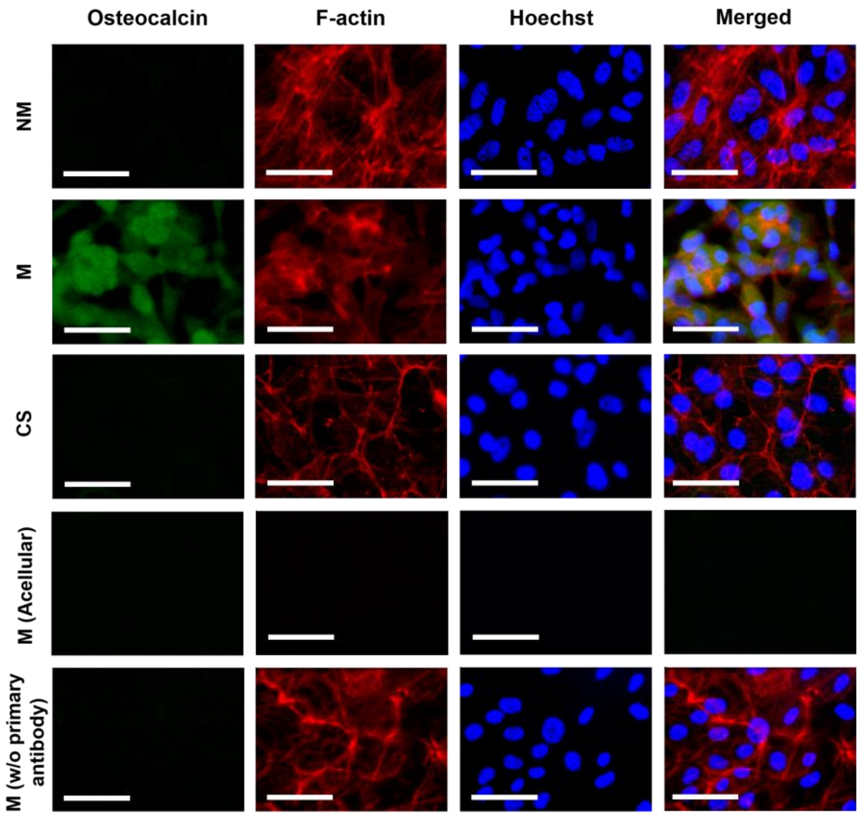

Figure 3.S4. High magnification images of immunofluorescent staining for OCN (green), F-actin (red), and nuclei (blue; Hoechst).

hiPSCs were cultured for 28 days on non-mineralized (NM) and mineralized (M) hydrogels and coverslips (CS). Acellular mineralized hydrogels (M-Acellular) show minimal to no staining for osteocalcin, F-actin, and Hoechst. Similarly, cell-seeded mineralized hydrogels show minimal to no staining for osteocalcin in the absence of primary antibody (w/o primary antibody). Scale bars indicate 50 μm.

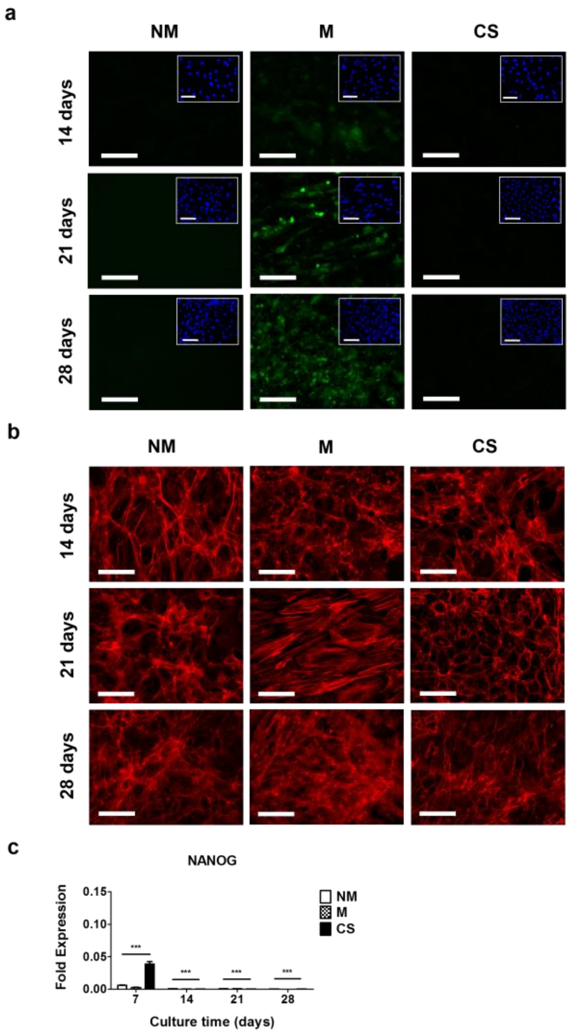

Figure 3.S5. Immunofluorescent staining for (a) OCN (green) and corresponding nucleus (blue; inset) and (b) F-actin as well as (c) NANOG gene expression as a function of culture time.

hiPSCs were cultured on non-mineralized (NM) and mineralized (M) hydrogels and gelatin-coated coverslips (CS). Scale bars indicate 100 µm. Data are presented as fold expression of target genes after normalization to undifferentiated, pluripotent hiPSCs. Data are displayed as mean ± standard errors (n=3). All the groups were compared to undifferentiated, pluripotent hiPSCs prior to their culture on all matrices by two-way ANOVA with Bonferroni post-hoc test. Asterisks indicate statistical significances corresponding to p-values (***: $p < 0.001$).

3.9. Tables

Table 3.S1. List of primers used in PCR experiments to quantify gene expression of hiPSCs.

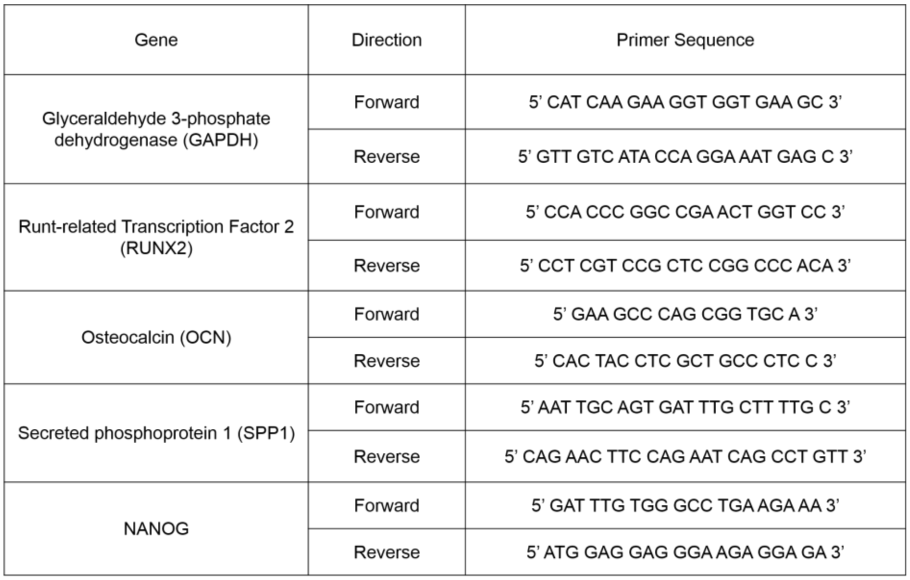

Gene	Direction	Primer Sequence
Glyceraldehyde 3-phosphate dehydrogenase (GAPDH)	Forward	5’ CAT CAA GAA GGT GGT GAA GC 3’
	Reverse	5’ GTT GTC ATA CCA GGA AAT GAG C 3’
Runt-related Transcription Factor 2 (RUNX2)	Forward	5’ CCA CCC GGC CGA ACT GGT CC 3’
	Reverse	5’ CCT CGT CCG CTC CGG CCC ACA 3’
Osteocalcin (OCN)	Forward	5’ GAA GCC CAG CGG TGC A 3’
	Reverse	5’ CAC TAC CTC GCT GCC CTC C 3’
Secreted phosphoprotein 1 (SPP1)	Forward	5’ AAT TGC AGT GAT TTG CTT TTG C 3’
	Reverse	5’ CAG AAC TTC CAG AAT CAG CCT GTT 3’
NANOG	Forward	5’ GAT TTG TGG GCC TGA AGA AA 3’
	Reverse	5’ ATG GAG GAG GGA AGA GGA GA 3’

Chapter 4: Biomineralized matrices dominate soluble cues to direct osteogenic differentiation of human mesenchymal stem cells through adenosine signaling

4.1. Abstract

Stem cell differentiation is determined by a repertoire of signals from its microenvironment, which includes the extracellular matrix (*ECM*) and soluble cues. The ability of mesenchymal stem cells (MSCs), a common precursor for the skeletal system, to differentiate into osteoblasts and adipocytes in response to their local cues plays an important role in skeletal tissue regeneration and homeostasis. In this study, we investigated whether a bone-specific calcium phosphate (CaP) mineral environment could induce osteogenic differentiation of human MSCs, while inhibiting their adipogenic differentiation, in the presence of adipogenic-inducing medium. We also examined the mechanism through which the mineralized matrix suppresses adipogenesis of hMSCs to promote their osteogenic differentiation. Our results show that hMSCs cultured on mineralized matrices underwent osteogenic differentiation despite being cultured in presence of adipogenic medium, which indicates the dominance of matrix-based cues of the mineralized matrix in directing osteogenic commitment of stem cells. Furthermore, the mineralized matrix-driven attenuation of adipogenesis was reversed with the inhibition of A2b adenosine receptor (A2bR), implicating a role of adenosine signaling in mineralized environment-mediated inhibition of adipogenesis. Such synthetic matrices with an intrinsic ability to direct differentiation of multipotent adult stem cells

towards a targeted phenotype while inhibiting their differentiation into other lineages will not only be a powerful tool in delineating the role of complex microenvironmental cues on stem cell commitment, but also contribute to functional tissue engineering and their translational applications.

4.2. Introduction

Adult stem cells such as mesenchymal stem cells (MSCs) have been shown to differentiate into osteoblasts, adipocytes, and chondrocytes by responding to soluble cues.[54, 181, 182] MSCs have been considered precursors for osteoblasts and adipocytes and their ability to differentiate into desirable somatic cell types by responding to tissue-specific requirements is a key in maintaining musculoskeletal tissue homeostasis and repair. Maintaining a strict balance between osteogenesis and adipogenesis has been considered to be a prerequisite for sustaining healthy skeletal tissue function. A large number of *in vitro* studies point towards the existence of an inverse correlation between adipogenesis and osteogenesis.[183-185] While most of these studies were performed *in vitro*, it is conceivable that such a correlation could also exist *in vivo*. A disruption in the balance of adipogenesis and osteogenesis is often observed in various pathologies that affect the musculoskeletal system.[186] For instance, studies have shown a close relationship between fat and bone mass, where the high fat mass increases the risk of bone fragility.[187, 188] Similarly, excessive accumulation of bone marrow adipocytes along with a decline in bone mineral mass is a characteristic of osteoporosis, obesity, diabetes, anorexia nervosa, and skeletal unloading.[186, 189] Preserving such a highly coordinated differentiation of multipotent precursors relies on delicate and intricate interactions between cells and the surrounding microenvironment or niche.

Previous studies have identified various biochemical- and hormone-based signaling underlying various musculoskeletal pathologies.[190-193] Some of these biochemical and hormonal factors have been shown to play a direct role in determining differentiation commitment of MSCs towards osteogenic or adipogenic lineages.[194, 195] Besides growth factor- or hormone-based signaling, physical and chemical cues of the extracellular matrix also play an equally important role in tissue homeostasis and regeneration through modulating stem cell commitment.[160] This includes MSCs as their differentiation into numerous specialized phenotypes can be significantly influenced by various matrix-based cues.[196-200] Given the propensity of MSCs to differentiate into osteoblasts and adipocytes, a number of studies have investigated the role of various matrix cues and geometrical constraints in stimulating differentiation of MSCs using mixed media containing osteogenic- and adipogenic-inducing components.[180, 201, 202] However, to our knowledge, there are no precedent studies that have investigated the impact of matrix-based cues on directing stem cell fate in the presence of medium conditions providing an opposing effect.

In this study, we address this question by investigating the effect of calcium phosphate (CaP)-rich mineralized environment on differentiation commitment of hMSCs in presence of adipogenic-inducing medium. We chose mineralized environment because CaP minerals are a major constituent of bone ECM and play a key role in bone homeostasis and function.[203, 204] Additionally, a large number of studies show the prevalent effect of CaP minerals on osteogenic differentiation of stem and progenitor cells.[39, 59, 70, 71, 132] A detailed understanding of the effect of mineral environment on differentiation commitment of hMSCs in presence of adipogenic-inducing medium might provide novel insights into the role of mineral environment on maintaining bone and marrow homeostasis and function.

4.3. Materials and Methods

4.3.1. Synthesis of hydrogels

Poly(ethylene glycol)-diacrylate (PEGDA; M_n = 6 kDa) and N-acryloyl 6-aminocaproic acid (A6ACA) were prepared as described elsewhere.[70] In brief, 1 M A6ACA was dissolved in 1 M NaOH and 2% (w/v) PEGDA was added to this solution. The precursor solution was mixed with 0.5% (w/v) ammonium persulfate (APS) and 0.15% (v/v) N, N, N’, N’-tetramethylethylenediamine (TEMED) at 25 °C for 15 min. to allow free radical copolymerization and yielded crosslinked hydrogels. The resultant ~ 1 mm-thick hydrogel sheets were allowed to reach equilibrium-swelling in phosphate buffered saline (PBS; pH = 7.4) for 48 h with two changes of PBS and then punched into discs of 1 cm^2 (area) x 1 mm (thickness) dimensions.

4.3.2. Mineralization of hydrogels

The hydrogel discs were mineralized as described elsewhere.[70] Briefly, hydrogel discs were incubated in deionized (DI) water for 6 h and subsequently immersed in modified simulated body fluid (m-SBF; pH = 7.4) for 6 h. The main ionic components of m-SBF are 142.0 mM Na^+, 5.0 mM K^+, 1.5 mM Mg^{2+}, 2.5 mM Ca^{2+}, 103.0 mM Cl^-, 10.0 mM HCO_3^-, 1.0 mM HPO_4^{2-}, and 0.5 mM SO_4^{2-}.[178] The hydrogels were briefly rinsed in DI water and soaked in a solution containing 40 mM Ca^{2+} and 24 mM HPO_4^{2-} (pH = 5.2) at 25 °C for 45 min. while using a rotating shaker (VWR Mini-shaker; catalog #: 12620-938) at 200 rpm. The hydrogels were briefly rinsed in DI water and further immersed in m-SBF at 37 °C for 48 h with the daily change of m-SBF. The hydrogels were then equilibrated in PBS for 6 h. The mineralized and non-mineralized PEGDA-*co*-A6ACA hydrogels were sterilized in 70% ethanol (EtOH) for 6 h. The EtOH-treated matrices were washed in PBS for 5 days with three daily changes of PBS prior to cell culture.

4.3.3. Scanning electron microscopy (SEM) & energy dispersive spectra (EDS)

SEM imaging was carried out to examine the morphology of biomineralized matrices. The elemental analysis was conducted by using Oxford Energy Dispersive Spectra (EDS) attachment. EDS was performed to examine the presence of calcium and phosphorous elements in biomineralized matrices as well as to determine their atomic ratio (Ca/P). Samples were prepared and imaged as described elsewhere.[71] In brief, samples were rinsed in DI water for 5 min and flash-frozen using liquid nitrogen and lyophilized for 24 h. The dried samples were coated with iridium for 7 s by using sputter coater (Emitech, catalog #: K575X) and then imaged under vacuum using Philips XL30 ESEM.

4.3.4. Calcium and phosphate assays

Calcium and phosphate assays were carried out to determine Ca^{2+} and PO_4^{3-} contents of mineralized matrices as well as the dissolution of CaP minerals from the mineralized matrices. To measure the amounts of Ca^{2+} and PO_4^{3-}, samples were briefly rinsed in DI water for 5 minutes, lyophilized for 16 h, and dry weights were measured. The dried samples were homogenized in 0.5 M HCl and vigorously agitated using a rotating shaker at 25 °C for 3 days. The homogenized samples were used for calcium and phosphate assays. To examine the dissociation of CaP minerals into Ca^{2+} and PO_4^{3-} ions from mineralized matrices, equilibrium-swollen mineralized hydrogels were incubated in 1.5 mL of 50 mM Tris-HCl solution (pH = 7.4) at 37 °C for 7 days. Approximately 300 µl of incubation solution was collected and replaced by fresh solution on a daily basis to examine the dissolution of CaP minerals as a function of time. Calcium assay was performed according to manufacturer's protocol (Calcium reagent set, Pointe Scientific, catalog #: C7503). In brief, 20 µl of sample solution was mixed with 1 mL of calcium assay reagent. The absorbance of the resultant solution was recorded at 570 nm using a UV/Vis spectrophotometer (Beckman Coulter, DU 730). Phosphate assay was carried out according to a method used elsewhere.[144] In brief, phosphate assay reagent was prepared by mixing 1 part 10 mM ammonium molybdate with 2 parts acetone and 1 part H_2SO_4. 125 µl of sample solution and 100 µl of 1 M citric acid were added to 1 mL of the phosphate assay reagent. Absorbance of the resultant solution was recorded at 380 nm using a UV/Vis spectrophotometer.

4.3.5. Cell culture

The hMSCs (Institute for Regenerative Medicine, Texas A&M University) were maintained in growth medium containing high glucose DMEM, 10% (v/v) fetal bovine serum (FBS; hyclone), 4 mM L-glutamine, and 50 U/mL penicillin/streptomycin. The cells were passaged at approximately 70% confluency.

Prior to seeding hMSCs, sterile non-mineralized and mineralized hydrogels as well as cell culture-grade coverslips (CS; diameter = 15 mm, Fisherbrand, catalog #: 1254582) were incubated in growth medium at 37 °C for 24 h to promote cell adhesion. Passage 5 (P5) hMSCs were plated at a density of 12,000 cells/cm^2 and cultured for 14 days using either growth medium or adipogenic medium, at 37 °C and 5% CO_2 with medium change every two days. Adipogenic medium was prepared by supplementing growth medium with 1 µM dexamethasone (Sigma-Aldrich, catalog #: D2915), 200 µM indomethacin (Sigma-Aldrich, catalog #: I7378), 0.5 µM 3-isobutyl-1-methylxanthine (IBMX; Sigma-Aldrich, catalog #: I5879), and 10 µg/mL of insulin (Sigma-Aldrich, insulin from bovine pancreas, catalog #: I6634). For pharmacological inhibition of A2bR, PSB 603 (Tocris Bioscience, catalog #: 3198) was added into growth medium or adipogenic medium at varying concentrations of 0, 0.5, 10, and 100 nM.

4.3.6. Cell tracker labeling

To visualize the attachment and growth of cells cultured on various matrices (non-mineralized and mineralized matrices as well as coverslips) under different medium conditions (growth medium or adipogenic medium), the cells were labeled with CellTracker fluorescent probes (Life Technologies, catalog number: C34552). Briefly, the cells grown on various matrices were incubated in 20 µM CellTracker fluorescent dyes in DMEM at 37 °C for 30 min and then in growth medium at 37 °C for an additional 30 min. The labeled cells were imaged using a fluorescence microscope (Carl Zeiss, Axio Observer.A1).

4.3.7. Quantitative polymerase chain reaction (qPCR) analysis

qPCR analysis was carried out to examine differences in gene expressions of hMSCs cultured on various matrices under different medium conditions. Cells were collected in 1 mL of TRIzol and their RNA was isolated using phenol-chloroform extraction method. For each sample, 1 µg of RNA was reverse-transcribed to cDNA using iScript cDNA synthesis kit (Bio-Rad, catalog #: 170-8891) according to manufacturer's protocol. cDNA solution was mixed with SYBR Select Master Mix (Life Technologies, catalog #: 4472908) and primers for various genes. The resulted solution was subject to qPCR analysis using ABI Prism 7700 Sequence Detection System (Applied Biosystems). The list of primer sequences is shown in Table 4.S1. Gene expressions for various osteogenic (RUNX2, OCN, and BSP) as well as adipogenic (PPAR-γ2, αP2, and LPL) markers were evaluated. The expression for each target gene was normalized to that of corresponding housekeeping gene (GAPDH). The expression level was quantified by $2^{-\Delta\Delta Ct}$ values. To compare gene expression of hMSCs cultured on various matrices under different medium conditions, the expression level was normalized to the corresponding cultures on coverslips under identical medium condition and presented as fold expression. To compare gene expression of hMSCs cultured on mineralized matrices using different medium conditions supplemented with PSB 603, the expression level was normalized to that of cells cultured in the corresponding medium condition devoid of PSB 603 and presented as fold expression.

4.3.8. Immunofluorescent staining

Immunofluorescent staining was performed for osteocalcin, a mature osteoblast-specific marker, and perilipin, a mature adipocyte-specific marker. Cells cultured on various matrices under different medium conditions were fixed in 4% formaldehyde at 25 °C for 10 min. The cells were washed with PBS and blocked by a blocking buffer composed of 3% (w/v) BSA and 0.1% (v/v) Triton™ X-100 dissolved in PBS at 25 °C for 60 min. The fixed cells were incubated in primary antibodies against osteocalcin (1:100; mouse monoclonal, Santa Cruz Biotechnology, catalog #: sc-74495) or perilipin (1:100; rabbit polyclonal, Santa Cruz Biotechnology, catalog #: 67164) diluted in the blocking buffer at 4 °C for 16 h. The cells were washed with PBS, exposed to secondary antibodies raised against mouse (goat anti-mouse, 1:250, Life Technologies, Alexa Fluor 568) or rabbit (goat anti-rabbit, 1:250, Life Technologies, Alexa Fluor 568) and phalloidin (1:100; Life Technologies, Alexa Fluor 488) diluted in the blocking buffer at 25 °C for 60 min., and washed with PBS. The nuclei of cells were stained using Hoechst 33342 solution (2 µg/mL; Life Technologies, catalog #: H1399) at 25 °C for 7 min and washed with PBS. The samples were mounted onto glass slides and imaged using a fluorescence microscope (Carl Zeiss, Axio Observer A1). The images were taken at a linear mode and the same exposure time was used for all samples. The background was uniformly subtracted for all images using ImageJ software, where a rolling ball algorithm with a rolling ball radius of 750 pixels was applied.

4.3.9. Statistical analysis

Graphpad Prism 5 was used to perform statistical analyses. Two groups were compared using two-tailed Student's *t*-test. Multiple groups were compared by one-way analysis of variance (ANOVA) with Tukey-Kramer post-hoc test. The *p*-values measuring less than 0.05 were considered statistical significances. Asterisks were assigned to represent different levels of statistical significances.

4.4. Results

4.4.1. Synthesis and characterization of mineralized matrices.

Synthetic matrices were developed by copolymerizing poly(ethylene glycol)-diacrylate (PEGDA) with N-acryloyl 6-aminocaproic acid (A6ACA) moieties as described elsewhere.[38] The PEGDA-*co*-A6ACA hydrogel matrices were biomineralized to incorporate CaP moieties into the matrix,[38] where the presence of pendant side chain terminating with carboxyl groups promoted the binding of Ca^{2+} ions and subsequently led to nucleation of CaP minerals. Gross images of mineralized matrices revealed their opaqueness in contrast to transparent non-mineralized controls (Figure 4.1a). Scanning electron microscopy (SEM) images of mineralized matrices showed a continuous layer of minerals (Figure 4.1b). Energy dispersive spectroscopy (EDS) analyses confirmed the presence of calcium and phosphorous elements in mineralized matrices with an atomic ratio (Ca/P) of 1.40 (Figure 4.1b). As expected, no peaks arising from such elements were observed in non-mineralized matrices. Measurements of Ca^{2+} and PO_4^{3-} contents of mineralized matrices showed that they contain 80.4 ± 1.5 mg of Ca^{2+} and 129.4 ± 3.8 mg of PO_4^{3-} per g of dry weight of matrices (Figures 4.1c-d), while negligible amounts of such ions were detected in non-mineralized matrices. The CaP minerals of the mineralized matrices dissociated into Ca^{2+} and PO_4^{3-} ions in a medium devoid of such ions (Figures 4.1e-f). Mineralized materials initially showed a rapid release of Ca^{2+} and PO_4^{3-} ions into the surrounding medium of Tris buffer within 1 day of incubation; thereafter, their ionic concentration in the surrounding medium did not vary significantly throughout the experimental time of 7 days.

4.4.2. Culture-dependent osteogenesis or adipogenesis of hMSCs.

We cultured hMSCs on non-mineralized and mineralized matrices and coverslips in either growth medium or adipogenic medium. All the matrices supported adhesion and spreading of cells with no significant differences both in growth medium and adipogenic medium (Figure 4.S1). Cells in all culture conditions proliferated and reached confluence within 10 days of culture. We next determined the effect of mineralized and non-mineralized matrices on differentiation of hMSCs in both growth and adipogenic medium and compared against those cultured on cell culture-grade coverslips under identical conditions. The cells cultured on mineralized matrices in growth medium exhibited a significant upregulation of various osteogenic markers (RUNX2, OCN, and BSP) compared to other matrices under investigation after 14 days of culture, which is in accordance with previous reports (Figure 4.2a).[132] Unlike osteogenic markers, adipogenic markers (PPAR-γ2, αP2, and LPL) were undetectable on any of the matrices in growth medium (Figure 4.2a). Findings from the gene expression profile were further confirmed by immunofluorescent staining for osteocalcin (osteoblast-specific marker) and perilipin (adipocyte-specific marker). The cells cultured on mineralized matrices in growth medium stained positive for osteocalcin (Figure 4.3a), while no positive staining for perilipin was observed on any of the matrices in growth medium (Figure 4.3b), consistent with the lack of adipogenic gene expression. The cells were also stained for F-actin and Hoechst (for nuclei). The gene expression profile along with immunofluorescent staining suggests that the mineralized matrices possess necessary cues to direct osteogenic differentiation of hMSCs in growth medium.

We next examined the effect of different matrices on hMSC differentiation in adipogenic medium. Specifically, we asked whether the cues from the mineralized matrices would be sufficient to direct osteogenic differentiation of hMSCs when cultured in adipogenic medium. The differentiation pattern of hMSCs on different matrices showed that the cells on non-mineralized matrices and coverslips exhibited a significant upregulation of adipogenic markers, while those on mineralized matrices had minimal to no expression of adipogenic markers (Figure 4.2b). Instead of undergoing adipogenesis, the cells on mineralized matrices underwent osteogenic differentiation and displayed an upregulation of various osteogenic markers despite being incubated in adipogenic medium (Figure 4.2b). Immunofluorescent staining for osteocalcin and perilipin further corroborated the findings from the gene expression. The hMSCs on mineralized matrices stained positive for osteocalcin (Figure 4.4a), with minimal to no positive staining for perilipin (Figure 4.4b). On the contrary, cells on non-mineralized matrices and coverslips stained positive for perilipin (Figure 4.4b) and exhibited no positive staining for osteocalcin (Figure 4.4a). Taken together, the results suggest that the cues provided by the mineralized matrices are effectively dominant in directing osteogenic differentiation of hMSCs while inhibiting their adipogenic differentiation, even in the presence of medium conditions that are known to drive adipogenic differentiation of hMSCs.

4.4.3. Role of adenosine signaling in mineral-aided inhibition of adipogenesis.

We have previously demonstrated the role of adenosine signaling in mineralized matrix-assisted osteogenesis of hMSCs.[39] Thus, we wondered whether adenosine signaling not only promotes osteogenic differentiation of hMSCs, but also attenuates their adipogenic differentiation in a mineral environment. In order to investigate the role of adenosine signaling in inhibition of adipogenesis on mineralized matrices, we examined the role of adenosine A2b receptor (A2bR). We chose A2bR due to its established role in mineralized matrix-mediated osteogenic differentiation of hMSCs.[39] We blocked A2bR with 8-[4-[4-(4-chlorophenzyl)piperazide-1-sulfonyl)phenyl]]-1-propylxanthine (PSB 603) to examine its effect on mineralized matrix-assisted suppression of adipogenesis of hMSCs. Consistent with our previous report, the hMSCs cultured on mineralized matrices in growth medium showed downregulation of osteogenic markers (RUNX2, OCN, and BSP) in presence of PSB 603 (Figure 4.5a).[39] The downregulation of osteogenic markers was further confirmed by immunofluorescent staining for osteocalcin, which showed that the positive signal of hMSCs on mineralized matrices diminished significantly in presence of PSB 603 (Figure 4.6a). The presence of PSB 603 in growth medium did not have any effect on adipogenesis and the expression levels of various adipogenic markers remained undetectable (Figure 4.5a). The cells on mineralized matrices stained negative for perilipin, both in the presence and absence of

PSB 603 in growth medium (Figure 4.6b), further confirming no influence of PSB 603 on adipogenic differentiation of hMSCs.

We next investigated the effect of adenosine signaling on mineralized matrix-mediated inhibition of adipogenesis in adipogenic medium. Similar to the cultures in growth medium, the hMSCs on mineralized matrices exhibited downregulation of osteogenic markers (RUNX2, OCN, and BSP) in adipogenic medium supplemented with PSB 603 (Figure 4.5b). Concomitant with the decrease in osteogenic gene expression pattern, we observed a significant upregulation of adipogenic markers (PPAR-γ2, αP2, and LPL; Figure 4.5b). This is in stark contrast to hMSCs on mineralized matrices in adipogenic medium without the inhibition of A2bR. The expression levels of adipogenic genes were found to be the highest for cultures containing 100 nM PSB 603. The gene expression pattern was further confirmed by immunofluorescent staining showing that the addition of PSB 603 into adipogenic medium resulted in the attenuation of positive osteocalcin staining in hMSCs on mineralized matrices (Figure 4.7a). The reduction in osteocalcin signaling was accompanied by positive staining for perilipin and its intensity increased as the concentration of PSB 603 in the medium increased (Figure 4.7b).

4.5. Discussion

Biomaterials recapitulating tissue-specific physical and chemical cues have been considered a powerful tool in directing stem cell differentiation commitment. Prevalent use of biomaterials to direct stem cell commitment to assist tissue repair, however, is dependent upon the dominancy of the matrix-based cues over competing soluble cues present in the milieu. This is paramount when the cells possess multipotency and a shift in differentiation of the progenitor cells could lead to pathologies. Biomaterials containing CaP minerals promote osteogenic differentiation of progenitor and stem cells[59, 70, 71, 132, 205] and a number of studies have used such mineralized materials to promote bone tissue formation *in vivo*.[20, 70, 77, 205] Given the propensity of MSCs to differentiate into both osteoblasts and adipocytes in response to the matrix or soluble cues, we examined the fate decision of hMSCs in an environment where disparate instructive cues are presented: the mineralized matrix provides cues relevant to osteogenesis while the adipogenic medium provides cues necessary for adipogenesis.

Our results showed that hMSCs cultured on various matrices in the presence and absence of adipogenic soluble supplements underwent differential fate into either osteogenic or adipogenic lineages, depending upon the local cues available from the matrices and/or medium conditions. Specifically, hMSCs on non-mineralized hydrogels and coverslips underwent adipogenic differentiation in adipogenic medium and no significant differentiation was observed in growth medium. However, intriguingly, hMSCs cultured on mineralized matrices underwent osteogenic differentiation, while inhibiting their adipogenic differentiation, despite being cultured in adipogenic medium. The inhibition of adipogenesis in presence of adipogenic medium was observed only on CaP-bearing matrices, indicating that the matrix-mediated inhibition is largely attributed to the mineral environment. A previous study by Jensen *et al*. has reported a similar finding, where the authors observed a significant decline in adipogenic differentiation of 3T3-L1 preadipocytes in adipogenic medium containing high levels of calcium supplements.[206] A number of studies have shown the importance of dissolution of CaP minerals in determining the osteoinductivity of mineralized matrices.[205] Biomineralized matrices used in this study contained apatite-like CaP minerals[38] that can be easily dissociated into Ca^{2+} and PO_4^{3-} ions. The dissolution and precipitation of CaP moieties regulate the levels of Ca^{2+} and PO_4^{3-} ions in the extracellular milieu.[20, 99, 100]

The mineralized matrix-assisted attenuation of adipogenesis of hMSCs was reversed upon blocking of A2bR, a Gαs/αq protein-coupled receptor, suggesting the role of adenosine signaling in this process. The adipogenic differentiation of hMSCs in presence of A2bR inhibitor was accompanied by inhibition of their osteogenic differentiation. This is in accordance with previous reports that have implicated the role of adenosine signaling, in particular, A2bR on osteogenic differentiation of MSCs[39, 207, 208] and our previous findings that adenosine signaling through phosphate metabolism and A2bR plays an important role in mineralized matrix-assisted osteogenic differentiation of hMSCs.[39] Studies have shown that, under culture conditions devoid of osteogenic cues, merely overexpressing A2bR in preosteoblasts increased osteoblast gene expression, but inhibited their adipogenesis in adipogenic-inducing medium.[209] This suggests A2bR signaling plays a key role in specifying osteogenic differentiation of progenitor cells *in vitro*. A2bR activates adenylate cyclase and increases intracellular cAMP levels to play an inhibitory role in adipogenesis.[210, 211] Findings in a recent study by Eisenstein *et al.* further demonstrate A2bR activation inhibits adipogenic differentiation of preadipocytes through the transcription factor Krüppel-like factor 4 (KLF4), which appears to be partially regulated by an increase in cAMP and activation of PKA.[212] However, other studies have shown that KLF4 directly binds

CCAAT/enhancer-binding protein β (C/EBPβ) promoter and is required for adipogenesis,[213] while ectopic overexpression of KLF4 attenuated osteoblast differentiation and mineralization.[214] In another study, suppression of KLF4 in hMSCs enhanced both osteogenic and adipogenic differentiation.[215] The discrepant role of KLF4 during osteogenic versus adipogenic fate regulation in these studies implies that the downstream molecular machinery of A2bR is dynamic and context-dependent, and remains to be elucidated. Nonetheless, A2bR clearly acts as a molecular switch to arbitrate cell fates in a competing environment containing CaP mineral-borne osteogenic cues and soluble adipogenic cues.

4.6. Conclusion

In summary, our results showed that the cues provided by the mineralized matrices promote osteogenic commitment of hMSCs as well as suppress their adipogenic differentiation even in the presence of adipogenic-inducing medium. Interestingly, the mineralized matrix-assisted diminution of adipogenic differentiation could be reversed through inhibition of A2bR signaling. To our knowledge, this is the first investigation of stem cell commitment in presence of competing matrix-based and soluble cues and demonstration for the dominance of mineralized matrix-based cues over soluble medium components in directing osteogenic commitment of hMSCs. Mineralized matrices that support osteogenic differentiation of progenitor and stem cells while inhibiting their adipogenic differentiation could have a significant impact in bone tissue regeneration. Since perturbed differentiation commitment of MSCs into adipogenic lineage over osteogenesis is implicated in various bone disorders, such instructive matrices with inherent bone tissue-specific cues could act as a technological platform to study various bone disorders and pathologies.

4.7. Acknowledgements

Authors gratefully acknowledge the financial support from National Institutes of Health (NIH; Grant 1 R01 AR063184-01A1) and California Institute of Regenerative Medicine (CIRM; RN2-00945 and RT2-01889). The hMSCs used in this study were provided by Texas A&M University from NIH (Grant P40RR017447).

Chapter 4, in full, is a reprint of the material as it appears in Biomacromolecules, vol. 16, 2015. “Biomineralized matrices dominate soluble cues to direct osteogenic differentiation of human mesenchymal stem cells through adenosine signaling”. Kang, Heemin; Shih, Yu-Ru V.; Varghese, Shyni. The dissertation author was the primary investigator and author of this paper.

4.8. Figures

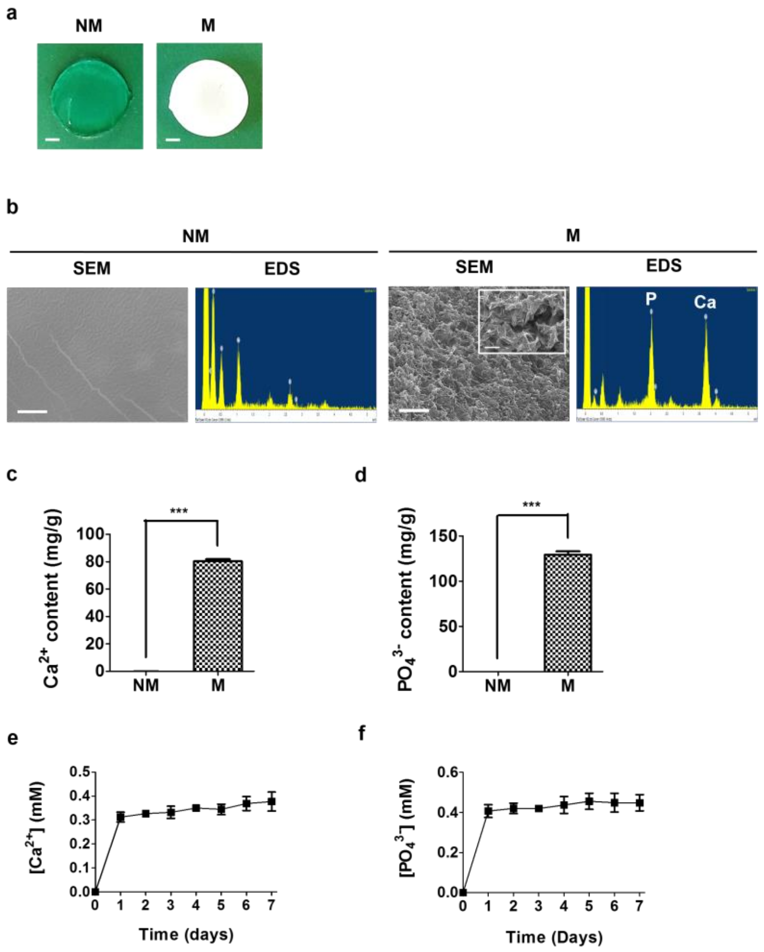

Figure 4.1. Characterization of biomineralized matrices.

(a) Gross images of non-mineralized (NM) and mineralized (M) hydrogel discs. Scale bars represent 2 mm. (b) Scanning electron microscopy (SEM) images and corresponding energy dispersive spectra (EDS) of non-mineralized and mineralized matrices. Scale bars indicate 2 µm. Inset shows high magnification images and scale bar represents 500 nm. (c) Ca^{2+} and (d) PO_4^{3-} amounts of non-mineralized and mineralized matrices after normalization to the dry weight of matrices. Release of (e) Ca^{2+} and (f) PO_4^{3-} from mineralized matrices in Tris buffer lacking such ions at 37 °C as a function of time. Data are presented as mean ± standard deviations (n = 3). Two groups were compared by employing two-tailed Student's *t*-test. Asterisks were assigned to *p*-values with statistical significances (***: $p < 0.001$).

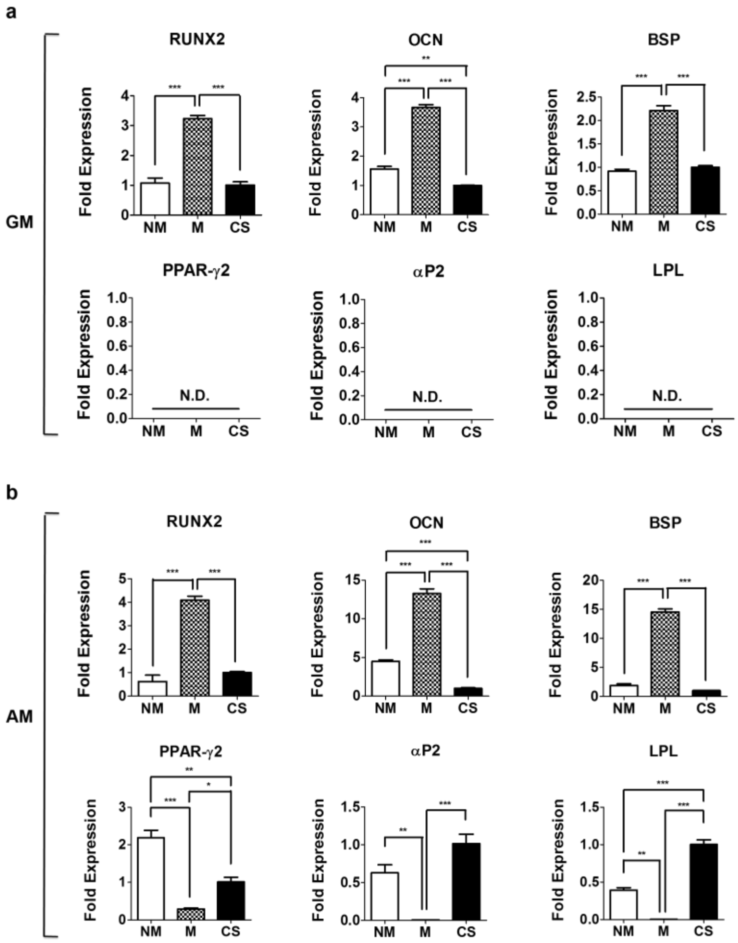

Figure 4.2. Quantitative PCR analyses of hMSCs cultured on various matrices in different medium conditions.

Gene expressions of hMSCs for osteogenic markers (RUNX2, OCN, and BSP) as well as adipogenic markers (PPAR-γ2, αP2, and LPL) after 14 days of culture. Cells were cultured on non-mineralized (NM) and mineralized (M) matrices and coverslips (CS) in (a) growth medium (GM) and (b) adipogenic medium (AM). N.D. indicates a non-detectable amplification signal. Data are presented as mean ± standard errors (n = 3). Groups with different matrices in the same medium were compared by using one-way ANOVA with Tukey-Kramer post-hoc test. Asterisks were assigned to p-values with statistical significances (*: $p < 0.05$; **: $p < 0.01$; ***: $p < 0.001$).

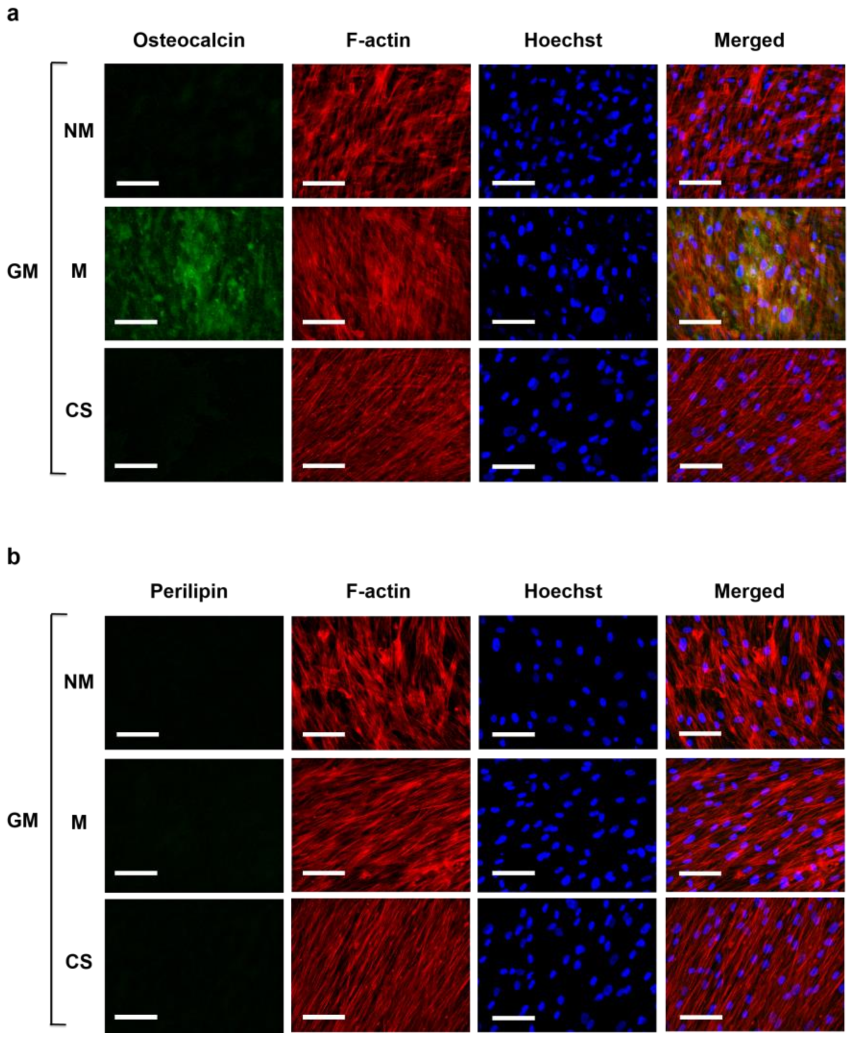

Figure 4.3. Immunofluorescent staining of (a) osteocalcin (green) and (b) perilipin (green) after 14 days of culture in growth medium (GM).

hMSCs were cultured on non-mineralized (NM) and mineralized (M) matrices and coverslips (CS). Corresponding F-actin (red) and nuclei (blue; Hoechst) are shown. Scale bars represent 100 µm.

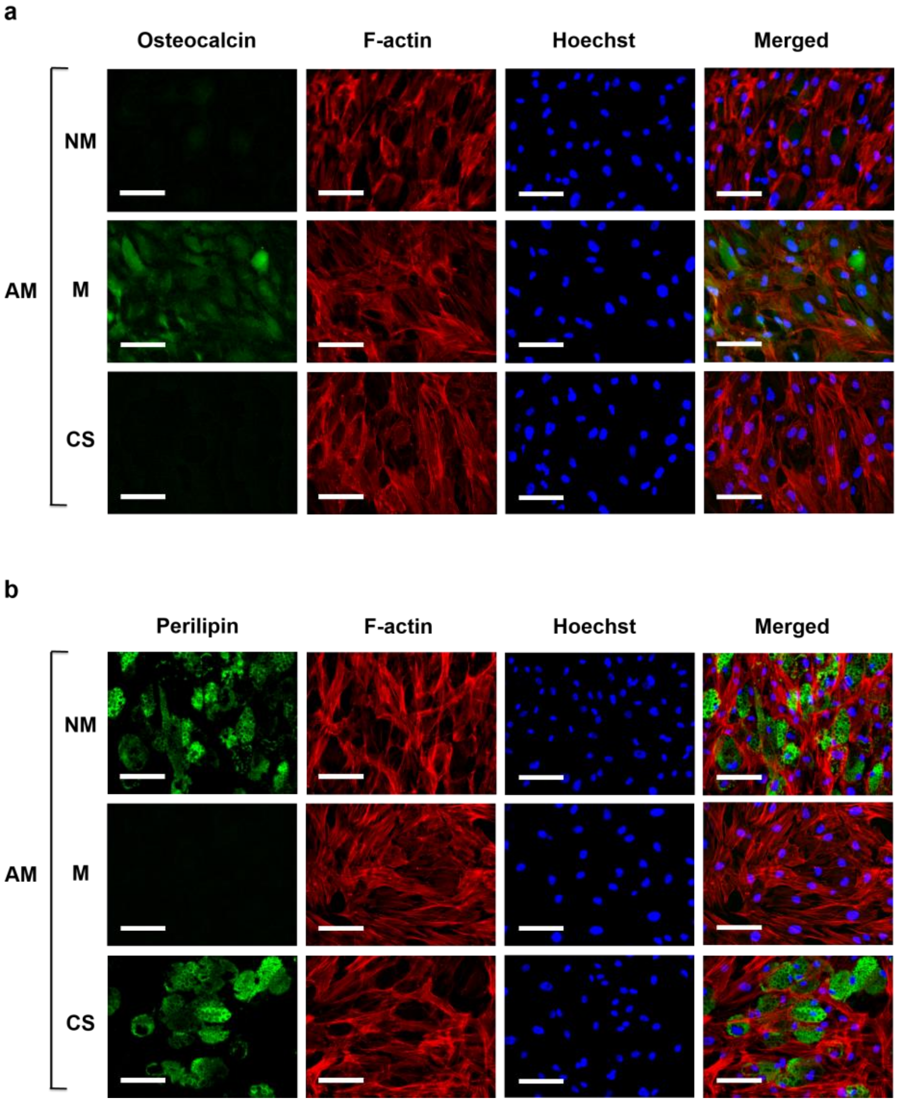

Figure 4.4. Immunofluorescent staining of (a) osteocalcin (green) and (b) perilipin (green) after 14 days of culture in adipogenic medium (AM).

hMSCs were cultured on non-mineralized (NM) and mineralized (M) matrices and coverslips (CS). Corresponding F-actin (red) and nuclei (blue; Hoechst) are shown. Scale bars represent 100 µm.

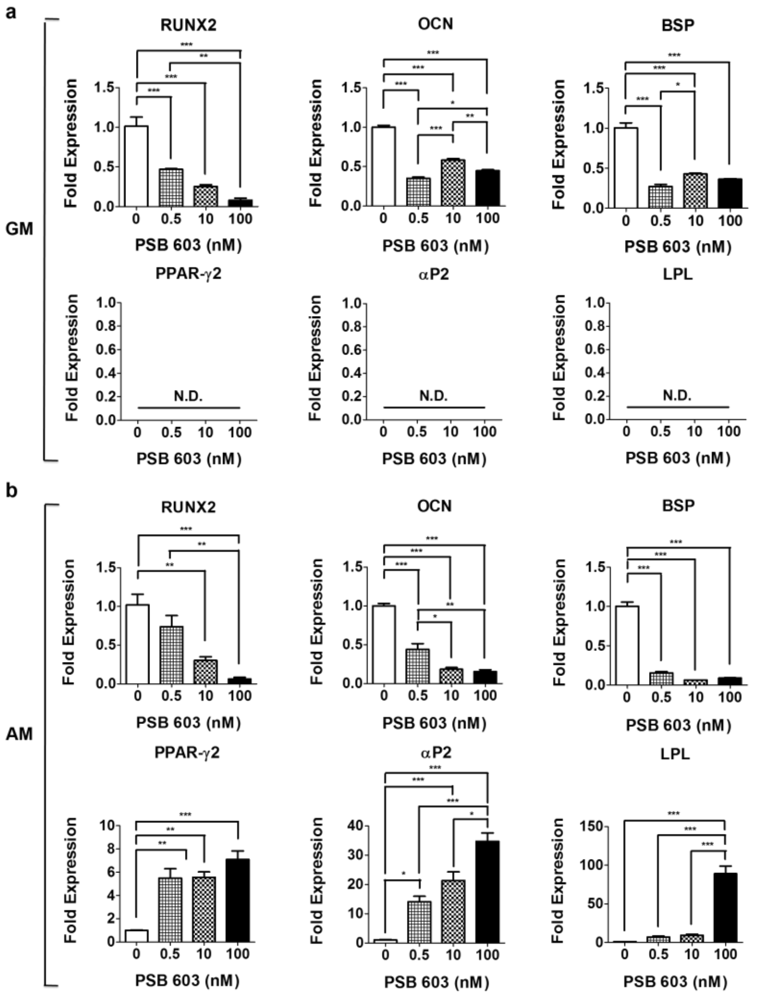

Figure 4.5. Quantitative PCR analyses of hMSCs cultured on mineralized matrices in different medium conditions with varying amounts of A2bR antagonist, PSB 603.

Fold expressions of hMSCs for osteogenic markers (RUNX2, OCN, and BSP) as well as adipogenic markers (PPAR-γ2, αP2, and LPL) after 14 days of culture. Cells were cultured in (a) growth medium (GM) and (b) adipogenic medium (AM) supplemented with PSB 603 at varying concentrations of 0, 0.5, 10, and 100 nM. N.D. indicates a non-detectable signal from PCR cycles. Data are presented as mean ± standard errors ($n = 3$). Groups with varying concentrations of PSB 603 under the same medium condition were compared by using one-way ANOVA with Tukey-Kramer post-hoc test. Asterisks were assigned to p-values with statistical significances (*: $p < 0.05$; **: $p < 0.01$; ***: $p < 0.001$).

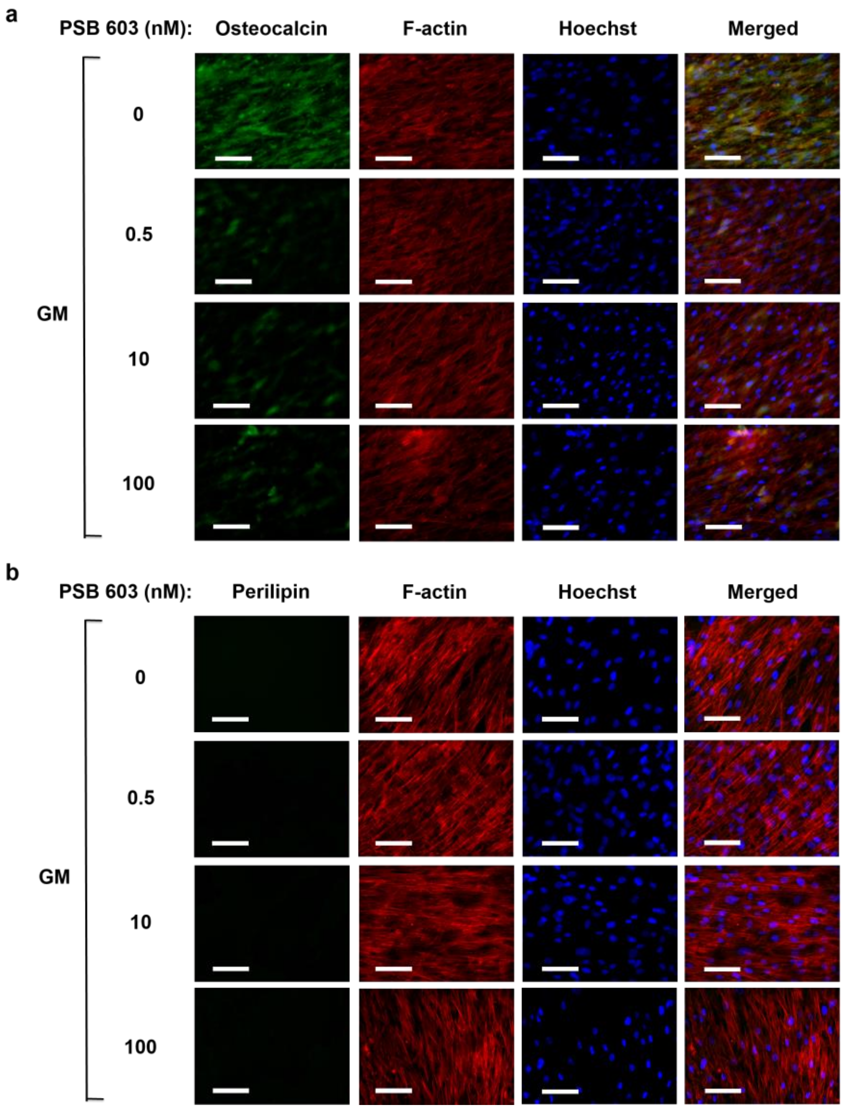

Figure 4.6. Immunofluorescent staining of (a) osteocalcin (green) and (b) perilipin (green) with A2bR inhibition in growth medium (GM).

hMSCs were cultured on mineralized matrices for 14 days in GM containing varying amounts (0, 0.5, 10, and 100 nM) of A2bR antagonist, PSB 603. Corresponding F-actin (red) and nuclei (blue; Hoechst) are shown. Scale bars represent 100 µm.

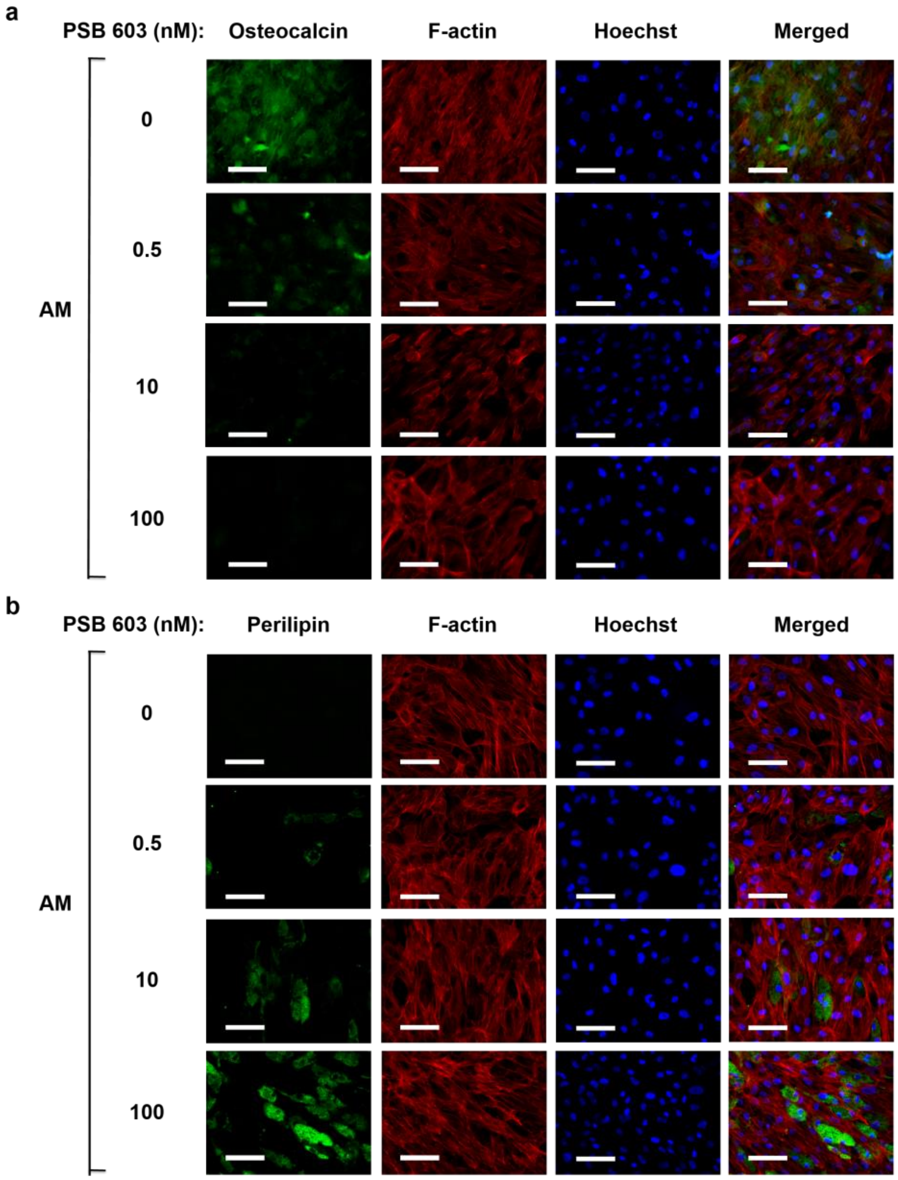

Figure 4.7. Immunofluorescent staining of (a) osteocalcin (green) and (b) perilipin (green) with A2bR inhibition in adipogenic medium (AM).

hMSCs were cultured on mineralized matrices for 14 days in AM containing varying amounts (0, 0.5, 10, and 100 nM) of A2bR antagonist, PSB 603. Corresponding F-actin (red) and nuclei (blue; Hoechst) are shown. Scale bars represent 100 µm.

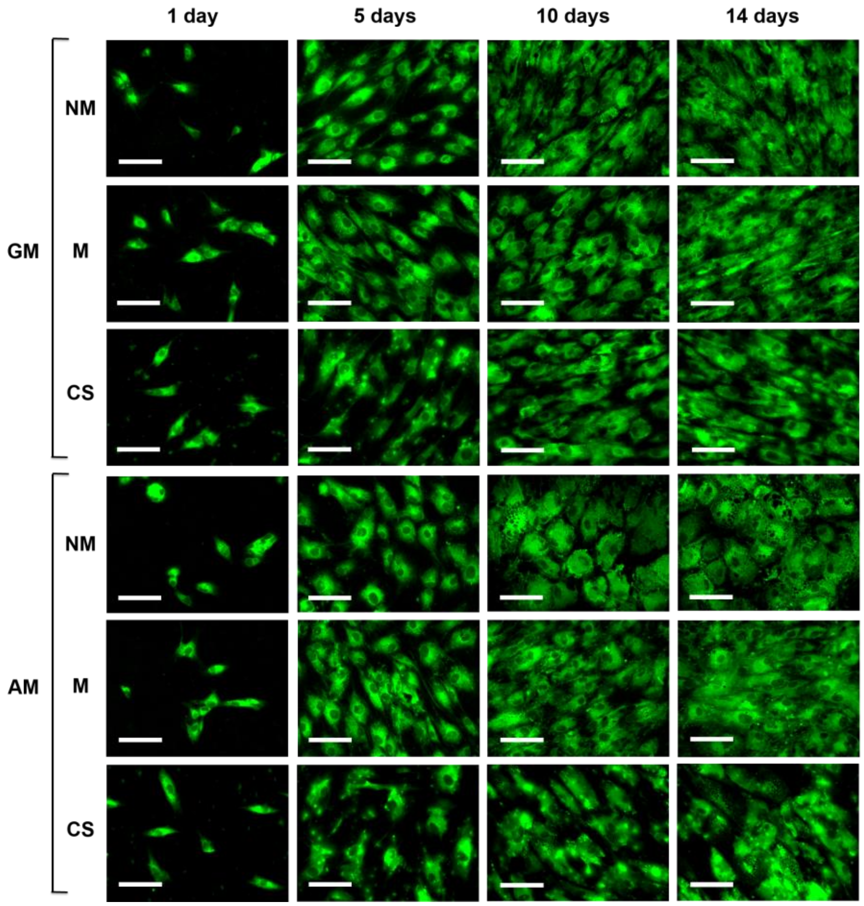

Figure 4.S1. Adhesion and growth of hMSCs on various matrices in different medium conditions.

The cells on different matrices (non-mineralized matrices [NM], mineralized matrices [M], and coverslips [CS]) and medium conditions (growth medium [GM] or adipogenic medium [AM]) were imaged as a function of culture time (1, 5, 10, and 14 days). The cells were labeled with CellTracker. Scale bars indicate 100 μm.

4.9. Tables

Table 4.S1. List of primer sequences used in quantitative PCR analyses.

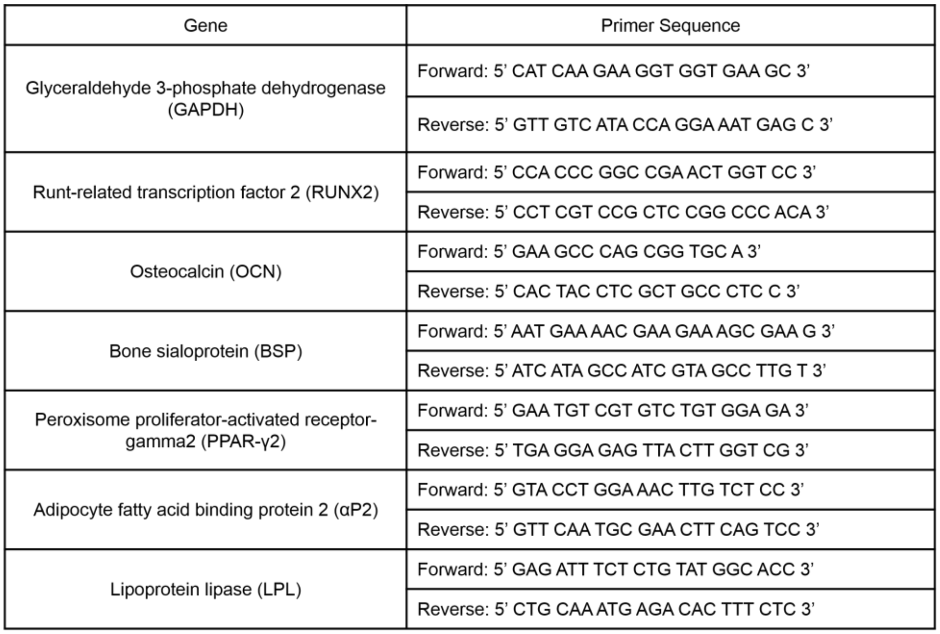

Gene	Primer Sequence
Glyceraldehyde 3-phosphate dehydrogenase (GAPDH)	Forward: 5’ CAT CAA GAA GGT GGT GAA GC 3’
	Reverse: 5’ GTT GTC ATA CCA GGA AAT GAG C 3’
Runt-related transcription factor 2 (RUNX2)	Forward: 5’ CCA CCC GGC CGA ACT GGT CC 3’
	Reverse: 5’ CCT CGT CCG CTC CGG CCC ACA 3’
Osteocalcin (OCN)	Forward: 5’ GAA GCC CAG CGG TGC A 3’
	Reverse: 5’ CAC TAC CTC GCT GCC CTC C 3’
Bone sialoprotein (BSP)	Forward: 5’ AAT GAA AAC GAA GAA AGC GAA G 3’
	Reverse: 5’ ATC ATA GCC ATC GTA GCC TTG T 3’
Peroxisome proliferator-activated receptor-gamma2 (PPAR-γ2)	Forward: 5’ GAA TGT CGT GTC TGT GGA GA 3’
	Reverse: 5’ TGA GGA GAG TTA CTT GGT CG 3’
Adipocyte fatty acid binding protein 2 (αP2)	Forward: 5’ GTA CCT GGA AAC TTG TCT CC 3’
	Reverse: 5’ GTT CAA TGC GAA CTT CAG TCC 3’
Lipoprotein lipase (LPL)	Forward: 5’ GAG ATT TCT CTG TAT GGC ACC 3’
	Reverse: 5’ CTG CAA ATG AGA CAC TTT CTC 3’

Chapter 5: Small molecule-driven direct conversion of human pluripotent stem cells into functional osteoblasts

5.1. Abstract

The ability of human pluripotent stem cells (hPSCs) to proliferate without phenotypic alteration and differentiate into tissue-specific progeny makes them promising cell sources for regenerative medicine to treat various debilitating diseases. Despite the opportunities, their efficient conversion into tissue-specific cells still remains a serious challenge. Herein, we report adenosine, a naturally occurring nucleoside in the human body, induced osteogenic differentiation of hPSCs, including both human embryonic stem cells (hESCs) and human induced pluripotent stem cells (hiPSCs). Their potency in directing osteogenesis of hPSCs was comparable to that of osteogenic induction medium including β-glycerophosphate, ascorbic acid 2-phosphate, and dexamethasone. Furthermore, we reveal that adenosine-mediated osteogenesis of hPSCs involved adenosine A2b receptor (A2bR) signaling. The hPSCs treated with adenosine not only expressed molecular signature of osteoblasts, but also produced calcified bone matrix. To our knowledge, this is the first demonstration of adenosine-mediated differentiation of hPSCs into functional osteoblasts. When osteoblasts derived from hiPSCs by adenosine were transplanted with macroporous matrices, they participated in the repair of critical-sized bone defects through the formation of bridged bone without teratoma formation. The engineered bone with hiPSC-derived osteoblasts recapitulated the attributes of native bone tissue in morphology and mineral density with anastomosed blood vessels and

feasible bone resorption. Such a novel strategy of utilizing a single small molecule with high osteostimulatory potential can present a simple, cost-effective, and robust method to derive functional osteoblasts from hPSCs to treat large bone defects.

5.2. Introduction

Human pluripotent stem cells (hPSCs), which include both human embryonic stem cells (hESCs) and human induced pluripotent stem cells (hiPSCs), is an optimal cell source for regenerative medicine, in vitro model systems to study embryogenesis and disease, and in vitro platforms for drug discovery [64, 156, 216]. While both cell sources have the ability to self-renew indefinitely and differentiate into all three germ layers, hiPSCs offer many clinical benefits, as they can be derived from patient’s own cells. Despite the opportunities, cost-effective and efficient differentiation of hPSCs into tissue-specific cells is still a challenge limiting their widespread applications [217, 218]. A typical application of hPSCs often involves their *in vitro* differentiation into desirable cell populations prior to use.

Over the past decade, substantial strides have been made to direct differentiation of stem cells by a variety of approaches, such as genetic manipulation, biomaterials, growth factors, and small molecules [160, 219-223]. Although the most prominent and efficient methodology to achieve homogenous differentiation of hPSCs has thus far been genetic manipulation, approaches such as employing small molecules to direct differentiation of hPSCs would be clinically highly desirable. Employing small molecule(s) to direct stem cell fate has been an active area of research and has resulted in identification of small molecules that promote self-renewal [224, 225] and differentiation of stem cells [121, 226-229], dedifferentiation [230] and transdifferentiation [231, 232] of somatic cells, and reprogramming of cells [233-235] as well as limit the aging of bone marrow-derived mesenchymal stem cells (MSCs) [236].

It has been shown that small molecules can promote osteogenic differentiation of mesenchymal stem cells or osteoprogenitor cells [237, 238]. For instance, purmorphamine and N^6-benzoyladenosine-3’,5’-cyclic monophosphate has been reported to direct osteogenic differentiation of mesenchymal progenitor cells [237] and osteoblast-like MC3T3-E1 cells [238], respectively. While these studies showed the application of small molecules to direct osteogenic differentiation of progenitor cells, the efficacy of small molecules to direct osteogenic differentiation of hPSCs is yet to be established. In a recent study, Kanke et al. used four different small molecules sequentially to derive osteoblasts from PSCs (mouse ESCs and iPSCs as well as hiPSCs) [229]. Specifically, PSCs were cultured in medium supplemented with CHIR99021 and cyclopamine to achieve mesoderm induction. These mesoderm-committed cells were differentiated to osteoblasts by using conventional osteogenic induction medium supplemented with smoothened agonist and helioxanthin-derivative 4-(4-methoxyphenyl)pyrido[40,30:4,5]thieno [2,3-b]pyridine-2-carboxamide.

Herein, we demonstrate direct conversion of hPSCs into osteoblasts by using a single small molecule—exogenous adenosine—without embryoid body (EBD) formation. These hiPSC-derived osteogenic cells contributed to bone tissue formation both *in vitro* and *in vivo*. Critical-sized cranial defects treated with the hiPSC-derived osteogenic cells were repaired through their contribution to the regeneration of new bone tissue without teratoma formation. To our knowledge, this is the first study reporting the sole use of a single small molecule to derive functional osteoblasts from hPSCs.

5.3. Materials and Methods

5.3.1. Maintenance of hPSCs

hESCs (HUES9) and hiPSCs (IMR90p18-iPS; WiCell Research Institute) [179] were maintained as described elsewhere [239]. Briefly, hPSCs were cultured on feeder layers of mitotically inactivated mouse embryonic fibroblasts (MEFs) using a medium consisting of Knockout DMEM (Life Technologies; catalog # 10829-018), 10% (v/v) Knockout serum replacement (Life Technologies, catalog # 10828028), 10% (v/v) human plasmanate (Talecris Biotherapeutics), 1% (v/v) non-essential amino acids, 1% (v/v) Gluta-MAX, 1% (v/v) penicillin/streptomycin, and 55 μM 2-mercaptoethanol. hPSCs were passaged using Accutase (Millipore) at approximately 80% confluence. The fresh medium was supplemented with 30 ng/mL of bFGF (Life Technologies) and replenished daily.

5.3.2. Differentiation of hPSCs

hPSCs were plated onto culture-grade coverslips (15 mm in diameter; Fisherbrand; catalog # 1254582) coated with Matrigel (BD Biosciences, catalog # 354277) following manufacturer's protocol. Matrigel coating was used to facilitate the adhesion of hPSCs [70]. Briefly, Matrigel was diluted in chilled DMEM at a ratio of 1:86. The coverslips were incubated with Matrigel solution at 4 °C for overnight and subsequently at 37 °C for 1 h. Pluripotent hPSCs were plated at a density of 10,000 cells/cm^2 and cultured in maintenance medium at 37 °C and 5% CO_2 for 3 days to allow the attachment of the cells onto the coverslips. After 3 days of culture, the maintenance medium was replaced with either growth medium (high glucose DMEM, 10% [v/v] fetal bovine serum [FBS; hyclone], 4 mM L-glutamine, and 50 U/ml penicillin/streptomycin), or growth medium supplemented with 30 μg/mL adenosine (Sigma-Aldrich; catalog #: A4036), or growth medium supplemented with 30 μg/mL adenosine and 100 nM PSB 603, or osteogenic-inducing medium (growth medium containing 10 mM β-glycerophosphate (Calbiochem; catalog # 35675), 50 µM ascorbic acid-2-phosphate (Sigma-Aldrich; catalog # A8960), and 100 nM dexamethasone (Sigma-Aldrich; catalog # D2915). The PSB 603 is a pharmacological inhibitor of adenosine A2b receptor (A2bR) [240] and was procured from Tocris Bioscience (catalog #: 3198). Each medium was replenished every two days.

5.3.3. Reverse transcription-polymerase chain reaction (RT-PCR) analysis

hPSCs cultured in various medium conditions were examined for changes in the gene expression as a function of culture time. RNA was extracted from cell cultures (n=3) using TRIzol according to manufacturer’s instructions. For each sample, 1 μg of RNA was reverse-transcribed to cDNA using iScript cDNA synthesis kit (Bio-Rad; catalog # 170-8891). Real-time PCR reactions were run on ABI Prism 7700 Real-time PCR Cycler (Applied Biosystems). Human Osteogenic PCR array (SA Biosciences, catalog # PAHS-026) was also used to examine osteogenic differentiation of hiPSCs. In the case of PCR array, 84 genes related to osteogenic differentiation were analyzed and their relative expressions were presented as a heat map. The colors of the heat map were scaled according to the relative expression of hiPSCs cultured in various medium conditions. Red color represents the highest expression while green color represents the lowest expression. The color between red and green represents the intermediate expression level. For quantitative PCR (qPCR) analysis, SYBR Select Master Mix (Life technologies, catalog # 4472908) was mixed with various primers (GAPDH, RUNX2, OCN, SPP1, NANOG, A1R, A2aR, A2bR, and A3R). The primer sequences are listed in Table 5.S1. The expression of each target gene was normalized to that of corresponding GAPDH, a housekeeping gene. The expression levels of hPSCs cultured using various medium conditions were normalized to that of undifferentiated, pluripotent hPSCs and presented as fold expression.

5.3.4. Immunofluorescent staining of monolayer cultures

Monolayer cultures were fixed using 4% (w/v) paraformaldehyde at 25 °C for 10 min and washed with PBS. The fixed cells were treated with blocking solution of 3% (w/v) bovine serum albumin and 0.1% (v/v) Triton-X in PBS at 25 °C for 60 min. The treated cells were incubated with primary antibody against osteocalcin (1:100, mouse, Santa Cruz Biotechnology, catalog # sc-74495) in blocking solution at 4 °C for 16 h and washed with PBS. The cells were incubated with secondary antibody (goat anti-mouse; 1:250, Life Technologies, Alexa Fluor 568) and phalloidin (1:100, Life Technologies, Alexa Fluor 488) in the blocking solution at 25 °C for 60 min and washed with PBS. The nuclei were stained by using 2 μg/mL Hoechst 33342 (Life Technologies, catalog #: H1399) in PBS at 25 °C for 10 min and washed with PBS. The stained cells were mounted onto glass slides and visualized by using a fluorescence microscope (Carl Zeiss, Axio Observer.A1). The images were acquired in a linear mode using the same exposure time for all groups. The background of images was identically subtracted for all images by using ImageJ software by applying a rolling ball algorithm with rolling ball radius of 750 pixels.

5.3.5. Alizarin Red S staining of monolayer cultures

The hPSC cultures were fixed with 4% (w/v) paraformaldehyde for 10 min and washed with PBS. The cells were stained with 2% (w/v) Alizarin Red S Solution (Sigma-Aldrich; catalog # A5533; pH=4.2) for 10 min and washed with PBS. The stained cells were visualized using a microscope under H-filter in color mode.

5.3.6. Preparation of macroporous matrices

To evaluate bone-forming ability of osteoblasts derived from hiPSCs by using adenosine (Ad-hiPSCs), poly(ethylene glycol) diacrylate-*co*-acryloyl 6-aminocaproic acid (PEGDA-*co*-A6ACA) macroporous hydrogels were prepared by either poly(methyl methacrylate) (PMMA) leaching method [70] or cryogelation [241]. Synthesis of PEGDA (M_n = 3.4 kDa) and A6ACA were carried out as previously reported [199, 242]. Briefly, a cylindrical polypropylene mold (5 mm in diameter) was packed with 30 mg of PMMA microspheres (150 - 180 µm in diameter, Bangs Laboratories, catalog # BB05N). Approximately, 18 µL of precursor solution containing 20% (w/v) PEGDA, 0.5 M A6ACA in 0.5 N NaOH, and 0.3% (w/v) Irgacure was added into the PMMA-packed mold and photopolymerized by using UV light (λ = 365 nm) for 10 min. PMMA beads were leached out using acetone for 3 days and hydrated in deionized (DI) water to yield macroporous hydrogels measuring 7 mm in diameter and 2 mm in thickness.

In the case of cryogelation to create macroporous hydrogels, 75 µL of chilled precursor solution containing 20% (w/v) PEGDA, 0.5 M A6ACA in 0.5 N NaOH, 0.5% (w/v) ammonium persulfate (APS), and 0.2% (v/v) N, N, N'-N'-tetramethylethylenediamine (TEMED) was dispensed into a chilled polystyrene dish. A chilled coverslip of 15 mm in diameter was placed onto the precursor solution and polymerized at -20 ^{o}C for 24 h. PBS was added into the dish to yield macroporous hydrogels by thawing ice crystals. The resultant macroporous hydrogels were punched into 4 mm in diameter with 0.7 mm in thickness. The macroporous hydrogels were sterilized in 70% ethanol for 3 h and washed with PBS for 5 d.

5.3.7. Scanning electron microscopy (SEM)

SEM imaging was carried out to examine structures of the macroporous hydrogels. Briefly, the matrices were rinsed with DI water, cut into thin slices, and subjected to flash-freezing and lyophilization for 24 h. The sliced samples were iridium-coated for 7 s using a sputter coater (Emitech, K575X) and imaged by using a SEM (Philips XL30 ESEM).

5.3.8. Cell seeding and in vitro culture

To evaluate bone-forming ability of Ad-hiPSCs, the cells were seeded into the macroporous matrices. hiPSCs cultured in growth medium without exogenous adenosine (d-hiPSCs) was used as a control. The hiPSCs cultured in growth medium with or without the presence of 30 μg/mL adenosine for 21 days were trypsinized and used for the experiments. Prior to cell (Ad-hiPSCs and d-hiPSCs) seeding, sterile macroporous matrices (7 mm diameter x 2 mm thickness) were incubated in 1.5 mL of growth medium at 37 °C for 24 h to promote cell adhesion. Approximately 20 µL of the medium was removed and 20 µL of the cell suspension containing 1.5 million cells was seeded into the matrices. The cell-laden matrices were incubated at 37°C for 2 h to allow cell infiltration and cultured in 1.5 mL of the growth medium supplemented with 10 mM β-glycerophosphate and 50 µM ascorbic acid-2-phosphate, but devoid of dexamethasone [243, 244]. The medium was replenished every two days.

5.3.9. Live-dead assay

To examine viability and distribution of seeded cells within the macroporous matrices, live-dead staining was conducted. At 3 days post-seeding, the samples were cut into thin slices and washed with PBS. The slices were incubated in a staining solution containing 0.05% (v/v) green-fluorescent calcein-AM and 0.2% (v/v) red-fluorescent ethidium homodimer-1 in DMEM at 37 °C for 30 min according to the manufacturer's instructions (Life technologies, catalog # L-3224). The stained slices were washed with PBS and imaged using a fluorescence microscope (Carl Zeiss, Axio Observer.A1).

5.3.10. Critical-sized cranial bone defects

For *in vivo* study, 12 immunodeficient mice (NOD.CB17-Prkdcscid/J, approximately 3-month-old) were used with the approval of the Institutional Animal Care and Use Committee (IACUC) at the University of California, San Diego. Prior to surgery, the mice were administered with ketamine (Ketaset, 100 mg/kg) and xylazine (AnaSed, 10 mg/kg) through an intraperitoneal injection. The anesthetized mice were subject to 15 mm-long incision on their skin of parietal skull bones and cranial surface was gently scrapped to remove the periosteum. The exposed cranial bone on the underlying dura mater was removed in full thickness with 4 mm in diameter to create critical-sized cranial bone defects [245]. Two cranial bone defects were created in left and right parietal skull bones in each mouse. Acellular and Ad-hiPSC-laden macroporous matrices (4 mm in diameter and 0.7 mm in thickness) cultured for 1 week *in vitro* and implanted into the defects. A sham control was also included for the defects that received no treatment. The skin of parietal skull bones was then carefully sutured. After the surgery, the mice were housed in separate cages and sacrificed after 4 and 16 weeks of implantation.

5.3.11. Micro-computed tomography (μCT)

μCT was used to examine the hard tissue formation both *in vitro* and *in vivo*. The *in vitro* cultured constructs and parietal skull bones including calvarial bone defects were fixed in 4% paraformaldehyde at 4 °C for 5 days and washed with PBS. The fixed samples were tightly packed between styrofoam spacers in 50 mL centrifuge tubes containing wet tissue wipes to maintain the hydration of the samples. The samples were scanned by using SkyScan 1076 μCT scanner (Bruker; pixel resolution: 9 μm, 50 kV, Al filter). The scanned images were reconstructed by using NRecon software (SkyScan, Bruker). The reconstructed images were assembled into 3-D models by using CT Analyser software (SkyScan, Bruker) or converted into 2-D cross-sectional images in coronal, transaxial, and sagittal planes of the matrices by using DataViewer software

(SkyScan, Bruker). To selectively account for positive signals from the calcified tissue, background signals were uniformly subtracted from the reconstructed images of all groups by applying a thresholding range of 90-255. Using 3-D models, mineral density within the matrices was quantified and presented as a percentage of bone volume per total volume (BV/TV).

5.3.12. Preparation for histological analysis

To perform histological analysis, paraffin-embedded sections were prepared as previously reported [145]. Briefly, the *in vitro* cultured matrices and parietal skull bones including the neobone tissue within calvarial bone defects were fixed in 4% paraformaldehyde at 4 °C for 5 days and washed with PBS for 6 h. The fixed samples were decalcified in 10% ethylenediaminetetraacetic acid (EDTA, pH = 7.3) at 4 °C for 2 weeks and washed with PBS for 6 h. The decalcified samples were dehydrated, equilibrated in Citrisolv, and incubated in a molten mixture of 95% (w/w) paraffin and 5% (w/w) poly(ethylene-*co*-vinyl acetate) (Sigma Aldrich, catalog #: 437220) at 70 °C under vacuum for 24 h. The paraffin-embedded samples were sliced into 10 µm-thick sections using a rotary microtome (Leica, RM2255). Prior to staining, the sections were deparaffinized in Citrisolv for 15 min and rehydrated.

5.3.13. Histochemical staining and histomorphometry

For H&E staining, the rehydrated sections were incubated in hematoxylin solution (Ricca, catalog #: 3536-16) for 7 min and washed with DI water. The sections were then immersed in Eosin-Y solution (Richard-Allan Scientific, catalog #: 7111) for 1 min and washed with DI water. The stained sections were dehydrated and imaged in a color mode under H filter. The stained images were stitched to acquire a continuous view of whole calvarial bone defects integrated with the native bone.

For histomorphometrical analysis, six representative H&E-stained images were selected (n=6) and the areal sum of engineered bone as well as defect area were quantified by using ImageJ. The areal density of the newly formed bone was presented as a percentage of bone area per defect area.

For tartrate-resistant acid phosphatase (TRAP) staining, a staining solution was formulated by following a manufacturer's protocol (Acid Phosphatase kit, Sigma-Aldrich, catalog # 387A). Briefly, 50 µL of Fast Garnet GBC base solution and 50 µL of sodium nitrite solution were mixed. After 2 min, the mixture was added into 4.5 mL of DI water prewarmed to 37 °C. To this solution, 50 µL of Naphthol AS-Bl phosphate solution, 200 µL of acetate solution, and 100 µL of tartrate solution were sequentially added to yield the staining solution. The rehydrated sections were incubated in the staining solution at 37 °C for 1 h while protecting from light. The stained sections were washed with DI water, dehydrated, and imaged in a color mode under H filter.

5.3.14. Immunohistochemical staining

The rehydrated sections were treated in 20 µg/mL proteinase K (Invitrogen, catalog #: 100005393) in a mixture of 95% (v/v) TE buffer (50 mM Tris-HCl, 1 mM EDTA, and 0.5% [v/v] Triton X-100; pH = 8.0) and 5% (v/v) glycerol at 37 °C for 15 min and washed with PBS. The treated sections were immersed in a blocking solution containing 3% (v/v) normal goat serum and 0.1% (v/v) Triton X-100 in PBS at 25 °C for

1 h and incubated with primary antibodies against osteocalcin (1:100, rabbit, Abcam, catalog # ab93876) or type X collagen (1:50, rabbit, Fitzerald, catalog # 20R-CR030) in the blocking solution at 4 °C for 16 h. The sections were washed with PBS and treated with 3% (v/v) hydrogen peroxide for 7 min and washed with PBS. The treated sections were incubated with horseradish peroxidase (HRP)-conjugated secondary antibody (1:200, donkey anti-rabbit, Jackson ImmunoResearch, catalog # 711-035-152) in the blocking solution at 25 °C for 60 min and washed with PBS. The sections were developed in 3-3' diaminobenzidine (DAB) substrate solution (Vector Laboratories, catalog # SK-4100) for 3 min. The stained sections were washed with PBS, dehydrated, and imaged in a color mode under H filter. The stained images for osteocalcin were stitched to show the continuous view of whole calvarial bone defects integrated with the surrounding native bone.

5.3.15. Immunohistofluorescent staining

The rehydrated sections were treated with 20 µg/mL proteinase K in TE buffer at 37 °C for 15 min and washed with PBS. The treated sections were permeabilized in 0.1% (v/v) Triton-X in PBS at 25 °C for 4 min and washed with PBS. The permeabilized sections were further treated in 2.5 mg/mL sodium borohydride (Fisher Scientific, catalog # 16940-66-2) in 50% EtOH at 25 °C for 30 min and washed with PBS. The treated sections were immersed in a blocking solution of 10% (v/v) donkey serum in PBS at 25 °C for 60 min. The sections were incubated in primary antibodies against lamin A/C (1:100, rabbit, Abcam, catalog # ab108595), osteocalcin (1:100, mouse, Santa Cruz Biotechnology; catalog # sc-74495), or CD31 (Platelet endothelial cell adhesion molecule

[PECAM-1], 1:100, goat, Santa Cruz Biotechnology, catalog # sc-1506) in the blocking solution at 4 °C for 16 h and washed with PBS. The sections were then incubated in secondary antibodies raised against rabbit (1:200, goat anti-rabbit, Life Technologies, Alexa Fluor 488, catalog # A11008), mouse (1:200, goat anti-mouse, Life Technologies, Alexa Fluor 568, catalog # A11004), or goat (1:200, donkey anti-goat, Jackson ImmunoResearch, Allophycocyanin, catalog # 705-136-147) as well as 2 µg/mL Hoechst 33342 (Life Technologies, catalog # H1399) in the blocking solution at 25 °C for 60 min and washed with PBS. The stained sections were imaged under confocal fluorescence microscope (Olympus FluoView FV1000). All images were taken using the same exposure time. The background was uniformly subtracted for all images using ImageJ software by applying a rolling ball algorithm (rolling ball radius: 750 pixels).

5.3.16. Statistical analysis

All experiments were repeated independently at least twice in addition to the triplicates used in each experiment. Using Graphpad Prism 5, statistical significances were considered for *p*-values less than 0.05. Two-tailed Student's t-test was used to compare two groups at the same time point. One-way analysis of variance (ANOVA) including Tukey-Kramer post-hoc test was employed to compare multiple groups at the same time point. Two-way ANOVA including Bonferroni post-hoc test was used to compare multiple groups across different time points.

5.4. Results

5.4.1. Exogenous adenosine-driven osteogenic differentiation of hPSCs.

Human induced pluripotent stem cells (hiPSCs) were seeded onto Matrigel-coated coverslips and cultured in either growth medium or growth medium supplemented with adenosine. The hiPSCs cultured in conventional osteogenic induction medium was used as a positive control. Previous studies have shown that hPSCs cultured in osteogenic induction medium undergo osteogenesis [138]. hiPSCs in all cultures grew to confluence within 10 days with no significant differences irrespective of the difference in medium compositions (Figure 5.S1a). Analysis of gene expression profile at 21 days of culture showed considerable upregulation of various genes relevant to osteogenesis in cells exposed to exogenous adenosine and osteogenic induction medium (Figure 5.1a). Osteogenic differentiation of hiPSCs was further evaluated through time-resolved quantitative analyses for various genes (RUNX2, OCN, and SPP1) relevant to cells undergoing osteogenesis. The qPCR analyses showed that hiPSCs cultured in presence of exogenous adenosine, similar to osteogenic induction medium, consistently exhibited an upregulation of RUNX2, OCN, and SPP1 expressions throughout 21 days of culture (Figure 5.1b). The hiPSCs, cultured under all medium conditions, showed downregulation of NANOG (a pluripotency marker), suggesting that the hiPSCs in all cultures lost pluripotency irrespective of whether the hiPSCs underwent osteogenic differentiation or not (Figure 5.1b).

In addition to gene expression profile, the conversion of hiPSCs into osteoblasts was evaluated by immunofluorescent staining for osteocalcin (an osteoblast-specific marker). In accordance with upregulated levels of osteogenic gene expression, hiPSCs cultured in presence of adenosine and osteogenic induction medium stained positive for osteocalcin in a majority of cells after 21 days of culture, suggesting the differentiation of hiPSCs into osteoblasts (Figure 5.1c). F-actin and nuclear staining of hiPSCs are also shown. The intensity of osteocalcin expression for hiPSCs undergoing osteogenic differentiation was also found to gradually increase with culture time (Figures 5.1c, 5.S3). No such osteocalcin expression was found for hiPSCs cultured in growth medium despite their loss of pluripotency.

To further confirm osteoblastic differentiation of hiPSCs, we examined the calcification of hiPSC cultures by staining for Alizarin Red S. hiPSCs cultured in both adenosine-supplemented growth medium as well as osteogenic-inducing medium exhibited positive Alizarin Red S staining after 21 days of culture (Figure 5.1c). The intensity for Alizarin Red S staining was found to become progressively prevalent with culture time (Figures 5.1c, 5.S3). Similar to osteocalcin staining, no calcification was observed for hiPSCs cultured in growth medium. Taken together, the results suggest the potent role of adenosine in directing osteogenic differentiation of hiPSCs.

Similar to hiPSCs, hESCs cultured in presence of osteogenic induction medium and growth medium supplemented with adenosine (Figure 5.S1b) underwent osteogenic differentiation. hESCs cultured in growth medium supplemented with adenosine as well as osteogenic induction medium consistently upregulated various osteogenic markers (Figure 5.S2a). In addition to gene expression, the cell cultures also stained positive for osteocalcin and exhibited accumulation of calcium (Figure 5.S2b).

5.4.2. Adenosine-stimulated osteogenesis of hPSCs involves A2bR signaling.

The effect of exogenous adenosine on hiPSCs and hESCs was examined for various adenosine receptor subtypes, A1R, A2aR, A2bR, and A3R. Both hiPSCs and hESCs cultured in adenosine-supplemented growth medium exhibited significant upregulation of A2bR expression (Figures 5.2a, 5.S4a). In contrast, no considerable differences in the expression of other genes, such as A1R, A2aR, or A3R were observed for the cells cultured in exogenous adenosine. Unlike cells in medium supplemented with adenosine, no consistent upregulation of any adenosine receptor subtypes was observed in the cells cultured in growth or osteogenic medium.

In order to verify the role of A2bR, if any, on adenosine-mediated osteogenic differentiation of hPSCs, we used A2bR antagonist, 8-[4-[4-(4-chlorophenzyl)piperazide-1-sulfonyl)phenyl]]-1-propylxanthine (PSB 603). Interestingly, the presence of PSB603 in hPSC cultures resulted in the downregulation of osteogenic markers that were otherwise upregulated in presence of exogenous adenosine (Figures 5.2b, 5.S4b). Consistent with other cultures, hPSCs cultured in presence of PSB 603 also showed downregulation of NANOG (Figures 5.2b, 5.S4b). The PSB 603-mediated attenuation of osteogenic differentiation was further confirmed by immunofluorescent staining for osteocalcin. The prevalence of osteocalcin protein observed in hPSCs (in exogenous adenosine) was significantly diminished in presence of PSB 603 (Figures 5.2c, 5.S4c). Inhibition of adenosine-mediated osteogenic differentiation of hPSCs, by blocking A2bR signaling, was further supported by Alizarin Red S staining, which showed significant reduction in calcification in presence of PSB 603 (Figures 5.2c, 5.S4c).

5.4.3. Bone tissue formation in vitro by hiPSC-derived osteoblasts.

Having established the ability of adenosine to direct osteogenic commitment of hPSCs, we next determined the bone tissue-forming ability of hiPSC-derived osteoblasts; hereafter named as Ad-hiPSCs. The hiPSCs were cultured in presence of exogenous adenosine for 21 days and the differentiated cells were loaded into poly(ethylene glycol) diacrylate-*co*-acryloyl 6-aminocaproic acid (PEGDA-*co*-A6ACA) macroporous hydrogels (Figures 5.S5a, 5.S6a). The hiPSCs cultured for 21 days under identical conditions but without being exposed to exogenous adenosine were used as a control; hereafter termed as d-hiPSCs. The schematic in Figure 5.3a reveals the experimental procedures.

After 3 days of cell seeding, live-dead staining showed that the cells were viable and homogeneously distributed within the macroporous matrices (Figures 5.S5b, 5.S6b). The gross appearance of the cell-laden matrices as a function of culture time revealed gradual build-up of calcification for cell-laden matrices involving Ad-hiPSCs (Figure 5.S5c). No such calcification or hard tissue formation was observed with cell-laden matrices that utilized d-hiPSCs. 3-D μCT images of the Ad-hiPSC-laden matrices showed progressive formation of calcified tissue throughout 3 weeks of culture (Figure 5.3b). In stark contrast, the matrices containing d-hiPSCs showed slight mineralization along the periphery of the matrices. Quantification of hard tissue formation from the 3-D μCT images corroborated the observations with significantly higher mineral density for the matrices containing Ad-hiPSCs as compared to d-hiPSCs (Figure 5.3c). 2-D cross-sectional images of the matrices containing Ad-hiPSCs, in three perpendicular planes, showed uniform hard tissue formation throughout the porous matrices after 3 weeks of culture (Figure 5.S5d).

Histological examination of the calcified tissues was performed to determine the formation of bone tissue. H&E staining showed the presence of dense extracellular matrix (ECM) resembling bone tissue for the cultures containing Ad-hiPSCs following 3 weeks of culture, while the cultures involving d-hiPSCs displaying minimal ECM deposition of such features (Figure 5.3d). The bone tissue formation was also confirmed by immunohistochemical staining for osteocalcin. The constructs involving Ad-hiPSCs were found to progressively develop osteocalcin-rich ECM over the course of 3 weeks (Figure 5.3d). On the contrary, minimal osteocalcin staining was observed in the cell-laden matrices containing d-hiPSCs.

5.4.4. hiPSC-derived osteoblasts participate in healing critical-sized defects.

The ability of hiPSC-derived osteoblasts (Ad-hiPSCs) to contribute to bone tissue repair was examined by using critical-sized cranial bone defects in mice. Ad-hiPSC-laden PEGDA-*co*-A6ACA matrices were cultured for 1 week prior to their implantation. µCT analyses of these cell-laden matrices prior to implantation indicated minimal hard tissue formation (Figure 5.S6c). The *in vivo* bone tissue formation of Ad-hiPSC-laden matrices was compared to those with acellular matrices and sham group. Bone tissue formation at 4 and 16 weeks post-implantation was evaluated through µCT analyses that showed formation of hard tissue in the defects treated with Ad-hiPSC-laden matrices (Figures 5.4a, 5.S7a). The newly formed hard tissue was found to cover the entire defect. On the contrary, minimal to no hard tissue formation was observed in sham control and the defects treated with acellular matrices exhibited partial calcification. Quantification of µCT images showed significantly increased hard tissue formation in the defects treated with Ad-hiPSCs compared to sham and acellular controls, with bone volume reaching similar to that of native bone by 16 weeks (Figure 5.4b).

H&E and osteocalcin staining, at 4 and 16 weeks post-treatment, confirmed the presence of neo-bone tissue in defects treated with Ad-hiPSCs (Figures 5.4c, 5.S7b). H&E-stained images of the tissue at 16 weeks showed formation of matured bone with osteocytes embedded in mineralized matrix resembling the morphology of native bone. The neo-bone tissue was also characterized by osteocalcin-rich ECM. Compared to Ad-hiPSCs, sham and acellular control groups showed minimal bone formation nonhomogeneously distributed within the defects. In contrast, the defects treated with Ad-hiPSCs showed homogenous bone tissue formation throughout the cranial defect. The neo-bone tissue was also found to be integrated with adjoining native bone. Together, the findings suggest complete healing of the defects treated with Ad-hiPSCs. The excised implants stained for type X collagen, a marker for hypertrophic cartilage, showed their absence across all groups at 4 and 16 weeks post-implantation (Figure 5.S9).

Histomorphometrical analysis of H&E-stained images corroborated the aforementioned observations that the defects treated with Ad-hiPSCs exhibiting significantly higher bone content compared to acellular and sham groups (Figure 5.4d). No evidence of teratoma formation or inflammation was observed in any of the animals treated with Ad-hiPSCs.

To determine the contribution of transplanted Ad-hiPSCs towards neo-bone tissue, human-specific lamin A/C staining was performed. Immunofluorescent staining of the newly formed bone with Ad-hiPSCs at 4 and 16 weeks post-implantation showed the colocalization of osteocalcin and human-specific lamin A/C (Figures 5.5a, 5.S8a). The new bone tissue was also filled with cells, which were positive for osteocalcin, but negative for lamin A/C, suggesting the contribution of host cells towards the formation of neo-bone tissue. Osteocalcin-positive cells were found in the defects treated with acellular matrices and sham group, indicating the infiltration of host cells into the implanted matrices and defect sites.

Not only that the transplanted cells survived and contributed to bone tissue formation, the cell-laden matrices also recapitulated vascular connections with the host tissue. The cell-laden matrices were permeated with intraluminal red blood cells (Figure 5.4c). Staining the implanted sections with platelet endothelial cell adhesion molecule antibody (CD31 also known as PECAM-1) further demonstrated the presence of vessels within the macroporous structures (Figures 5.5b, 5.S8b). The cell-laden implants also stained positive for tartrate-resistant acid phosphatase (TRAP) at 4 and 16 weeks post-treatment (Figures 5.5b, 5.S8b). Positive TRAP stains suggest presence of osteoclast-like cells within the regenerated bone tissue.

5.5. Discussion

Small molecule-directed differentiation of human pluripotent stem cells (hPSCs) could significantly contribute to their applications. Small molecules, which can be readily synthesized and remain relatively stable compared to growth factors, offer a simple, reproducible, and cost-effective strategy to generate large numbers of hPSC-derivatives.

In this study, we discuss the potential of exogenous adenosine to derive functional osteoblasts from hPSCs. Adenosine is a naturally occurring molecule, a purine nucleoside, which is a metabolite of ATP. Adenosine is known to play a number of physiological and pharmacological functions and has been used as a neuromodulator and vasodilator [246-249].

Consistent with previous findings, hESCs and hiPSCs cultured in the absence of soluble factors, such as basic fibroblast growth factor (bFGF) showed loss of pluripotency [250]. However, only the cells cultured in medium containing exogenous adenosine underwent osteogenic differentiation. Concomitant with undergoing osteoblastogenesis, the hPSCs cultured in exogenous adenosine showed an upregulation of adenosine A2b receptor (A2bR). A pharmacological inhibition of A2bR attenuated adenosine-induced osteogenic differentiation of the cells. Taken together, the data suggest the role of A2bR signaling in adenosine-induced osteogenic differentiation of hPSCs. This is in accordance with our prior studies that have discovered the pivotal role of A2bR in calcium phosphate biomaterial-mediated osteogenic differentiation of hMSCs and hESCs [39, 251]. There also exist a few studies reporting functionally dominant role of A2bR over other adenosine receptors in MSCs undergoing osteogenic differentiation [208, 252]. It was also reported that A2bR knockout mice exhibited lower bone development and delayed fracture repair compared to wild type mice [207].

The osteogenic cells derived from hiPSCs resulted in 3D bone tissue formation *in vitro* even in the absence of any osteoinductive molecules in culture medium. We chose macroporous PEGDA-*co*-A6ACA matrices as a scaffold (or artificial matrix) for both *in vitro* and *in vivo* bone tissue formation. Our previous studies showed that these macroporous matrices do not intrinsically possess any osteoinductivity [70, 77]. In addition to *in vitro* bone tissue formation, when implanted *in vivo*, the Ad-hiPSCs contributed to tissue repair through the regeneration of bone tissue integrated with adjacent native bone tissues. Further, the infiltrated host cells also contributed to bone tissue formation. Thus formed bone tissue resembled native bone tissue in morphology and mineral density by 16 weeks. However, as evident from the acellular control, the infiltration of host cells alone was not adequate to achieve homogeneous bone formation and complete healing of the defect.

Vascularization of the implant and the engineered tissue plays an important role in the survival of the transplanted cells and the neo-bone tissue formation. The implants were permeated with host blood vessels. Vascularization of the implant could be attributed to the macroporous structure of the PEGDA-*co*-A6ACA matrices that readily allowed for the invasion of vascular endothelial cells, consistent with a prior finding [253]. The presence of intraluminal red blood cells in the implants suggests that neo-vessel within the implant had anastomosed with the host vasculature. The presence of vascular network within the implant has likely promoted the survival of the transplanted cells and also recruitment of endogenous cells. Detection of TRAP-positive osteoclastic cells within the engineered bone implies the initiation of bone resorption [9]. It was previously reported that osteoblasts not only produce monocyte chemoattractant protein-1 (MCP-1) to recruit osteoclastic precursors, but also express receptor activator of nuclear factor kappa-B ligand (RANKL) to activate osteoclastic cells [254]. Co-presence of bone-synthesizing osteoblasts and bone-resorbing osteoclasts within the newly regenerated bone tissue suggests plausible physiological remodeling of the tissue, a key feature of native bone.

5.6. Conclusion

In summary, this study demonstrates that adenosine alone can direct osteoblastic differentiation of human pluripotent stem cells, such as hESCs and hiPSCs in growth medium lacking any other osteoinductive factors. The adenosine-mediated osteogenic commitment of hPSCs was shown to be regulated by A2bR signaling. To our knowledge, this is the first demonstration for direct conversion of hPSCs into osteoblasts solely by a single small molecule. Furthermore, hiPSC-derived osteoblasts contributed to the repair of critical-sized bone defects through formation of de novo bone, which was integrated with surrounding native tissue without teratoma formation. A simple, cost-effective, and efficient osteogenic induction protocol involving adenosine will allow obtaining a large number of clinically viable therapeutic cells to treat critical bone defects.

5.7. Acknowledgements

This work was supported by National Institutes of Health (NIH; Grant 1 R01 AR063184-01A1).

Chapter 5, in full is currently being prepared for submission for publication of the material. “Small molecule-driven direct conversion of human pluripotent stem cells into functional osteoblasts”. Kang, Heemin; Shih, Yu-Ru V.; Nakasaki, Manando; Kabra,

Harsha; Gonzalez-Diaz, Eva; Varghese, Shyni. The dissertation author was the primary investigator and author of this material.

5.8. Figures

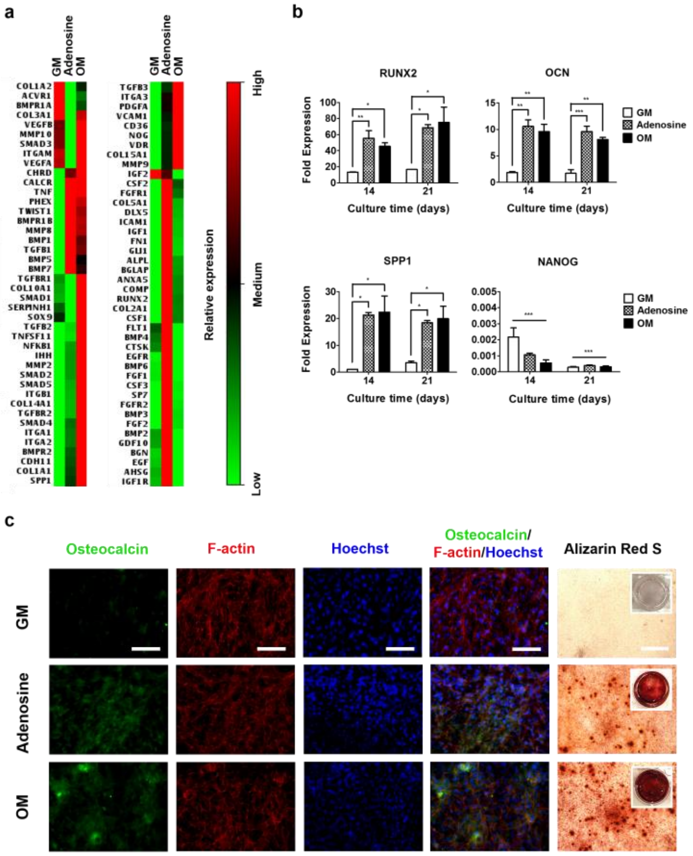

Figure 5.1. Adenosine induces osteogenic differentiation of hiPSCs.

(A) Transcription profile of 84 gene expressions relevant to osteogenic differentiation for hiPSCs cultured for 21 days in growth medium (GM), adenosine-supplemented growth medium (Adenosine), and osteogenic medium (OM). Relative expressions: red (high), black (medium), green (low). (B) Time-dependent quantitative gene expressions of hiPSCs for osteogenic markers (RUNX2, OCN, and SPP1) and pluripotent marker (NANOG) cultured in GM, Adenosine, and OM. (C) Staining of osteoblastic markers for hiPSCs cultured for 21 days in GM, Adenosine, and OM. Immunofluorescent staining of osteocalcin (green), F-actin (red), and nuclei (blue; Hoechst) as well as Alizarin Red S staining. Scale bars indicate 100 µm. Inset shows the stained images of whole wells. Data are presented as mean ± standard errors (n=3). Data are shown as fold expression of target genes after normalization to undifferentiated, pluripotent hiPSCs. For RUNX2, OCN, and SPP1, the groups with various medium conditions at the same culture time were compared by using one-way ANOVA with Tukey-Kramer post-hoc test. For NANOG, all the groups were compared to undifferentiated, pluripotent hiPSCs by two-way ANOVA with Bonferroni post-hoc test. Asterisks were assigned to *p*-values with statistical significances (*: $p < 0.05$; **: $p < 0.01$; ***: $p < 0.001$).

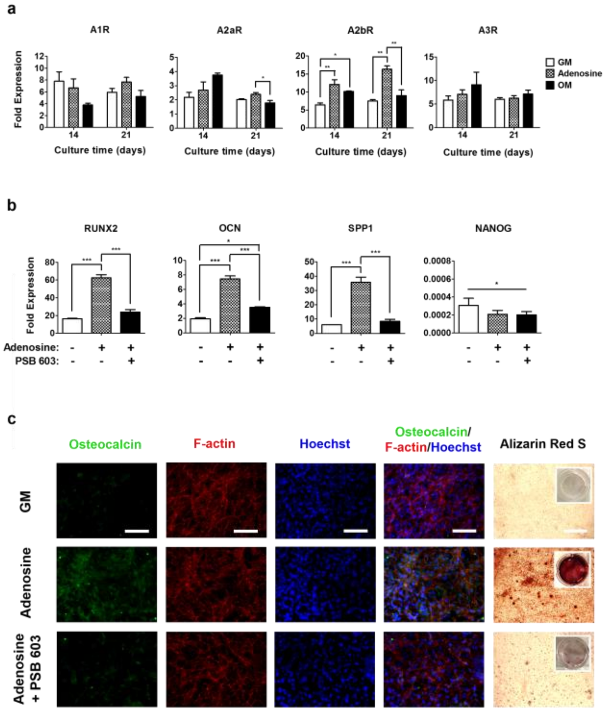

Figure 5.2. Adenosine-induced osteoblastic differentiation of hiPSCs is regulated by A2bR signaling.

(A) Time-dependent quantitative gene expressions of hiPSCs for adenosine receptor subtypes (A1R, A2aR, A2bR, and A3R) cultured in growth medium (GM), adenosine-supplemented growth medium (Adenosine), and osteogenic medium (OM). (B) Quantitative gene expression analysis of osteogenic markers (RUNX2, OCN, and SPP1) and pluripotent marker (NANOG) as well as (C) staining of osteoblastic markers for hiPSCs after 21 days of culture in presence and absence of adenosine and A2bR antagonist. The plus (+) and minus (-) symbols in gene expressions denote growth medium in presence and absence of adenosine and PSB 603 (A2bR antagonist), respectively. Immunofluorescent staining for osteocalcin (green), F-actin (red), and nuclei (blue; Hoechst) as well as Alizarin Red S staining. Various medium conditions include growth medium alone (GM) as well as growth medium in presence of adenosine (Adenosine) and co-presence of adenosine and PSB 603 (Adenosine + PSB 603). Scale bars indicate 100 μm. Inset shows the stained images of whole wells. Data are shown as mean ± standard errors (n=3). Data are presented as fold expression of target genes after normalization to undifferentiated, pluripotent hiPSCs. For A1R, A2aR, A2bR, and A3R as well as RUNX2, OCN, and SPP1, the groups with various medium conditions at the same culture time were compared by one-way ANOVA with Tukey-Kramer post-hoc test. For NANOG, all the groups were compared to undifferentiated, pluripotent hiPSCs by two-way ANOVA with Bonferroni post-hoc test. Asterisks indicate statistical significances according to *p*-values (*: $p < 0.05$; **: $p < 0.01$; ***: $p < 0.001$).

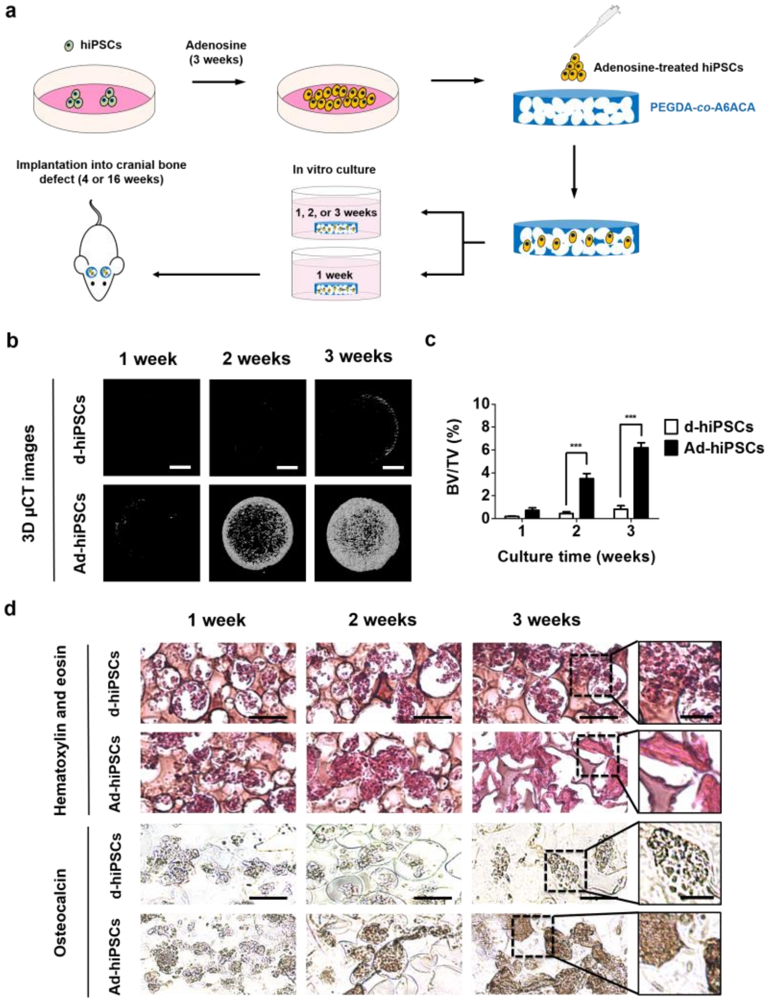

Figure 5.3. hiPSC-derived osteoblasts produce calcified bone tissue *in vitro*.

(A) Schematic for an experimental protocol used to examine bone-forming ability of hiPSC-derived osteoblasts within the macroporous matrices both *in vitro* and *in vivo*. (B) 3-D micro-computed tomography (µCT) images and (C) corresponding bone mineral densities (BV/TV: Bone volume/total volume) as well as (D) hematoxylin and eosin (H&E) staining and immunohistochemical staining for osteocalcin of the macroporous matrices containing non-adenosine-treated hiPSCs (d-hiPSCs) and adenosine-treated hiPSCs (Ad-hiPSCs) following 1, 2, and 3 weeks of *in vitro* culture. Scale bars in 3-D µCT images represent 2 mm. Scale bars in staining images indicate 100 µm. High magnification staining images are also provided. Scale bars represent 50 µm. Data are displayed as mean ± standard errors (n=4). Two groups at the same culture time were compared by two-tailed Student’s t-test. Asterisks indicate statistical significances according to *p*-values (**: $p < 0.01$).

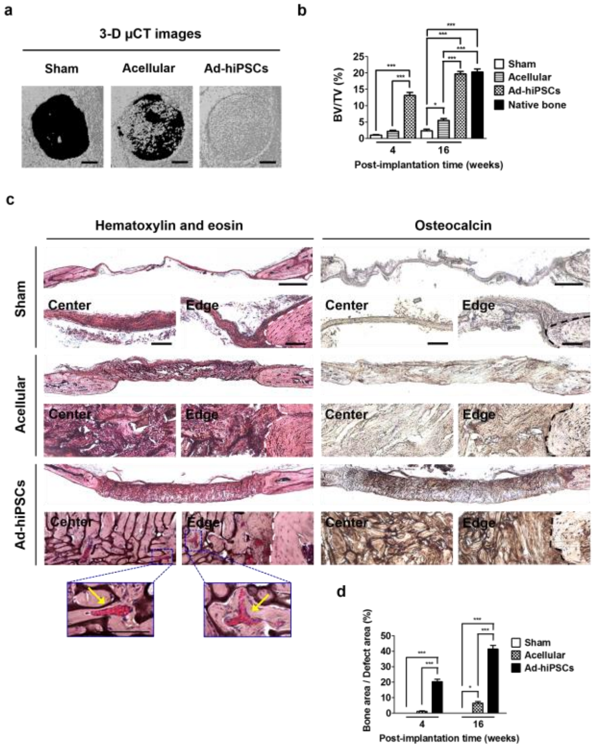

Figure 5.4. hiPSC-derived osteoblasts promote the healing of critical-sized bone defects through integrated bone formation *in vivo*.

(A) 3-D micro-computed tomography (µCT) images of cranial bone defects with no implantation (Sham) as well as implantation of the macroporous matrices alone (Acellular) or loaded with adenosine-treated hiPSCs (Ad-hiPSCs) following 16 weeks of *in vivo* implantation. Scale bars indicate 1 mm. (B) Bone mineral densities (BV/TV: Bone volume/total volume) within cranial bone defects for Sham, Acellular, and Ad-hiPSCs groups following 4 and 16 weeks of implantation. Native mouse cranial bone was used as a control. (C) Hematoxylin and eosin (H&E) staining and immunohistochemical staining for osteocalcin of cranial bone defects for Sham, Acellular, and Ad-hiPSCs groups after 16 weeks of implantation. Scale bars represent 500 µm. High magnification images show the center and edge of cranial bone defects. White and black dotted lines at the defect edge indicate the interface between engineered tissue within the bone defect and adjoining native bone tissue. Yellow arrows in H&E staining indicate microvessels containing red blood cells. Scale bars indicate 100 µm. (D) Histomorphometric analysis for neo-bone density within cranial bone defects (Bone area/Defect area) determined from H&E staining images for Sham, Acellular, and Ad-hiPSCs groups after 4 and 16 weeks of implantation. Data are shown as mean ± standard errors (n=6). Multiple groups at the same implantation time were compared by one-way ANOVA with Tukey-Kramer post-hoc test. Asterisks were assigned to p-values with statistical significances (*: $p < 0.05$; ***: $p < 0.001$).

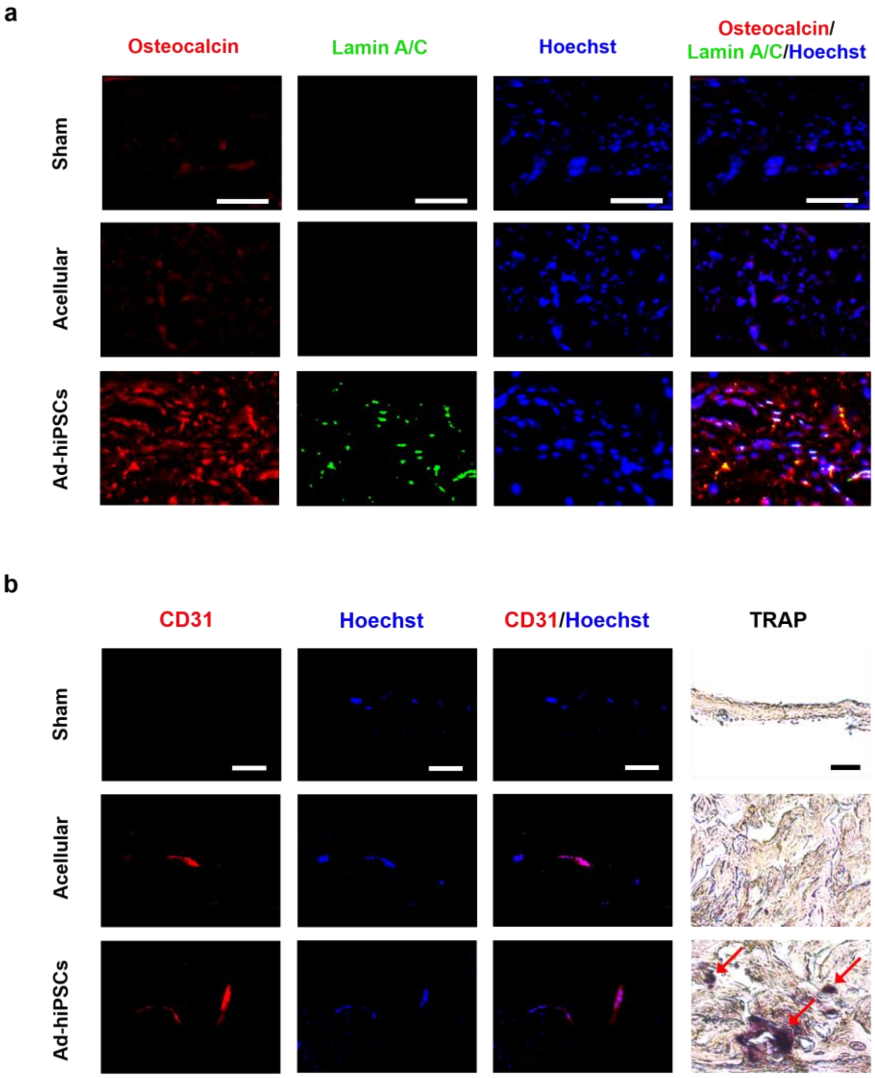

Figure 5.5. hiPSC-derived osteoblasts participate in the formation of neo-bone tissue that recapitulates vascular and bone-resorptive cells.

Immunofluorescent staining for (A) osteocalcin (red) and human-specific lamin A/C (green) and (B) CD31 (red) along with nuclei (blue; Hoechst) as well as tartrate-resistant acid phosphatase (TRAP) staining of calvarial bone defects with no implantation (Sham) as well as implantation of the macroporous matrices alone (Acellular) or seeded with adenosine-treated hiPSCs (Ad-hiPSCs) after 16 weeks of implantation. Red arrows indicate TRAP-positive stains. Scale bars represent 50 µm.

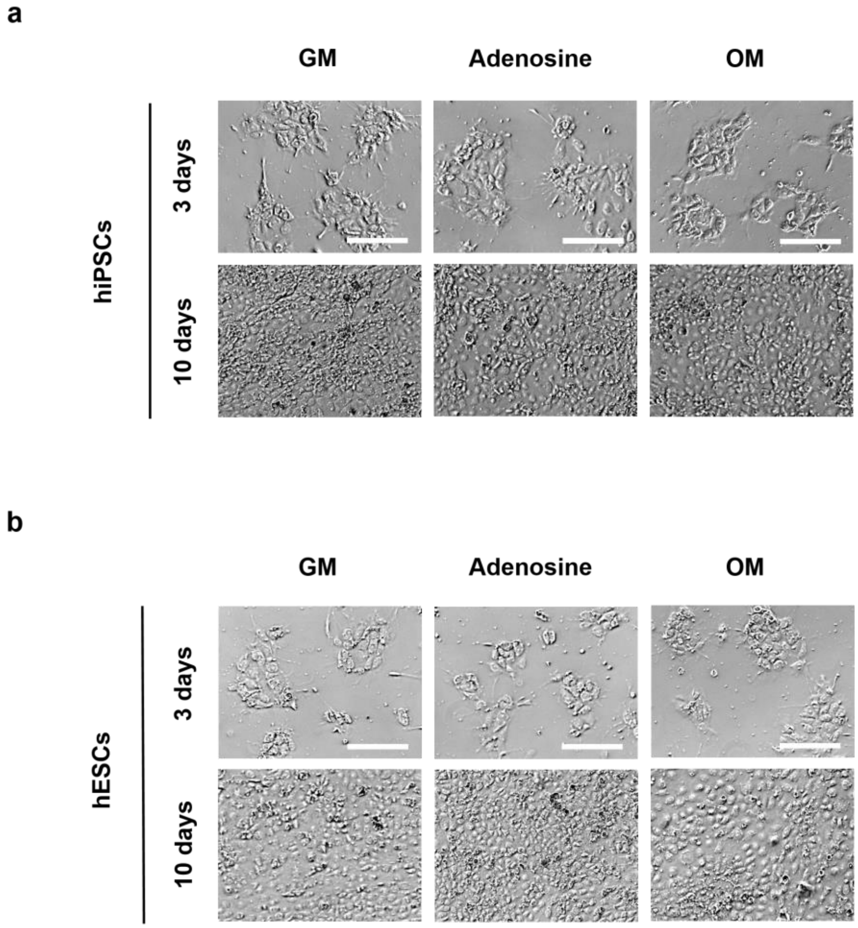

Figure 5.S1. Attachment and growth of hPSCs cultured under various medium conditions.

Bright-field images of (A) hiPSCs and (B) hESCs cultured for 3 and 10 days in growth medium (GM), growth medium supplemented with adenosine (Adenosine), and osteogenic-inducing medium (OM). Scale bars indicate 200 µm.

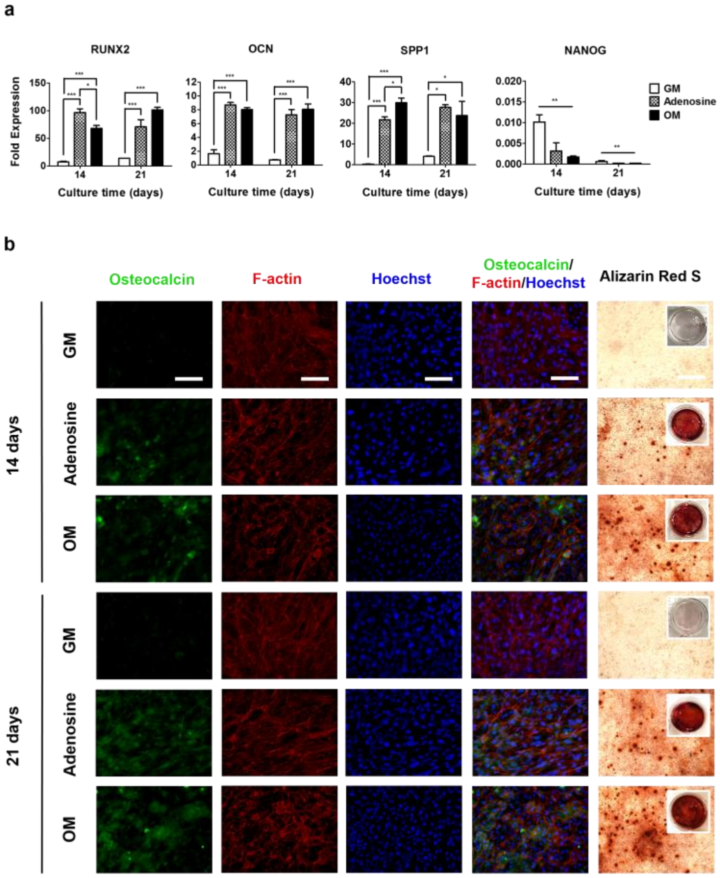

Figure 5.S2. Adenosine directs osteogenic differentiation of hESCs.

(A) Time-dependent quantitative gene expressions of hESCs for osteogenic markers (RUNX2, OCN, and SPP1) and pluripotent marker (NANOG) cultured in growth medium (GM), adenosine-supplemented growth medium (Adenosine), and osteogenic medium (OM). (B) Staining of osteoblastic markers for hESCs cultured for 14 and 21 days in GM, Adenosine, and OM. Immunofluorescent staining of osteocalcin (green), F-actin (red), and nuclei (blue; Hoechst) as well as Alizarin Red S staining. Scale bars indicate 100 µm. Inset shows the stained images of whole wells. Data are shown as mean ± standard errors (n=3). Data are presented as fold expression of target genes after normalization to undifferentiated, pluripotent hESCs. For RUNX2, OCN, and SPP1, the groups with various medium conditions at the same culture time were compared by using one-way ANOVA with Tukey-Kramer post-hoc test. For NANOG, all the groups were compared to undifferentiated, pluripotent hESCs by two-way ANOVA with Bonferroni post-hoc test. Asterisks indicate statistical significances according to *p*-values (*: $p < 0.05$; **: $p < 0.01$; ***: $p < 0.001$).

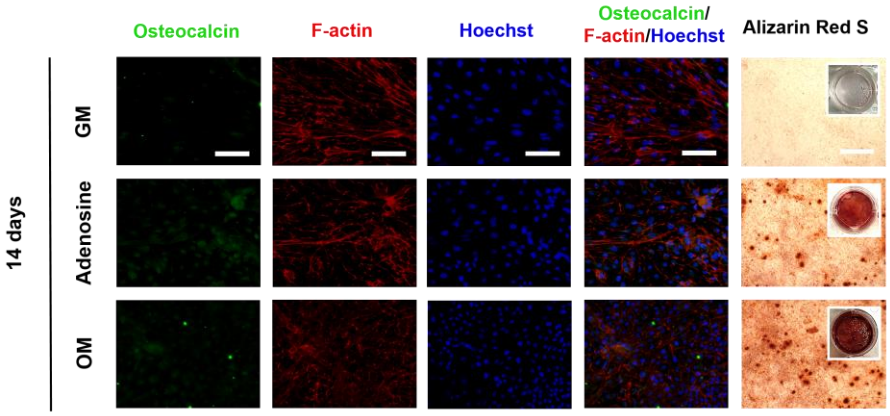

Figure 5.S3. Staining of osteoblastic markers for hiPSCs after their culture in various medium conditions.

hiPSCs were cultured in growth medium (GM), growth medium supplemented with adenosine (Adenosine), and osteogenic induction medium (OM). Immunofluorescent staining of osteocalcin (green), F-actin (red), and nuclei (blue; Hoechst) as well as Alizarin Red S staining for hiPSCs cultured for 14 days. Scale bars indicate 100 µm. Inset shows the stained images of whole wells.

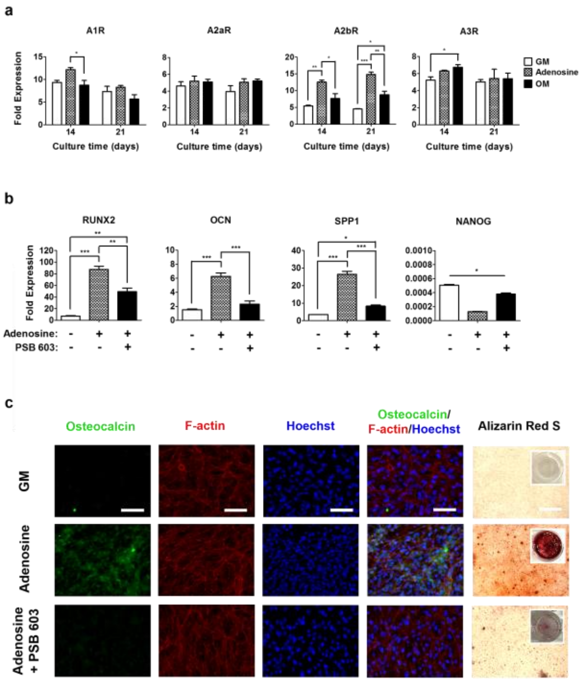

Figure 5.S4. Adenosine-directed osteoblastic differentiation of hESCs is mediated by A2bR signaling.

(A) Time-dependent quantitative gene expressions of hESCs for adenosine receptor subtypes (A1R, A2aR, A2bR, and A3R) cultured in growth medium (GM), adenosine-supplemented growth medium (Adenosine), and osteogenic medium (OM). (B) Quantitative gene expression analysis of osteogenic markers (RUNX2, OCN, and SPP1) and pluripotent marker (NANOG) as well as (C) staining of osteoblastic markers for hESCs after 21 days of culture in presence and absence of adenosine and A2bR antagonist. The plus (+) and minus (-) symbols in gene expressions denote growth medium in presence and absence of adenosine and PSB 603 (A2bR antagonist), respectively. Immunofluorescent staining for osteocalcin (green), F-actin (red), and nuclei (blue; Hoechst) as well as Alizarin Red S staining. Various medium conditions include growth medium alone (GM) as well as growth medium in presence of adenosine (Adenosine) and co-presence of adenosine and PSB 603 (Adenosine + PSB 603). Scale bars represent 100 µm. Inset shows the stained images of whole wells. Data are presented as mean ± standard errors (n=3). Data are shown as fold expression of target genes after normalization to undifferentiated, pluripotent hESCs. For A1R, A2aR, A2bR, and A3R as well as RUNX2, OCN, and SPP1, the groups with various medium conditions at the same culture time were compared by one-way ANOVA with Tukey-Kramer post-hoc test. For NANOG, all the groups were compared to undifferentiated, pluripotent hESCs by two-way ANOVA with Bonferroni post-hoc test. Asterisks were assigned to *p*-values with statistical significances (*: $p < 0.05$; **: $p < 0.01$; ***: $p < 0.001$).

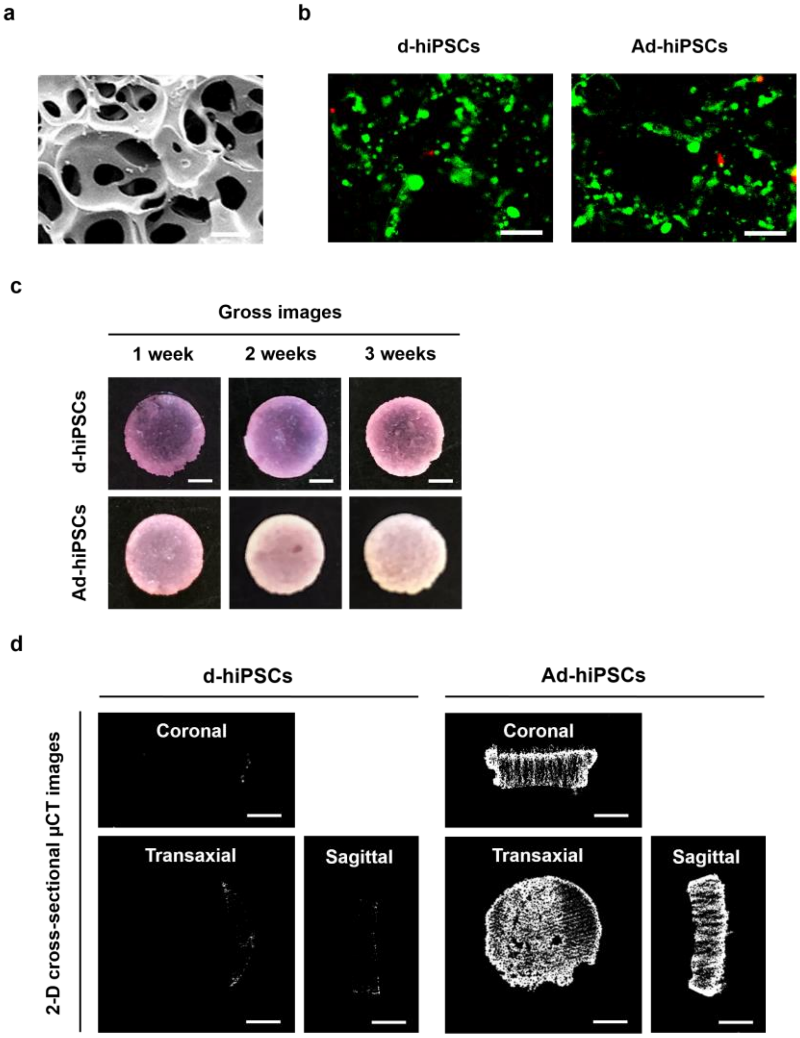

Figure 5.S5. Characterization of macroporous matrices and their use for *in vitro* culture of hiPSC-derived osteoblasts.

(A) Scanning electron microscopy (SEM) image of macroporous matrices prepared by using PMMA templates. Scale bar indicates 50 µm. (B) Fluorescent live-dead staining for non-adenosine treated hiPSCs (d-hiPSCs) and adenosine-treated hiPSCs (Ad-hiPSCs) seeded into the macroporous matrices after 3 days of *in vitro* culture. Scale bars represent 100 µm. (C) Gross morphology and (D) 2-D cross-sectional micro-computed tomography (µCT) images in coronal, transaxial, and sagittal planes of the macroporous matrices containing d-hiPSCs and Ad-hiPSCs after 1, 2, and 3 weeks of *in vitro* culture. Scale bars represent 2 mm.

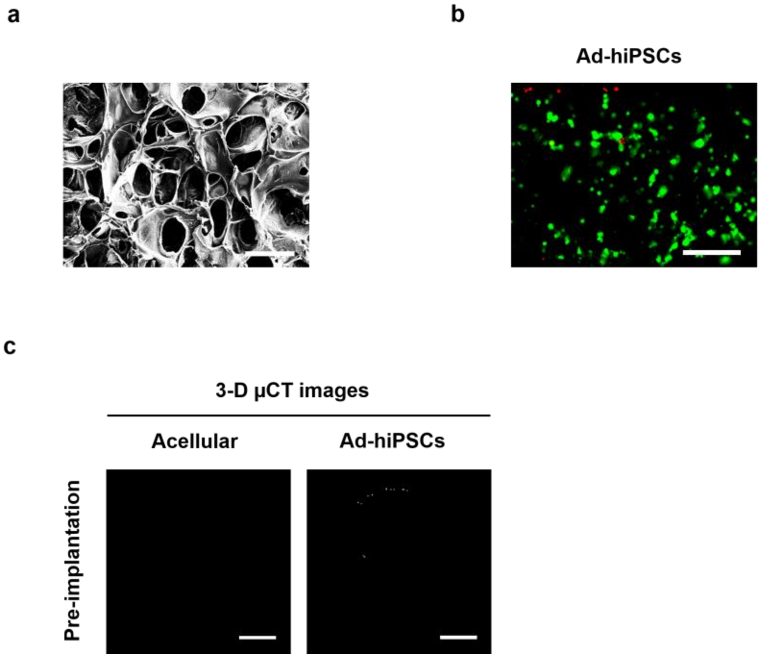

Figure 5.S6. Characterization of macroporous matrices and their use for transplantation of hiPSC-derived osteoblasts to treat critical-sized bone defects.

(A) Scanning electron microscopy (SEM) image of macroporous matrices prepared by cryogelation. Scale bar represents 50 μm. (B) Fluorescent live-dead staining for adenosine-treated hiPSCs (Ad-hiPSCs) seeded into the macroporous matrices after 3 days of *in vitro* culture. Scale bar indicate 100 μm. (C) 3-D micro-computed tomography (μCT) images of the macroporous matrices alone (Acellular) or loaded with Ad-hiPSCs after 1 week of *in vitro* culture, prior to *in vivo* implantation. Scale bars represent 1 mm.

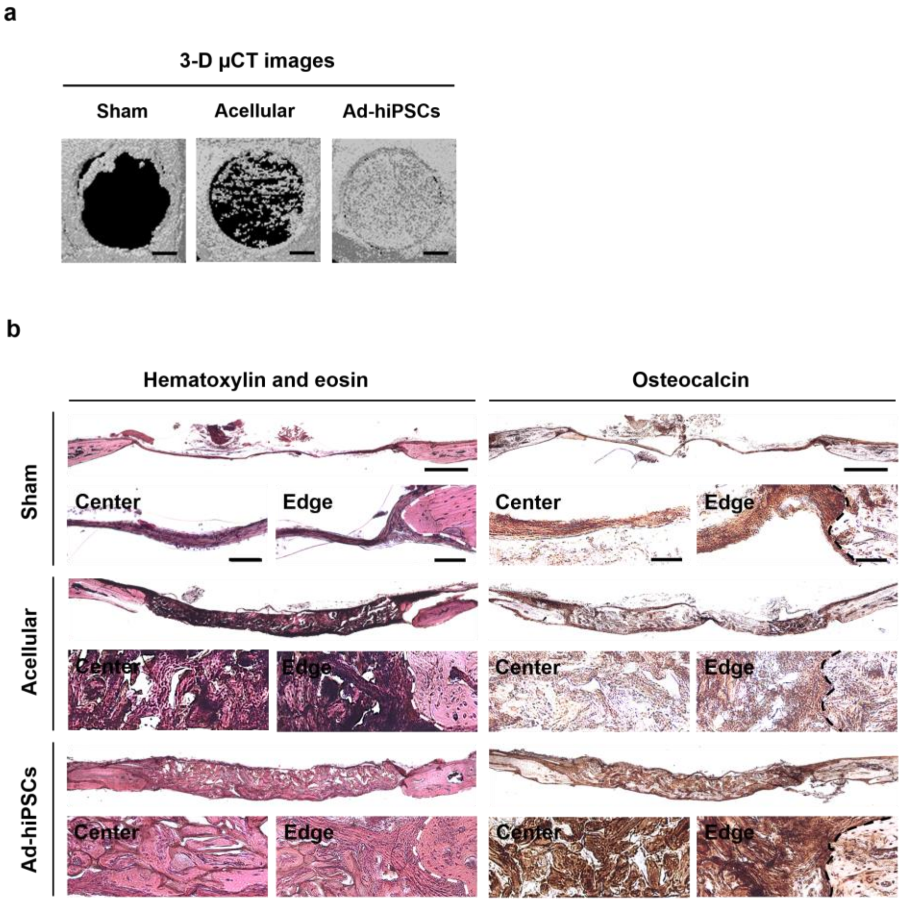

Figure 5.S7. hiPSC-derived osteoblasts facilitate the repair of critical-sized bone defects *in vivo*.

(A) 3-D micro-computed tomography (µCT) images and (B) hematoxylin and eosin (H&E) staining as well as immunohistochemical staining for osteocalcin of calvarial bone defects with no implantation (Sham) as well as implantation of the macroporous matrices alone (Acellular) or seeded with adenosine-treated hiPSCs (Ad-hiPSCs) following 4 weeks of *in vivo* implantation. Scale bars for 3-D µCT images indicate 1 mm. Scale bars for staining images represent 500 µm. High magnification images show the center and edge of calvarial bone defects. White and black dotted lines at the defect edge indicate the interface between engineered tissue within the bone defect and adjoining native bone tissue. Scale bars indicate 100 µm.

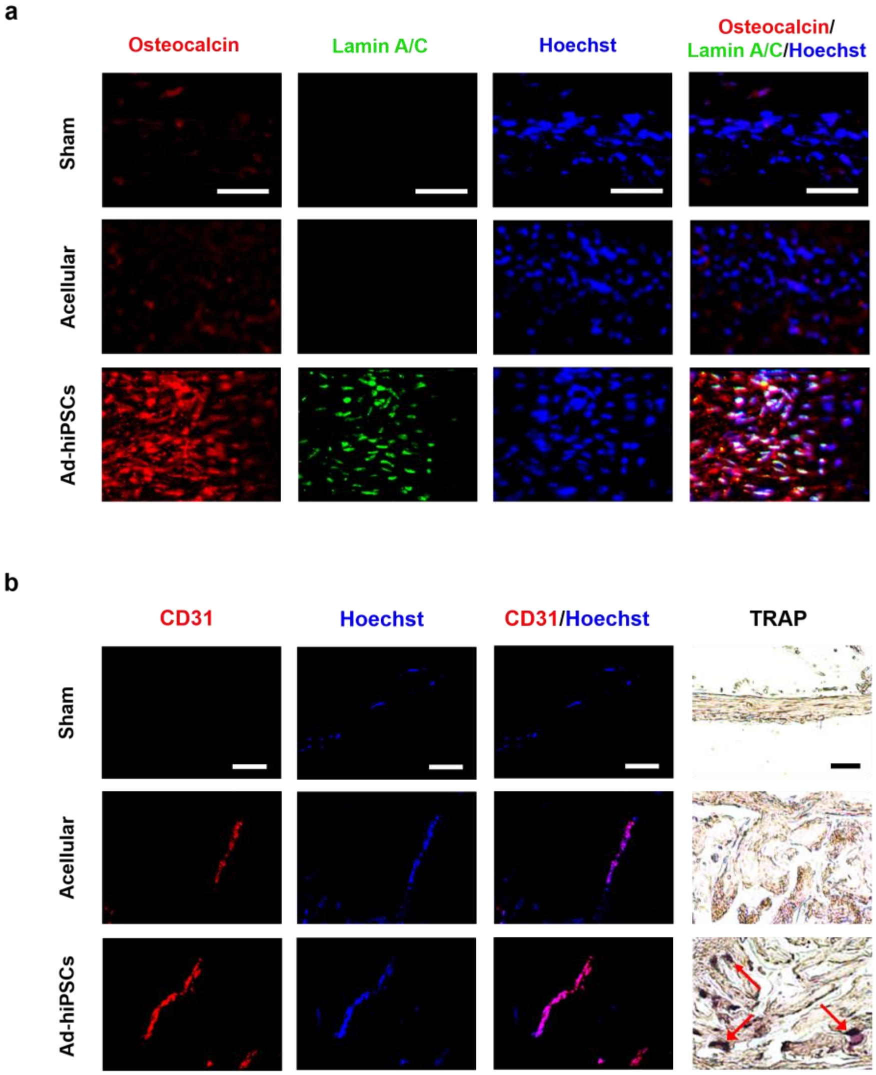

Figure 5.S8. hiPSC-derived osteoblasts contribute to the development of neo-bone tissue that recapitulates vascular endothelial and osteoclastic cells.

Immunofluorescent staining for (A) osteocalcin (red) and lamin A/C with human specificity (green) and (B) CD31 (red) along with nuclei (blue; Hoechst) as well as tartrate-resistant acid phosphatase (TRAP) staining of cranial bone defects with no implantation (Sham) as well as implantation of the macroporous matrices alone (Acellular) or loaded with adenosine-treated hiPSCs (Ad-hiPSCs) following 4 weeks of implantation. Red arrows indicate TRAP-positive stains. Scale bars indicate 50 µm.

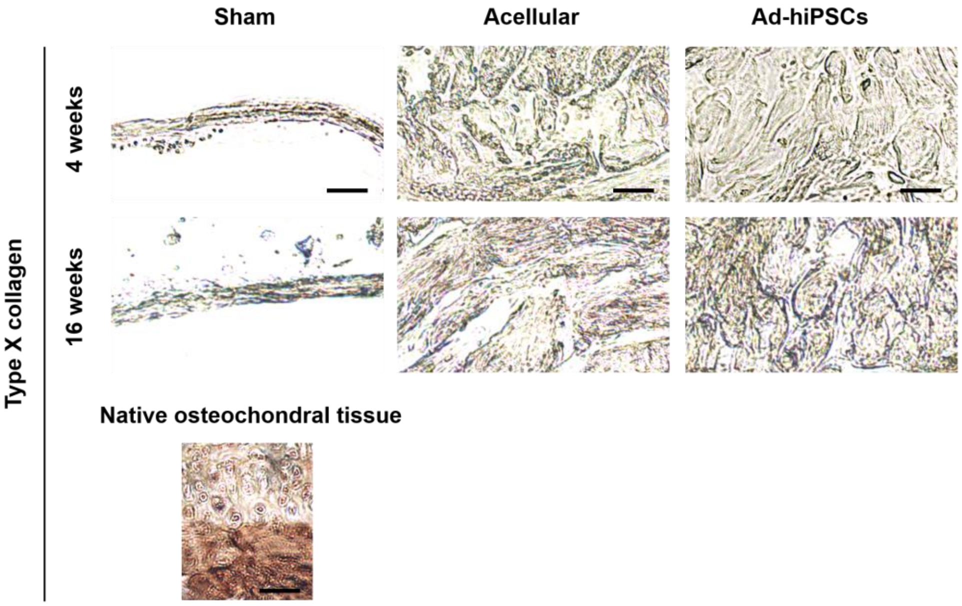

Figure 5.S9. Immunohistochemical staining for type X collagen after *in vivo* treatments.

Staining within cranial bone defects with no implantation (Sham) as well as implantation of the macroporous matrices alone (Acellular) or seeded with adenosine-treated hiPSCs (Ad-hiPSCs) after 4 and 16 weeks of implantation. Native mouse osteochondral tissue was used as a control. Scale bars represent 50 µm.

5.9. Tables

Table 5.S1. The list of primer sequences used for qPCR analysis.

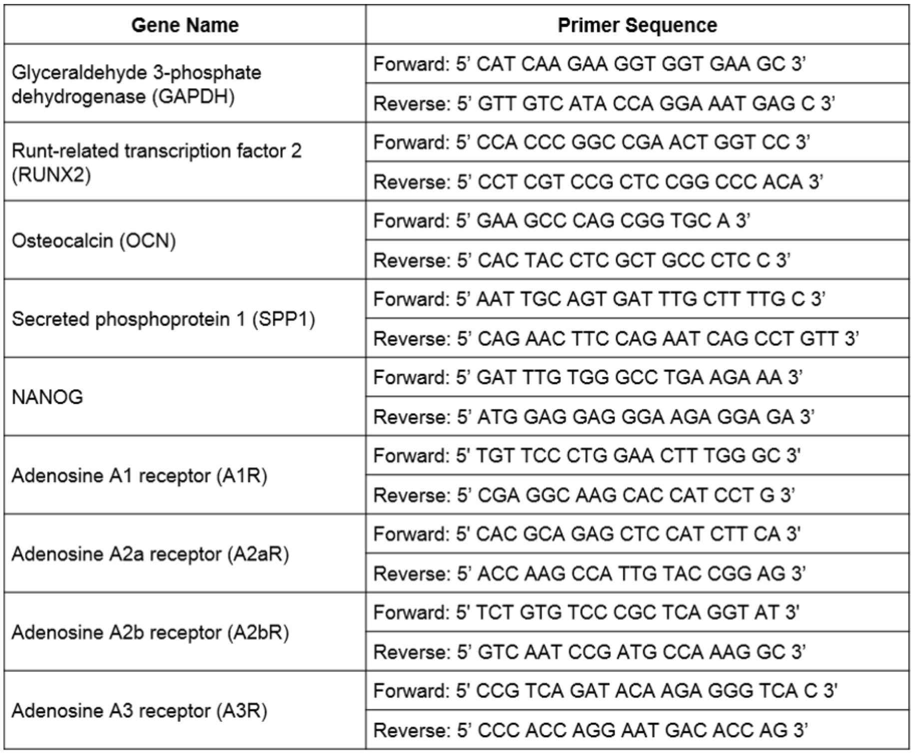

Gene Name	Primer Sequence
Glyceraldehyde 3-phosphate dehydrogenase (GAPDH)	Forward: 5’ CAT CAA GAA GGT GGT GAA GC 3’
	Reverse: 5’ GTT GTC ATA CCA GGA AAT GAG C 3’
Runt-related transcription factor 2 (RUNX2)	Forward: 5’ CCA CCC GGC CGA ACT GGT CC 3’
	Reverse: 5’ CCT CGT CCG CTC CGG CCC ACA 3’
Osteocalcin (OCN)	Forward: 5’ GAA GCC CAG CGG TGC A 3’
	Reverse: 5’ CAC TAC CTC GCT GCC CTC C 3’
Secreted phosphoprotein 1 (SPP1)	Forward: 5’ AAT TGC AGT GAT TTG CTT TTG C 3’
	Reverse: 5’ CAG AAC TTC CAG AAT CAG CCT GTT 3’
NANOG	Forward: 5’ GAT TTG TGG GCC TGA AGA AA 3’
	Reverse: 5’ ATG GAG GAG GGA AGA GGA GA 3’
Adenosine A1 receptor (A1R)	Forward: 5' TGT TCC CTG GAA CTT TGG GC 3'
	Reverse: 5’ CGA GGC AAG CAC CAT CCT G 3’
Adenosine A2a receptor (A2aR)	Forward: 5' CAC GCA GAG CTC CAT CTT CA 3'
	Reverse: 5’ ACC AAG CCA TTG TAC CGG AG 3’
Adenosine A2b receptor (A2bR)	Forward: 5' TCT GTG TCC CGC TCA GGT AT 3'
	Reverse: 5’ GTC AAT CCG ATG CCA AAG GC 3’
Adenosine A3 receptor (A3R)	Forward: 5' CCG TCA GAT ACA AGA GGG TCA C 3'
	Reverse: 5’ CCC ACC AGG AAT GAC ACC AG 3’

Chapter 6: In vivo engineering of stratified, integrated osteochondral tissue by trilayered scaffold with varying pore microstructure and osteoinductivity

6.1. Abstract

Osteochondral tissue consists of stratified organization of disparate cells and extracellular matrix (ECM) that determines its function. Simultaneous *in vivo* regeneration of integrated, distinct cartilage and bone tissue recapitulating stratified anatomical features of native tissue still remains a challenge. In this study, we developed monolithic trilayered hydrogel with superficial, columnar, and spongy layer to guide stratified, integrated osteochondral tissue formation. Specifically, bilayer containing columnar and spongy structure of pores was synthesized by sequential cryogelation. The spongy layer further recapitulated calcium phosphate (CaP)-rich bone-specific ECM through selective biomineralization. By employing the trilayered scaffold, we show that superficial and columnar layer with stratified microstructure conduced for human mesenchymal stem cells (hMSCs) to contribute to stratified cartilage formation *in vitro*, while acellular spongy layer lacked any tissue formation. Furthermore, the trilayered scaffold subcutaneously implanted into mice supported *in vivo* formation of stratified osteochondral tissue. The stratified neo-cartilage formed within the superficial and columnar layer through the contribution of hMSCs was found to be integrated with subchondral neo-bone formed within the biomineralized spongy layer through host cell recruitment. In particular, the superficial layer recapitulated lubricin, responsible for

lubricating function of cartilage. To our knowledge, this is the first demonstration for *in vivo* engineering of integrated osteochondral tissue recapitulating anatomical attributes of native tissue. Such multilayered biomaterials with unique, varying microstructure and tissue-specific inductivity that yield stratified, integrated osteochondral tissue *in vivo* hold great promise for treating osteochondral defects.

6.2. Introduction

Osteochondral tissue consists of cartilage and bone tissue with intricate arrangement of discrete cells and ECM that dictate its function [255-257]. Chondrocytes and osteoblasts are spatially organized within discrete, but integrated ECM. Human mesenchymal stem cells (hMSCs) are powerful cell sources to regenerate osteochondral tissue due to their ability to differentiate into tissue-specific cell types, including chondrocytes and osteoblasts [54, 258]. However, it remains a significant challenge to control simultaneous differentiation of stem and progenitor cells into disparate cell types in a spatially organized fashion to guide the growth of both cartilage and bone tissue.

Simultaneous regeneration of cartilage and bone tissue by using stem cells has been achieved through spatially controlled delivery of disparate soluble instructive factors, such as biochemicals [259], growth factors [260, 261], and genes [262] to induce their chondrogenesis and osteogenesis. Emerging studies showed that biomaterials emulating tissue-specific ECM can be designed with an ability to drive specialization of stem cells [160, 220, 263]. In particular, biomaterials recapitulating CaP-rich bone mineral environment were shown to direct osteogenic differentiation of stem cells *in vitro* and *in vivo* in the absence of any osteogenic-inducing factors [58-60, 70, 264, 265]. Furthermore, CaP-based biomaterials with macroporous structure exhibited an intrinsic ability to recruit endogenous cells, which could include stem and progenitor cells, and drive their osteogenesis for bone formation *in vivo* [55, 77, 266]. Such ability of CaP-based biomaterials could offer benefits in promoting the integration of subchondral bone to adjoining cartilage that has been reported to play an important role in the function of osteochondral tissue [267].

In addition to the integrated structure of cartilage and bone tissue, osteochondral tissue exhibits a stratified anatomy with zonal organization of cells and ECM that determines the function [255-257]. In the superficial zone of cartilage, collagen fibrils and lubricin with chondrocytes are oriented relatively parallel to the cartilage surface to resist friction. In the deep zone of cartilage, collagen fibrils are arranged in vertical columnar arrays, which integrate with subchondral bone. Recently, biomimetic approaches have led to designing biomaterials mimicking such stratified ECM arrangement of cartilage tissue [268-271]. For example, fibrous layer in multilayered biomaterials was designed to mimic horizontal alignment of collagen fibrils in the superficial zone of cartilage [269-271]. A recent study by Bhumiratana et al. showed that cartilage with stratified alignment of chondrocytes and ECM was engineered *in vitro*, which yielded biomechanical properties comparable to those of native cartilage [272]. However, to our knowledge, there are no reports showing *in vivo* engineering of stratified cartilage tissue integrated with subchondral bone recapitulating zonal organization of disparate cells and ECM.

In this study, we developed monolithic trilayered hydrogel recapitulating stratified pore microstructure through sequential cryogelation and spatially confined CaP minerals through templated biomineralization. By utilizing the trilayered scaffold containing stem cells, we demonstrate for the first time *in vivo* formation of stratified, integrated osteochondral tissue. Specifically, the varying microarchitecture in the superficial and columnar layer guided transplanted stem cells to contribute to stratified cartilage formation. Furthermore, the stratified neo-cartilage was integrated with subchondral spongy bone formed by recruited host cells into the acellular biomineralized spongy layer.

6.3. Materials and Methods

6.3.1. Synthesis of bilayered cryogel

Synthesis of poly(ethylene glycol)-diacrylate (PEGDA, Mn = 3.4 kDa) and N-acryloyl 6-aminocaproic acid (A6ACA) was carried out as previously described [199, 242]. Bottom and middle layer of trilayered hydrogel were prepared via consecutive cryogelation in the presence and absence of underlying ice template to modulate their pore directionality [77]. Bottom cryogel layer with isotropic, interconnected pores (referred to as spongy layer) was synthesized by dispensing 30 µL of chilled precursor solution containing 20% (w/v) PEGDA and 0.5 M A6ACA in 0.5 N NaOH with 0.5% (w/v) ammonium persulfate (APS) and 0.2% (v/v) N, N, N’-N’-tetramethylethylenediamine (TEMED) into a chilled cylindrical polypropylene mold (5 mm in diameter) and allowing it to polymerize at -20 ^{o}C for 1 day. The succeeding cryogel layer with directional, columnar pores (referred to as columnar layer) was synthesized by adding 40 µL of chilled precursor solution containing 20% (w/v) PEGDA in deionized (DI) water with 0.5% (w/v) APS and 0.2% (v/v) TEMED onto the surface of the frozen bottom cryogel layer and allowing it to polymerize at -20 ^{o}C for 1 day. The frozen, polymerized bilayers were then placed into phosphate-buffered saline (PBS) to yield bilayered cryogel by thawing ice crystals. The resulting bilayered cryogel was washed in PBS three times and exhibited 8 mm in diameter with approximately 2 mm and 2.5 mm in thickness for spongy and columnar layer, respectively.

6.3.2. Biomineralization of the bilayered cryogel

The bilayered cryogel with PEGDA-*co*-A6ACA spongy layer and PEGDA columnar layer was subject to biomineralization process by utilizing A6ACA moieties as a template as described elsewhere [38]. Briefly, the bilayered cryogel was equilibrated in DI water for 6 h and soaked in modified-simulated body fluid (m-SBF, pH = 7.4) at 25 ^{o}C for 6 h. The m-SBF solution consists of 142.0 mM Na^+, 5.0 mM K^+, 1.5 mM Mg^{2+}, 2.5 mM Ca^{2+}, 103.0 mM Cl^-, 10.0 mM HCO_3^-, 1.0 mM HPO_4^{2-}, and 0.5 mM SO_4^{2-} as previously reported [178]. The bilayered cryogel was briefly rinsed with DI water and incubated in 40 mM Ca^{2+} and 24 mM HPO_4^{2-} solution (pH = 5.2) at 25 ^{o}C for 30 min on a rotating shaker (VWR, 12620-938) at 200 rpm. The bilayered cryogel was briefly rinsed with DI water, incubated in m-SBF at 37 ^{o}C for 2 days with daily change of m-SBF, and washed with PBS to obtain biomineralized bilayered cryogel. The biomineralized bilayered cryogel was sterilized by immersing them in 70% ethanol for 6 h. The ethanol-treated cryogel was washed with sterile PBS for 5 days with four times of daily change of PBS to ensure complete removal of residual ethanol.

6.3.3. Cell culture

Human mesenchymal stem cells (hMSCs) were obtained from Institute for Regenerative Medicine at Texas A&M University. hMSCs were maintained in growth medium containing high glucose DMEM, 10% (v/v) fetal bovine serum (FBS, hyclone), 4 mM L-glutamine, and 50 U/mL penicillin/streptomycin. hMSCs were passaged at approximately 70-80% confluency.

Passage 5 (P5) hMSCs were used to generate hMSC aggregates by using a rotational method as described elsewhere [273]. Briefly, 1 million hMSCs were suspended in 10 mL of growth medium and plated onto a petri dish (10 cm in diameter). The plated cells were subject to gentle rotation at 100 rpm using VWR shaker for 1 day.

Chondrocytes were isolated by using a previously reported procedure [274]. Briefly, articular cartilage was dissected from femoral condyle and patellar groove of 8 week-old bovine legs. The dissected cartilage pieces were digested in DMEM containing 0.15% (w/v) collagenase (Worthington Biochemical, LS004177) and 5% (v/v) FBS for 16 h at 37 ^{o}C and 5% CO_2. The resulting cell suspension was filtered through 70 μm nylon cell strainer (Falcon) and washed with PBS containing 50 U/mL penicillin/streptomycin to obtain primary chondrocytes.

6.3.4. Cell-laden trilayered scaffold and in vitro culture

To evaluate the ability of varying microarchitecture in the trilayered hydrogel to support stem cell contribution to stratified neo-tissue formation, we incorporated hMSCs into the trilayered hydrogel. We seeded hMSCs and chondrocytes with a ratio of 7:3 into the columnar layer. We included chondrocytes to promote chondrogenic differentiation and inhibit hypertrophy of hMSCs [275, 276]. Prior to cell seeding, sterile biomineralized bilayered cryogel were incubated in growth medium at 37 °C for 1 day to promote cell adhesion. Approximately 35 µL of growth medium was removed from the incubated cryogel and 35 µL of the cell suspension containing 1.05 million P5 hMSCs and 0.45 million primary chondrocytes was seeded into the columnar layer of bilayered cryogel. The cell-laden bilayered cryogel were incubated at 37°C and 5% CO_2 for 2 h to allow cell infiltration and further incubated in 1.5 mL of growth medium for 1 day to allow cell attachment.

hMSCs were further incorporated into the top hydrogel layer (referred to as superficial layer) as aggregates to mimic natural developmental program of mesenchymal condensation [272, 277]. 1 million P5 hMSCs as aggregates were suspended in 15 µL of a precursor solution containing 10% (w/v) PEGDA with 0.05% (w/v) Irgacure 2959 photoinitiator. The precursor solution containing hMSC aggregates was dispensed onto the surface of columnar layer of the equilibrium-swollen bilayered cryogel and photopolymerized under UV light for 5 min to yield cell-laden trilayered hydrogel. The superficial layer of the trilayered hydrogel exhibited approximately 0.5 mm in thickness. Top view of encapsulated hMSC aggregates was visualized by bright-field images and approximate size of the aggregates was determined for 10 aggregates from each of three different images (n=30) by using ImageJ. The data are presented as mean ± standard errors.

The cell-laden trilayered hydrogel was cultured under chondrogenic-inducing medium at 37 °C and 5% CO_2 with medium change every two days. Chondrogenic-inducing medium was prepared by supplementing DMEM with 1% (v/v) Corning ITS Premix Universal Culture Supplement (CB-40352), 100 nM dexamethasone (Sigma-Aldrich, D2915), 40 µg/mL L-Proline (Sigma-Aldrich, P5607), 50 µg/mL L-Ascorbic acid 2-phosphate (Sigma-Aldrich, A8960), 100 µg/mL sodium pyruvate (Life Technologies, 11360-070), 50 U/mL penicillin/streptomycin, and 10 ng/mL human recombinant TGF-β1 (Fitzgerald, 30R-AT027).

6.3.5. Scanning electron microscopy (SEM) and energy-dispersive spectra (EDS)

To examine varying pore microstructure and biominerals within the trilayered hydrogel, SEM imaging was performed. To determine the composition of biominerals, EDS analysis was conducted. Samples were briefly rinsed with DI water and cut into thin slices to visualize the cross-section of the trilayered hydrogel. The slices were subject to flash-freezing and lyophilization. The sliced samples were Iridium-coated for 7 s in the sputter (Emitech, K575X). The superficial, columnar, and spongy layer of the trilayered hydrogel was imaged by using SEM (Philips XL30 ESEM) and analyzed for elemental spectra by using integrated EDS system. INCA software was used to further quantify Ca/P atomic ratio of the biominerals from elemental spectra. The pore size in major and minor axis for columnar and spongy layer of the trilayered hydrogel was calculated from roughly 10 pores chosen from each of three SEM images (n=30) by using ImageJ. Pore aspect ratio was determined as a ratio of pore size in major axis to minor axis for the columnar and spongy layer of the trilayered hydrogel (n=30). Macropores were not observed from the superficial layer of the trilayered hydrogel and thus their size and aspect ratio were not determined.

6.3.6. Live-dead staining

To examine viability and distribution of the encapsulated cell aggregates and seeded cells and in the superficial and columnar layer of the trilayered hydrogel, respectively, live-dead staining was conducted. After 3 days of culture, samples were sliced into thin pieces to visualize the cross-section of the cell-laden trilayered hydrogel and washed with PBS. The flat slices were incubated in DMEM containing 0.05% (v/v) green-fluorescent calcein-AM and 0.2% (v/v) red-fluorescent ethidium homodimer-1 at 37 °C for 30 min using Live/Dead Viability/Cytotoxicity kit, (Life technologies, L-3224). The stained slices were washed with PBS and imaged by using a fluorescence microscope (Carl Zeiss, Axio Observer.A1).

6.3.7. Subcutaneous implantation

For *in vivo* study, eight immunodeficient mice (NOD.CB17-Prkdcscid/J, 3-month-old) were used with the approval of the Institutional Animal Care and Use Committee (IACUC) at the University of California, San Diego. Two of eight mice were used to obtain native osteochondral tissue from their hindlimbs. Six of eight mice were used for implantation of the cell-laden trilayered hydrogel. Prior to surgery, the mice were administered with ketamine (Ketaset, 100 mg/kg) and xylazine (AnaSed, 10 mg/kg) intraperitoneally. The anesthetized mice were subject to 1.5 cm-long incision on their back and four subcutaneous pouches (cranial-left, cranial-right, caudal-left, and caudal-right) were exposed. 24 cell-laden trilayered hydrogels (8 mm in diameter and 5 mm in height) were preconditioned for 1 week, implanted into four subcutaneous pouches of six mice, and their skin was closed with sutures. Two mice were sacrificed immediately after implantation (0 week post-implantation) and each of two mice were sacrificed after 4 and 8 weeks of implantation.

6.3.8. Micro-computed tomography (μCT)

μCT analysis was carried out to evaluate hard tissue formation both *in vitro* and *in vivo*. The samples were fixed in 4% paraformaldehyde at 4 °C for 4 days. The fixed samples were tightly placed between styroform disks in 15 ml centrifuge tubes. The samples were imaged by using SkyScan 1076 μCT scanner (Bruker, pixel resolution: 9 μm, 50 kV, Al filter). The acquired images were reconstructed by using NRecon software (SkyScan, Bruker). The reconstructed images were built into 3-D models by using CT Analyser software (SkyScan, Bruker). Using 3-D images, strongly positive signals were selected to indicate calcified tissue formation (colored in red) by applying threshold range of 70-255, while weakly positive signals within threshold range of 35-70 were chosen to represent non-calcified tissue (colored in blue). Strongly positive signals of 3-D images selected to indicate calcified tissue formation were utilized to determine calcification density. The quantification was performed by selecting six different areas (n=6) from each of superficial, columnar, and spongy layer of the cell-laden trilayered hydrogel. The reconstructed images were converted into 2-D coronal cross-sectional images to visualize a planar view of calcified tissue formation by using DataViewer software (SkyScan, Bruker).

6.3.9. Preparation for histological staining

To examine neo-tissue formation within the cell-laden trilayered hydrogel both *in vitro* and *in vivo*, histological staining was carried out. Native osteochondral tissue was used as a control. The paraffin-embedded sections were prepared using a previously reported procedure [145]. The constructs were fixed with 4% paraformaldehyde at 4 °C for 4 days, demineralized in 10% ethylenediaminetetraacetic acid (EDTA, pH = 7.3) at 4 °C for 7 days, and washed with PBS for 6 h. The demineralized samples were dehydrated, equilibrated in Citrisolv solution for 1 h, and incubated in a molten mixture of 95% (w/w) paraffin and 5% (w/w) poly(ethylene-*co*-vinyl acetate) (Sigma Aldrich, 437220) at 70 °C under vacuum for 1 day. The paraffin-embedded samples were sliced into 10 µm-thick cross-sections of the trilayered hydrogel using a microtome (Leica, RM2255). The sections were deparaffinized in Citrisolv for 15 min and rehydrated prior to staining.

6.3.10. Fluorescent staining

The rehydrated sections were incubated in 2 µg/mL Hoechst 33342 solution (Life Technologies, H1399) at 25 °C for 10 min and washed with PBS. The stained sections were imaged for cross-section of the cell-laden trilayered hydrogel using a fluorescence microscope.

6.3.11. Histochemical staining

For H&E staining, the rehydrated sections were incubated in hematoxylin solution (Ricca, 3536-16) for 4 min and washed with DI water. The sections were then immersed in Eosin-Y solution (Richard-Allan Scientific, 7111) for 1 min and washed with DI water. For Alcian Blue staining, the rehydrated sections were stained in a solution containing 1% (w/v) Alcian Blue (National diagnostics, HS-504) in 0.1 M HCl (pH = 1.0) for 1 h. The stained sections were washed with 0.1 M HCl. The stained sections by H&E or Alcian Blue were imaged for cross-section of the cell-laden trilayered hydrogel and native osteochondral tissue in a color mode under H filter.

6.3.12. Immunohistochemical staining

The rehydrated sections were incubated in 20 µg/mL proteinase K solution (Invitrogen, 100005393) in a mixture of 95% (v/v) TE buffer (50 mM Tris-HCl and 1 mM EDTA, and 0.5% [v/v] Triton X-100; pH = 8.0) and 5% (v/v) glycerol at 37 °C for 15 minutes and washed with PBS. The treated sections were immersed in a blocking solution containing 3% (v/v) normal goat serum and 0.1% (v/v) Triton X-100 at 25 °C for 1 h. The blocked sections were incubated in primary antibodies against type I collagen (1:100, rabbit polyclonal, Fitzerald, 70R-CR007x), type II collagen (1:50, rabbit polyclonal, Fitzerald, 70R-CR008), type X collagen (1:50, rabbit polyclonal, Fitzerald, 20R-CR030), osteocalcin (1:100, rabbit polyclonal, Abcam, ab93876), lubricin (1:50, goat polyclonal, Santa Cruz Biotechnology, sc-50079), or lamin B (1:100, rabbit polyclonal, Thermo scientific, RB10569-P0) in the blocking solution at 4 °C for 16 h. The sections were washed with PBS and treated with 3% (v/v) hydrogen peroxide for 7 min to deactivate endogenous peroxidase. The treated sections were incubated with horseradish peroxidase (HRP)-conjugated secondary antibodies against rabbit (1:200, donkey anti-rabbit, Jackson ImmunoResearch, 711-035-152) or goat (1:100, donkey anti-goat, Jackson ImmunoResearch, 705-035-003) in the blocking solution at 25 °C for 1 h and washed with PBS. The sections were immersed in a developing solution containing 3-3' diaminobenzidine (DAB) substrate (Vector Laboratories, SK-4100) for 5 min to produce a brown reaction product and washed with PBS. The stained sections were imaged for the cross-section of the cell-laden trilayered hydrogel and native osteochondral tissue in a color mode under H filter.

6.3.13. Statistical analysis

Graphpad Prism 5 was used to perform statistical analyses. Statistical significances were indicated as asterisks for *p*-values less than 0.05. Two-tailed Student's t-test was used to compare two groups at the same time point. One-way analysis of variance (ANOVA) with Tukey-Kramer post-hoc test was employed to compare multiple groups at the same time point.

6.4. Results

6.4.1. Monolithic trilayered hydrogel with varying structure and CaP minerals

Synthetic trilayered hydrogel was developed by using cryogelation and biomineralization. Bilayered cryogel with poly(ethylene glycol)-diacrylate-*co*-N-acryloyl-6-aminocaproic acid (A6ACA) (PEGDA-*co*-A6ACA) bottom layer and PEGDA middle layer were synthesized via sequential cryogelation in the absence and presence of underlying ice template to vary pore microstructure, respectively. PEGDA hydrogel as a superficial top layer was added onto the bilayered cryogel to obtain trilayered hydrogel. The schematic in Figure 6.1a reveals the stepwise synthesis procedures. Scanning electron microscopy (SEM) images showed distinct pore microstructures in the trilayered hydrogel (Figure 6.1b). While the bottom layer showed isotropic, round interconnected macropores (hereafter termed as spongy layer), the middle layer exhibited directional, columnar macropores (hereafter named as columnar layer). The top hydrogel layer did not exhibit any visible macropores (hereafter termed as superficial layer). The trilayered hydrogel exhibited highly integrated microstructure. Furthermore, pore size in major and minor axis as well as pore aspect ratio confirmed the anisotropicity of pores. While the pore size in major axis (132.6 ± 24.2 µm) exhibited significantly higher than that in minor axis (37.5 ± 8.6 µm) in the columnar layer, they showed comparable size in the spongy layer (33.6 ± 13.2 µm vs. 27.4 ± 11.1 µm) (Figure 6.1c). The corresponding pore aspect ratio of the columnar layer (3.6 ± 0.6) was significantly higher than that of the spongy layer (1.3 ± 0.2) (Figure 6.1d).

The trilayered hydrogel was designed to selectively incorporate CaP minerals into the spongy layer by utilizing A6ACA moieties as a template for biomineralization [38]. SEM image and energy-dispersive spectroscopy (EDS) analysis demonstrated that CaP minerals found in the spongy layer exhibited a plate-like morphology and Ca/P ratio of 1.23, which remained absent in the other layers (Figure 6.1b).

6.4.2. The anisotropic structure conduces to stratified cartilage formation *in vitro*.

The ability of modular scaffold with stratified microstructure to support stem cell contribution to stratified cartilage formation was evaluated *in vitro*. We created cell-laden trilayered scaffold by seeding hMSCs and chondrocytes with a ratio of 7:3 into the columnar layer and encapsulating hMSC aggregates into the superficial layer. The cell-laden trilayered hydrogel was cultured under chondrogenic-inducing medium. Figure 6.2a summarizes the experimental procedures.

After 3 days of culture, live-dead staining showed that the cells were found to be mostly viable and homogeneously populated within the superficial and columnar layer, which remained absent in the spongy layer (Figure 6.2b). The viable, encapsulated hMSC aggregates were found to be closely packed within the superficial layer exhibiting the size of 98.9 ± 3.4 µm (Figure 6.S1). Following 9 weeks of culture, fluorescent Hoechst (nucleus) staining showed that the cells in the superficial layer were randomly populated while those in the columnar layer were vertically aligned, in contrast to the spongy layer that remained acellular (Figure 6.2b).

We next examined whether stratified microstructure-mediated cellular arrangement yielded the formation of stratified cartilage tissue. H&E staining after 5 and 9 weeks of culture demonstrated chondrocyte-like cells in lacunae-like structure within cartilage-like ECM in the superficial and columnar layer, which remained absent in the spongy layer (Figure 6.S2). Alcian Blue staining and immunohistochemical staining for type II collagen, cartilage-specific ECM protein after 5 and 9 weeks of culture revealed pervasiveness and homogeneity of glycosaminoglycan (GAG) and type II collagen in the superficial and columnar layer (Figures 6.S3, 6.S4). In contrast, negative stains for such cartilage markers were observed in the spongy layer. Furthermore, chondrocytes within cartilaginous ECM showed relatively horizontal and vertical alignment in the superficial and columnar layer, respectively, revealing stratified microstructure-mediated arrangement of cells and ECM. The stratified, homogeneous cartilage formed in the superficial and columnar layer of the trilayered hydrogel after 5 and 9 weeks of culture was found to be negative for lubricin (Figure 6.S5).

Human-specific lamin B staining was performed to confirm stratified alignment of human cells in the stratified neo-cartilage. Immunohistochemical staining for lamin B was found to be positive both in the superficial and columnar layer with horizontal and vertical alignment of cells after 9 weeks of culture, respectively, in contrast to negative staining in the spongy layer (Figure 6.S6). This suggests that varying microstructure conduced human stem cells to contribute to stratified cartilage formation.

We investigated whether stratified neo-cartilage formed in the superficial and columnar layer included any neo-bone tissue, if any, formed by potential influence of CaP biomineral-borne cues from the spongy layer. 3-D micro-computed tomography (μCT) image showed that the trilayered hydrogel remained minimally calcified throughout 9 weeks of culture (Figure 6.S7). Furthermore, cartilage tissue formed in the superficial and columnar layer was found to be negative for type X collagen expression, suggesting no sign of hypertropic cartilage (Figure 6.S8). Concurrently, minimal to negative staining for type I collagen and osteocalcin revealed no bone formation in the superficial and columnar layer, suggesting that the effect of CaP biomineral-based cues was spatially confined within the spongy layer (Figures 6.S9, 6.S10).

6.4.3. The anisotropic structure supports stratified cartilage formation *in vivo*.

We examined the potential of cell-laden trilayered scaffold with varying microstructure and CaP biominerals to support simultaneous formation of stratified, integrated cartilage and bone tissues *in vivo*. We preconditioned the cell-laden trilayered scaffold under chondrogenic induction medium for 1 week prior to their implantation. We compared the anatomical features of *in vivo* engineered tissue formed within the trilayered scaffold to those of native osteochondral tissue. Gross examination of the retrieved implants at 4 and 8 weeks post-implantation revealed two distinct tissue layers with glistening, white upper layer integrated with lower layer (Figure 6.3a). Fluorescent nucleus staining at 8 weeks post-implantation showed randomly populated cells in the superficial layer and vertically aligned cells in the columnar layer while cells were also found in the biomineralized spongy layer (Figure 6.3b). H&E staining of the implants demonstrated gradual formation of two disparate, integrated tissues throughout 8 weeks of implantation (Figures 6.3c, 6.S11). In particular, chondrocyte-like cells were found within cartilage-like ECM in the superficial and columnar layer compared to the cells found within dense ECM in the biomineralized spongy layer, resembling the morphology of native osteochondral tissue.

Alcian Blue staining and immunohistochemical staining for type II collagen of the implants demonstrated gradual accumulation of prevalent and homogeneous GAG and type II collagen in the superficial and columnar layer throughout 8 weeks post-implantation, analogous to the anatomy of native osteochondral tissue (Figures 6.4, 6.S12). In contrast, minimum stains were found in the spongy layer. In addition, chondrocytes were relatively horizontally aligned in the superficial layer, while those were mostly vertically aligned within lamellar columns of neo-cartilage in the columnar layer, suggesting that varying microstructure supported stratified, homogeneous cartilage formation *in vivo*.

The contribution of transplanted human stem cells towards *in vivo* formation of stratified cartilage was examined. Immunohistochemical staining for lamin B was found to be positive for the cells in the superficial and columnar layer with their relatively horizontal and vertical alignment following 8 weeks of implantation, respectively, which remained negative in the spongy layer (Figure 6.S13).

The stratified neo-cartilage formed *in vivo* through contribution of transplanted stem cells recapitulated ECM protein responsible for function of cartilage. Lubricin, present in the superficial zone of native cartilage that renders its lubrication property, was exclusively found in the superficial layer at 4 and 8 weeks post-implantation in a progressively increased manner, analogous to native osteochondral tissue (Figures 6.4, 6.S12). This implies the potential in the mechanical function of the *in vivo* engineered, stratified cartilage.

6.4.4. Biomineralized spongy layer induces *in vivo* bone formation.

Having established the ability of trilayered scaffold with varying microstructure to mediate the formation of stratified cartilage *in vivo*, we next determined whether the biomineralized spongy layer simultaneously induced subchondral bone formation that integrates with the engineered cartilage. The acellular biomineralized spongy layer exhibited homogenous distribution of cell population after 8 weeks of implantation, suggesting the recruitment of endogenous cells (Figure 6.3b). 3-D μCT analyses of the cell-laden trilayered scaffold prior to implantation indicated the absence of hard tissue formation (Figure 6.5a). 3-D μCT image of the implants showed progressive development of calcified tissue concentrated within the lower layer throughout 8 weeks of post-implantation as compared to non-calcified upper layer, suggesting *in vivo* hard tissue formation within the biomineralized spongy layer. 2-D coronal cross-sectional μCT image for the implants following 4 and 8 weeks of implantation demonstrated hard tissue formation within the macroporous network of biomineralized spongy layer (Figure 6.S14). Quantification of calcified tissue formation from 3-D μCT image of the implants at 4 and 8 weeks post-implantation confirmed significantly higher calcification density in the biomineralized spongy layer compared to the other layers (Figure 6.5b).

The calcified tissue formed within the biomineralized spongy layer was found to be positive for type I collagen following 4 and 8 weeks of implantation, while minimal stains were detected in the other layers, similar to native osteochondral tissue (Figures 6.5c, 6.S15). Prevalent staining for osteocalcin, bone-specific ECM protein secreted by osteoblasts, was detected in the type I collagen-rich biomineralized spongy layer at 4 and 8 weeks post-implantation, revealing subchondral bone formation *in vivo* by the recruited host cells (Figures 6.5c, 6.S15). In stark contrast, osteocalcin staining was found to be nearly negative in the engineered cartilage formed within the other layers, resembling native osteochondral tissue. Together, the findings suggest simultaneous *in vivo* formation of integrated, distinct cartilage and bone tissues within the trilayered hydrogel. Furthermore, subchondral bone formed in the biomineralized spongy layer was found to be positive for type X collagen at 4 and 8 weeks post-implantation (Figure 6.S16). This contrasted sharply with minimal to negative staining for type X collagen in the engineered cartilage formed within the other layers.

6.5. Discussion

Osteochondral tissue is a structurally complex tissue exhibiting stratified organization of discrete cells and ECM that governs the function. The regeneration of osteochondral tissue has been pursued for decades, but recapitulation of zonal architecture of integrated osteochondral tissue *in vivo* remains a significant challenge. To this end, both donor and host stem and progenitor cells can be utilized to yield chondrocytes and osteoblasts; however, their spatially controlled differentiation in stratified architecture is required. Porous biomaterials offer benefits with the ability in conducing tissue formation with the morphology conforming to the pore architecture [278]. In this study, spongy pores were designed to support the formation of spongy structure of subchondral bone, while columnar pores were developed to guide the formation of vertically aligned cartilage mimicking deep zone of native cartilage. The thin superficial layer was also created to conduce the formation of horizontally aligned cartilage similar to superficial zone of native cartilage. In addition to designing unique, varying microarchitecture, we recapitulated CaP biominerals into the spongy layer to harness their inherent osteoinductivity and osteoconductivity to recruit host cells for in situ bone formation [77, 266]. In this study, we examined whether trilayered scaffold with varying pore microstructure and osteoinductive CaP biominerals can facilitate *in vivo* engineering of anatomical analog of integrated osteochondral tissue.

Our results show that trilayered hydrogel was developed through a monolithic assembly with heterogeneous pore microstructure by sequential cryogelation to allow for stratified tissue formation. While we and others have demonstrated the synthesis of cryogels with various pore microstructures [77, 279-282], the development of bilayered cryogel with disparate macroporous architecture is unprecedented. Spongy cryogel layer was formed under isotropic cooling to build randomly oriented, interconnected ice network, thus yielding spongy pores. Using frozen, underlying spongy cryogel layer as an ice template, columnar cryogel layer was sequentially formed under directional cooling that initiated from the ice template in a vertical manner, thereby producing aligned, microtubular pores [77, 280]. Superficial hydrogel layer devoid of macropores was created on the spongy-columnar bilayered cryogel in the absence of cooling to obtain integrated, trilayered hydrogel.

Varying microarchitecture in the superficial and columnar layer conduced stem cells to contribute to stratified cartilage formation without hypertrophy, both *in vitro* and *in vivo*. Interestingly, 1 week of *in vitro* preconditioning under chondrogenic induction medium was sufficient for stem cells to undergo chondrogenic differentiation to contribute to *in vivo* formation of homogenous cartilage. This could be attributed to the presence of chondrocytes in the co-culture, which has been reported to promote chondrogenesis of MSCs, thereby enhancing the function of engineered cartilage, and secrete parathyroid hormone–related protein (PTHrP) to inhibit hypertropic development of MSCs [275, 276, 283, 284]. While cartilage in the superficial zone was formed by pure contribution of stem cell-derived chondrocytes, the donor chondrocytes and infiltrated host cells could also contribute to cartilage formation in the columnar layer. Furthermore, by utilizing varying micromorphology of the trilayered hydrogel, stratified cartilage tissue was engineered to closely mimic an anatomy of native tissue. The tangentially aligned cartilage in the superficial layer and vertically aligned lamellar columns of cartilage in the columnar layer recapitulated morphological features of superficial and deep zone of native cartilage, respectively. In particular, lubricin-rich cartilaginous ECM deposited within the superficial layer of the *in vivo* engineered, stratified cartilage potentially suggests the low-frictional function. Lubricin, known as superficial zone protein (SZP), is produced by chondrocytes in the superficial zone that serves as a boundary lubricant to resist against shear [285-287]. The lubricin production could be promoted by shear force exerted by subcutaneous tissue *in vivo* since dynamic shear application has been shown to stimulate lubricin secretion at cartilage surface [288]. Functional properties of the *in vivo* engineered, stratified cartilage with lubricin-rich surface, however, remain to be validated.

The *in vivo* formed, stratified neo-cartilage guided by the stratified superficial and columnar layer was highly integrated with underlying subchondral neo-bone formed within the osteoinductive biomineralized spongy layer through host cell recruitment. This reveals simultaneous *in vivo* formation for the anatomical analog of integrated cartilage and bone tissue. It is similar to our previous findings showing that biomineralized macroporous material recruited host cells for *in vivo* formation of bone tissue that functionally integrated with native bone [266]. The spatially confined recapitulation of CaP minerals into the spongy layer was facilitated by templated biomineralization utilizing A6ACA moieties. We previously showed that carboxylate end group of pendant side chain promoted the binding of Ca^{2+} ions, thereby leading to subsequent nucleation and growth of CaP minerals [38]. The CaP biominerals were shown to readily release Ca^{2+} and PO_4^{3-} ions into extracellular milieu [39, 58]. The released Ca^{2+} and PO_4^{3-} ions from the CaP-based biomineralized layer have likely promoted the recruitment of host cells that could include stem and progenitor cells, analogous to recent studies showing that biphasic calcium phosphate ceramics facilitated the recruitment of MSCs and preosteoblasts *in vitro* and *in vivo* [134, 289]. Furthermore, host cell infiltration into the biomineralized layer could be promoted by highly interconnected spongy pores [290]. In addition to host cell recruitment, the extracellular Ca^{2+} and PO_4^{3-} ions have been shown to promote osteogenic differentiation of stem and progenitor cells through various regulatory pathways [39, 105, 106, 291], thereby leading to bone synthesis. While the extracellular Ca^{2+} ions were shown to promote osteogenesis of MSCs through L-type calcium channels [105, 106], we previously showed that PO_4^{3-} ions liberated from biomineralized material mediate osteogenic differentiation of hMSCs through phosphate metabolism and adenosine signaling [39]. Furthermore, CaP biominerals can regulate binding and release of osteoinductive soluble factors, such as bone morphogenetic proteins (BMPs) through dissolution and re-precipitation of Ca^{2+} and PO_4^{3-} ions, which could further assist osteogenesis of stem and progenitor cells [85, 107].

6.6. Conclusion

In summary, we developed modular trilayered scaffold with varying pore microarchitecture and selective CaP biominerals. By employing the trilayered scaffold containing stem cells, we showed varying microstructure-guided stratified cartilage formation *in vitro*. Furthermore, subcutaneous implantation of cell-laden trilayered scaffold yielded *in vivo* formation of stratified, integrated neo-osteochondral tissue. The heterogenous microstructure-mediated formation of stratified neo-cartilage was integrated with subchondral spongy bone formed by the osteoinductive biomineralized layer. The *in vivo* engineered anatomical analog of integrated osteochondral tissue recapitulated lubricin, a functional molecular marker in the superficial layer. Such multilayered biomaterials with varying microstructure and osteoinductivity that facilitate *in vivo* formation of stratified, integrated osteochondral tissue will present a viable strategy in treating osteoarthritis.

6.7. Acknowledgements

Authors gratefully acknowledge the financial support from National Institutes of Health (NIH, Grant 1 R01 AR063184-01A1). The hMSCs used in this study were provided by Texas A&M University (NIH, Grant P40RR017447).

Chapter 6, in full is currently being prepared for submission for publication of the material. “In vivo engineering of stratified, integrated osteochondral tissue by trilayered scaffold with varying pore microstructure and osteoinductivity”. Kang, Heemin; Shih, Yu-Ru V.; Kar, Mrityunjoy; Hwang, Yongsung; Zeng, Yuze; Varghese, Shyni. The dissertation author was the primary investigator and author of this material.

6.8. Figures

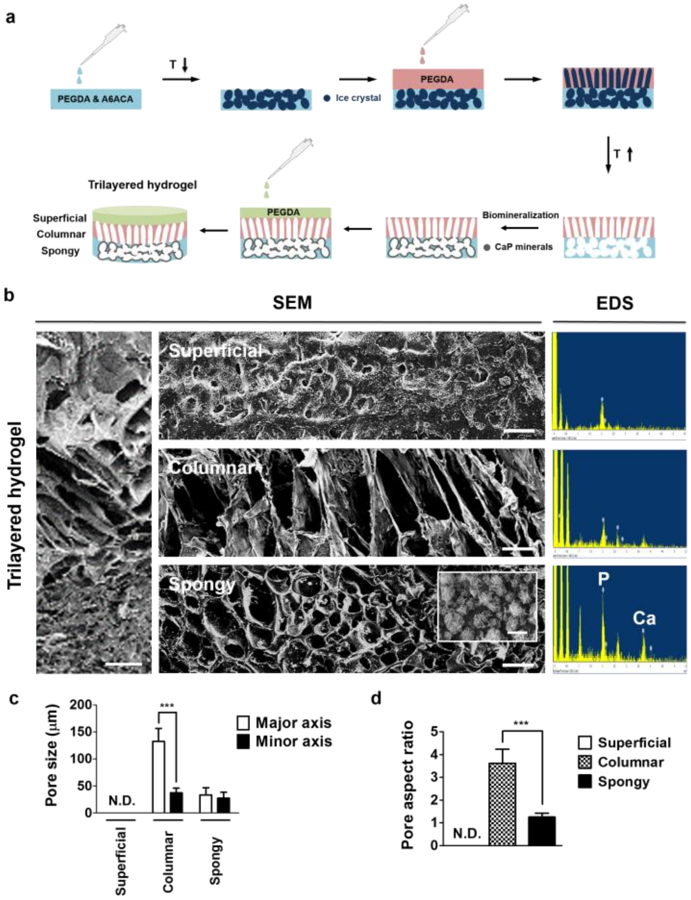

Figure 6.1. Trilayered hydrogel exhibits layer-dependent varying pore microstructure and CaP biominerals.

(A) Schematic for stepwise synthesis of the trilayered hydrogel. (B) Scanning electron microscopy (SEM) image for cross-section of the trilayered hydrogel. Scale bar represents 200 µm. High magnification SEM images and corresponding energy dispersive spectra (EDS) of superficial, columnar, and spongy layer of the trilayered hydrogel are also shown. Scale bars indicate 50 µm. Inset shows a close-up SEM image of CaP biominerals in the spongy layer of the trilayered hydrogel. Scale bar represents 2 µm. (C) Pore size in major and minor axis as well as (D) pore aspect ratio calculated from SEM images of superficial, columnar, and spongy layer of the trilayered hydrogel. N.D. indicates non-detectable pores from the superficial layer of the trilayered hydrogel. The data are presented as mean ± standard deviations (n=30). Two-tailed Student's t-test was used to compare two groups. Asterisks indicate statistical significances according to p-values (***: $p < 0.001$).

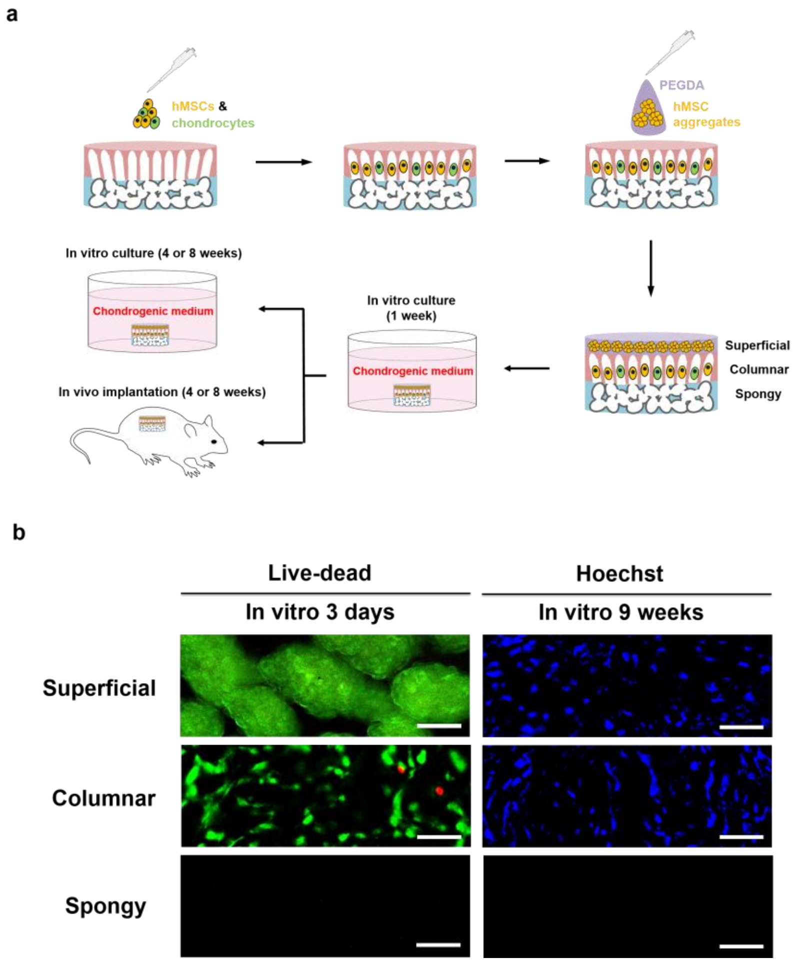

Figure 6.2. The cell-laden superficial and columnar layer conduce to stratified cellular alignment after *in vitro* culture.

(A) Schematic for an experimental protocol used to examine tissue-forming ability of the cell-laden trilayered hydrogel both in vitro and in vivo. (B) Fluorescent live-dead staining for superficial, columnar, and spongy layer of the cell-laden trilayered hydrogel after 3 days of in vitro culture. (C) Fluorescent nucleus (Hoechst) staining for superficial, columnar, and spongy layer of the cell-laden trilayered hydrogel following 9 weeks of in vitro culture. Scale bars represent 50 μm.

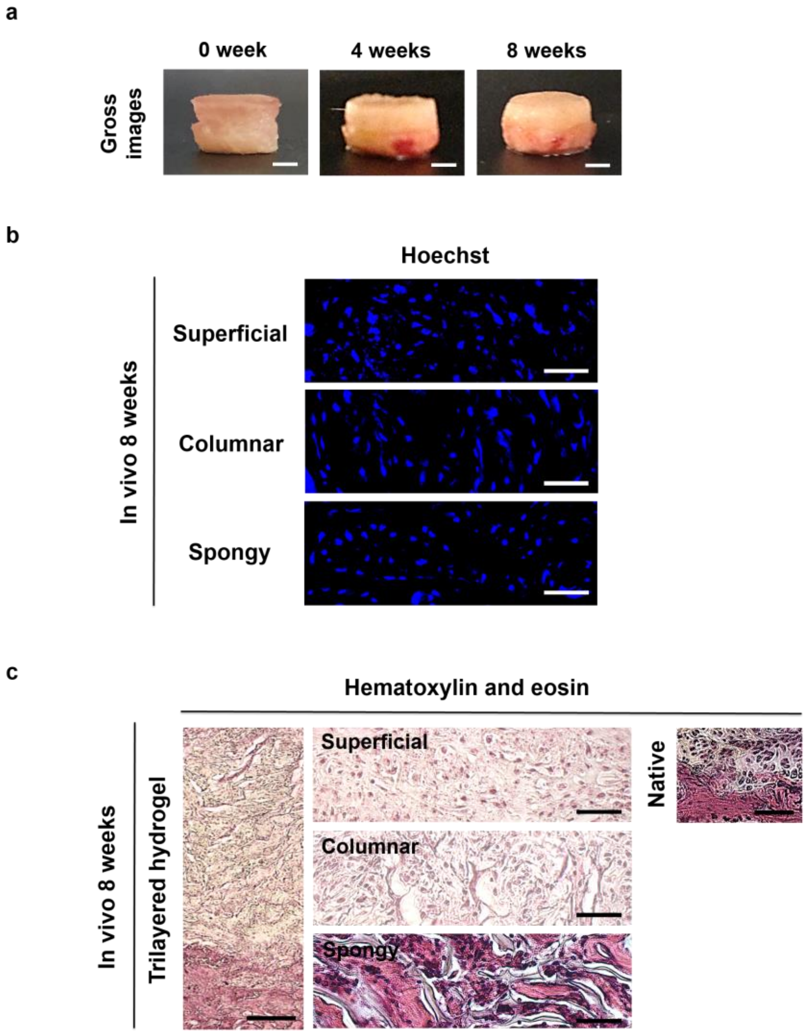

Figure 6.3. The cell-laden trilayered hydrogel facilitates the formation of integrated, distinct cartilage- and bone-like tissues *in vivo*.

(A) Gross images of the cell-laden trilayered hydrogel after 0, 4, and 8 weeks of in vivo implantation. Scale bars indicate 2 mm. (B) Fluorescent nucleus (Hoechst) staining for superficial, columnar, and spongy layer of the cell-laden trilayered hydrogel after 8 weeks of in vivo implantation. Scale bars represent 50 µm. (C) H&E staining of the cell-laden trilayered hydrogel following 8 weeks of implantation. Scale bars indicate 200 µm. High magnification images for superficial, columnar, and spongy layer of the trilayered hydrogel as well as native osteochondral tissue are also provided. Scale bars represent 50 µm.

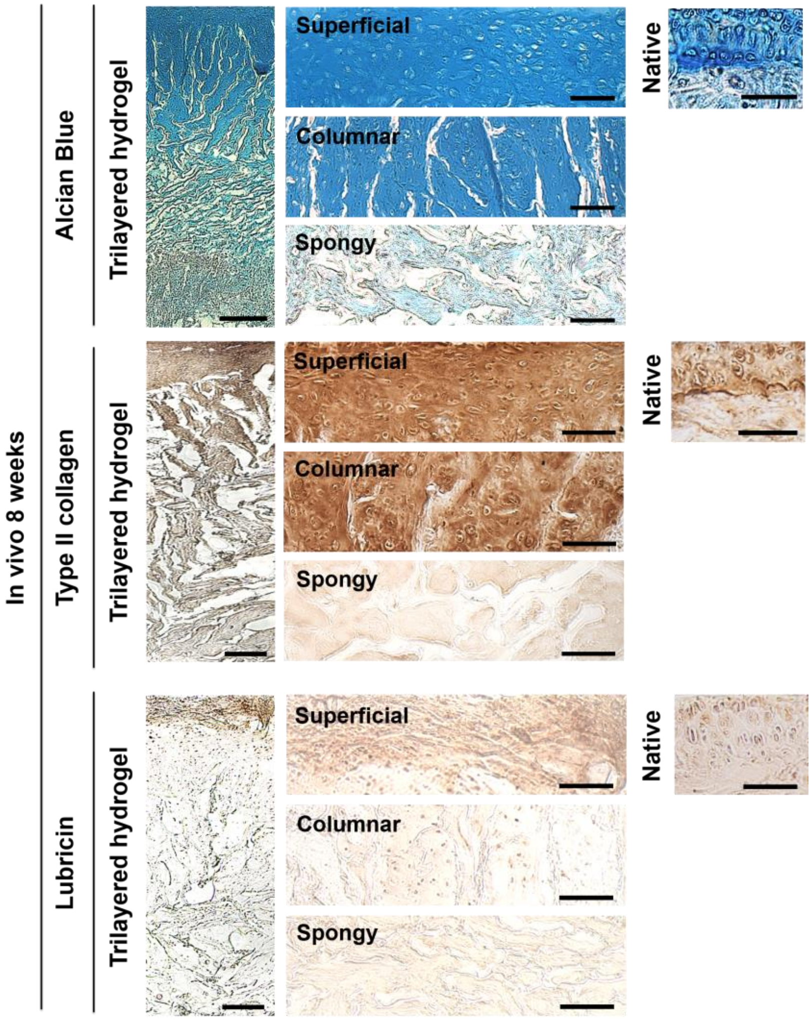

Figure 6.4. The cell-laden superficial and columnar layer support *in vivo* formation of stratified cartilage with lubricin-rich surface.

Alcian Blue staining and immunohistochemical staining for type II collagen and lubricin of the cell-laden trilayered hydrogel at 8 weeks post-implantation. Scale bars represent 200 µm. High magnification images for superficial, columnar, and spongy of the trilayered hydrogel as well as native osteochondral tissue are also shown. Scale bars indicate 50 µm.

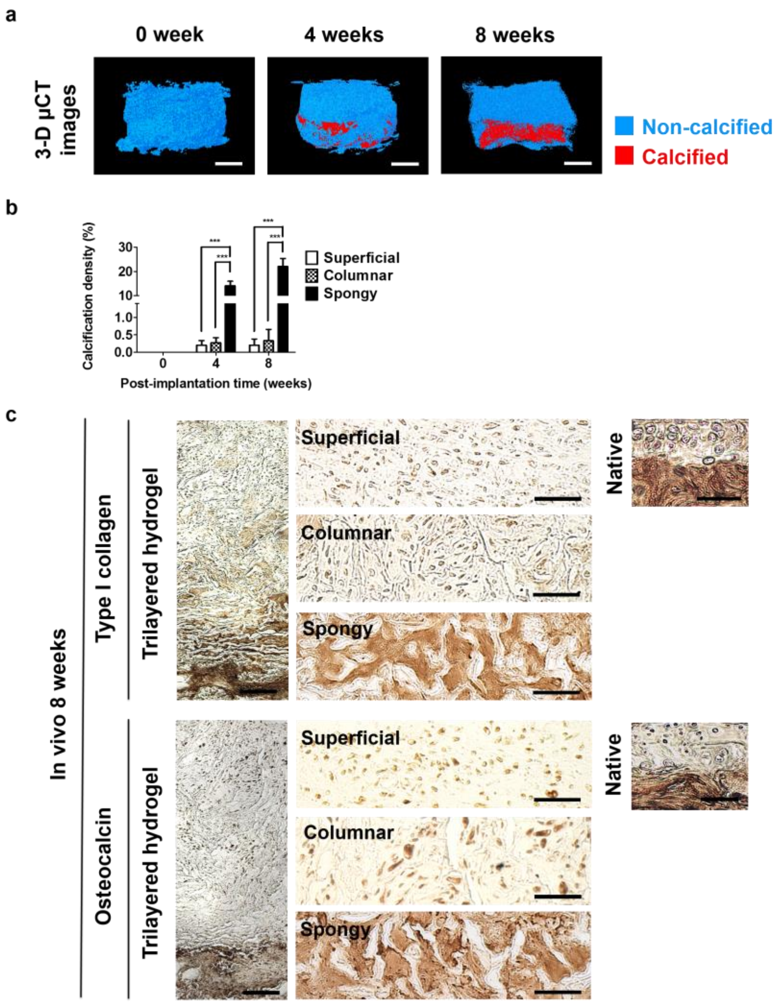

Figure 6.5. The acellular biomineralized spongy layer induces de novo formation of spongy bone *in vivo*.

(A) 3-D µCT models of the cell-laden trilayered hydrogel after 0, 4, and 8 weeks of in vivo implantation. Calcified and non-calcified tissues are shown in red and blue, respectively. Scale bars indicate 2 mm. (B) Calcification density determined from 3-D µCT models of superficial, columnar, and spongy layer of the cell-laden trilayered hydrogel as a function of post-implantation time. (C) Immunohistochemical staining for type I collagen and osteocalcin of the cell-laden trilayered hydrogel following 8 weeks of implantation. Scale bars indicate 200 µm. High magnification images for superficial, columnar, and spongy layer of the trilayered hydrogel as well as native osteochondral tissue are also provided. Scale bars represent 50 µm. Data are shown as mean ± standard errors (n=6). Comparisons of multiple groups in the same time point were made by one-way ANOVA with Tukey-Kramer post-hoc test. Asterisks indicate statistical significances according to p-values (***: $p < 0.001$).

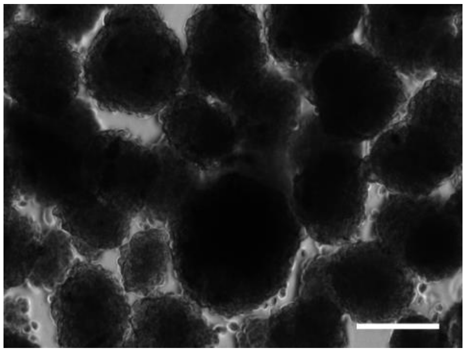

Figure 6.S1. Bright-field image for top view of encapsulated hMSC aggregates within the superficial layer of the cell-laden trilayered hydrogel.

Scale bar represents 100 μm.

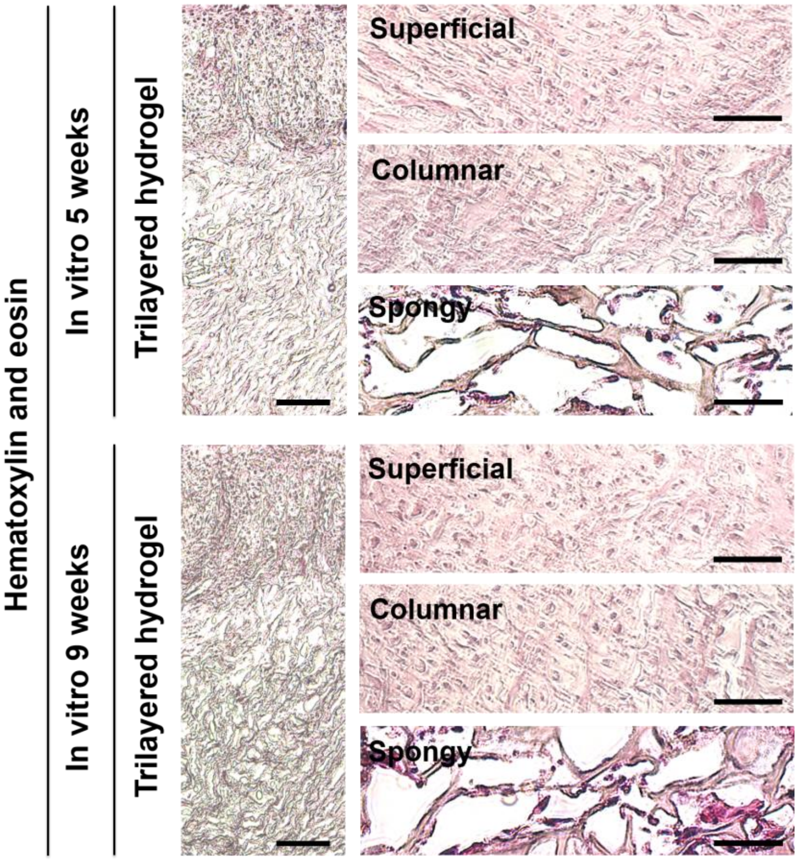

Figure 6.S2. H&E staining for the cell-laden trilayered hydrogel after 5 and 9 weeks of *in vitro* culture.

Scale bars represent 200 μm. High magnification images for superficial, columnar, and spongy layer of the trilayered hydrogel are also shown. Scale bars indicate 50 μm.

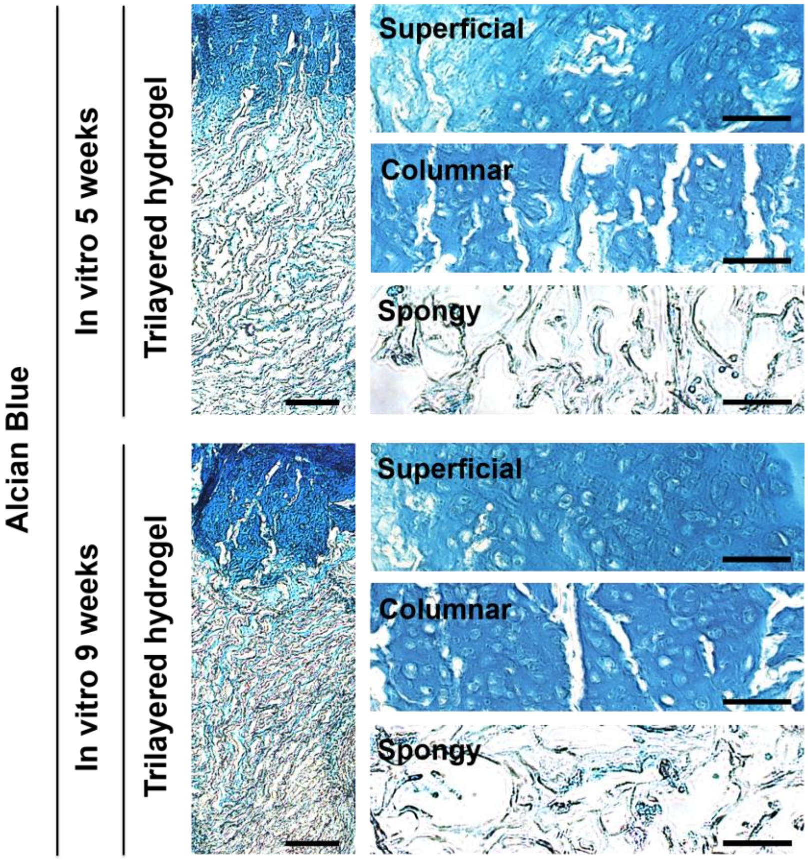

Figure 6.S3. Alcian Blue staining for the cell-laden trilayered hydrogel following 5 and 9 weeks of *in vitro* culture.

Scale bars indicate 200 µm. High magnification images for superficial, columnar, and spongy layer of the trilayered hydrogel are also shown. Scale bars represent 50 µm.

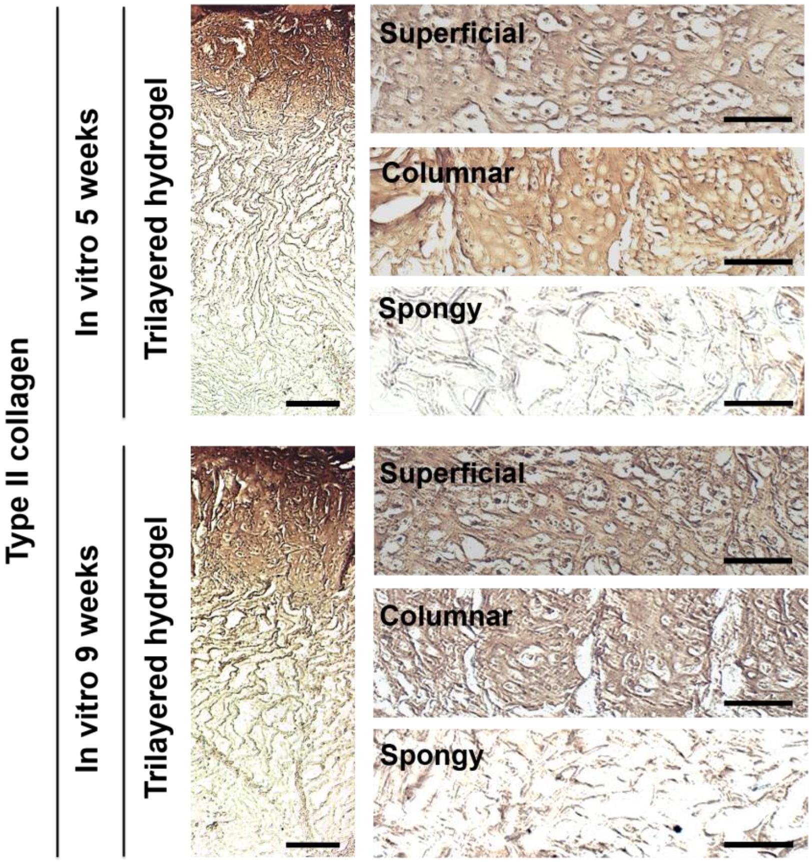

Figure 6.S4. Immunohistochemical staining for type II collagen of the cell-laden trilayered hydrogels after 5 and 9 weeks of *in vitro* culture.

Scale bars indicate 200 μm. High magnification images for superficial, columnar, and spongy layer of the trilayered hydrogel are also provided. Scale bars represent 50 μm.

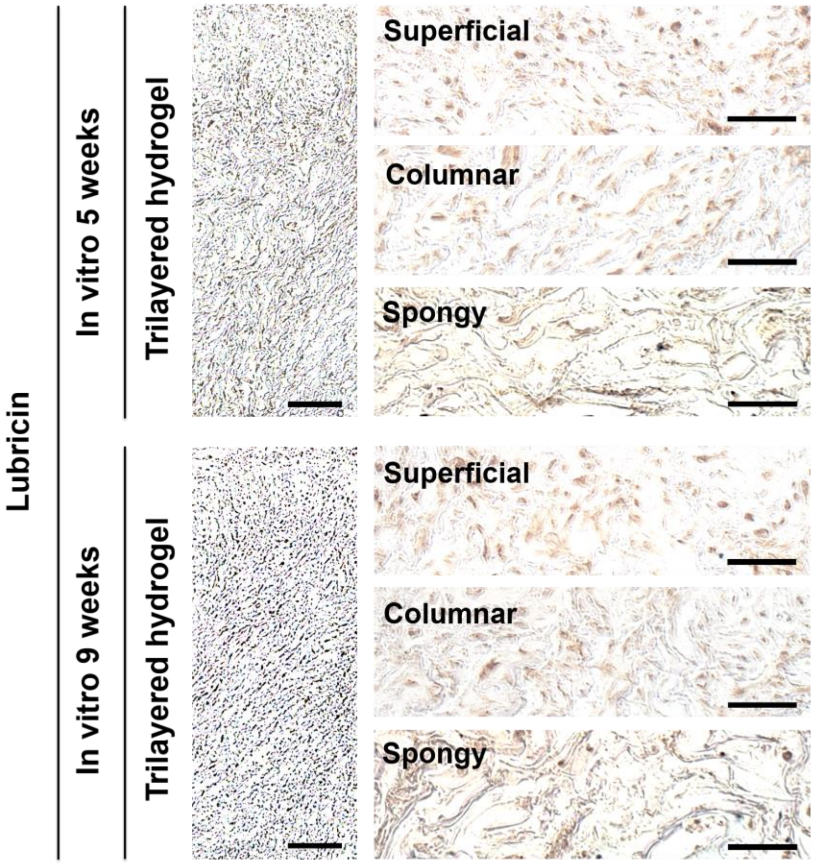

Figure 6.S5. Immunohistochemical staining for lubricin of the cell-laden trilayered hydrogels following 5 and 9 weeks of *in vitro* culture.

Scale bars represent 200 μm. High magnification images for superficial, columnar, and spongy layer of the trilayered hydrogel are also presented. Scale bars indicate 50 μm.

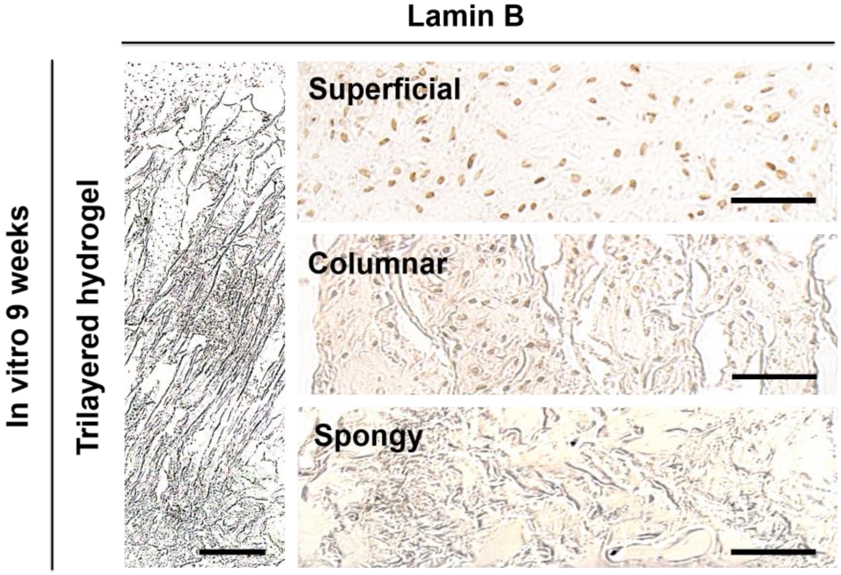

Figure 6.S6. Immunohistochemical staining for lamin B of the cell-laden trilayered hydrogel following 9 weeks of *in vitro* culture.

Scale bar represents 200 μm. High magnification images for superficial, columnar, and spongy layer of the trilayered hydrogel are also shown. Scale bars represent 50 μm.

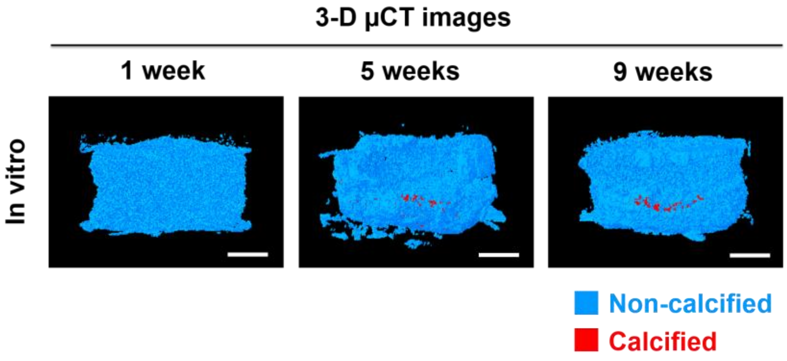

Figure 6.S7. 3-D µCT models of the cell-laden trilayered hydrogel after 1, 5, and 9 weeks of *in vitro* culture.

Calcified and non-calcified tissues are shown in red and blue, respectively. Scale bars represent 2 mm.

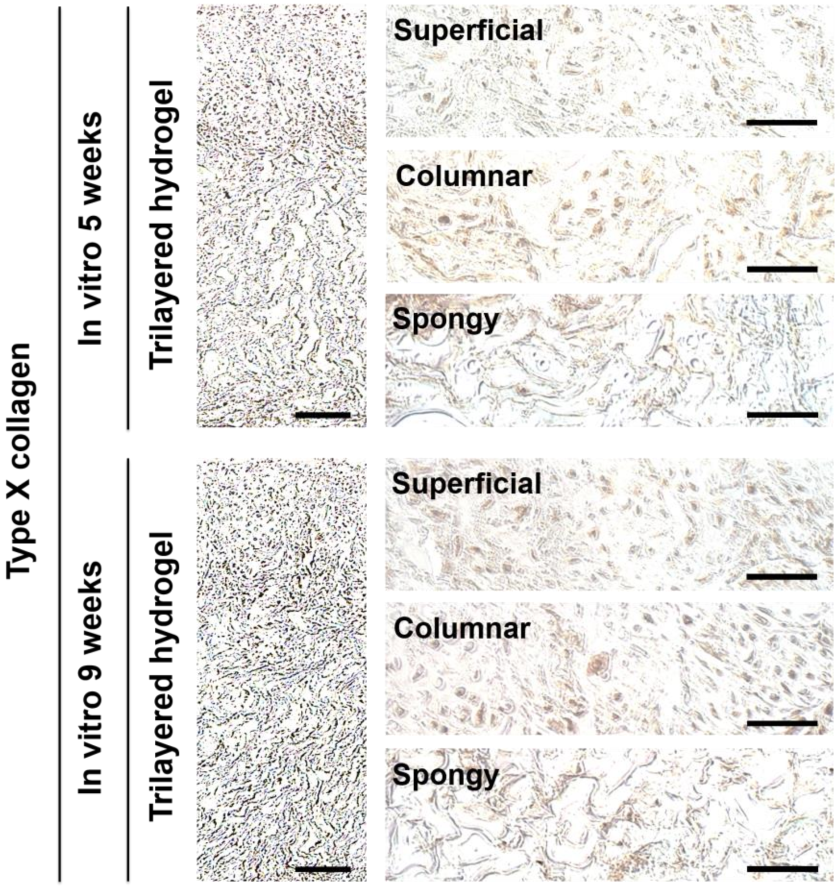

Figure 6.S8. Immunohistochemical staining for type X collagen of the cell-laden trilayered hydrogel after 5 and 9 weeks of *in vitro* culture.

Scale bars indicate 200 µm. High magnification images for superficial, columnar, and spongy layer of the trilayered hydrogel are also provided. Scale bars represent 50 µm.

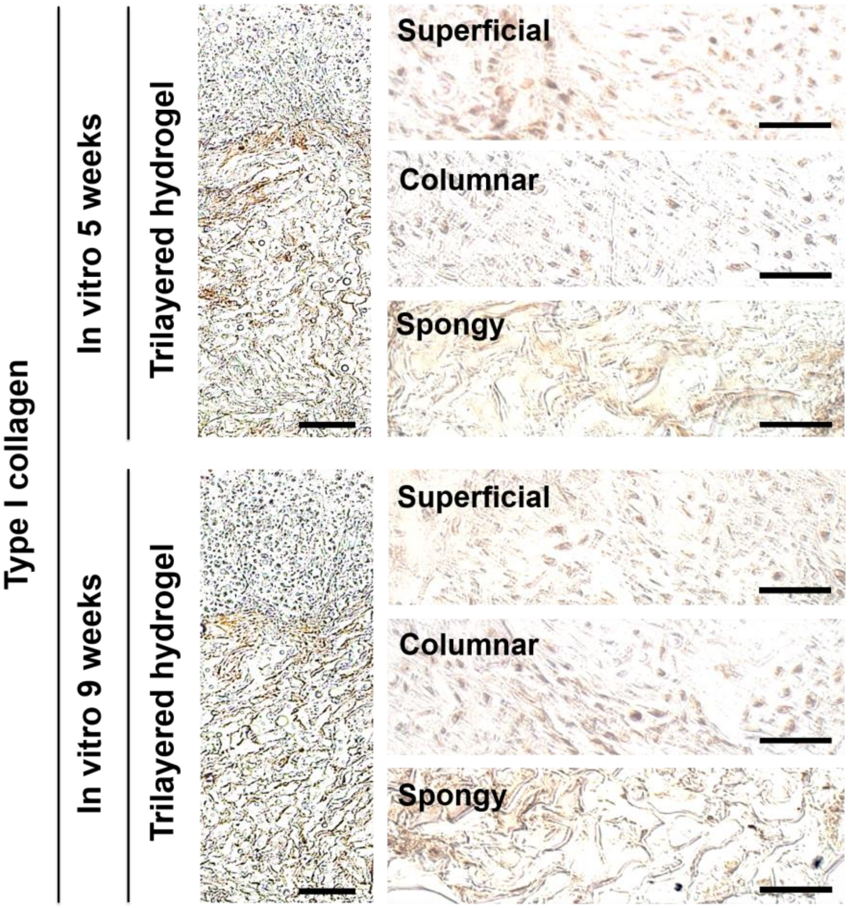

Figure 6.S9. Immunohistochemical staining for type I collagen of the cell-laden trilayered hydrogel following 5 and 9 weeks of *in vitro* culture.

Scale bars represent 200 μm. High magnification images for superficial, columnar, and spongy layer of the trilayered hydrogel are also shown. Scale bars indicate 50 μm.

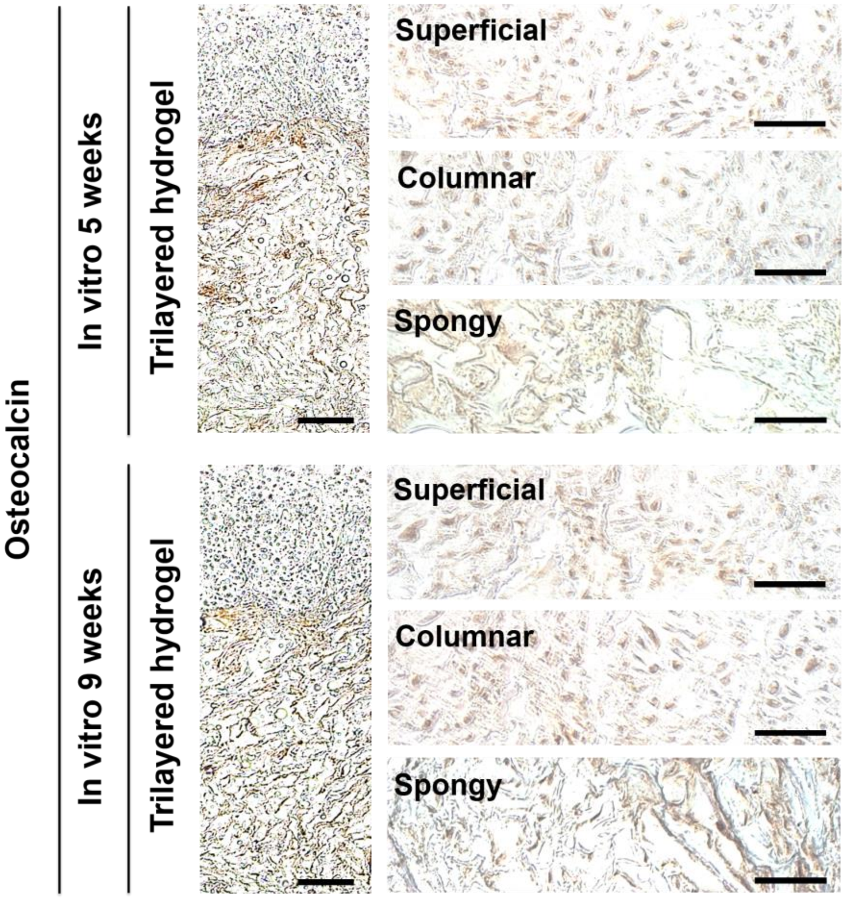

Figure 6.S10. Immunohistochemical staining for osteocalcin of the cell-laden trilayered hydrogel following 5 and 9 weeks of *in vitro* culture.

Scale bars indicate 200 µm. High magnification images for superficial, columnar, and spongy layer of the trilayered hydrogel are also provided. Scale bars represent 50 µm.

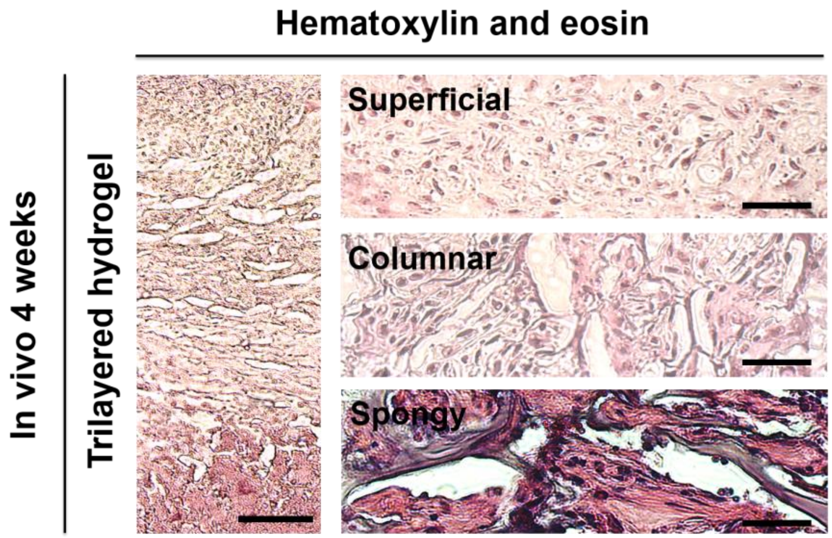

Figure 6.S11. H&E staining for the cell-laden trilayered hydrogel at 4 weeks post-implantation.

Scale bars represent 200 μm. High magnification images for superficial, columnar, and spongy layer of the trilayered hydrogel are also presented. Scale bars indicate 50 μm.

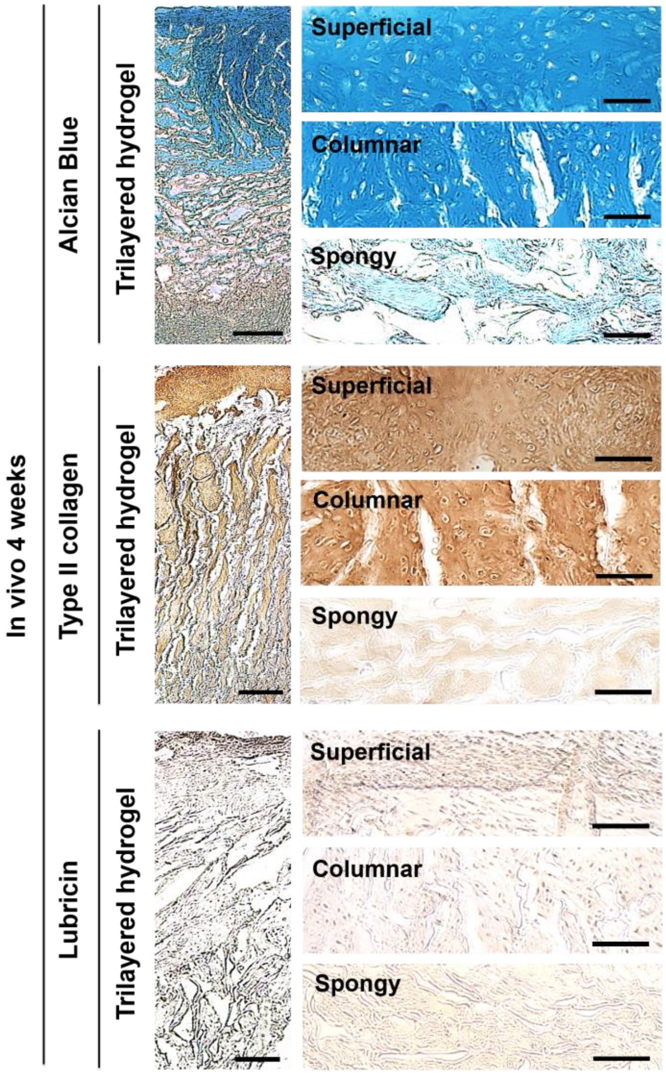

Figure 6.S12. The cell-laden superficial and columnar layer yield stratified neo-cartilage *in vivo*.

Alcian Blue staining and immunohistochemical staining for type II collagen and lubricin of the cell-laden trilayered hydrogel following 4 weeks of implantation. Scale bars indicate 200 μm. High magnification images for superficial, columnar, and spongy layer of the trilayered hydrogel are also provided. Scale bars represent 50 μm.

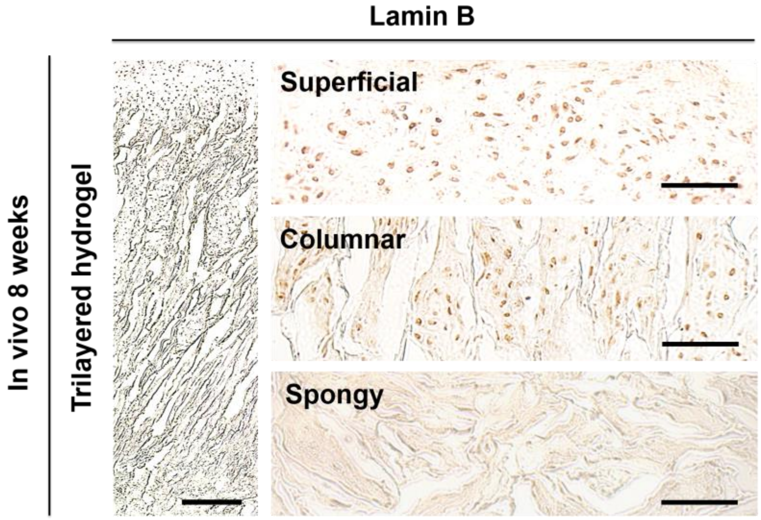

Figure 6.S13. Immunohistochemical staining for lamin B of the cell-laden trilayered hydrogel following 8 weeks of *in vivo* implantation.

Scale bar represents 200 μm. High magnification images for superficial, columnar, and spongy layer of the trilayered hydrogel are also shown. Scale bars represent 50 μm.

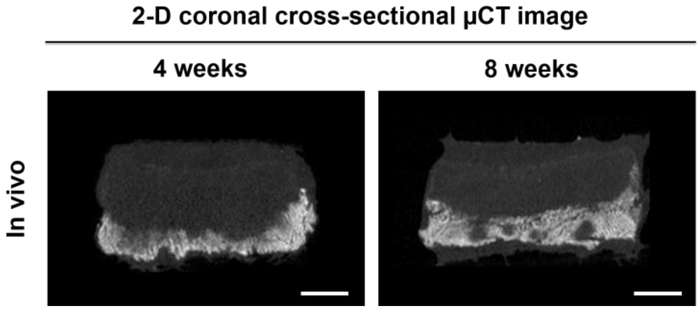

Figure 6.S14. The acellular biomineralized spongy layer induces calcified tissue formation within macroporous network *in vivo*.

2-D cross-sectional μCT image in coronal plane for the cell-laden trilayered hydrogel at 4 and 8 weeks post-implantation. Colors in white and gray indicate calcified and non-calcified tissue, respectively. Scale bars represent 2 mm.

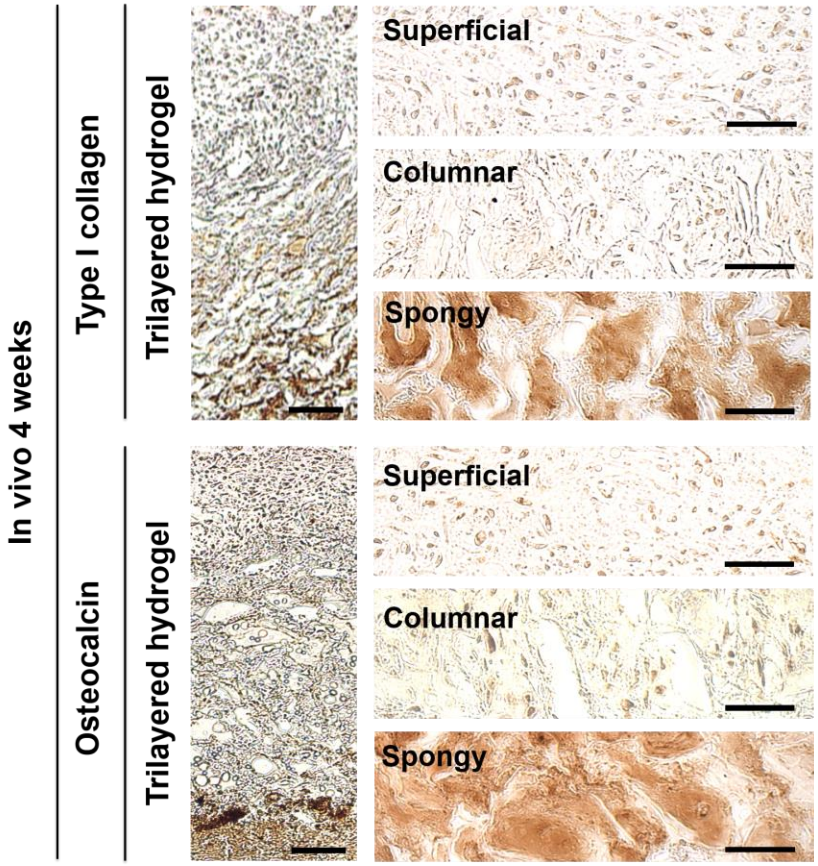

Figure 6.S15. The acellular biomineralized spongy layer facilitates neo-bone formation *in vivo*.

Immunohistochemical staining for type I collagen and osteocalcin of the cell-laden trilayered hydrogel at 4 weeks post-implantation. Scale bars represent 200 μm. High magnification images for superficial, columnar, and spongy layer of the trilayered hydrogel are also presented. Scale bars indicate 50 μm.

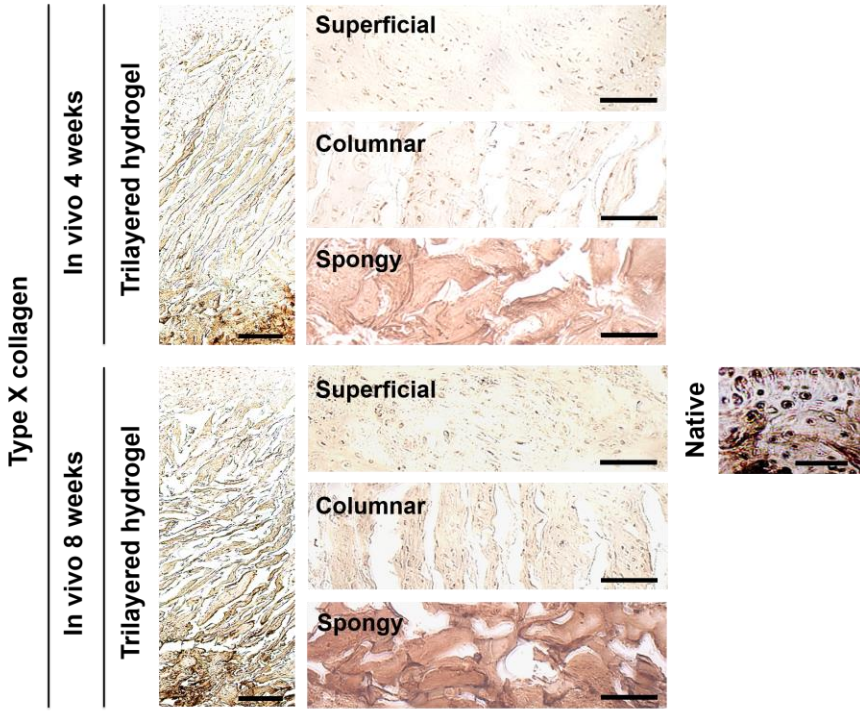

Figure 6.S16. Immunohistochemical staining for type X collagen of the cell-laden trilayered hydrogel after 4 and 8 weeks of *in vivo* implantation.

Scale bars indicate 200 μm. High magnification images for superficial, columnar, and spongy layer of the trilayered hydrogel as well as native osteochondral tissue are also presented. Scale bars represent 50 μm.

Chapter 7: Future Directions

The findings presented in this dissertation demonstrated osteogenicity of bone-mimetic biomineralized matrix and small molecule to direct osteogenic differentiation of human pluripotent stem cells (hPSCs) for bone tissue engineering. Furthermore, biomineralized matrix was found to be osteoinductive towards subchondral bone formation *in vivo* through host cell recruitment. In addition to biomineralized matrix, a small molecule, adenosine was found to direct conversion of hPSCs into functional osteoblasts such that hPSC-derived osteoblasts contributed to the healing of critical-sized bone defects. As an extension of these works, such osteogenicity of biomineralized matrix and small molecule can further lead to functional bone tissue engineering for translational applications. The underlying mechanisms of biomineralized matrix- and small molecule-driven osteogenic differentiation of hPSCs can be further investigated in a fundamental perspective. This chapter will discuss future directions that could extend from the presented works.

The application of biomineralized matrix or osteoblasts derived from small molecule-treated stem cells to functional healing of defects in load-bearing bone can accelerate the clinical use of such strategies. Recent studies by Reichert et al. showed superior biomechanical function of regenerated load-bearing bone when treated with tricalcium phosphate and bone morphogenetic protein-7 as compared to autografts [28]. Such findings present bright prospects for replacing the current use of native bone in treating segmental bone defects. Similarly, our results showing the healing of critical-sized bone defects by utilizing osteoblasts derived from human induced pluripotent stem cells (hiPSCs) through adenosine treatment suggest high potential of our presented strategies to regenerate such functional bone tissue without involving growth factors.

The utilization of biomineralized matrix for functional bone regeneration can extend to engineering functional osteochondral tissue, adding a new dimension to the application. Bhumiratana et al. recently demonstrated that biomechanical function of cartilage grown *in vitro* was similar to that of native cartilage [272]. Such findings show great promise for functional repair of cartilage defects *in vivo*. We demonstrated *in vivo* engineering of integrated osteochondral tissue with lubricin-rich surface by employing a trilayered scaffold containing biomineralized layer. Since lubricin is known to be responsible for lubricating function of cartilage, our findings suggest high feasibility of biomechanical function of the *in vivo* engineered osteochondral tissue. Furthermore, the *in vivo* engineered cartilage tissue was found to be integrated with subchondral neo-bone formed within the biomineralized layer through host cell recruitment. The ability of the biomineralized layer to recruit endogenous cells for in situ neo-bone formation suggests high potential to facilitate integration of the engineered osteochondral tissue with native bone, thereby promoting the repair of osteochondral defect. Together, the ability of the trilayered scaffold containing biomineralized layer for functional repair of osteochondral defect remains to be evaluated.

In addition to utilizing the osteogenicity of biomineralized matrix and small molecule for functional bone tissue engineering, the fundamental mechanism through which the biomineralized matrix and small molecule direct osteogenic differentiation of hPSCs necessitates further elucidation. We demonstrated the role of adenosine A2b receptor (A2bR) signaling in adenosine-induced osteogenic differentiation of hPSCs.

This is in accordance with our recent studies that have discovered the pivotal role of A2bR in biomineralized matrix-driven osteogenic differentiation of human mesenchymal stem cells (hMSCs) and human embryonic stem cells (hESCs) [39, 251]. Prior studies showed functionally dominant role of A2bR over other adenosine receptors in osteogenic differentiation of MSCs [208, 252]. It was also reported that A2bR knockout mice exhibited lower bone development and delayed bone fracture repair compared to wild type mice [207]. The role of A2bR in mediating osteogenesis of MSCs by activating adenylate cyclase and elevating intracellular cyclic adenosine monophosphate (cAMP) levels has been extensively documented [207, 252, 292, 293]. Recent studies showed that cAMP-mediated PKA activation promotes osteogenesis of human MSCs and *in vivo* bone formation [294]. On the other hand, it was recently reported that cAMP signaling suppressed osteogenesis of mouse ESCs at an early stage, but enhanced their osteogenic differentiation at a late stage [295]. Therefore, although A2bR signaling upregulates cAMP levels, downstream signaling cascades of A2bR may be cell species- or type-dependent and thus have yet to be revealed for hPSCs. Furthermore, it has been shown that A2aR mediates osteogenic differentiation of MSCs at a late stage, while A1aR inhibits osteogenesis of osteoprogenitor cells [208, 209]. Although we did not detect differences in the expression of other adenosine receptors during adenosine-induced osteogenesis, we do not rule out their possible involvement during osteogenic differentiation of hPSCs. Whether other adenosine receptors mediate the osteogenic commitment of hPSCs in a similar manner to somatic stem cells remains to be explored. Taken together, an increased understanding of underlying mechanisms for biomineralized matrix- and small molecule-mediated stem cell osteogenesis will accelerate their translational applications for functional bone tissue engineering.

References

[1] Wang Y, Azaïs T, Robin M, Vallée A, Catania C, Legriel P, Pehau-Arnaudet G, Babonneau F, Giraud-Guille M-M, Nassif N. The predominant role of collagen in the nucleation, growth, structure and orientation of bone apatite. Nature materials 2012;11:724-33.

[2] Roach H. Why does bone matrix contain non-collagenous proteins? The possible roles of osteocalcin, osteonectin, osteopontin and bone sialoprotein in bone mineralisation and resorption. Cell biology international 1994;18:617-28.

[3] Grynpas M. The crystallinity of bone mineral. Journal of Materials Science 1976;11:1691-6.

[4] Weiner S, Traub W. Bone structure: from angstroms to microns. The FASEB journal 1992;6:879-85.

[5] Launey ME, Buehler MJ, Ritchie RO. On the mechanistic origins of toughness in bone. Annual Review of Materials Research 2010;40:25-53.

[6] Ritchie RO. The conflicts between strength and toughness. Nature materials 2011;10:817-22.

[7] Lian JB, Stein GS. Concepts of osteoblast growth and differentiation: basis for modulation of bone cell development and tissue formation. Critical Reviews in Oral Biology & Medicine 1992;3:269-305.

[8] Ducy P, Schinke T, Karsenty G. The osteoblast: a sophisticated fibroblast under central surveillance. Science 2000;289:1501-4.

[9] Teitelbaum SL. Bone resorption by osteoclasts. Science 2000;289:1504-8.

[10] Spicer PP, Kretlow JD, Young S, Jansen JA, Kasper FK, Mikos AG. Evaluation of bone regeneration using the rat critical size calvarial defect. Nature protocols 2012;7:1918-29.

[11] Giannoudis PV, Dinopoulos H, Tsiridis E. Bone substitutes: an update. Injury 2005;36:S20-S7.

[12] Bhatt RA, Rozental TD. Bone graft substitutes. Hand clinics 2012;28:457-68.

[13] Shibuya N, Jupiter DC, Clawson LD, La Fontaine J. Incorporation of bovine-based structural bone grafts used in reconstructive foot surgery. The Journal of Foot and Ankle Surgery 2012;51:30-3.

[14] Li S, Chen H-C, Pierson D, Yuen D, Hansen P. NuOss™, a Bone Grafting Material for Oral Surgery: A Comparative Study with BioOss. White paper: Collagen Matrix Inc 2005.

[15] Berglundh T, Lindhe J. Healing around implants placed in bone defects treated with Bio-Oss®. An experimental study in the dog. Clinical Oral Implants Research 1997;8:117-24.

[16] Schliephake H, Scharnweber D, Dard M, Röβler S, Sewing A, Hüttmann C. Biological performance of biomimetic calcium phosphate coating of titanium implants in the dog mandible. Journal of Biomedical Materials Research Part A 2003;64:225-34.

[17] Geesink R, de Groot K, Klein C. Bonding of bone to apatite-coated implants. Journal of Bone & Joint Surgery, British Volume 1988;70:17-22.

[18] Le Guéhennec L, Soueidan A, Layrolle P, Amouriq Y. Surface treatments of titanium dental implants for rapid osseointegration. Dental materials 2007;23:844-54.

[19] Hayakawa T, Yoshinari M, Kiba H, Yamamoto H, Nemoto K, Jansen JA. Trabecular bone response to surface roughened and calcium phosphate (Ca-P) coated titanium implants. Biomaterials 2002;23:1025-31.

[20] LeGeros RZ. Calcium phosphate-based osteoinductive materials. Chemical reviews 2008;108:4742-53.

[21] Markovic M, Fowler BO, Tung MS. Preparation and comprehensive characterization of a calcium hydroxyapatite reference material. Journal of Research of the National Institute of Standards and Technology 2004;109:553-68.

[22] Famery R, Richard N, Boch P. Preparation of α-and β-tricalcium phosphate ceramics, with and without magnesium addition. Ceramics International 1994;20:327-36.

[23] LeGeros RZ. Preparation of octacalcium phosphate (OCP): a direct fast method. Calcified tissue international 1985;37:194-7.

[24] T FULMER M, Brown P. Hydrolysis of dicalcium phosphate dihydrate to hydroxyapatite. Journal of Materials Science: Materials in Medicine 1998;9:197-202.

[25] LeGeros R, Lin S, Rohanizadeh R, Mijares D, LeGeros J. Biphasic calcium phosphate bioceramics: preparation, properties and applications. Journal of materials science: Materials in Medicine 2003;14:201-9.

[26] Eanes ED. Amorphous calcium phosphate. Octacalcium Phosphate: Monogr. Oral Sci. Basel, Karger; 2001. p. 130-47.

[27] Moore WR, Graves SE, Bain GI. Synthetic bone graft substitutes. ANZ journal of surgery 2001;71:354-61.

[28] Reichert JC, Cipitria A, Epari DR, Saifzadeh S, Krishnakanth P, Berner A, Woodruff MA, Schell H, Mehta M, Schuetz MA. A tissue engineering solution for segmental defect regeneration in load-bearing long bones. Science Translational Medicine 2012;4:141ra93-ra93.

[29] Hwang NS, Varghese S, Lee HJ, Zhang Z, Elisseeff J. Biomaterials Directed In Vivo Osteogenic Differentiation of Mesenchymal Cells Derived from Human Embryonic Stem Cells. Tissue Engineering Part A 2013;19:1723-32.

[30] Yaylaoğlu M, Korkusuz P, Örs Ü, Korkusuz F, Hasirci V. Development of a calcium phosphate–gelatin composite as a bone substitute and its use in drug release. Biomaterials 1999;20:711-9.

[31] Song J, Xu J, Filion T, Saiz E, Tomsia AP, Lian JB, Stein GS, Ayers DC, Bertozzi CR. Elastomeric high-mineral content hydrogel-hydroxyapatite composites for orthopedic applications. Journal of Biomedical Materials Research Part A 2009;89:1098-107.

[32] Bhumiratana S, Grayson WL, Castaneda A, Rockwood DN, Gil ES, Kaplan DL, Vunjak-Novakovic G. Nucleation and growth of mineralized bone matrix on silk-hydroxyapatite composite scaffolds. Biomaterials 2011;32:2812-20.

[33] Woo KM, Seo J, Zhang R, Ma PX. Suppression of apoptosis by enhanced protein adsorption on polymer/hydroxyapatite composite scaffolds. Biomaterials 2007;28:2622-30.

[34] Rezwan K, Chen Q, Blaker J, Boccaccini AR. Biodegradable and bioactive porous polymer/inorganic composite scaffolds for bone tissue engineering. Biomaterials 2006;27:3413-31.

[35] Gkioni K, Leeuwenburgh SC, Douglas TE, Mikos AG, Jansen JA. Mineralization of hydrogels for bone regeneration. Tissue Engineering Part B: Reviews 2010;16:577-85.

[36] Kretlow JD, Mikos AG. Review: mineralization of synthetic polymer scaffolds for bone tissue engineering. Tissue engineering 2007;13:927-38.

[37] Murphy WL, Mooney DJ. Bioinspired growth of crystalline carbonate apatite on biodegradable polymer substrata. Journal of the American Chemical Society 2002;124:1910-7.

[38] Phadke A, Zhang C, Hwang Y, Vecchio K, Varghese S. Templated mineralization of synthetic hydrogels for bone-like composite materials: Role of matrix hydrophobicity. Biomacromolecules 2010;11:2060-8.

[39] Shih Y-RV, Hwang Y, Phadke A, Kang H, Hwang NS, Caro EJ, Nguyen S, Siu M, Theodorakis EA, Gianneschi NC. Calcium phosphate-bearing matrices induce osteogenic differentiation of stem cells through adenosine signaling. P Natl Acad Sci USA 2014;111:990-5.

[40] Suárez-González D, Barnhart K, Saito E, Vanderby R, Hollister SJ, Murphy WL. Controlled nucleation of hydroxyapatite on alginate scaffolds for stem cell-based bone tissue engineering. Journal of Biomedical Materials Research Part A 2010;95:222-34.

[41] Kawashita M, Nakao M, Minoda M, Kim H-M, Beppu T, Miyamoto T, Kokubo T, Nakamura T. Apatite-forming ability of carboxyl group-containing polymer gels in a simulated body fluid. Biomaterials 2003;24:2477-84.

[42] Suzuki S, Whittaker MR, Grøndahl L, Monteiro MJ, Wentrup-Byrne E. Synthesis of soluble phosphate polymers by RAFT and their in vitro mineralization. Biomacromolecules 2006;7:3178-87.

[43] Ball V, Michel M, Boulmedais F, Hemmerle J, Haikel Y, Schaaf P, Voegel JC. Nucleation kinetics of calcium phosphates on polyelectrolyte multilayers displaying internal secondary structure. Crystal growth & design 2006;6:327-34.

[44] Tanahashi M, Matsuda T. Surface functional group dependence on apatite formation on self-assembled monolayers in a simulated body fluid. Journal of biomedical materials research 1997;34:305-15.

[45] Osathanon T, Linnes ML, Rajachar RM, Ratner BD, Somerman MJ, Giachelli CM. Microporous nanofibrous fibrin-based scaffolds for bone tissue engineering. Biomaterials 2008;29:4091-9.

[46] Jongpaiboonkit L, Franklin-Ford T, Murphy WL. Mineral-Coated Polymer Microspheres for Controlled Protein Binding and Release. Advanced Materials 2009;21:1960-3.

[47] Suarez-Gonzalez D, Barnhart K, Migneco F, Flanagan C, Hollister SJ, Murphy WL. Controllable mineral coatings on PCL scaffolds as carriers for growth factor release. Biomaterials 2012;33:713-21.

[48] Pederson AW, Ruberti JW, Messersmith PB. Thermal assembly of a biomimetic mineral/collagen composite. Biomaterials 2003;24:4881-90.

[49] Douglas TE, Messersmith PB, Chasan S, Mikos AG, de Mulder EL, Dickson G, Schaubroeck D, Balcaen L, Vanhaecke F, Dubruel P. Enzymatic mineralization of hydrogels for bone tissue engineering by incorporation of alkaline phosphatase. Macromolecular bioscience 2012;12:1077-89.

[50] Bongio M, Nejadnik MR, Birgani ZT, Habibovic P, Kinard LA, Kasper FK, Mikos AG, Jansen JA, Leeuwenburgh SC, van den Beucken JJ. In Vitro and In Vivo Enzyme-Mediated Biomineralization of Oligo (poly (ethylene glycol) Fumarate Hydrogels. Macromolecular bioscience 2013;13:777-88.

[51] Choi S, Murphy WL. The effect of mineral coating morphology on mesenchymal stem cell attachment and expansion. Journal of Materials Chemistry 2012;22:25288-95.

[52] Song J, Saiz E, Bertozzi CR. A new approach to mineralization of biocompatible hydrogel scaffolds: an efficient process toward 3-dimensional bonelike composites. Journal of the American Chemical Society 2003;125:1236-43.

[53] Song J, Malathong V, Bertozzi CR. Mineralization of synthetic polymer scaffolds: a bottom-up approach for the development of artificial bone. Journal of the American Chemical Society 2005;127:3366-72.

[54] Hwang NS, Zhang C, Hwang YS, Varghese S. Mesenchymal stem cell differentiation and roles in regenerative medicine. Wiley Interdiscip Rev Syst Biol Med 2009;1:97-106.

[55] Yuan H, Fernandes H, Habibovic P, de Boer J, Barradas AM, de Ruiter A, Walsh WR, van Blitterswijk CA, de Bruijn JD. Osteoinductive ceramics as a synthetic alternative to autologous bone grafting. Proceedings of the National Academy of Sciences 2010;107:13614-9.

[56] Grayson WL, Bhumiratana S, Cannizzaro C, Chao P-HG, Lennon DP, Caplan AI, Vunjak-Novakovic G. Effects of initial seeding density and fluid perfusion rate on formation of tissue-engineered bone. Tissue Engineering Part A 2008;14:1809-20.

[57] Ter Brugge P, Wolke J, Jansen J. Effect of calcium phosphate coating crystallinity and implant surface roughness on differentiation of rat bone marrow cells. Journal of biomedical materials research 2002;60:70-8.

[58] Phadke A, Shih YR, Varghese S. Mineralized synthetic matrices as an instructive microenvironment for osteogenic differentiation of human mesenchymal stem cells. Macromol Biosci 2012;12:1022-32.

[59] Müller P, Bulnheim U, Diener A, Lüthen F, Teller M, Klinkenberg ED, Neumann HG, Nebe B, Liebold A, Steinhoff G. Calcium phosphate surfaces promote osteogenic

differentiation of mesenchymal stem cells. Journal of cellular and molecular medicine 2008;12:281-91.

[60] Cameron K, Travers P, Chander C, Buckland T, Campion C, Noble B. Directed osteogenic differentiation of human mesenchymal stem/precursor cells on silicate substituted calcium phosphate. J Biomed Mater Res A 2013;101:13-22.

[61] Both SK, van Apeldoorn AA, Jukes JM, Englund MC, Hyllner J, van Blitterswijk CA, de Boer J. Differential bone-forming capacity of osteogenic cells from either embryonic stem cells or bone marrow-derived mesenchymal stem cells. Journal of tissue engineering and regenerative medicine 2011;5:180-90.

[62] Marolt D, Knezevic M, Novakovic GV. Bone tissue engineering with human stem cells. Stem Cell Res Ther 2010;1.

[63] Teng S, Liu C, Krettek C, Jagodzinski M. The Application of Induced Pluripotent Stem Cells for Bone Regeneration: Current Progress and Prospects. Tissue Engineering Part B: Reviews 2014;20:328-39.

[64] Amabile G, Meissner A. Induced pluripotent stem cells: current progress and potential for regenerative medicine. Trends in molecular medicine 2009;15:59-68.

[65] Levi B, Hyun JS, Montoro DT, Lo DD, Chan CK, Hu S, Sun N, Lee M, Grova M, Connolly AJ. In vivo directed differentiation of pluripotent stem cells for skeletal regeneration. Proceedings of the National Academy of Sciences 2012;109:20379-84.

[66] Marcos-Campos I, Marolt D, Petridis P, Bhumiratana S, Schmidt D, Vunjak-Novakovic G. Bone scaffold architecture modulates the development of mineralized bone matrix by human embryonic stem cells. Biomaterials 2012;33:8329–42.

[67] Marolt D, Campos IM, Bhumiratana S, Koren A, Petridis P, Zhang G, Spitalnik PF, Grayson WL, Vunjak-Novakovic G. Engineering bone tissue from human embryonic stem cells. Proceedings of the National Academy of Sciences 2012;109:8705-9.

[68] de Peppo GM, Marcos-Campos I, Kahler DJ, Alsalman D, Shang L, Vunjak-Novakovic G, Marolt D. Engineering bone tissue substitutes from human induced pluripotent stem cells. Proceedings of the National Academy of Sciences 2013;110:8680-5.

[69] Kang R, Luo Y, Zou L, Xie L, Lysdahl H, Jiang X, Chen C, Bolund L, Chen M, Besenbacher F. Osteogenesis of human induced pluripotent stem cells derived mesenchymal stem cells on hydroxyapatite contained nanofibers. RSC Advances 2014;4:5734-9.

[70] Kang H, Wen C, Hwang Y, Shih Y-RV, Kar M, Seo SW, Varghese S. Biomineralized matrix-asssisted osteogenic differentiation of human embryonic stem cells. Journal of Materials Chemistry B 2014;2:5676-88.

[71] Kang H, Shih Y-RV, Hwang Y, Wen C, Rao V, Seo T, Varghese S. Mineralized gelatin methacrylate-based matrices induce osteogenic differentiation of human induced pluripotent stem cells. Acta Biomaterialia 2014;10:4961–70.

[72] Zhang Z-Y, Teoh S-H, Chong MS, Lee ES, Tan L-G, Mattar CN, Fisk NM, Choolani M, Chan J. Neo-vascularization and bone formation mediated by fetal mesenchymal stem cell tissue-engineered bone grafts in critical-size femoral defects. Biomaterials 2010;31:608-20.

[73] Kadiyala S, Jaiswal N, Bruder SP. Culture-expanded, bone marrow-derived mesenchymal stem cells can regenerate a critical-sized segmental bone defect. Tissue engineering 1997;3:173-85.

[74] Yuan J, Cui L, Zhang WJ, Liu W, Cao Y. Repair of canine mandibular bone defects with bone marrow stromal cells and porous β-tricalcium phosphate. Biomaterials 2007;28:1005-13.

[75] Marcacci M, Kon E, Moukhachev V, Lavroukov A, Kutepov S, Quarto R, Mastrogiacomo M, Cancedda R. Stem cells associated with macroporous bioceramics for long bone repair: 6-to 7-year outcome of a pilot clinical study. Tissue engineering 2007;13:947-55.

[76] Burdick JA, Mauck RL, Gorman JH, Gorman RC. Acellular biomaterials: an evolving alternative to cell-based therapies. Science translational medicine 2013;5:176ps4-ps4.

[77] Phadke A, Hwang Y, Hee Kim S, Hyun Kim S, Yamaguchi T, Masuda K, Varghese S. Effect of scaffold microarchitecture on osteogenic differentiation of human mesenchymal stem cells. Eur Cells Mater 2013;25:114-29.

[78] Suzuki O, Kamakura S, Katagiri T, Nakamura M, Zhao B, Honda Y, Kamijo R. Bone formation enhanced by implanted octacalcium phosphate involving conversion into Ca-deficient hydroxyapatite. Biomaterials 2006;27:2671-81.

[79] Hong SG, Winkler T, Wu C, Guo V, Pittaluga S, Nicolae A, Donahue RE, Metzger ME, Price SD, Uchida N. Path to the Clinic: Assessment of iPSC-Based Cell Therapies In Vivo in a Nonhuman Primate Model. Cell reports 2014;7:1298-309.

[80] Imranul Alam M, Asahina I, Ohmamiuda K, Takahashi K, Yokota S, Enomoto S. Evaluation of ceramics composed of different hydroxyapatite to tricalcium phosphate ratios as carriers for rhBMP-2. Biomaterials 2001;22:1643-51.

[81] Bose S, Tarafder S. Calcium phosphate ceramic systems in growth factor and drug delivery for bone tissue engineering: a review. Acta biomaterialia 2012;8:1401-21.

[82] Urist MR, Lietze A, Dawson E. β-tricalcium Phosphate Delivery System for Bone Morphogenetic Protein. Clinical orthopaedics and related research 1984;187:277-80.

[83] Urist M, Huo Y, Brownell A, Hohl W, Buyske J, Lietze A, Tempst P, Hunkapiller M, DeLange R. Purification of bovine bone morphogenetic protein by hydroxyapatite chromatography. Proceedings of the National Academy of Sciences 1984;81:371-5.

[84] Liu Y, Hunziker EB, Layrolle P, De Bruijn JD, De Groot K. Bone morphogenetic protein 2 incorporated into biomimetic coatings retains its biological activity. Tissue engineering 2004;10:101-8.

[85] Yuan H, Zou P, Yang Z, Zhang X, De Bruijn J, De Groot K. Bone morphogenetic protein and ceramic-induced osteogenesis. Journal of Materials Science: Materials in Medicine 1998;9:717-21.

[86] Alam M, Asahina I, Ohmamiuda K, Enomoto S. Comparative study of biphasic calcium phosphate ceramics impregnated with rhBMP-2 as bone substitutes. Journal of biomedical materials research 2001;54:129-38.

[87] Tsiridis E, Bhalla A, Ali Z, Gurav N, Heliotis M, Deb S, DiSilvio L. Enhancing the osteoinductive properties of hydroxyapatite by the addition of human mesenchymal stem cells, and recombinant human osteogenic protein-1 (BMP-7) in vitro. Injury 2006;37:S25-S32.

[88] Kong Z, Lin J, Yu M, Yu L, Li J, Weng W, Cheng K, Wang H. Enhanced loading and controlled release of rhBMP-2 in thin mineralized collagen coatings by aid of chitosan nanospheres and its biological evaluations. Journal of Materials Chemistry B 2014;2:4572-82.

[89] Yu X, Khalil A, Dang PN, Alsberg E, Murphy WL. Multilayered Inorganic Microparticles for Tunable Dual Growth Factor Delivery. Advanced Functional Materials 2014;24:3082-93.

[90] Maus U, Andereya S, Gravius S, Ohnsorge JA, Siebert CH, Niedhart C. BMP-2 incorporated in a tricalcium phosphate bone substitute enhances bone remodeling in sheep. Journal of biomaterials applications 2008;22:559-76.

[91] Matsumoto G, Omi Y, Kubota E, Ozono S, Tsuzuki H, Kinoshita Y, Yamamoto M, Tabata Y. Enhanced regeneration of critical bone defects using a biodegradable gelatin sponge and β-tricalcium phosphate with bone morphogenetic protein-2. Journal of biomaterials applications 2009;24:327-42.

[92] den Boer FC, Wippermann BW, Blokhuis TJ, Patka P, Bakker FC, Haarman HJTM. Healing of segmental bone defects with granular porous hydroxyapatite augmented with recombinant human osteogenic protein-I or autologous bone marrow. Journal of orthopaedic research 2003;21:521-8.

[93] Curtin CM, Cunniffe GM, Lyons FG, Bessho K, Dickson GR, Duffy GP, O'Brien FJ. Innovative Collagen Nano-Hydroxyapatite Scaffolds Offer a Highly Efficient Non-Viral Gene Delivery Platform for Stem Cell-Mediated Bone Formation. Advanced Materials 2012;24:749-54.

[94] Krebs MD, Salter E, Chen E, Sutter KA, Alsberg E. Calcium phosphate-DNA nanoparticle gene delivery from alginate hydrogels induces in vivo osteogenesis. Journal of Biomedical Materials Research Part A 2010;92:1131-8.

[95] Karageorgiou V, Kaplan D. Porosity of 3D biomaterial scaffolds and osteogenesis. Biomaterials 2005;26:5474-91.

[96] Kasten P, Beyen I, Niemeyer P, Luginbühl R, Bohner M, Richter W. Porosity and pore size of β-tricalcium phosphate scaffold can influence protein production and osteogenic differentiation of human mesenchymal stem cells: an in vitro and in vivo study. Acta Biomaterialia 2008;4:1904-15.

[97] Yang H, Zeng H, Hao L, Zhao N, Du C, Liao H, Wang Y. Effects of hydroxyapatite microparticles morphology on bone mesenchymal stem cell behavior. Journal of Materials Chemistry B 2014;2:4703-10.

[98] Choi S, Murphy WL. A screening approach reveals the influence of mineral coating morphology on human mesenchymal stem cell differentiation. Biotechnology journal 2013;8:496–501.

[99] Ducheyne P, Radin S, King L. The effect of calcium phosphate ceramic composition and structure on in vitro behavior. I. Dissolution. Journal of biomedical materials research 1993;27:25-34.

[100] Radin S, Ducheyne P. The effect of calcium phosphate ceramic composition and structure on in vitro behavior. II. Precipitation. Journal of biomedical materials research 1993;27:35-45.

[101] Chai YC, Roberts SJ, Desmet E, Kerckhofs G, van Gastel N, Geris L, Carmeliet G, Schrooten J, Luyten FP. Mechanisms of ectopic bone formation by human osteoprogenitor cells on CaP biomaterial carriers. Biomaterials 2012;33:3127-42.

[102] Barradas AM, Monticone V, Hulsman M, Danoux C, Fernandes H, Tahmasebi Birgani Z, Barrere-de Groot F, Yuan H, Reinders M, Habibovic P, van Blitterswijk C, de Boer J. Molecular mechanisms of biomaterial-driven osteogenic differentiation in human

mesenchymal stromal cells. Integrative biology : quantitative biosciences from nano to macro 2013;5:920-31.

[103] Hu Q, Tan Z, Liu Y, Tao J, Cai Y, Zhang M, Pan H, Xu X, Tang R. Effect of crystallinity of calcium phosphate nanoparticles on adhesion, proliferation, and differentiation of bone marrow mesenchymal stem cells. Journal of Materials Chemistry 2007;17:4690-8.

[104] Liu YK, Lu QZ, Pei R, Ji HJ, Zhou GS, Zhao XL, Tang RK, Zhang M. The effect of extracellular calcium and inorganic phosphate on the growth and osteogenic differentiation of mesenchymal stem cells in vitro: implication for bone tissue engineering. Biomedical Materials 2009;4:025004.

[105] Wen L, Wang Y, Wang H, Kong L, Zhang L, Chen X, Ding Y. L-type calcium channels play a crucial role in the proliferation and osteogenic differentiation of bone marrow mesenchymal stem cells. Biochemical and Biophysical Research Communications 2012;424: 439–45.

[106] Barradas A, Fernandes HA, Groen N, Chai YC, Schrooten J, van de Peppel J, van Leeuwen JP, van Blitterswijk CA, de Boer J. A calcium-induced signaling cascade leading to osteogenic differentiation of human bone marrow-derived mesenchymal stromal cells. Biomaterials 2012;33:3205-15.

[107] Suárez-González D, Lee JS, Lan Levengood SK, Vanderby Jr R, Murphy WL. Mineral coatings modulate β-TCP stability and enable growth factor binding and release. Acta biomaterialia 2012;8:1117-24.

[108] Zhang W, Liao S, Cui F. Hierarchical self-assembly of nano-fibrils in mineralized collagen. Chemistry of Materials 2003;15:3221-6.

[109] Liao S, Cui F, Zhang W, Feng Q. Hierarchically biomimetic bone scaffold materials: Nano-HA/collagen/PLA composite. Journal of Biomedical Materials Research Part B: Applied Biomaterials 2004;69:158-65.

[110] Nassif N, Gobeaux F, Seto J, Belamie E, Davidson P, Panine P, Mosser G, Fratzl P, Giraud Guille M-M. Self-assembled collagen− apatite matrix with bone-like hierarchy. Chemistry of Materials 2010;22:3307-9.

[111] Liu X, Lin K, Wu C, Wang Y, Zou Z, Chang J. Multilevel Hierarchically Ordered Artificial Biomineral. Small 2014;10:152-9.

[112] Gbureck U, Hölzel T, Klammert U, Würzler K, Müller FA, Barralet JE. Resorbable dicalcium phosphate bone substitutes prepared by 3D powder printing. Advanced Functional Materials 2007;17:3940-5.

[113] Leukers B, Gülkan H, Irsen SH, Milz S, Tille C, Schieker M, Seitz H. Hydroxyapatite scaffolds for bone tissue engineering made by 3D printing. Journal of Materials Science: Materials in Medicine 2005;16:1121-4.

[114] Seitz H, Rieder W, Irsen S, Leukers B, Tille C. Three-dimensional printing of porous ceramic scaffolds for bone tissue engineering. Journal of Biomedical Materials Research Part B: Applied Biomaterials 2005;74:782-8.

[115] Warnke PH, Seitz H, Warnke F, Becker ST, Sivananthan S, Sherry E, Liu Q, Wiltfang J, Douglas T. Ceramic scaffolds produced by computer-assisted 3D printing and sintering: Characterization and biocompatibility investigations. Journal of Biomedical Materials Research Part B: Applied Biomaterials 2010;93:212-7.

[116] Scotti C, Piccinini E, Takizawa H, Todorov A, Bourgine P, Papadimitropoulos A, Barbero A, Manz MG, Martin I. Engineering of a functional bone organ through endochondral ossification. Proceedings of the National Academy of Sciences 2013;110:3997-4002.

[117] Odorico JS, Kaufman DS, Thomson JA. Multilineage differentiation from human embryonic stem cell lines. Stem Cells 2001;19:193-204.

[118] Murry CE, Keller G. Differentiation of embryonic stem cells to clinically relevant populations: lessons from embryonic development. Cell 2008;132:661-80.

[119] Wobus AM, Boheler KR. Embryonic stem cells: prospects for developmental biology and cell therapy. Physiological reviews 2005;85:635-78.

[120] Borowiak M, Maehr R, Chen S, Chen AE, Tang W, Fox JL, Schreiber SL, Melton DA. Small molecules efficiently direct endodermal differentiation of mouse and human embryonic stem cells. Cell stem cell 2009;4:348-58.

[121] Zhu S, Wurdak H, Wang J, Lyssiotis CA, Peters EC, Cho CY, Wu X, Schultz PG. A small molecule primes embryonic stem cells for differentiation. Cell stem cell 2009;4:416-26.

[122] Pang ZP, Yang N, Vierbuchen T, Ostermeier A, Fuentes DR, Yang TQ, Citri A, Sebastiano V, Marro S, Sudhof TC, Wernig M. Induction of human neuronal cells by defined transcription factors. Nature 2011;476:220-3.

[123] Marklein RA, Burdick JA. Controlling stem cell fate with material design. Adv Mater 2010;22:175-89.

[124] Benoit DS, Schwartz MP, Durney AR, Anseth KS. Small functional groups for controlled differentiation of hydrogel-encapsulated human mesenchymal stem cells. Nat Mater 2008;7:816-23.

[125] Ayala R, Zhang C, Yang D, Hwang Y, Aung A, Shroff SS, Arce FT, Lal R, Arya G, Varghese S. Engineering the cell-material interface for controlling stem cell adhesion, migration, and differentiation. Biomaterials 2011;32:3700-11.

[126] Dalby MJ, Gadegaard N, Tare R, Andar A, Riehle MO, Herzyk P, Wilkinson CD, Oreffo RO. The control of human mesenchymal cell differentiation using nanoscale symmetry and disorder. Nat Mater 2007;6:997-1003.

[127] Engler AJ, Sen S, Sweeney HL, Discher DE. Matrix elasticity directs stem cell lineage specification. Cell 2006;126:677-89.

[128] Huebsch N, Arany PR, Mao AS, Shvartsman D, Ali OA, Bencherif SA, Rivera-Feliciano J, Mooney DJ. Harnessing traction-mediated manipulation of the cell/matrix interface to control stem-cell fate. Nat Mater 2010;9:518-26.

[129] Lutolf MP, Gilbert PM, Blau HM. Designing materials to direct stem-cell fate. Nature 2009;462:433-41.

[130] Lutolf MP, Hubbell JA. Synthetic biomaterials as instructive extracellular microenvironments for morphogenesis in tissue engineering. Nat Biotechnol 2005;23:47-55.

[131] Hwang Y, Phadke A, Varghese S. Engineered microenvironments for self-renewal and musculoskeletal differentiation of stem cells. Regenerative medicine 2011;6:505-24.

[132] Phadke A, Shih YRV, Varghese S. Mineralized synthetic matrices as an instructive microenvironment for osteogenic differentiation of human mesenchymal stem cells. Macromolecular bioscience 2012;12:1022-32.

[133] Phadke A, Hwang Y, Hee Kim S, Hyun Kim S, Yamaguchi T, Masuda K, Varghese S. Effect of scaffold microarchitecture on osteogenic differentiation of human mesenchymal stem cells. Eur Cell Mater 2013;25:114-29.

[134] Song G, Habibovic P, Bao C, Hu J, van Blitterswijk CA, Yuan H, Chen W, Xu HH. The homing of bone marrow MSCs to non-osseous sites for ectopic bone formation induced by osteoinductive calcium phosphate. Biomaterials 2013;34:2167–76.

[135] Roberts SJ, Geris L, Kerckhofs G, Desmet E, Schrooten J, Luyten FP. The combined bone forming capacity of human periosteal derived cells and calcium phosphates. Biomaterials 2011;32:4393-405.

[136] Chou YF, Huang W, Dunn JC, Miller TA, Wu BM. The effect of biomimetic apatite structure on osteoblast viability, proliferation, and gene expression. Biomaterials 2005;26:285-95.

[137] Vaquette C, Ivanovski S, Hamlet SM, Hutmacher DW. Effect of culture conditions and calcium phosphate coating on ectopic bone formation. Biomaterials 2013;34:5538-51.

[138] Sottile V, Thomson A, McWhir J. In vitro osteogenic differentiation of human ES cells. Cloning & Stem Cells 2003;5:149-55.

[139] Bielby RC, Boccaccini AR, Polak JM, Buttery LD. In vitro differentiation and in vivo mineralization of osteogenic cells derived from human embryonic stem cells. Tissue engineering 2004;10:1518-25.

[140] Smith LA, Liu X, Hu J, Ma PX. The enhancement of human embryonic stem cell osteogenic differentiation with nano-fibrous scaffolding. Biomaterials 2010;31:5526-35.

[141] Hwang Y, Zhang C, Varghese S. Poly (ethylene glycol) cryogels as potential cell scaffolds: effect of polymerization conditions on cryogel microstructure and properties. Journal of Materials Chemistry 2010;20:345-51.

[142] Bryant SJ, Cuy JL, Hauch KD, Ratner BD. Photo-patterning of porous hydrogels for tissue engineering. Biomaterials 2007;28:2978-86.

[143] Chang CW, Hwang Y, Brafman D, Hagan T, Phung C, Varghese S. Engineering cell-material interfaces for long-term expansion of human pluripotent stem cells. Biomaterials 2013;34:912-21.

[144] Heinonen JK, Lahti RJ. A New and Convenient Colorimetric Determination of Inorganic Ortho-Phosphate and Its Application to the Assay of Inorganic Pyrophosphatase. Anal Biochem 1981;113:313-7.

[145] Lim JI, Lee Y-K. EVA-enhanced embedding medium for histological analysis of 3D porous scaffold material. Micron 2009;40:756-60.

[146] Phadke A, Zhang C, Hwang Y, Vecchio K, Varghese S. Templated mineralization of synthetic hydrogels for bone-like composite materials: role of matrix hydrophobicity. Biomacromolecules 2010;11:2060-8.

[147] Maxian SH, Di Stefano T, Melican MC, Tiku ML, Zawadsky JP. Bone cell behavior on Matrigel-coated Ca/P coatings of varying crystallinities. J Biomed Mater Res 1998;40:171-9.

[148] Ducheyne P, Radin S, King L. The effect of calcium phosphate ceramic composition and structure on in vitro behavior. I. Dissolution. Journal of biomedical materials research 1993;27:25-34.

[149] Radin SR, Ducheyne P. The effect of calcium phosphate ceramic composition and structure on in vitro behavior. II. Precipitation. J Biomed Mater Res 1993;27:35-45.

[150] Autefage H, Briand-Mesange F, Cazalbou S, Drouet C, Fourmy D, Goncalves S, Salles JP, Combes C, Swider P, Rey C. Adsorption and release of BMP-2 on nanocrystalline apatite-coated and uncoated hydroxyapatite/beta-tricalcium phosphate porous ceramics. Journal of biomedical materials research Part B, Applied biomaterials 2009;91:706-15.

[151] Lee JS, Suarez-Gonzalez D, Murphy WL. Mineral coatings for temporally controlled delivery of multiple proteins. Adv Mater 2011;23:4279-84.

[152] Wen L, Wang Y, Wang H, Kong L, Zhang L, Chen X, Ding Y. L-type calcium channels play a crucial role in the proliferation and osteogenic differentiation of bone marrow mesenchymal stem cells. Biochemical and biophysical research communications 2012;424:439-45.

[153] Allegrucci C, Young LE. Differences between human embryonic stem cell lines. Human reproduction update 2007;13:103-20.

[154] Both SK, van Apeldoorn AA, Jukes JM, Englund MC, Hyllner J, van Blitterswijk CA, de Boer J. Differential bone-forming capacity of osteogenic cells from either embryonic stem cells or bone marrow-derived mesenchymal stem cells. J Tissue Eng Regen Med 2011;5:180-90.

[155] Yuan H, Fernandes H, Habibovic P, de Boer J, Barradas AM, de Ruiter A, Walsh WR, van Blitterswijk CA, de Bruijn JD. Osteoinductive ceramics as a synthetic alternative to autologous bone grafting. Proceedings of the National Academy of Sciences of the United States of America 2010;107:13614-9.

[156] Wobus AM, Boheler KR. Embryonic stem cells: prospects for developmental biology and cell therapy. Physiological reviews 2005;85:635-78.

[157] Takahashi K, Tanabe K, Ohnuki M, Narita M, Ichisaka T, Tomoda K, Yamanaka S. Induction of pluripotent stem cells from adult human fibroblasts by defined factors. cell 2007;131:861-72.

[158] Teng S, Liu C, Krettek C, Jagodzinski M. The Application of Induced Pluripotent Stem Cells for Bone Regeneration: Current Progress and Prospects. Tissue Engineering Part B: Reviews 2013.

[159] Illich DJ, Demir N, Stojković M, Scheer M, Rothamel D, Neugebauer J, Hescheler J, Zöller JE. Concise review: induced pluripotent stem cells and lineage reprogramming: prospects for bone regeneration. Stem Cells 2011;29:555-63.

[160] Discher DE, Mooney DJ, Zandstra PW. Growth factors, matrices, and forces combine and control stem cells. Science 2009;324:1673-7.

[161] Hwang Y, Phadke A, Varghese S. Engineered microenvironments for self-renewal and musculoskeletal differentiation of stem cells. Regenerative medicine 2011;6:505-24.

[162] Saha K, Pollock JF, Schaffer DV, Healy KE. Designing synthetic materials to control stem cell phenotype. Current opinion in chemical biology 2007;11:381-7.

[163] Phadke A, Hwang Y, Hee Kim S, Hyun Kim S, Yamaguchi T, Masuda K, Varghese S. Effect of scaffold microarchitecture on osteogenic differentiation of human mesenchymal stem cells. European cells & materials 2013;25:114-29.

[164] Seyedjafari E, Soleimani M, Ghaemi N, Shabani I. Nanohydroxyapatite-coated electrospun poly (l-lactide) nanofibers enhance osteogenic differentiation of stem cells and induce ectopic bone formation. Biomacromolecules 2010;11:3118-25.

[165] Kang H, Wen C, Hwang Y, Shih Y-RV, Kar M, Seo SW, Varghese S. Biomineralized matrix-assisted osteogenic differentiation of human embryonic stem cells Journal of Materials Chemistry B 2014.

[166] Heino J. The collagen family members as cell adhesion proteins. Bioessays 2007;29:1001-10.

[167] Hutson CB, Nichol JW, Aubin H, Bae H, Yamanlar S, Al-Haque S, Koshy ST, Khademhosseini A. Synthesis and characterization of tunable poly (ethylene glycol): gelatin methacrylate composite hydrogels. Tissue Engineering Part A 2011;17:1713-23.

[168] Chen YC, Lin RZ, Qi H, Yang Y, Bae H, Melero-Martin JM, Khademhosseini A. Functional human vascular network generated in photocrosslinkable gelatin methacrylate hydrogels. Advanced functional materials 2012;22:2027-39.

[169] Talwar R, Di Silvio L, Hughes FJ, King GN. Effects of carrier release kinetics on bone morphogenetic protein-2-induced periodontal regeneration in vivo. Journal of clinical periodontology 2001;28:340-7.

[170] Park KM, Lee Y, Son JY, Oh DH, Lee JS, Park KD. Synthesis and characterizations of in situ cross-linkable gelatin and 4-arm-PPO-PEO hybrid hydrogels via enzymatic reaction for tissue regenerative medicine. Biomacromolecules 2012;13:604-11.

[171] Benton JA, DeForest CA, Vivekanandan V, Anseth KS. Photocrosslinking of gelatin macromers to synthesize porous hydrogels that promote valvular interstitial cell function. Tissue Engineering Part A 2009;15:3221-30.

[172] Nichol JW, Koshy ST, Bae H, Hwang CM, Yamanlar S, Khademhosseini A. Cell-laden microengineered gelatin methacrylate hydrogels. Biomaterials 2010;31:5536-44.

[173] Zou L, Luo Y, Chen M, Wang G, Ding M, Petersen CC, Kang R, Dagnaes-Hansen F, Zeng Y, Lv N. A simple method for deriving functional MSCs and applied for osteogenesis in 3D scaffolds. Scientific reports 2013;3.

[174] Ardeshirylajimi A, Dinarvand P, Seyedjafari E, Langroudi L, Adegani FJ, Soleimani M. Enhanced reconstruction of rat calvarial defects achieved by plasma-treated electrospun scaffolds and induced pluripotent stem cells. Cell and tissue research 2013;354:849-60.

[175] Ardeshirylajimi A, Hosseinkhani S, Parivar K, Yaghmaie P, Soleimani M. Nanofiber-based polyethersulfone scaffold and efficient differentiation of human induced pluripotent stem cells into osteoblastic lineage. Molecular biology reports 2013:1-8.

[176] Liu J, Chen W, Zhao Z, Xu HH. Reprogramming of mesenchymal stem cells derived from iPSCs seeded on biofunctionalized calcium phosphate scaffold for bone engineering. Biomaterials 2013;34:7862-72.

[177] Bryant SJ, Cuy JL, Hauch KD, Ratner BD. Photo-patterning of porous hydrogels for tissue engineering. Biomaterials 2007;28:2978-86.

[178] Oyane A, Kim HM, Furuya T, Kokubo T, Miyazaki T, Nakamura T. Preparation and assessment of revised simulated body fluids. J Biomed Mater Res A 2003;65:188-95.

[179] Yu J, Vodyanik MA, Smuga-Otto K, Antosiewicz-Bourget J, Frane JL, Tian S, Nie J, Jonsdottir GA, Ruotti V, Stewart R. Induced pluripotent stem cell lines derived from human somatic cells. Science 2007;318:1917-20.

[180] McBeath R, Pirone DM, Nelson CM, Bhadriraju K, Chen CS. Cell shape, cytoskeletal tension, and RhoA regulate stem cell lineage commitment. Developmental cell 2004;6:483-95.

[181] Deans RJ, Moseley AB. Mesenchymal stem cells: biology and potential clinical uses. Experimental hematology 2000;28:875-84.

[182] Baksh D, Song L, Tuan R. Adult mesenchymal stem cells: characterization, differentiation, and application in cell and gene therapy. Journal of cellular and molecular medicine 2004;8:301-16.

[183] Beresford J, Bennett J, Devlin C, Leboy P, Owen M. Evidence for an inverse relationship between the differentiation of adipocytic and osteogenic cells in rat marrow stromal cell cultures. Journal of cell science 1992;102:341-51.

[184] Jaiswal RK, Jaiswal N, Bruder SP, Mbalaviele G, Marshak DR, Pittenger MF. Adult human mesenchymal stem cell differentiation to the osteogenic or adipogenic lineage is regulated by mitogen-activated protein kinase. Journal of Biological Chemistry 2000;275:9645-52.

[185] Cheng S-L, Shao J-S, Charlton-Kachigian N, Loewy AP, Towler DA. MSX2 promotes osteogenesis and suppresses adipogenic differentiation of multipotent mesenchymal progenitors. Journal of Biological Chemistry 2003;278:45969-77.

[186] Rosen CJ, Bouxsein ML. Mechanisms of disease: is osteoporosis the obesity of bone? Nature Clinical Practice Rheumatology 2006;2:35-43.

[187] Zhao LJ, Jiang H, Papasian CJ, Maulik D, Drees B, Hamilton J, Deng HW. Correlation of obesity and osteoporosis: effect of fat mass on the determination of osteoporosis. Journal of Bone and Mineral Research 2008;23:17-29.

[188] Schnitzler CM. Bone quality: a determinant for certain risk factors for bone fragility. Calcified tissue international 1993;53:S27-S31.

[189] Devlin MJ, Rosen CJ. The bone–fat interface: basic and clinical implications of marrow adiposity. The Lancet Diabetes & Endocrinology 2014.

[190] Pino AM, Ríos S, Astudillo P, Fernández M, Figueroa P, Seitz G, Rodríguez JP. Concentration of adipogenic and proinflammatory cytokines in the bone marrow supernatant fluid of osteoporotic women. Journal of Bone and Mineral Research 2010;25:492-8.

[191] Cao JJ. Effects of obesity on bone metabolism. J Orthop Surg Res 2011;6:30-6.

[192] Makki K, Froguel P, Wolowczuk I. Adipose tissue in obesity-related inflammation and insulin resistance: cells, cytokines, and chemokines. ISRN inflammation 2013;2013.

[193] Misra M, Klibanski A. Anorexia nervosa, obesity and bone metabolism. Pediatric endocrinology reviews: PER 2013;11:21-33.

[194] Scheller EL, Song J, Dishowitz MI, Soki FN, Hankenson KD, Krebsbach PH. Leptin functions peripherally to regulate differentiation of mesenchymal progenitor cells. Stem Cells 2010;28:1071-80.

[195] Xian L, Wu X, Pang L, Lou M, Rosen CJ, Qiu T, Crane J, Frassica F, Zhang L, Rodriguez JP. Matrix IGF-1 maintains bone mass by activation of mTOR in mesenchymal stem cells. Nature medicine 2012;18:1095-101.

[196] Engler AJ, Sen S, Sweeney HL, Discher DE. Matrix elasticity directs stem cell lineage specification. Cell 2006;126:677-89.

[197] Young DA, Choi YS, Engler AJ, Christman KL. Stimulation of adipogenesis of adult adipose-derived stem cells using substrates that mimic the stiffness of adipose tissue. Biomaterials 2013;34:8581-8.

[198] Dalby MJ, Gadegaard N, Tare R, Andar A, Riehle MO, Herzyk P, Wilkinson CD, Oreffo RO. The control of human mesenchymal cell differentiation using nanoscale symmetry and disorder. Nat Mater 2007;6:997-1003.

[199] Ayala R, Zhang C, Yang D, Hwang Y, Aung A, Shroff SS, Arce FT, Lal R, Arya G, Varghese S. Engineering the cell–material interface for controlling stem cell adhesion, migration, and differentiation. Biomaterials 2011;32:3700-11.

[200] Benoit DS, Schwartz MP, Durney AR, Anseth KS. Small functional groups for controlled differentiation of hydrogel-encapsulated human mesenchymal stem cells. Nature materials 2008;7:816-23.

[201] Kilian KA, Bugarija B, Lahn BT, Mrksich M. Geometric cues for directing the differentiation of mesenchymal stem cells. Proceedings of the National Academy of Sciences 2010;107:4872-7.

[202] Guvendiren M, Burdick JA. The control of stem cell morphology and differentiation by hydrogel surface wrinkles. Biomaterials 2010;31:6511-8.

[203] Bouillon R, Suda T. Vitamin D: calcium and bone homeostasis during evolution. BoneKEy reports 2014;3.

[204] Barrère F, van Blitterswijk CA, de Groot K. Bone regeneration: molecular and cellular interactions with calcium phosphate ceramics. international Journal of Nanomedicine 2006;1:317.

[205] Kang H, Shih Y-RV, Rao V, Varghese S. Biomineralized matrices as intelligent scaffolds for bone tissue regeneration. In: Khang G, editor. Handbook of Intelligent Scaffolds for Tissue Engineering and Regenerative Medicine, 2nd Edition: Pan Stanford Publishing Pte. Ltd. ; in press.

[206] Jensen B, Farach-Carson MC, Kenaley E, Akanbi KA. High extracellular calcium attenuates adipogenesis in 3T3-L1 preadipocytes. Experimental cell research 2004;301:280-92.

[207] Carroll SH, Wigner NA, Kulkarni N, Johnston-Cox H, Gerstenfeld LC, Ravid K. A2B adenosine receptor promotes mesenchymal stem cell differentiation to osteoblasts and bone formation in vivo. Journal of Biological Chemistry 2012;287:15718-27.

[208] Gharibi B, Abraham AA, Ham J, Evans BA. Adenosine receptor subtype expression and activation influence the differentiation of mesenchymal stem cells to osteoblasts and adipocytes. Journal of Bone and Mineral Research 2011;26:2112-24.

[209] Gharibi B, Abraham A, Ham J, Evans B. Contrasting effects of A1 and A2b adenosine receptors on adipogenesis. International journal of obesity 2011;36:397-406.

[210] Zhang L, Paddon C, Lewis MD, Grennan-Jones F, Ludgate M. Gsα signalling suppresses PPARγ2 generation and inhibits 3T3L1 adipogenesis. Journal of Endocrinology 2009;202:207-15.

[211] Liu X, Malbon CC, Wang H-y. Identification of amino acid residues of Gsα critical to repression of adipogenesis. Journal of Biological Chemistry 1998;273:11685-94.

[212] Eisenstein A, Carroll SH, Johnston-Cox H, Farb M, Gokce N, Ravid K. An Adenosine Receptor-Krüppel-like Factor 4 Protein Axis Inhibits Adipogenesis. Journal of Biological Chemistry 2014;289:21071-81.

[213] Birsoy K, Chen Z, Friedman J. Transcriptional regulation of adipogenesis by KLF4. Cell metabolism 2008;7:339-47.

[214] Kim JH, Kim K, Youn BU, Lee J, Kim I, Shin H-I, Akiyama H, Choi Y, Kim N. Kruppel-like factor 4 attenuates osteoblast formation, function, and cross talk with osteoclasts. The Journal of cell biology 2014;204:1063-74.

[215] Li J, Dong J, Zhang Zh, Zhang DC, You XY, Zhong Y, Chen MS, Liu SM. miR-10a restores human mesenchymal stem cell differentiation by repressing KLF4. Journal of cellular physiology 2013;228:2324-36.

[216] Pera MF, Trounson AO. Human embryonic stem cells: prospects for development. Development 2004;131:5515-25.

[217] Hwang NS, Varghese S, Elisseeff J. Controlled differentiation of stem cells. Advanced drug delivery reviews 2008;60:199-214.

[218] Murry CE, Keller G. Differentiation of embryonic stem cells to clinically relevant populations: lessons from embryonic development. Cell 2008;132:661-80.

[219] Lebkowski JS, Gold J, Xu C, Funk W, Chiu C-P, Carpenter MK. Human embryonic stem cells: culture, differentiation, and genetic modification for regenerative medicine applications. Cancer journal (Sudbury, Mass) 2000;7:S83-93.

[220] Lutolf MP, Gilbert PM, Blau HM. Designing materials to direct stem-cell fate. Nature 2009;462:433-41.

[221] Schugar R, Robbins P, Deasy B. Small molecules in stem cell self-renewal and differentiation. Gene therapy 2008;15:126-35.

[222] Li W, Ding S. Small molecules that modulate embryonic stem cell fate and somatic cell reprogramming. Trends in pharmacological sciences 2010;31:36-45.

[223] Brey DM, Motlekar NA, Diamond SL, Mauck RL, Garino JP, Burdick JA. High-throughput screening of a small molecule library for promoters and inhibitors of mesenchymal stem cell osteogenic differentiation. Biotechnology and bioengineering 2011;108:163-74.

[224] Tsutsui H, Valamehr B, Hindoyan A, Qiao R, Ding X, Guo S, Witte ON, Liu X, Ho C-M, Wu H. An optimized small molecule inhibitor cocktail supports long-term maintenance of human embryonic stem cells. Nature communications 2011;2:167.

[225] Chen S, Do JT, Zhang Q, Yao S, Yan F, Peters EC, Schöler HR, Schultz PG, Ding S. Self-renewal of embryonic stem cells by a small molecule. Proceedings of the National Academy of Sciences 2006;103:17266-71.

[226] Chen S, Borowiak M, Fox JL, Maehr R, Osafune K, Davidow L, Lam K, Peng LF, Schreiber SL, Rubin LL. A small molecule that directs differentiation of human ESCs into the pancreatic lineage. Nature chemical biology 2009;5:258-65.

[227] Minami I, Yamada K, Otsuji TG, Yamamoto T, Shen Y, Otsuka S, Kadota S, Morone N, Barve M, Asai Y. A small molecule that promotes cardiac differentiation of human pluripotent stem cells under defined, cytokine-and xeno-free conditions. Cell reports 2012;2:1448-60.

[228] Siller R, Greenhough S, Naumovska E, Sullivan GJ. Small-Molecule-Driven Hepatocyte Differentiation of Human Pluripotent Stem Cells. Stem cell reports 2015;4:939-52.

[229] Kanke K, Masaki H, Saito T, Komiyama Y, Hojo H, Nakauchi H, Lichtler AC, Takato T, Chung U-i, Ohba S. Stepwise Differentiation of Pluripotent Stem Cells into Osteoblasts Using Four Small Molecules under Serum-free and Feeder-free Conditions. Stem Cell Reports 2014;2:751-60.

[230] Chen S, Zhang Q, Wu X, Schultz PG, Ding S. Dedifferentiation of lineage-committed cells by a small molecule. Journal of the American Chemical Society 2004;126:410-1.

[231] Ladewig J, Mertens J, Kesavan J, Doerr J, Poppe D, Glaue F, Herms S, Wernet P, Kögler G, Müller F-J. Small molecules enable highly efficient neuronal conversion of human fibroblasts. Nature methods 2012;9:575-8.

[232] Wang H, Cao N, Spencer CI, Nie B, Ma T, Xu T, Zhang Y, Wang X, Srivastava D, Ding S. Small molecules enable cardiac reprogramming of mouse fibroblasts with a single factor, Oct4. Cell reports 2014;6:951-60.

[233] Lin T, Ambasudhan R, Yuan X, Li W, Hilcove S, Abujarour R, Lin X, Hahm HS, Hao E, Hayek A. A chemical platform for improved induction of human iPSCs. Nature methods 2009;6:805-8.

[234] Huangfu D, Maehr R, Guo W, Eijkelenboom A, Snitow M, Chen AE, Melton DA. Induction of pluripotent stem cells by defined factors is greatly improved by small-molecule compounds. Nature biotechnology 2008;26:795-7.

[235] Hou P, Li Y, Zhang X, Liu C, Guan J, Li H, Zhao T, Ye J, Yang W, Liu K. Pluripotent stem cells induced from mouse somatic cells by small-molecule compounds. Science 2013;341:651-4.

[236] Misra J, Mohanty ST, Madan S, Fernandes JA, Ebetino FH, Graham R, Russell G, Bellantuono I. Zoledronate Attenuates Accumulation of DNA Damage in Mesenchymal Stem Cells and Protects their Function. Stem cells 2015.

[237] Wu X, Ding S, Ding Q, Gray NS, Schultz PG. A small molecule with osteogenesis-inducing activity in multipotent mesenchymal progenitor cells. Journal of the American Chemical Society 2002;124:14520-1.

[238] Lo KWH, Kan HM, Ashe KM, Laurencin CT. The small molecule PKA-specific cyclic AMP analogue as an inducer of osteoblast-like cells differentiation and mineralization. Journal of tissue engineering and regenerative medicine 2012;6:40-8.

[239] Chang C-W, Hwang Y, Brafman D, Hagan T, Phung C, Varghese S. Engineering cell–material interfaces for long-term expansion of human pluripotent stem cells. Biomaterials 2013;34:912-21.

[240] Borrmann T, Hinz S, Bertarelli DC, Li W, Florin NC, Scheiff AB, Müller CE. 1-Alkyl-8-(piperazine-1-sulfonyl) phenylxanthines: development and characterization of adenosine A2B receptor antagonists and a new radioligand with subnanomolar affinity and subtype specificity. Journal of medicinal chemistry 2009;52:3994-4006.

[241] Hwang YS, Zhang C, Varghese S. Poly(ethylene glycol) cryogels as potential cell scaffolds: effect of polymerization conditions on cryogel microstructure and properties. Journal of Materials Chemistry 2010;20:345-51.

[242] Lin S, Sangaj N, Razafiarison T, Zhang C, Varghese S. Influence of physical properties of biomaterials on cellular behavior. Pharmaceutical research 2011;28:1422-30.

[243] Bellows C, Heersche J, Aubin J. Inorganic phosphate added exogenously or released from β-glycerophosphate initiates mineralization of osteoid nodules in vitro. Bone and mineral 1992;17:15-29.

[244] Cheng S-L, Yang JW, Rifas L, Zhang S-F, Avioli LV. Differentiation of human bone marrow osteogenic stromal cells in vitro: induction of the osteoblast phenotype by dexamethasone. Endocrinology 1994;134:277-86.

[245] Cowan CM, Shi Y-Y, Aalami OO, Chou Y-F, Mari C, Thomas R, Quarto N, Contag CH, Wu B, Longaker MT. Adipose-derived adult stromal cells heal critical-size mouse calvarial defects. Nature biotechnology 2004;22:560-7.

[246] Daval J-L, Nehlig A, Nicolas F. Physiological and pharmacological properties of adenosine: therapeutic implications. Life sciences 1991;49:1435-53.

[247] Layland J, Carrick D, Lee M, Oldroyd K, Berry C. Adenosine: Physiology, pharmacology, and clinical applications. JACC: Cardiovascular Interventions 2014;7:581-91.

[248] Cunha R. Adenosine as a neuromodulator and as a homeostatic regulator in the nervous system: different roles, different sources and different receptors. Neurochemistry international 2001;38:107-25.

[249] Collis MG. The vasodilator role of adenosine. Pharmacology & therapeutics 1989;41:143-62.

[250] Xu C, Rosler E, Jiang J, Lebkowski JS, Gold JD, O'Sullivan C, Delavan-Boorsma K, Mok M, Bronstein A, Carpenter MK. Basic fibroblast growth factor supports undifferentiated human embryonic stem cell growth without conditioned medium. Stem cells 2005;23:315-23.

[251] Rao V, Shih Y-RV, Kang H, Kabra H, Varghese S. Adenosine signaling mediates osteogenic differentiation of human embryonic stem cells on mineralized matrices. Frontiers in bioengineering and biotechnology 2015;3:1-10.

[252] Ciciarello M, Zini R, Rossi L, Salvestrini V, Ferrari D, Manfredini R, Lemoli RM. Extracellular purines promote the differentiation of human bone marrow-derived mesenchymal stem cells to the osteogenic and adipogenic lineages. Stem cells and development 2012;22:1097-111.

[253] Kaigler D, Wang Z, Horger K, Mooney DJ, Krebsbach PH. VEGF scaffolds enhance angiogenesis and bone regeneration in irradiated osseous defects. Journal of Bone and Mineral Research 2006;21:735-44.

[254] Matsuo K, Irie N. Osteoclast–osteoblast communication. Archives of biochemistry and biophysics 2008;473:201-9.

[255] Poole CA. Review. Articular cartilage chondrons: form, function and failure. Journal of anatomy 1997;191:1-13.

[256] Broom N. Further insights into the structural principles governing the function of articular cartilage. Journal of anatomy 1984;139:275.

[257] Wong M, Carter D. Articular cartilage functional histomorphology and mechanobiology: a research perspective. Bone 2003;33:1-13.

[258] Filardo G, Madry H, Jelic M, Roffi A, Cucchiarini M, Kon E. Mesenchymal stem cells for the treatment of cartilage lesions: from preclinical findings to clinical application in orthopaedics. Knee Surgery, Sports Traumatology, Arthroscopy 2013;21:1717-29.

[259] Erisken C, Kalyon DM, Wang H, Örnek-Ballanco C, Xu J. Osteochondral tissue formation through adipose-derived stromal cell differentiation on biomimetic polycaprolactone nanofibrous scaffolds with graded insulin and beta-glycerophosphate concentrations. Tissue Eng Pt A 2011;17:1239-52.

[260] Re'em T, Witte F, Willbold E, Ruvinov E, Cohen S. Simultaneous regeneration of articular cartilage and subchondral bone induced by spatially presented TGF-beta and BMP-4 in a bilayer affinity binding system. Acta biomaterialia 2012;8:3283-93.

[261] Dormer NH, Singh M, Wang L, Berkland CJ, Detamore MS. Osteochondral interface tissue engineering using macroscopic gradients of bioactive signals. Annals of biomedical engineering 2010;38:2167-82.

[262] Chen J, Chen H, Li P, Diao H, Zhu S, Dong L, Wang R, Guo T, Zhao J, Zhang J. Simultaneous regeneration of articular cartilage and subchondral bone in vivo using MSCs induced by a spatially controlled gene delivery system in bilayered integrated scaffolds. Biomaterials 2011;32:4793-805.

[263] Marklein RA, Burdick JA. Controlling stem cell fate with material design. Advanced Materials 2010;22:175-89.

[264] Kang H, Shih Y-RV, Hwang Y, Wen C, Rao V, Seo T, Varghese S. Mineralized gelatin methacrylate-based matrices induce osteogenic differentiation of human induced pluripotent stem cells. Acta Biomaterialia 2014.

[265] Wen C, Kang H, Shih Y-RV, Hwang Y, Varghese S. In vivo comparison of biomineralized scaffold-directed osteogenic differentiation of human embryonic and mesenchymal stem cells. Drug delivery and translational research 2015:1-11.

[266] Shih Y-R, Phadke A, Yamaguchi T, Kang H, Inoue N, Masuda K, Varghese S. Synthetic bone mimetic matrix-mediated in situ bone tissue formation through host cell recruitment. Acta Biomater 2015;19:1-9.

[267] Gomoll AH, Madry H, Knutsen G, van Dijk N, Seil R, Brittberg M, Kon E. The subchondral bone in articular cartilage repair: current problems in the surgical management. Knee Surgery, Sports Traumatology, Arthroscopy 2010;18:434-47.

[268] Klein TJ, Malda J, Sah RL, Hutmacher DW. Tissue engineering of articular cartilage with biomimetic zones. Tissue Eng Pt B-Rev 2009;15:143-57.

[269] Steele J, McCullen S, Callanan A, Autefage H, Accardi M, Dini D, Stevens M. Combinatorial scaffold morphologies for zonal articular cartilage engineering. Acta Biomater 2014;10:2065-75.

[270] Woodfield T, Blitterswijk CV, Wijn JD, Sims T, Hollander A, Riesle J. Polymer scaffolds fabricated with pore-size gradients as a model for studying the zonal organization within tissue-engineered cartilage constructs. Tissue Eng 2005;11:1297-311.

[271] McCullen SD, Autefage H, Callanan A, Gentleman E, Stevens MM. Anisotropic fibrous scaffolds for articular cartilage regeneration. Tissue Engineering Part A 2012;18:2073-83.

[272] Bhumiratana S, Eton RE, Oungoulian SR, Wan LQ, Ateshian GA, Vunjak-Novakovic G. Large, stratified, and mechanically functional human cartilage grown in vitro by mesenchymal condensation. Proceedings of the National Academy of Sciences 2014;111:6940-5.

[273] Moscona A. Rotation-mediated histogenetic aggregation of dissociated cells: a quantifiable approach to cell interactions in vitro. Experimental cell research 1961;22:455-75.

[274] Manning WK, Bonner WM. Isolation and culture of chondrocytes from human adult articular cartilage. Arthritis & Rheumatism 1967;10:235-9.

[275] Hwang NS, Varghese S, Puleo C, Zhang Z, Elisseeff J. Morphogenetic signals from chondrocytes promote chondrogenic and osteogenic differentiation of mesenchymal stem cells. Journal of cellular physiology 2007;212:281-4.

[276] Fischer J, Dickhut A, Rickert M, Richter W. Human articular chondrocytes secrete parathyroid hormone–related protein and inhibit hypertrophy of mesenchymal stem cells in coculture during chondrogenesis. Arthritis & Rheumatism 2010;62:2696-706.

[277] Tacchetti C, Tavella S, Dozin B, Quarto R, Robino G, Cancedda R. Cell condensation in chondrogenic differentiation. Experimental cell research 1992;200:26-33.

[278] Hutmacher DW. Scaffold design and fabrication technologies for engineering tissues—state of the art and future perspectives. Journal of Biomaterials Science, Polymer Edition 2001;12:107-24.

[279] Henderson TM, Ladewig K, Haylock DN, McLean KM, O'Connor AJ. Cryogels for biomedical applications. J Mater Chem B 2013;1:2682-95.

[280] Zhang H, Hussain I, Brust M, Butler MF, Rannard SP, Cooper AI. Aligned two-and three-dimensional structures by directional freezing of polymers and nanoparticles. Nat Mater 2005;4:787-93.

[281] Bai H, Wang D, Delattre B, Gao W, De Coninck J, Li S, Tomsia AP. Biomimetic gradient scaffold from ice-templating for self-seeding of cells with capillary effect. Acta Biomater 2015;20:113-9.

[282] Wu J, Zhao Q, Sun J, Zhou Q. Preparation of poly (ethylene glycol) aligned porous cryogels using a unidirectional freezing technique. Soft Matter 2012;8:3620-6.

[283] Lai JH, Kajiyama G, Smith RL, Maloney W, Yang F. Stem cells catalyze cartilage formation by neonatal articular chondrocytes in 3D biomimetic hydrogels. Sci Rep 2013;3.

[284] Bian L, Zhai DY, Mauck RL, Burdick JA. Coculture of human mesenchymal stem cells and articular chondrocytes reduces hypertrophy and enhances functional properties of engineered cartilage. Tissue Eng Pt A 2011;17:1137-45.

[285] Schumacher BL, Block J, Schmid T, Aydelotte M, Kuettner K. A novel proteoglycan synthesized and secreted by chondrocytes of the superficial zone of articular cartilage. Archives of biochemistry and biophysics 1994;311:144-52.

[286] Zappone B, Greene GW, Oroudjev E, Jay GD, Israelachvili JN. Molecular aspects of boundary lubrication by human lubricin: Effect of disulfide bonds and enzymatic digestion. Langmuir 2008;24:1495-508.

[287] Bao J-p, Chen W-p, Wu L-d. Lubricin: a novel potential biotherapeutic approaches for the treatment of osteoarthritis. Mol Biol Rep 2011;38:2879-85.

[288] Nugent GE, Aneloski NM, Schmidt TA, Schumacher BL, Voegtline MS, Sah RL. Dynamic shear stimulation of bovine cartilage biosynthesis of proteoglycan 4. Arthritis & Rheumatism 2006;54:1888-96.

[289] Sendemir-Urkmez A, Jamison RD. The addition of biphasic calcium phosphate to porous chitosan scaffolds enhances bone tissue development in vitro. J Biomed Mater Res A 2007;81:624-33.

[290] Silva M, Cyster L, Barry J, Yang X, Oreffo R, Grant D, Scotchford C, Howdle S, Shakesheff K, Rose F. The effect of anisotropic architecture on cell and tissue infiltration into tissue engineering scaffolds. Biomaterials 2006;27:5909-17.

[291] Duncan RL, Akanbi KA, Farach-Carson MC. Calcium signals and calcium channels in osteoblastic cells. Seminars in nephrology: [New York, NY]: Grune & Stratton,[c1981]-; 1998. p. 178-90.

[292] Mediero A, Cronstein BN. Adenosine and bone metabolism. Trends in Endocrinology & Metabolism 2013;24:290-300.

[293] Ham J, Evans BAJ. An emerging role for adenosine and its receptors in bone homeostasis. Frontiers in endocrinology 2012;3.

[294] Siddappa R, Martens A, Doorn J, Leusink A, Olivo C, Licht R, van Rijn L, Gaspar C, Fodde R, Janssen F. cAMP/PKA pathway activation in human mesenchymal stem cells in vitro results in robust bone formation in vivo. Proceedings of the National Academy of Sciences 2008;105:7281-6.

[295] Zhang S, Kaplan F, Shore E. Different roles of GNAS and cAMP signaling during early and late stages of osteogenic differentiation. Hormone and metabolic research= Hormon-und Stoffwechselforschung= Hormones et metabolisme 2012;44:724.